Investigating Ultrafast Condensed-Phase Chemical Dynamics with Coherent Multidimensional Spectroscopy

by

Carlos R. Baiz

A dissertation submitted in partial fulfillment
of the requirements for the degree of
Doctor of Philosophy
(Chemistry)
in the University of Michigan
2011

Doctoral Committee:

Assistant Professor Kevin J. Kubarych, Chair
Professor Eitan Geva
Professor Roseanne J. Sension
Assistant Professor Barry. D. Dunietz
Assistant Professor Jennifer P. Ogilvie

To Sarah

Acknowledgements

I am indebted to the people who made my graduate experience at Michigan immensely enjoyable, intellectually challenging and particularly fruitful.

Firstly I thank Prof. Kevin Kubarych for training me to think as a scientist. His remarkable insights, creativity, physical intuition, and clear explanations have been central to my scientific development. His passion for science and continued enthusiasm for discussing experimental and simulation results has made my experience in his group truly enjoyable, rewarding, and productive.

I thank past and present members of the Kubarych group: Dr. Matthew Nee who taught me the numerous intricacies of non-linear IR experiments; Robert (Bobby) McCanne for the many insightful discussions on transient-2DIR spectroscopy; Matthew Ross whose practical knowledge of optics and electronics has been quite beneficial to the entire group; and Jessica Anna whose work on upconversion-detected 2DIR has greatly improved in the quality of the measured spectra.

I thank Prof. Barry Dunietz for teaching me electronic structure theory. His practical advice on selecting the proper electronic structure method for the system at hand and his deep insights into many practical problems has been central to the success of several projects. I also thank Prof. Dunietz for kindly providing access to his computational resources for many of the projects.

Through many intense discussions, Prof. Eitan Geva has taught me the majority of what I know about chemical dynamics from a theoretical perspective. I am very grateful to have had the opportunity to work with Prof. Geva on modeling experimental results. These joint collaborations have greatly enriched my knowledge of physical chemistry.

Prof. Edwin Sibert (University of Wisconsin-Madison) has taught me a lot about vibrational structure. I thank him for his patience in answering my newbie questions about coupled Morse oscillators. The collaboration project with him has been particularly instructive and rewarding.

I am thankful to my candidacy committee members, Prof. Barry Dunietz, Prof. Eitan Geva, Prof. Kevin Kubarych, Prof. Jennifer Ogilvie and Prof. Roseanne Sension for all the scientific and academic advice that they have provided throughout my graduate career.

I acknowledge funding from the University of Michigan, in particular the Rackham Graduate School for a Pre-doctoral Fellowship, a Graduate Student Instructor Award, a Graduate Student Research Grant, and numerous Travel Grants. I thank the Chemistry Department for an Excellence in Research Fellowship.

Lastly, I would like to thank my parents Ana and Gustavo Baiz for all their support during my undergraduate years.

I dedicate this work to my wife and best friend Sarah Baiz.

Table of Contents

List of Figures

List of Tables

List of Abbreviations

1D: one dimensional
2D: two dimensional
2DIR: two dimensional infrared (spectrocopy)
B3LYP: Becke's three-parameter/ Lee Yang Parr
BBO: beta-barium borate
bET: back electron transfer
BP86: Becke 1989 /Perdew 1986 (functional)
CCD: charged coupled device
CIS: configuration interaction single excitations
CP: chirped pulse
CPU: chirped pulse upconversion
DFG: difference frequency generation
DFT: density functional theory
DMDC: dimanganese decacarbonyl
DSE: Debye-Stokes-Einstein (theory)
DVE: dispersed vibrational echo
ESA: excited-state absorption
FT: Fourier transform
FTIR: Fourier transform infrared (spectroscopy)
FWHM: full-width at half maximum
GSB: ground-state bleach
HDVE: heterodyned dispersed vibrational echo
HF: Hartree-Fock
HOMO: highest occupied molecular orbital
IHT: intramolecular hydrogen-atom transfer
IntraCA: intraband coupling approximation
IR: infrared
IVR: intramolecular vibrational redistribution
LNB: lithium niobate
LUMO: lowest unoccupied molecular orbital
MCT: mercury cadmium telluride (detector)
MD: molecular dynamics
NMR: nuclear magnetic resonance
NOPA: noncollinear optical parametric amplifier
NP: noise percentage
NPT: number of particles, pressure, temperature (conserved)
NVE: number of particles, volume, energy (conserved)
OD: optical density
OPA: optical parametric amplifier
PES: potential energy surface
QME: quantum master equation
RDC: acetilacetonato rhodium dicarbonyl
RESP: restrained electrostatic potential
RMS: root mean square
RWA: rotating wave approximation
SNR: signal-to-noise ratio
t-2DIR: transient two dimensional infrared spectroscopy
TA: transient absorption
TE: triggered-exchange
TS: transition state
UHF: unrestricted Hartree-Fock
UV: ultraviolet
VER: vibrational energy relaxation
VPT2: second order vibrational perturbation theory
VSE: vibrational Stark-effect (spectroscopy)

Abstract

Experimental and theoretical studies of ultrafast chemical dynamics in solution are presented in this work. Condensed-phase chemical reactions are investigated with newly-developed experimental techniques, including non-equilibrium two-dimensional infrared spectroscopy, transient-dispersed vibrational echo spectroscopy, and vibrational Stark-effect spectroscopy. The experiments are aimed at elucidating the complex relationship between molecules and their solvent environment under equilibrium and non-equilibrium conditions. The orientational relaxation rates of hot radical molecules in non-polar solvents were measured with transient-two-dimensional infrared spectroscopy to obtain the vibrational energy relaxation (cooling) rates following a homolytic bond cleavage reaction. Experimental studies of the asymmetric, solvent-caged radical recombination reactions offered new insights into the solvent role in determining the branching ratios and recombination rates in these asymmetric reactions.

Dynamic vibrational Stark-effect spectroscopy is demonstrated as a new probe of molecular dynamics in solution. Within this method, a charge-transfer reaction is optically triggered, causing a change in the electric field at the nearby solvent molecules. The vibrational response of the solvent molecules serves to map the electrostatic changes at the chromophore as well as elucidate the dynamics of the molecules within the first solvation shell. The solvent response is measured upon optically triggering an electron-transfer reaction in the solvatochromic dye Betaine-30. The rate of the back-electron transfer, which returns the dye molecules to the ground state, has been measured from the solvent response.

In addition to molecular dynamics, two-dimensional infrared spectroscopy can directly access the one- and two-quanta energy levels of the system which directly reports on the anharmonic potential of the molecules. The potential surface of dimanganese decacarbonyl and its photoproducts has been modeled up to fourth order in the normal-mode coordinates using *ab-initio* electronic structure methods. The energy levels are found to

be in agreement with experiment. The vibrational dynamics of dimanganese decacarbonyl are modeled using a Markovian quantum master equation with bilinear system-bath coupling. The model accounts for vibrational relaxation, coherence dephasing, coherence transfer and coherence-population coupling. The transport rates are computed using input from molecular dynamics simulations.

Chapter 1

Introduction

1.1 Condensed-phase Chemical Dynamics

From proton-transfer[1-6] to protein folding,[7-17] liquid-phase chemical reactions are guided by the motions of the solvent.[15, 18] Fluctuations of the solvent govern the dynamics of the reactants and transition states, and in many cases also determine the outcome of a chemical reaction. In turn, the solute influences the dynamics of the nearby solvent molecules[19-21] and the timescales of chemical reactions are dictated in part by the interactions with the solvent: Diffusion rates determine the frequency of molecular collisions, and the solvent relaxation—how rapidly molecules adapt to a new electrostatic environment—determines the stability of transition states and products.[22, 23]

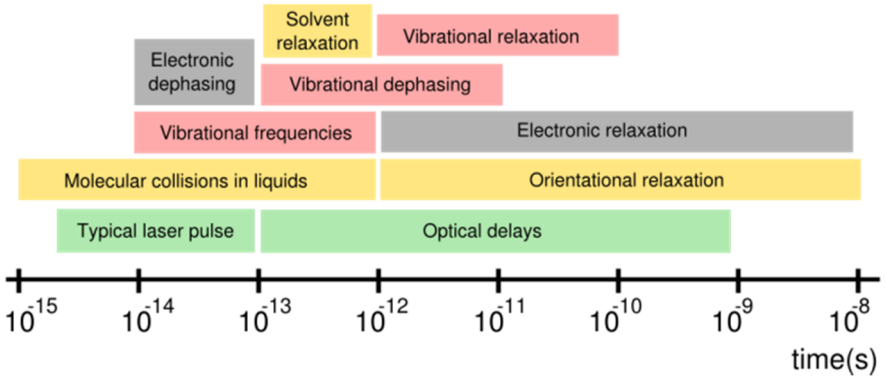

Figure 1.1: Relevant timescales of condensed-phase chemical dynamics and spectroscopy. Adapted from reference 24.

One particular goal of physical chemistry is to understand how these microscopic fluctuations affect the kinetic rates of chemical reactions. Understanding complex, condensed-phase systems over a wide range of timescales is a difficult challenge for experiment and theory. While experiments are now beginning to access molecular dynamics on multiple timescales, molecular simulations are limited to a smaller range of timescales.[10, 25-27] For example, it is extremely challenging to simulate the minute-long folding reaction of a protein but it is relatively straightforward to simulate the pico to nanosecond equilibrium fluctuations of the same system.[10] Consequently, there is great interest in understanding how the nature of subpicosecond, microscopic fluctuations affects the pathways and rates of chemical reactions. The work presented in the following chapters explores the role of the solvent in determining the ultrafast chemical dynamics of species under non-equilibrium conditions. The experiments are carried out using variants of transient multidimensional infrared spectroscopy supported by classical and quantum dynamics simulations. In this chapter a general background of chemical dynamics and multidimensional spectroscopy is presented, including a brief discussion of the experimental methods and theoretical models related to the work presented in the following chapters. Figure 1.1 shows relevant timescales for condensed-phase dynamics and ultrafast spectroscopy.

1.2 Nonlinear Spectroscopy

Measuring ultrafast condensed-phase dynamics requires sub-Angstrom and sub-picosecond resolution. The energy levels of the molecules provide the spatial resolution as these are highly dependent on the molecular geometry as well as the microscopic environment of the solvent.[28-30] The time-resolution is afforded by the ultrafast laser pulses—typically ranging from 10-100 fs in duration—which measure the transitions between energy levels. Molecular dynamics are often measured in the form of time-dependent absorbances. For example, ultrafast transient-absorption spectroscopy measures the changes in reactant and product absorptions as a function of time delay after a molecule is excited or a reaction is initiated by a laser pulse.[31, 32]

Unlike nuclear spin resonances, electronic and vibrational transitions are particularly sensitive to the microscopic environment surrounding a molecule; different environments give rise to slightly different transition frequencies which are typically observed as an overall

broadening of the absorption peaks.[33] While strong electronic transitions make UV/Visible transient-absorption spectroscopy well suited to measuring small differences in the number of reactants or products following optically-triggered reactions, vibrational frequencies can be readily mapped to chemical structures. Therefore, vibrational spectroscopy provides a level of microscopic detail not typically afforded by its electronic counterpart.[30, 34] Given a sufficiently accurate theoretical description of the system, vibrational spectroscopy can provide a bond-by-bond view of the geometric changes—bond lengths, bond angles—occurring during a chemical reaction in bulk solution or in a protein matrix.[34]

1.3 Coherent Multidimensional Spectroscopy

Coherent multidimensional spectroscopy, a technique developed over the last decade, measures joint correlation maps between frequencies in a sample. Structural information is extracted from the two-dimensional peak positions and intensities, whereas dynamics are typically extracted from the time evolution of the spectra following excitation.[35, 36] The multiple light-matter interactions of ultrafast multidimensional spectroscopy serve to map out the energy-level structure of the system and to measure the correlations between the fluctuating frequencies within the various transitions.[37, 38] Vibrational dynamics, such as energy redistribution or vibrational relaxation, are usually measured in the form of time-dependent amplitudes of the peaks as a function of the delay between the excitation and detection processes .[38, 39]

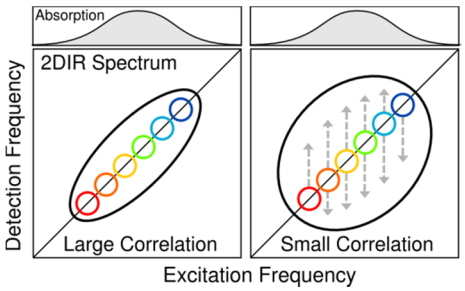

Figure 1.2 : Schematic representation of two-dimensional spectra at different waiting times. The different microstates are indicated by the circles. The arrows represent the changes in frequencies due to fluctuations of the solvent environment around the chromophores. The upper panels show how the absorption spectrum in both cases would look qualitatively similar.

Conceptually two-dimensional infrared (2DIR) spectroscopy[40] can be thought of as a sequence of interactions between the vibrations and the electric fields of the laser pulses:

these are described as an excitation interaction, a waiting period, and a detection interaction. The two axes in a 2DIR spectrum correspond to the excitation frequency and the detection frequency (first and third interactions) while the evolution of the peaks along the waiting time is usually plotted separately. The theoretical framework and experimental implementation of 2DIR and its non-equilibrium variants will be discussed in Chapter 2; here we discuss some aspects of 2DIR in more general terms. In essence, a 2DIR spectrum is a two-dimensional correlation map between a set of excited frequencies and a set of detected frequencies.[40, 41] By varying the time delay between excitation and detection, the loss of frequency correlation can be directly measured.[42, 43] Figure 1.2 shows a schematic representation of how two-dimensional spectroscopy measures the loss of correlation: In the left panel the molecular environments remain 'static' whereas in the right panel the molecules exchange environments during the waiting time, giving rise to a broadened two-dimensional peak; this is known as *spectral diffusion*. While absorption spectroscopy provides a highly-averaged view of the system, two-dimensional spectroscopy extracts structural and dynamical information from these broad, featureless peaks by separating the molecular sub-ensembles underneath the lineshapes and measuring their relative exchange rates.[1, 44]

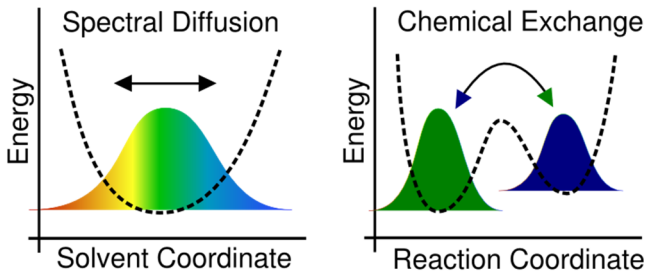

Figure 1.3: Spectral diffusion is analogous to chemical exchange, but instead of a chemical reaction, the diffusion coordinates refer to the degrees of freedom of the solvent, and the energetics arise as a result of favorable or unfavorable solvent configurations surrounding a solute. In the case of chemical exchange the different populations are usually discrete, with a well-defined barrier and exchange rate. The colors represent different transition frequencies of the different micro-environments.

From a thermodynamic perspective, the solvent provides a large number of degrees of freedom. Different microstates in solution reside within a shallow "solvent well" where each solvent configuration has a slightly different energy. The width of the peak is given by the distribution of environments as well as by the rate at which the molecules sample the different environments. Motional narrowing, which occurs when the molecules sample

different configurations at a faster rate than the timescale of the experiment, leads to narrower lineshapes than would be observed from the static distributions of environments. Another factor affecting the width of the peak is the sensitivity of the particular transition to the solvent configurations (further discussion given in Chapter 8). Chemical exchange can be thought of as a particular case of spectral diffusion with an energetic barrier separating the different sub-ensembles. Consider two species in solution, **A** and **B**; assuming that the two species have non-overlapping absorption peaks, 2DIR can directly measure their exchange rate, by measuring amplitude growth of the cross peaks in the spectrum (e.g excitation of **A** and detection of **B**, and vice versa).[45-47] Figure 1.4 shows a schematic set of 2DIR spectra under different scenarios: In the first case, the two species are independent with no exchange occurring on the timescale of the experiment. In the second case, chemical exchange occurs as observed by the cross peaks. This description of chemical exchange is very general and can refer to a wide range of chemical processes. Indeed, 2DIR exchange-spectroscopy has been used to measure hydrogen bond breaking/formation,[7, 8, 48-53] protein folding and peptide dynamics,[16, 34, 49, 54-57] and isomerization reactions,[45, 58, 59] among other processes.

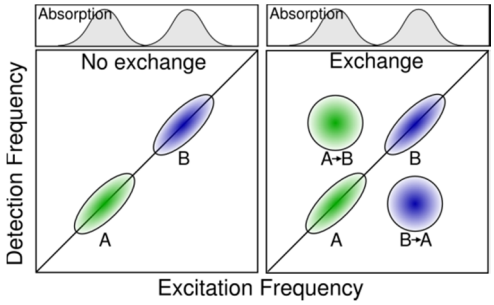

Figure 1.4: Schematic representation of how 2DIR spectroscopy measures chemical exchange between two species **A** and **B**. Absorption spectra are largely insensitive to chemical exchange.

In addition to chemical exchange, cross-peaks can also be observed as a result of vibrational coupling and vibrational energy transfer. Transitions sharing a common ground state, such as different normal modes within a molecule, will lead cross-peaks in the spectrum.[60] If two independent chromophores become coupled new excitonic states arise. Depending on the strength of the coupling, these states can split the energy levels and induce cross-peaks in the measured 2DIR spectrum.[43] This effect can be used to resolve chemical structure in solution, and a significant theoretical effort has gone towards modeling dynamical couplings in systems such as O-H (O-D) stretches in liquid water, or amide-I

modes in proteins.[61] Through its ability to measure chemical exchange, energy transfer and couplings, 2DIR not only has the power to resolve chemical structures, but also to separate mixtures of components in solution. Absorption spectroscopy alone cannot distinguish between two different molecules in solution versus two-transitions in the same molecule (see Figure 1.4).[58, 59] In this work we present a particularly illustrative example consisting of two slow-exchanging isomers in solution, where the weaker transitions of one species remain 'hidden' underneath the strong transitions of the second.[62] Using the 2DIR cross-peaks we were able to resolve the frequencies of the hidden peaks belonging to the first isomer.

From a spectroscopic perspective, 2DIR can be considered an excitation-frequency-resolved analog of IR/IR transient absorption. Figure 1.5 shows the pulse sequence along with the energy-level diagrams for a two-level system. In the time-domain (Fourier-transform) 2DIR implementation, the excitation is caused by a two-pulse interaction, starting from the ground state (00) the first pulse creates a coherent superposition between the system eigenstates (01 or 10)—referred to as a coherence, and represented by an off-diagonal density matrix element—and the second pulse transfers the coherence into a population, shown as a diagonal matrix element (00 or 11). The third pulse then puts the system back into a coherence (01 or 10). 2DIR spectra are essentially a frequency-domain 2D map of the coherences created by the excitation and by the detection interactions.[63] In a multi-level system there are many possible combinations of coherences and populations, also known as the Liouiville pathways, which can be selected for by detecting the signal in a specific direction; this is referred to as phase-matching. There are two main phase matching conditions: *rephasing* is where the phase along the detection axis is conjugate to the excitation (for example: 01—11—10), and *non-rephasing*, where the system oscillates with the same phase during both excitation and detection times (for example: 01—11—01). If the frequency fluctuations are very fast compared to the time scale of the experiment, the two pathways will have similar contributions, but if the frequencies are 'static' on the same timescale, the rephasing contribution will dominate.[63, 64] In terms of phase matching the two conditions can be written as:

$$\text{Rephasing:} \quad -k_s - k_1 + k_2 + k_3 = 0$$

$$\text{Non-rephasing:} \quad -k_s + k_1 - k_2 + k_3 = 0$$

Where k_1, k_2, k_3, and k_s represent the electric-field wavevectors of the first, second, third, and signal pulses respectively. Conservation of momentum dictates that all the wavevectors must add up to zero. Note that in the rephasing condition k_1 and k_3 have opposite sign, whereas in the non-rephasing they have equal sign.

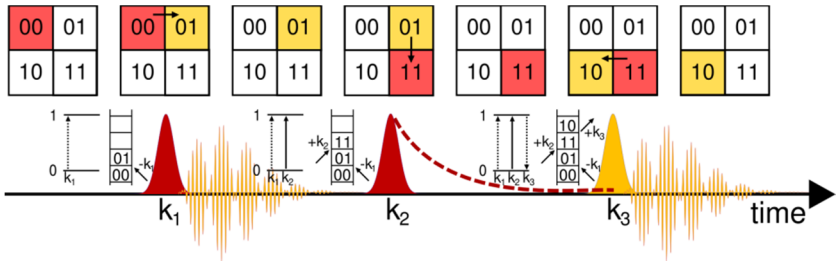

Figure 1.5: Sequence of light-matter interactions contributing to a rephasing spectrum in a two-level system. The density matrix representation is shown on the top with the Liouville states are represented as $01 = |0\rangle\langle 1|$, etc. The arrows indicate a transition between two states. Energy-level and Feynman (ladder) diagrams for the same transitions are shown next to the laser pulses.

1.4 Non-equilibrium Multidimensional Spectroscopy

Though conventional 2DIR spectroscopy remains a powerful experimental method to study chemical dynamics, it is limited to processes occurring in the electronic ground state. In the last five years, non-equilibrium variants of 2DIR have been developed to study structure and dynamics of light-induced chemical reactions.[37, 62, 65-69] Similar to UV-Vis/IR transient-absorption spectroscopy, in non-equilibrium 2DIR an ultraviolet or visible pulse perturbs the system before or during the 2DIR measurement while the infrared pulses interrogate the frequencies of the molecules undergoing the chemical transformation. In the following chapters we present two particular projects that highlight the ability of transient-2DIR spectroscopy to resolve structure and dynamics in solution. The first project describes the orientational dynamics of hot molecules following a metal-metal bond cleavage reaction by UV photoexcitation. The second project highlights the inherent structure-specificity and ultrafast time resolution of 2DIR spectroscopy in a study of bond formation between two radical species in solution.

Figure 1.6 shows the pulse sequences for various equilibrium and non-equilibrium experiments presented in the following chapters. The weak infrared pulses minimally perturb the system, therefore the system is usually considered to remain at equilibrium during a

2DIR experiment,[46] namely, the dynamics of the system are unaffected by infrared excitation. The non-equilibrium pulse sequences contain an additional UV/visible pulse which serves to induce an electronic excitation. It is worth noting here that much of ultrafast spectroscopy is described within the context of perturbation theory, meaning that the system remains near equilibrium and is only minimally perturbed by the light.[63] In the case of highly nonequilibrium processes, such as charge-transfer or bond dissociation reactions, perturbation theory may not be applicable, therefore one must exercise caution when using such terminology to describe non-equilibrium experiments.

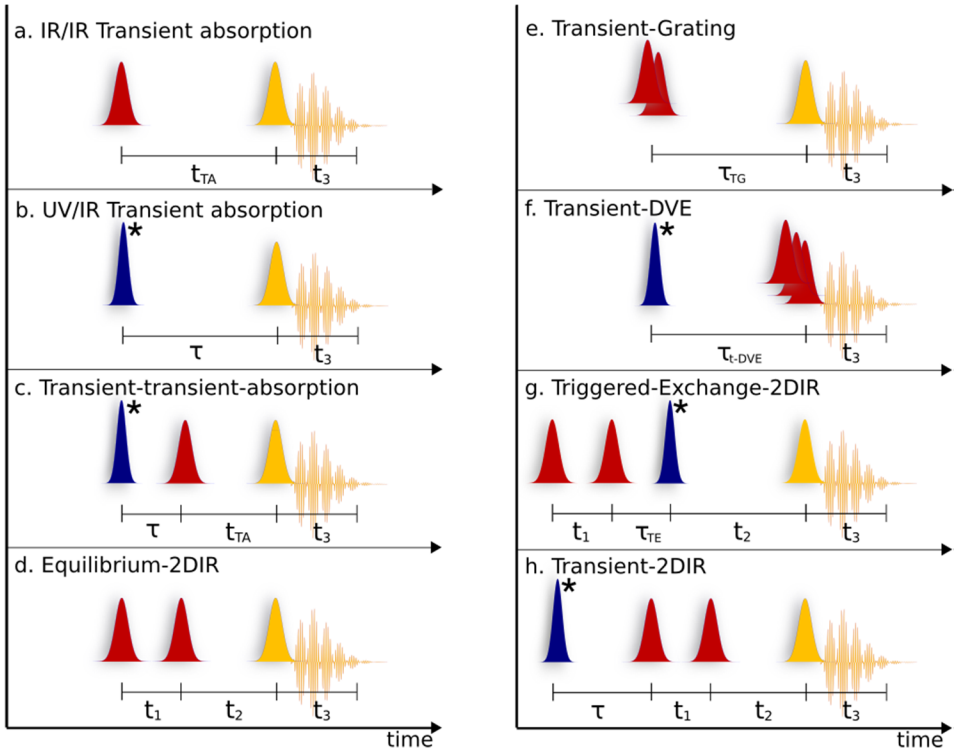

Figure 1.6: Pulse sequences used for the various experiments presented in this thesis. The red and yellow pulses correspond to infrared excitation/detection, and the blue pulse (starred) corresponds to a UV/Visible phototrigger. The pulses are color coded such that a coherent phase relationship exists only between two pulses of the same color.

Sequence (a) represents an IR/IR transient absorption (IR pump/probe) experiment: the first pulse creates vibrational population and the second pulse probes the excited-state absorption and ground-state bleaches. In broad terms, IR/IR transient absorption measures intramolecular vibrational redistribution, vibrational energy relaxation, and orientational relaxation. Sequence (b) represents a UV/IR transient absorption experiment: The first pulse

triggers a chemical reaction and the second pulse probes the infrared absorption of the system as the reaction takes place. The information obtained from this experiment is highly dependent on the system, but, in general, reaction rates, and reaction mechanisms are studied with this technique.[70, 71] Method (c) combines UV/IR with IR/IR transient absorption: this method can measure the vibrational dynamics of transient species.[72] 2DIR is shown in pulse sequence (d). Transient grating spectroscopy (sequence (e)) is similar to 2DIR with the main exception that the delay between the first two pulses is set to zero, and the signal measurement lacks phase information (only the spectral content is measured). The information content of a transient-grating spectrum can be easily extracted from 2DIR spectra.[73] If all three IR pulses are time-overlapped, the experiment is referred to as a dispersed vibrational echo (DVE). Pulse sequence (f) shows a transient dispersed vibrational echo pulse sequence, in this scenario the UV/Vis pulse triggers a chemical reaction while the three-IR pulses measure the vibrational dynamics of the transient molecules. Transient-DVE spectroscopy yields information content similar to UV/IR transient absorption spectroscopy but with improved signal-to-noise ratios. This technique is discussed in detail in the next chapter.[74] A variant of DVE spectroscopy is heterodyne-detected DVE (HDVE) which relies on an external reference pulse to recover the amplitude and phase information of the signal.[42] HDVE outperforms homodyne-detected DVE in cases where the signal is particularly weak, but requires additional information (usually a IR/IR transient-absorption spectrum) to recover the original signal phase. Triggered-exchange spectroscopy (g), is an extremely powerful method to map the identity of the vibrational states from reactants to products in phototriggered reactions.[65, 66, 75] The first two pulses excite the vibrational modes of the reactants, the UV pulse then triggers a chemical reaction, and the last pulse probes the new vibrational frequencies within the products. Unfortunately, when two or more strongly coupled transitions are present in the system, intramolecular vibrational redistribution (IVR) limits the dynamic range of this technique to a few picoseconds. Sequence (h) can be considered a UV/2DIR pump probe experiment, and extends 2DIR to non-equilibrium processes.[62, 72] Analogous to UV/IR transient-absorption, the optical delay between the UV and IR pulses can be scanned from a <100 fs, up to ~10 ns, offering a wide dynamic range. Although the optical implementation of transient-2DIR may be quite demanding, the UV/IR and IR/IR transient-absorption, DVE, and transient-DVE signals can be unambiguously recovered from a transient-2DIR spectrum.

1.5 Molecular Models of Chemical Structure and Dynamics

Frequencies and intensities alone seldom provide an atomistic view of the underlying molecular processes that give rise to the measured signals. In many cases a theoretical model is needed to extract a microscopic view of the processes.[76] The quality of the supporting theoretical model largely determines the amount of information that can be extracted from experiment. What makes NMR spectroscopy such a powerful technique to study complex multi-step chemical reactions such as protein folding? The answer is that spin resonance frequencies and spin-spin coupling strengths can be accurately modeled using standard electronic structure methods.[77] This is in contrast to vibrational spectroscopy where computing anharmonic vibrational frequencies and couplings remains a significant theoretical challenge.[68] In terms of vibrational dynamics, recent theoretical models have provided an atomistic description of the underlying molecular processes that give rise to vibrational dephasing, energy redistribution and ultimate relaxation to the solvent (see Chapter 6).

Vibrational Structure

Vibrational frequencies are often computed from electronic-structure models such as density functional theory (DFT).[78] Depending on the nature of the chemical bonds involved in the different vibrational modes, electronic-structure methods are able to compute frequencies that match the experimental values to within a few percent accuracy.[79-81] These frequencies report on the curvature of the 3N-6-dimensional molecular potential at the energy minimum. Nonlinear infrared spectroscopy measures transitions between the one and two-quanta energy levels; these are related to the anharmonic behavior of the potential, or how the curvature differs from a quadratic polynomial as the atoms undergo large displacements from the equilibrium configuration.[82] While second-order force constants, and subsequent harmonic frequencies, can usually be computed analytically, obtaining anharmonic frequencies is significantly more challenging as the method requires a large number of single-point or harmonic-frequency calculations to map the potential near the equilibrium geometry.[83, 84] In Chapter 5 we compute the third- and fourth-order anharmonic force constants of a ten-oscillator model, and compare the results to those obtained using a harmonically-coupled set of Morse oscillators.

Vibrational Dynamics

Vibrational dynamics arise from anharmonic coupling between the system and the bath degrees of freedom.[85-87] It is important to note 'bath' usually describes the solvent, however, in large systems the low-frequency modes can also constitute the bath. In chapter 6 we model vibrational dynamics using a Markovian quantum-master equation approach with a Hamiltonian of the following form:

$$\hat{H} = \hat{H}_S + \hat{H}_B + \hat{H}_{BS}$$

Where $\hat{H}_S$, $\hat{H}_B$, $\hat{H}_{BS}$ represent the system, bath, and system-bath Hamiltonians respectively. The system Hamiltonian is assumed to be time-independent and accounts for the anharmonic vibrational structure of a molecule. Electronic-structure methods are generally used to obtain a description of the system Hamiltonian. The specific nature of the bath Hamiltonian determines the initial state of the system, and the vibrational dynamics are dictated by the system-bath coupling. The coupling is described in terms of time correlation functions of the forces exerted by the solvent onto the normal modes of the solute. Coupling schemes can be either first-order (linear) or higher-order (e.g. quadratic) in the system and bath coordinates. Chapter 6 presents a dynamic model that accounts for effects such as dephasing, population relaxation and coherence-transfer based on a linear system-bath coupling Hamiltonian.

1.6 Thesis Outline

The remainder of this thesis is structured as follows: Chapter 2 describes two new ultrafast techniques—transient-2DIR and triggered-exchange-2DIR spectroscopy—within the Fourier-transform implementation of 2DIR and demonstrates their applicability to the study of metal carbonyl photodissociation and geminate recombination reactions. The implementation of transient-dispersed vibrational echo spectroscopy is described and compared to conventional UV/IR transient-absorption spectroscopy. In addition, the chapter describes a new implementation of a recently-demonstrated optical setup to generate an infrared continuum spanning from <400 cm^{-1} up to >4100 cm^{-1} through plasma

filamentation in air. Broadband detection (~600 cm^{-1} full-width-at-half-maximums) is achieved through sum-frequency mixing of the continuum with a 15 ps chirped pulse.

Chapter 3 presents a solute-centric view of nonequilibrium chemical dynamics. The orientational dynamics and vibrational relaxation (cooling) of radical species in solution is studied with transient-2DIR and transient-dispersed vibrational echo spectroscopy. The first part of the chapter describes an experiment where a metal-metal bond is homolytically cleaved by a UV pulse and the orientational relaxation of the photoproducts is subsequently followed with 2DIR spectroscopy. The second part presents a study of a structure-specific bond-formation reaction using transient-2DIR and transient-DVE spectroscopy. The favored recombination channels and rebinding rates are measured in different solvents.

Chapter 4 describes the new studies of nonequilibrium chemical dynamics from the solvent's perspective. Directly probing the vibrational response of the molecules in the first solvation shell upon inducing a charge transfer reaction within the chromophore opens a new window into the study of solvation dynamics. The experiment is based on the vibrational Stark effect which slightly shifts the frequencies of the first solvation shell molecules in response to the changing electric field induced by a charge-transfer reaction within the chromophore. The results suggest that vibrational Stark-effect spectroscopy is a powerful tool to study reaction dynamics in highly-interacting solvents.

Chapter 5 describes a project aimed computing the anharmonic vibrational structure of large, highly-coupled systems from first-principles. The anharmonic energy-level structure of dicarbonyl acetylacetonato rhodium(I), manganese pentacarbonyl, and dimanganese decacarbonyl, in the terminal carbonyl stretching region is modeled using a variety of density functional theory methods. Anharmonicities and mode-mode couplings are explored in the normal mode representations using cubic and quartic force constants The results are found to be consistent and in overall agreement with experiment.

Chapter 6 presents a new theoretical and computational framework for modeling infrared spectra of a vibrational excitonic system in liquid solution. The system's vibrational dynamics are modeled using a quantum master equation with a Markovian bath. Spectroscopic signatures of population relaxation, dephasing, coherence-coherence and coherence-population couplings are explored with this method and the waiting time-

evolution of selected two-dimensional peaks are compared to recent experimental results. As the model is based on electronic structure calculations combined with molecular dynamics simulations, it does not require any phenomenological inputs; the only free parameters are the choice of electronic structure method and the force field used for molecular dynamics.

Chapter 7 presents a theoretical investigation of hydrogen-atom transfer reactions in model systems. Electron delocalization and conjugation effects on the thermodynamics of hydrogen transfer reactions are explored in the ground and excited states using electronic structure theory. The results suggest that, by stabilizing products and transition states, the nature of the extended conjugated system has a sizable effect on the thermodynamics of hydrogen-atom transfer reactions.

The last chapter summarizes the results and draws general conclusions in the context of equilibrium and nonequilibrium vibrational structure and dynamics and discusses the dynamical effects in relation to multidimensional spectroscopy.

References

1. S. T. Roberts, K. Ramasesha, and A. Tokmakoff, "Structural Rearrangements in Water Viewed Through Two-Dimensional Infrared Spectroscopy," Accounts of Chemical Research **42**(9), 1239-1249 (2009).

2. J. T. Hynes, "Physical chemistry: the peripatetic proton," Nature **446**(7133), 270-273 (2007).

3. K. Sakota, C. Okabe, N. Nishi, and H. Sekiya, "Excited-State Double-Proton Transfer in the 7-Azaindole Dimer in the Gas Phase. 3. Reaction Mechanism Studied by Picosecond Time-Resolved REMPI Spectroscopy," Journal of Physical Chemistry A **109**(24), 5245-5247 (2005).

4. T. Schultz, E. Samoylova, W. Radloff, I. V. Hertel, A. L. Sobolewski, and W. Domcke, "Efficient Deactivation of a Model Base Pair via Excited-State Hydrogen Transfer," Science **306**(5702), 1765 - 1768-1765 - 1768 (2004).

5. S. Scheiner, "Theoretical Studies of Excited State Proton Transfer in Small Model Systems," Journal of Physical Chemistry A **104**(25), 5898-5909 (2000).

6. A. Douhal, F. o. Lahmani, and A. H. Zewail, "Proton-transfer reaction dynamics," Chemical Physics **207**(2-3), 477--498 (1996).

7. E. H. G. Backus, R. Bloem, P. M. Donaldson, J. A. Ihalainen, R. Pfister, B. Paoli, A. Caflisch, and P. Hamm, "2D-IR Study of a Photoswitchable Isotope-Labeled alpha-Helix," Journal of Physical Chemistry B **114**(10), 3735-3740 (2010).

8. J. A. Ihalainen, B. Paoli, S. Muff, E. H. G. Backus, J. Bredenbeck, G. A. Woolley, A. Caflisch, and P. Hamm, "alpha-Helix folding in the presence of structural constraints," Proceedings of the National Academy of Sciences of the United States of America **105**(28), 9588-9593 (2008).

9. H. S. Chung, M. Khalil, A. W. Smith, Z. Ganim, and A. Tokmakoff, "Conformational changes during the nanosecond-to-millisecond unfolding of ubiquitin," Proceedings of the National Academy of Sciences of the United States of America **102**(3), 612-617 (2005).

10. V. S. Pande, K. Beauchamp, and G. R. Bowman, "Everything you wanted to know about Markov State Models but were afraid to ask," Methods **52**(1), 99-105 (2010).

11. S. Park, T. E. Klein, and V. S. Pande, "Folding and misfolding of the collagen triple helix: Markov analysis of molecular dynamics simulations," Biophysical Journal **93**(12), 4108-4115 (2007).

12. Z. Ganim, K. C. Jones, and A. Tokmakoff, "Insulin dimer dissociation and unfolding revealed by amide I two-dimensional infrared spectroscopy," Physical Chemistry Chemical Physics **12**(14), 3579-3588 (2010).

13. J. A. Izaguirre, C. R. Sweet, and V. S. Pande, "Multiscale dynamics of macromolecules using normal mode langevin," Pacific Symposyum on Biocomputing, 240-251 (2010).

14. C. M. Dobson, "Protein folding and misfolding," Nature **426**(6968), 884-890 (2003).

15. D. Lucent, V. Vishal, and V. S. Pande, "Protein folding under confinement: a role for solvent," Proc Natl Acad Sci U S A **104**(25), 10430-10434 (2007).

16. H. S. Chung and A. Tokmakoff, "Temperature-dependent downhill unfolding of ubiquitin. I. Nanosecond-to-millisecond resolved nonlinear infrared spectroscopy," Proteins **72**(1), 474-487 (2008).

17. H. S. Chung, Z. Ganim, K. C. Jones, and A. Tokmakoff, "Transient 2D IR spectroscopy of ubiquitin unfolding dynamics," Proceedings of the National Academy of Sciences of the United States of America **104**(36), 14237-14242 (2007).

18. H. Frauenfelder, G. Chen, J. Berendzen, P. W. Fenimore, H. Jansson, B. H. McMahon, I. R. Stroe, J. Swenson, and R. D. Young, "A unified model of protein dynamics," Proceedings of the National Academy of Sciences of the United States of America **106**(13), 5129-5134 (2009).

19. E. E. Fenn, D. B. Wong, and M. D. Fayer, "Water dynamics at neutral and ionic interfaces," Proceedings of the National Academy of Sciences of the United States of America **106**(36), 15243-15248 (2009).

20. A. A. Bakulin, C. Liang, T. la Cour Jansen, D. A. Wiersma, H. J. Bakker, and M. S. Pshenichnikov, "Hydrophobic solvation: a 2D IR spectroscopic inquest," Accounts of Chemical Research **42**(9), 1229-1238 (2009).

21. C. Petersen, A. A. Bakulin, V. G. Pavelyev, M. S. Pshenichnikov, and H. J. Bakker, "Femtosecond midinfrared study of aggregation behavior in aqueous solutions of amphiphilic molecules," Journal of Chemical Physics **133**(16), 164514 (2010).

22. J. Asbury, Y. Wang, and T. Lian, "Time-dependent vibration Stokes shift during solvation: Experiment and theory," Bulletin of the Chemical Society of Japan **75**(5), 973-983 (2002).

23. S. Arzhantsev, K. A. Zachariasse, and M. Maroncelli, "Photophysics of trans-4-(dimethylamino)-4 '-cyanostilbene and its use as a solvation probe," Journal of Physical Chemistry A **110**(10), 3454-3470 (2006).

24. G. R. Fleming and P. G. Wolynes, "Chemical Dynamics," Physics Today **43**(5), 36-43 (1990).

25. G. R. Bowman, X. Huang, and V. S. Pande, "Network models for molecular kinetics and their initial applications to human health," Cell Research **20**(6), 622-630 (2010).

26. G. R. Bowman and V. S. Pande, "Protein folded states are kinetic hubs," Proceedings of the National Academy of Sciences of the United States of America **107**(24), 10890-10895 (2010).

27. D. Rother, G. Sapiro, and V. Pande, "Statistical characterization of protein ensembles," IEEE/ACM Trans Comput Biol Bioinform **5**(1), 42-55 (2008).

28. P. Bour and T. A. Keiderling, "Empirical modeling of the peptide amide I band IR intensity in water solution," Journal of Chemical Physics **119**(21), 11253-11262 (2003).

29. T. L. Jansen, A. G. Dijkstra, T. M. Watson, J. D. Hirst, and J. Knoester, "Modeling the amide I bands of small peptides," Journal of Chemical Physics **125**(4), - (2006).

30. T. L. Jansen and J. Knoester, "A transferable electrostatic map for solvation effects on amide I vibrations and its application to linear and two-dimensional spectroscopy," Journal of Chemical Physics **124**(4), - (2006).

31. P. A. Anfinrud, C. Han, and R. M. Hochstrasser, "Direct Observations of Ligand Dynamics in Hemoglobin by Subpicosecond Infrared-Spectroscopy," Proceedings of the National Academy of Sciences of the United States of America **86**(21), 8387-8391 (1989).

32. T. Polack, J. P. Ogilvie, S. Franzen, M. H. Vos, M. Joffre, J. L. Martin, and A. Alexandrou, "CO Vibration as a Probe of Ligand Dissociation and Transfer in Myoglobin," Physical Review Letters **93**(1), 018102-018102 (2004).

33. S. A. Corcelli, C. P. Lawrence, and J. L. Skinner, "Combined electronic structure/molecular dynamics approach for ultrafast infrared spectroscopy of dilute HOD in liquid H2O and D2O," Journal of Chemical Physics **120**(17), 8107-8117 (2004).

34. A. W. Smith, J. Lessing, Z. Ganim, C. S. Peng, A. Tokmakoff, S. Roy, T. L. Jansen, and J. Knoester, "Melting of a beta-hairpin peptide using isotope-edited 2D IR spectroscopy and simulations," Journal of Physical Chemistry B **114**(34), 10913-10924 (2010).

35. E. T. J. Nibbering, H. Fidder, and E. Pines, "Ultrafast chemistry: Using time-resolved vibrational spectroscopy for interrogation of structural dynamics," Annual Review of Physical Chemistry **56**, 337-367 (2005).

36. J. P. Oglivie and K. J. Kubarych, "Chapter 5 Multidimensional Electronic and Vibrational Spectroscopy: An Ultrafast Probe of Molecular Relaxation and Reaction Dynamics," Advances In Atomic, Molecular, and Optical Physics **57**, 249-321 (2009).

37. C. Baiz, M. Nee, R. McCanne, and K. Kubarych, "Ultrafast nonequilibrium Fourier-transform two-dimensional infrared spectroscopy," Optics Letters **33**(21), 2533-2535 (2008).

38. M. Nee, C. Baiz, J. Anna, R. McCanne, and K. Kubarych, "Multilevel vibrational coherence transfer and wavepacket dynamics probed with multidimensional IR spectroscopy," Journal of Chemical Physics **129**(8), 084503 (2008).

39. C. R. Baiz, R. McCanne, M. J. Nee, and K. J. Kubarych, "Orientational dynamics of transient molecules measured by non-equilibrium two-dimensional infrared spectroscopy," Journal of Physical Chemistry A **ASAP**(2009).

40. M. Cho, *Two-dimensional optical spectroscopy* (CRC Press, Boca Raton, 2009), p. 378 p.

41. J. Zheng, K. Kwak, and M. Fayer, "Ultrafast 2D IR vibrational echo spectroscopy," Accounts of Chemical Research **40**(1), 75-83 (2007).

42. K. C. Jones, Z. Ganim, and A. Tokmakoff, "Heterodyne-Detected Dispersed Vibrational Echo Spectroscopy," Journal of Physical Chemistry A **113**(51), 14060-14066 (2009).

43. J. T. King, C. R. Baiz, and K. J. Kubarych, "Solvent-dependent spectral diffusion in a hydrogen bonded "vibrational aggregate"," Journal of Physical Chemistry A **114**(39), 10590-10604 (2010).

44. I. R. Piletic, D. E. Moilanen, N. E. Levinger, and M. D. Fayer, "What nonlinear-IR experiments can tell you about water that the IR spectrum cannot," Journal of the American Chemical Society **128**(32), 10366-10367 (2006).

45. J. Zheng, K. Kwak, J. Xie, and M. D. Fayer, "Ultrafast carbon-carbon single-bond rotational isomerization in room-temperature solution," Science **313**(5795), 1951-1955 (2006).

46. J. Zheng, K. Kwak, J. Asbury, X. Chen, I. R. Piletic, and M. D. Fayer, "Ultrafast dynamics of solute-solvent complexation observed at thermal equilibrium in real time," Science **309**(5739), 1338-1343 (2005).

47. J. F. Cahoon, K. R. Sawyer, J. P. Schlegel, and C. B. Harris, "Determining Transition-State Geometries in Liquids Using 2D-IR," Science **319**(5871), 1820 - 1823-1820 - 1823 (2008).

48. S. T. Roberts, P. B. Petersen, K. Ramashesha, and A. Tokmakoff, "The Dynamics of Aqueous Hydroxide Ion Transport Probed via Ultrafast Vibrational Echo Experiments," Proceedings of the Conference on Ultrafast Phenomena XVI **92**, 481-483 1031 (2009).

49. S. Roberts, K. Ramasesha, and A. Tokmakoff, "Structural rearrangements in water viewed through two-dimensional infrared spectroscopy," Accounts of Chemical Research **42**, 1239-1249 (2009).

50. J. J. Loparo, S. T. Roberts, and A. Tokmakoff, "Multidimensional infrared spectroscopy of water. I. Vibrational dynamics in two-dimensional IR line shapes," Journal of Chemical Physics **125**(19), 194521 (2006).

51. J. J. Loparo, S. T. Roberts, and A. Tokmakoff, "Multidimensional infrared spectroscopy of water. II. Hydrogen bond switching dynamics," Journal of Chemical Physics **125**(19), 194522 (2006).

52. C. J. Fecko, J. J. Loparo, S. T. Roberts, and A. Tokmakoff, "Local hydrogen bonding dynamics and collective reorganization in water: Ultrafast infrared spectroscopy of HOD/D2O," Journal of Chemical Physics **122**(5), - (2005).

53. S. Woutersen, Y. Mu, G. Stock, and P. Hamm, "Hydrogen-bond lifetime measured by time-resolved 2D-IR spectroscopy: N-methylacetamide in methanol," Chemical Physics **266**(2-3), 137-147 (2001).

54. L. P. Deflores, Z. Ganim, R. A. Nicodemus, and A. Tokmakoff, "Amide I'-II' 2D IR spectroscopy provides enhanced protein secondary structural sensitivity," Journal of the American Chemical Society **131**(9), 3385-3391 (2009).

55. H. S. Chung and A. Tokmakoff, "Temperature-dependent downhill unfolding of ubiquitin. II. Modeling the free energy surface," Proteins **72**(1), 488-497 (2008).

56. J. Bredenbeck and P. Hamm, "Peptide structure determination by two-dimensional infrared spectroscopy in the presence of homogeneous and inhomogeneous broadening," Journal of Chemical Physics **119**(3), 1569-1578 (2003).

57. S. Woutersen, R. Pfister, P. Hamm, Y. G. Mu, D. S. Kosov, and G. Stock, "Peptide conformational heterogeneity revealed from nonlinear vibrational spectroscopy and molecular-dynamics simulations," Journal of Chemical Physics **117**(14), 6833-6840 (2002).

58. J. M. Anna and K. J. Kubarych, "Watching solvent friction impede ultrafast barrier crossings: A direct test of Kramers theory," Journal of Chemical Physics **133**(17), - (2010).

59. J. M. Anna, M. R. Ross, and K. J. Kubarych, "Dissecting Enthalpic and Entropic Barriers to Ultrafast Equilibrium Isomerization of a Flexible Molecule Using 2DIR Chemical Exchange Spectroscopy," Journal of Physical Chemistry A **113**(24), 6544-6547 (2009).

60. M. J. Nee, C. R. Baiz, J. M. Anna, R. McCanne, and K. J. Kubarych, "Multilevel vibrational coherence transfer and wavepacket dynamics probed with multidimensional IR spectroscopy," Journal of Chemical Physics **129**(8), 084503 (2008).

61. M. L. Cowan, B. D. Bruner, N. Huse, J. R. Dwyer, B. Chugh, E. T. Nibbering, T. Elsaesser, and R. J. Miller, "Ultrafast memory loss and energy redistribution in the hydrogen bond network of liquid H2O," Nature **434**(7030), 199-202 (2005).

62. C. R. Baiz, R. McCanne, and K. J. Kubarych, "Structurally selective geminate rebinding dynamics of solvent-caged radicals studied with nonequilibrium infrared echo spectroscopy," Journal of the American Chemical Society **131**(38), 13590-13591 (2009).

63. S. Mukamel, *Principles of nonlinear optical spectroscopy*, Oxford series in optical and imaging sciences 6 (Oxford University Press, New York, 1995), pp. xviii, 543 p.

64. D. M. Jonas, "Two-dimensional femtosecond spectroscopy," Annual Review of Physical Chemistry **54**, 425-463 (2003).

65. J. Bredenbeck, J. Helbing, and P. Hamm, "Labeling vibrations by light: Ultrafast transient 2D-IR spectroscopy tracks vibrational modes during photoinduced charge transfer," Journal of the American Chemical Society **126**(4), 990-991 (2004).

66. J. Bredenbeck, J. Helbing, C. Kolano, and P. Hamm, "Ultrafast 2D-IR Spectroscopy of transient species," Chemphyschem **8**(12), 1747-1756 (2007).

67. C. R. Baiz, P. L. McRobbie, J. M. Anna, E. Geva, and K. J. Kubarych, "Two-Dimensional Infrared Spectroscopy of Metal Carbonyls," Accounts of Chemical Research **42**(9), 1395-1404 (2009).

68. C. R. Baiz, P. L. McRobbie, N. K. Preketes, K. J. Kubarych, and E. Geva, "Two-dimensional infrared spectroscopy of dimanganese decacarbonyl and its photoproducts: an ab initio study," Journal of Physical Chemistry A **113**(35), 9617-9623 (2009).

69. W. Xiong, J. E. Laaser, P. Paoprasert, R. A. Franking, R. J. Hamers, P. Gopalan, and M. T. Zanni, "Transient 2D IR Spectroscopy of Charge Injection in Dye-Sensitized Nanocrystalline Thin Films," Journal of the American Chemical Society **131**(50), 18040-18041 (2009).

70. C. E. Crespo-Hernandez, B. Cohen, and B. Kohler, "Base stacking controls excited-state dynamics in A.T DNA," Nature **436**(7054), 1141 (2005).

71. W. J. Schreier, T. E. Schrader, F. O. Koller, P. Gilch, C. E. Crespo-Hernandez, V. N. Swaminathan, T. Carell, W. Zinth, and B. Kohler, "Thymine Dimerization in DNA Is an Ultrafast Photoreaction," Science **315**(5812), 625 - 629-625 - 629 (2007).

72. C. R. Baiz, R. McCanne, M. J. Nee, and K. J. Kubarych, "Orientational dynamics of transient molecules measured by nonequilibrium two-dimensional infrared spectroscopy," Journal of Physical Chemistry A **113**(31), 8907-8916 (2009).

73. A. Tokmakoff, "Orientational correlation functions and polarization selectivity for nonlinear spectroscopy of isotropic media .1. Third order," Journal of Chemical Physics **105**(1), 1-12 (1996).

74. C. R. Baiz, R. McCanne, and K. J. Kubarych, "Transient vibrational echo versus transient absorption spectroscopy: a direct experimental and theoretical comparison," Applied Spectroscopy **64**(9), 1037-1044 (2010).

75. J. Bredenbeck and P. Hamm, "Transient 2D-IR spectroscopy: Towards a molecular movie," Chimia **61**(1-2), 45-46 (2007).

76. J. R. Schmidt, S. T. Roberts, J. J. Loparo, A. Tokmakoff, M. D. Fayer, and J. L. Skinner, "Are water simulation models consistent with steady-state and ultrafast vibrational spectroscopy experiments?," Chemical Physics **341**(1-3), 143-157 (2007).

77. D. Massiot, F. Fayon, M. Capron, I. King, S. Le Calve, B. Alonso, J. O. Durand, B. Bujoli, Z. H. Gan, and G. Hoatson, "Modelling one- and two-dimensional solid-state NMR spectra," Magnetic Resonance in Chemistry **40**(1), 70-76 (2002).

78. R. J. Meier, "Calculating the vibrational spectra of molecules: An introduction for experimentalists with contemporary examples," Vibrational Spectroscopy **43**(1), 26-37 (2007).

79. A. P. Scott and L. Radom, "Harmonic vibrational frequencies: An evaluation of Hartree-Fock, Moller-Plesset, quadratic configuration interaction, density functional theory, and semiempirical scale factors," Journal of Physical Chemistry **100**(41), 16502-16513 (1996).

80. G. Rauhut and P. Pulay, "Transferable Scaling Factors for Density-Functional Derived Vibrational Force-Fields," Journal of Physical Chemistry **99**(10), 3093-3100 (1995).

81. M. W. Wong, "Vibrational frequency prediction using density functional theory," Chemical Physics Letters **256**(4-5), 391-399 (1996).

82. N. A. Mathew, L. A. Yurs, S. B. Block, A. V. Pakoulev, K. M. Kornau, E. L. Sibert, and J. C. Wright, "Fully and Partially Coherent Pathways in Multiply Enhanced Odd-Order Wave-Mixing Spectroscopy," Journal of Physical Chemistry A **114**(2), 817-832 (2010).

83. V. Barone, "Anharmonic vibrational properties by a fully automated second-order perturbative approach," Journal of Chemical Physics **122**(1), 014108-014110 (2004).

84. W. Schneider and W. Thiel, "Anharmonic force fields from analytic second derivatives: Method and application to methyl bromide," Chemical Physics Letters **157**(4), 367-373 (1989).

85. F. Haake, "Statistical treatment of open systems by generalized master equations," Springer Tracts Mod. Phys. **66**, 98 (1973).

86. I. Oppenheim, K. E. Shuler, and G. H. Weiss, *Stochastic Processes in Chemical Physics: The Master Equation* (MIT Press, Cambridge MA, 1977).

87. A. G. Redfield, "On the theory of relaxation processes," IBM Journal **1**, 19 (1957).

Chapter 2

Expanding the Spectroscopic Toolbox: Development of Novel Ultrafast Techniques

The work presented in this chapter has been published in the following three papers:

1. C.R. Baiz, R. McCanne and K.J. Kubarych, " *Ultrafast nonequilibrium Fourier-transform two-dimensional infrared spectroscopy*", Optics Letters, **33**(21), 2533-2535, 2008.
2. C.R. Baiz, R. McCanne and K.J. Kubarych, "*Transient Vibrational Echo versus Transient Absorption Spectroscopy: A Direct Experimental and Theoretical Comparison*", Applied Spectroscopy, 64 (9), 1037-1044, 2010.
3. C.R. Baiz, K.J. Kubarych, " *Ultrabroadband detection of a mid-infrared continuum by chirped-pulse upconversion*", Optics Letters, In Press, 2011.

2.1 Introduction

Over the last ten years infrared spectroscopy on the subpicosecond timescale has provided remarkable insights into fundamental processes in chemistry and biology, from bond formation[1], dissociation[2] and isomerization,[3] to protein folding[4] and aggregation.[5] Time-resolved vibrational spectroscopy probes transient molecular processes by enabling the direct measurement of the vibrational frequencies in a chemical system during a non-equilibrium process. The well-established method of transient infrared absorption spectroscopy (TA) consists of monitoring the infrared absorption spectrum of a system as a

function of the time delay after an event—usually a photochemical or photophysical process initiated by a laser pulse.[6] This technique is relatively straightforward to implement and the data can provide rich structural and dynamical information such as reaction rates or orientational lifetimes.[7, 8] Though TA can provide high time resolution of transient processes, the spectral measurement is one-dimensional (1D), and is thus limited in its dynamical information content. To circumvent the inherent limitations of 1D spectroscopy, multidimensional techniques have now gained wide adoption.[9-12] Coherent two-dimensional infrared (2DIR) spectroscopy, a third-order non-linear technique, offers a direct measurement of the full vibrational Hamiltonian, including anharmonicities and couplings[13-15] while providing a separation between inhomogeneous and homogeneous broadening. 2DIR effectively spreads the infrared spectrum onto two axes, corresponding to excitation and detection frequencies, and the dynamics are contained in the dependence of peak amplitudes on the time delay between excitation and detection as well as the peak line shapes, whereas structural information is generally contained in the off-diagonal peak amplitudes.[16-18]

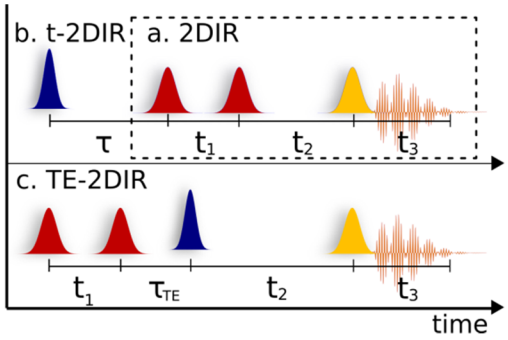

Figure 2.1: Fourier-transform (a) 2DIR, (b) transient-2DIR, and (c) Triggered-Exchange-2DIR pulse sequences. Red pulses represent $\mathbf{k}_1$ and $\mathbf{k}_2$, yellow represents $\mathbf{k}_3$, the radiated signal is shown in orange, and UV pulses in blue.

To date, the bulk of 2DIR has focused on systems in electronic ground states. Hamm *et al.*, have developed non-equilibrium variants of 2DIR [19, 20] to study photoswitchable peptides[5], disulfide bond breaking[6] and metal-to-ligand charge transfer.[7] In addition, Chung *et al.* have used Fourier transform (FT) 2DIR as a probe of protein unfolding dynamics.[8] In the next section we introduce transient photochemistry to the background-free FT implementation of 2DIR, a technique which offers advantages in sensitivity, and independent temporal and spectral resolution.[9] Further, we have combined

transient 2DIR spectroscopy with the chirped-pulse upconversion detection technique.[10,11] Non-equilibrium 2DIR describes two different techniques: *Triggered-Exchange* 2DIR (TE-2DIR), and *transient*-2DIR (t-2DIR). TE-2DIR provides vibrational mode correlation in optically-triggered processes by mapping reactant vibrations to product vibrations, avoiding ambiguities associated with one-dimensional transient absorption methods.[3] Transient-2DIR extends to transient species the structurally-sensitive information inherent to 2DIR, such as normal-mode coupling and vibrational energy transfer rates with a temporal dynamic range spanning multiple timescales. Previous TE-2DIR experiments used a narrowband-pump/broadband-probe approach, with the IR pump spectral resolution determined by the bandwidth of a tunable Fabry-Perot etalon—typically 5-10 cm^{-1}—resulting in IR pump pulses of several ps duration, thus linking temporal and spectral resolution.[9] A key advantage of the FT implementation of TE-2DIR is that all pulses are ultrashort, and the spectral resolution is limited by the maximum coherence time delay. Since the second field-matter interaction is with an ultrashort pulse, smaller waiting time delays can be probed, and the UV pulse initiating the chemical reaction can excite the system before appreciable IVR has taken place. This is significant when IVR is fast (<1-2 ps), as the excitation energy rapidly randomizes among the modes and excitation-detection frequency correlation is rapidly lost.[18, 21] A disadvantage of FT 2DIR, however, lies in the technical difficulty of implementing the technique as well as the higher demand for phase stability. Combining the structural specificity and femtosecond time resolution inherent to FT 2DIR with UV photoexcitation, these techniques offer valuable insight into condensed-phase photochemistry.

The principles of 2DIR spectroscopy have been described in detail elsewhere.[2] Briefly, a 2DIR spectrum is obtained by applying three femtosecond infrared pulses with wavevectors $\mathbf{k}_1$, $\mathbf{k}_2$, and $\mathbf{k}_3$, separated by time delays t_1 and t_2, producing a signal in a phase-matched background-free direction (Figure 2.1a). The electric field is recovered by interferometric superposition with a local oscillator in a spectrometer. In TE-2DIR, after vibrational labeling by the first two IR pulses, an additional pulse is applied to trigger a chemical process; the third pulse then probes the transient photoproducts, which are correlated to the initially excited reactant frequencies (Figure 2.1c). A t-2DIR spectrum is measured by applying the excitation pulse before the three IR pulses, thus obtaining a full 2D correlation spectrum of the transient species (Figure 2.1b). In this chapter we describe

the optical setup used to obtain non-equilibrium 2DIR of $Mn_2(CO)_{10}$ and its photoproducts following UV excitation.

Since transient-2DIR spectroscopy is a time-consuming method, and is subject to slow drift in the experimental apparatus, often it is desirable to track reactions using a 1D probe to extract kinetic information, while relying upon a few transient 2DIR spectra in order to extract dynamics or to assign the 1D spectrum.[22, 23] In section 2.3 we report on a one-dimensional variant of transient-2DIR spectroscopy: transient-dispersed vibrational echo (t-DVE) spectroscopy, a technique which provides largely similar information than transient absorption spectroscopy but with improved signal to noise ratios.

Most ultrafast infrared spectroscopy, including 2DIR and its non-equilibrium variants, have been constrained to a narrow region of the vibrational spectrum. The maximum spectral width achievable using conventional setups based on non-linear optical parametric amplification and difference-frequency generation techniques is constrained to ~300 cm^{-1}. This range is given by phase matching in the pulse generation as well as by the detection. Recent developments in IR continuum generation[24-29] through plasma filamentation in air lifted the generation constraint, but the detection challenge still remained. In the last section we report on new developments of an IR continuum generation and detection setup using chirped-pulse upconversion.

2.2 Ultrafast Transient Fourier-transform 2DIR Spectroscopy

The 2DIR spectrometer used here has been described in detail elsewhere.[11] Briefly, 1 mJ of the 2-mJ output of a regeneratively-amplified Ti:Sapphire laser, centered at 800 nm with 1-kHz repetition rate generates near-IR pulses using β-barium borate (BBO) in a dual optical parametric amplifier (OPA), which are then used to generate two mid-IR pulses (3 μJ, 100 fs), centered at 2000 cm^{-1} with ~100 cm^{-1} FWHM bandwidth, by difference frequency generation (DFG) in separate 1-mm GaSe crystals. The first IR beam is split into $\mathbf{k}_1$ and $\mathbf{k}_2$, and the second IR beam is split into $\mathbf{k}_3$, tracer, and local oscillator (Figure 2.2). The beams are aligned in a box geometry, and the rephasing signal is measured in the $k_s = -\mathbf{k}_1+\mathbf{k}_2+\mathbf{k}_3$ direction. The signal and reference local oscillator are upconverted by sum frequency

generation in a 0.5-mm MgO:$LiNbO_3$ crystal using a 45-μJ highly-chirped pulse centered at 800 nm derived from the Ti:Sapphire amplifier before compression.[11] The upconverted light is dispersed and detected with a 1340x100-pixel silicon CCD detector whose 20 active rows are vertically binned before readout, enabling single-shot detection at 1 kHz. To record a 2DIR spectrum for a given waiting time (t_2), the first time delay (t_1) is scanned continuously and the heterodyned spectra along with the corresponding motor positions are collected synchronized to the laser. Rephasing 2DIR spectra require less than 8 seconds of total data acquisition time for ~16 ps of maximum t_1 delay, yielding a Fourier transform resolution of 2 cm^{-1}.

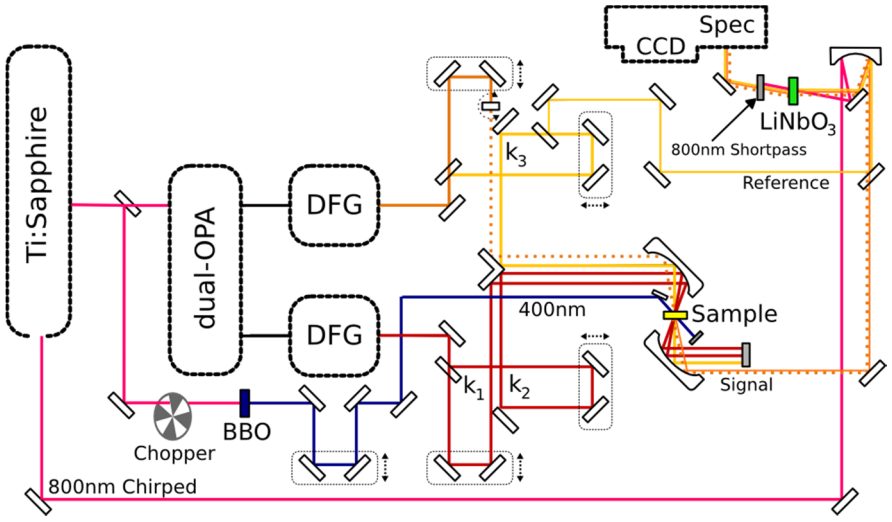

Figure 2.2: Non-equilibrium 2DIR spectrometer. The IR and UV beams are color coded according to the pulse sequences in Figure 2.1. The dotted beam represents the tracer used for alignment and one-dimensional transient absorption measurements.

Ultraviolet pulses centered at 400 nm (>30 μJ, ~100 fs) are generated by frequency doubling ~200 μJ of the amplifier output in a 0.4-mm BBO crystal. The UV beam is mechanically chopped to 250 Hz (25% duty cycle). Alignment of the UV beam is optimized by maximizing the contrast (pump-on versus pump-off) of the dispersed vibrational echo (DVE, t_1=t_2=0) signal. Following alignment, the UV power is adjusted such that the bleach is <25% of the total DVE signal intensity, corresponding to 15-20 μJ of UV focused to a spot size of 300 μm FWHM. The UV-IR time overlap is also set using the DVE signal; τ=0 is determined by scanning the UV pulse until the DVE bleaches decrease to 50% of the maximum value. A gravity-driven wire-guided liquid jet provides excellent film stability with

a film thickness of approximately 200 μm, and an adequate linear flow refreshes the sample between laser shots.[30] The jet minimizes UV/IR temporal walk-off while reducing nonresonant signal contributions. Because the reference beam is routed around the sample, film stability is critical for maintaining a constant relative phase between the signal and reference. Film fluctuations measured by fringe-tracking interferometry were found to have <60-nm RMS deviations. Although the film profile introduces small lensing effects, proper focusing and alignment of the beams minimizes these effects on the 2D signal. The collected data set contains both pumped (pump-on) and unpumped (pump-off) ω_3 spectra as a function of t_1. After de-interlacing (Figure 2.3), the pumped and unpumped data sets are Fourier-transformed separately. Difference 2D spectra are obtained by subtracting the unpumped from the pumped absolute-value rephasing 2DIR spectra. The 25% chopper duty cycle provides three unpumped spectra for every pumped spectrum corresponding to 1, 2 and 3 ms sample refresh times. Proper flow rate was verified by comparing the difference spectra at the different refresh times.

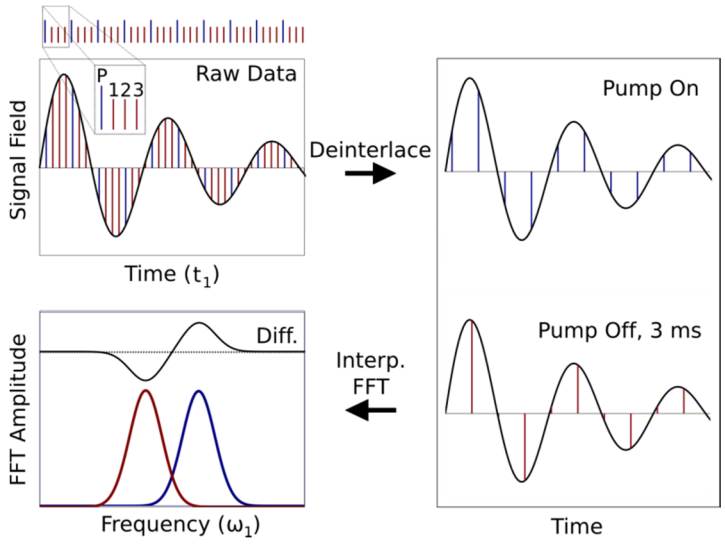

Figure 2.3: Schematic representation of the 2D data analysis process with a 25% chopper duty time. The two sets of data (with and without UV pump) are collected simultaneously. After deinterlacing, the two sets are interpolated to uniform time points and Fourier-transformed separately; the final difference spectrum is computed in the frequency domain.

The described setup has enabled us to measure TE-2DIR and t-2DIR spectra of $Mn_2(CO)_{10}$ in cyclohexane at 6 mM concentration, where excitation at 400 nm primarily cleaves the Mn–Mn bond[31] yielding two $Mn(CO)_5$. $Mn_2(CO)_{10}$, whose 2DIR spectrum has

been reported previously,[11,13] exhibits three absorption peaks 1983, 2013, and 2045 cm^{-1} and one main photoproduct band centered at 1982 cm^{-1}.

The TE-2DIR spectrum at τ_{TE}=1 ps, t_2=25 ps (Figure 2.4a) shows a positive peak at ω_1=2013 cm^{-1}, ω_3=1982 cm^{-1} indicating correlation between the 2013 cm^{-1} mode in $Mn_2(CO)_{10}$ and the 1982 cm^{-1} mode in $Mn(CO)_5$. The t-2DIR spectrum at τ=25 ps, t_2=1 ps (Figure 2.4b) shows a dominant feature centered around ω_1=1982 cm^{-1}, ω_3=1982 cm^{-1}, corresponding to the photoproduct. The broadness of this feature indicates that 25 ps after photolysis, the product molecules remain vibrationally hot, in agreement with previous transient UV pump-IR probe experiments.[31] The difference in relative amplitudes of the transient features in TE-2DIR and t-2DIR is attributed to different overlap with the IR pulse envelopes, spectral overlap with the parent bleaches, as well as differences in rotational diffusion and differences in oscillator strength. Low-frequency diagonal and off-diagonal bleaches are suppressed by tuning the mid-IR pump pulses to the high-frequency region of the spectrum so as to minimize the amplitude and 2D lineshape distortion of the transient features due to spectral overlap.

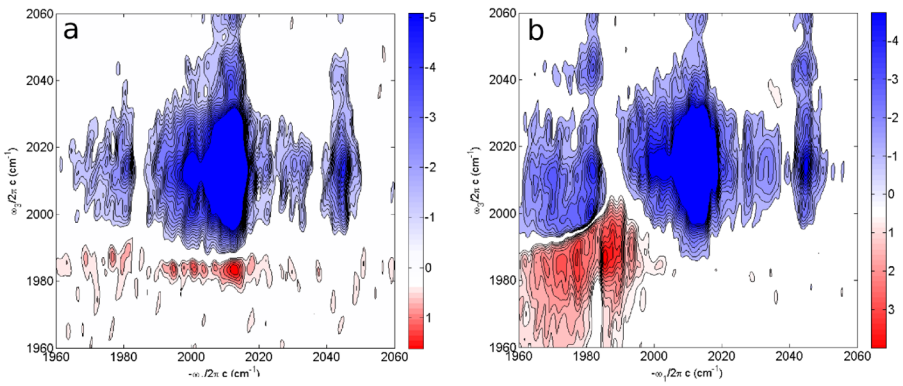

Figure 2.4: (a) Triggered–exchange 2DIR spectrum at τTE = 1 ps, t2 = 25 ps. (b) Transient 2DIR spectrum of $Mn_2(CO)_{10}$ at τ = 25 ps, t2 = 1 ps. Negative features (blue) arise from the depletion of ground-state reactant molecules, while positive features (red) are due to the non-equilibrium photoproducts. Contours smaller than 2% and larger than 30% of the maximum amplitude are omitted for clarity. The spectra are not corrected for the amplitude envelope of the mid-IR pulses.

$Mn_2(CO)_{10}$ presents a useful model system due to its strong carbonyl stretching modes, rich vibrational level structure and well-defined photoproduct. An attractive feature of t-2DIR is that despite spectral overlap with the parent molecule, the product spectrum

can still be easily separated. Additionally, since the equilibrium dynamics of $Mn_2(CO)_{10}$ can be determined by 2DIR, the photoproduct contribution can be isolated—a capability unavailable in conventional transient absorption spectroscopy. A full characterization of the photochemistry of $Mn_2(CO)_{10}$, including reaction pathways, vibrational and electronic relaxation, as well as geminate rebinding ratios can be investigated with non-equilibrium 2DIR and will be reported in the next chapter. Further enhancements of the technique will include transient differential absorptive 2D spectra by recording both rephasing and non-rephasing signals, using the unpumped data for phasing. This is a general technique and can be used to study a wide range of photochemical processes with femtosecond time resolution and spectral resolution limited only by the molecular transitions.

2.3 Transient Absorption vs. Transient Vibrational Echo Spectroscopy

In this section, we consider nonlinear dispersed vibrational echo spectroscopy, in the context of 2DIR spectroscopy, as a sensitive probe of chemical kinetics and compare it to the well-established transient absorption spectroscopy. The experimental and theoretical comparison is approached from a practical perspective considering issues such as signal intensities and noise fluctuations while providing a framework for obtaining kinetic information such as reaction rates and quantum yields from transient dispersed vibrational echo (t-DVE) measurements. In addition, we derive the equations needed for estimating the signal-to-noise ratios for t-DVE and TA under different experimental conditions.

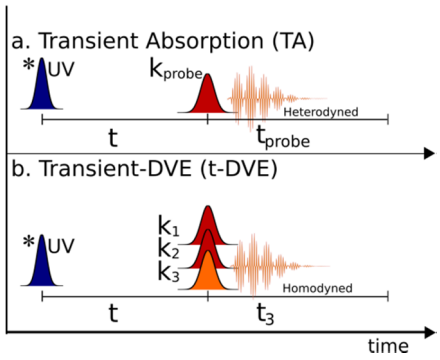

Figure 2.5: Pulse sequence used for (a) transient absorption and (b) transient-DVE measurements. The UV pulse (blue) is chopped to half the laser repetition rate and a differential signal is recorded.

A vibrational echo experiment is carried out by applying three non-collinear infrared pulses resonant with a molecular transition and measuring an emitted signal—or vibrational echo—in a phase-matched direction. For a simple one-oscillator system, the experiment can be described as follows: The first pulse creates a coherent superposition between the ground (ν=0) and first-excited (ν=1) vibrational levels of the specific mode. The second incoming pulse creates a population in either the ground or first excited state depending on the phase-difference with respect to the first pulse. The third pulse finally puts the sample back into a coherent superposition between the ground and first excited states and between the first and second excited states. The final superposition results in an oscillating dipole which then radiates at either the ν=0→1 or the ν=1→2 transition frequencies. The emitted signal is usually measured using a conventional grating spectrometer. The anharmonicity of the mode dictates the difference between the ν=0→1 and ν=1→2 transition frequencies. From a molecular structure perspective, vibrational echo spectroscopy provides a direct measure of the normal-mode anharmonicity, a measurement which cannot be obtained from linear absorption spectroscopy. If the system contains multiple infrared-active modes, signal contributions can be observed from anharmonic transitions involving two different modes. Detailed descriptions of vibrational echo spectroscopy, including lineshape comparisons and the effects of concentration and oscillator strength on the signal amplitude have been presented elsewhere.[32] Finally, due to the nonlinear nature of the light-matter interaction the vibrational echo signal arising from a low concentration of strong absorbers generally dominates the signal due to a high concentration of weak absorbers.[32] This selectivity for transitions with strong transition dipole moments was recently illustrated very clearly in a study of a dye-sensitized semiconductor system.[33] Typical transient IR absorption measurements contain a very large and relatively uninformative continuum absorption due to free electrons in the semiconductor. In the transient 2DIR measurements, however, the free-carrier continuum was not present in the two-dimensional plots. Suppression of low-oscillator strength background signals, like sensitivity to anharmonicity, is another advantage of t-DVE that is separate from signal-to-noise ratio considerations.

In general, two-dimensional infrared spectra are measured using two different experimental approaches: time-domain Fourier-transform (FT) 2DIR, or frequency-resolved dynamic hole burning (frequency-domain)-2DIR. In principle, both techniques provide

identical information, but practical differences limit the information provided by hole-burning at early waiting times. A thorough comparison between the two methods has been published previously.[34] In the case of background-free FT-2DIR, three IR pulses are applied to the sample and the amplitude and phase of the echo signal is measured by interferometry with a reference pulse in a spectrometer.[18] One feature of the Fourier-transform approach is that by time-overlapping the three IR pulses and blocking the reference pulse, one obtains a dispersed vibrational echo (DVE) spectrum. The pulse sequences for TA and transient-DVE are shown in Figure 2.5. A DVE spectrum corresponds to the square of the projection of the 2DIR spectrum on to the detection axis. The DVE signal, which arises from the same pulse interactions as the 2DIR signal, can provide structural information not available in a one-dimensional absorption spectrum. The most notable difference between DVE and TA is DVE's sensitivity to vibrational anharmonicity. Similar to 2DIR, the DVE measurements can also be performed on a non-equilibrium system by applying an extra laser pulse before the three infrared pulses: transient-DVE (or t-DVE) spectroscopy. This technique yields similar information to TA spectroscopy, but since t-DVE is a non-linear probe, the data analysis can be somewhat more complicated than TA.

Recently, Jones and coworkers[35] demonstrated the use of heterodyne-detected vibrational echo (HDVE) spectroscopy as a method to characterize non-equilibrium dynamics and compared it to DVE and TA. Similar to 2DIR, an HDVE spectrum is obtained by interferometric superposition of the signal with an external reference pulse. One of the key advantages of HDVE lies in its ability to separate the absorptive and diffractive components of the molecular response function. Although as an interferometric method, HDVE has the ability to amplify weak signals by using a strong reference which can be advantageous when working with weak absorbers or low concentrations, the presence of a strong reference pulse in HDVE greatly reduces the dynamic detection range. Homodyne detected DVE, on the other hand, is a background-free method is able to make use of the entire dynamic range of the detector.

In a recent publication (see chapter 3),[36] we employed transient-2DIR and transient-DVE, to measure the asymmetric rebinding of cyclopentadienylmolybdenum(II) tricarbonyl dimer, a dimetal carbonyl molecule that exists in two different isomer conformations *trans*,

and *gauche*. The equilibrium constant of the two isomers, $K_{G/T}$, is approximately 0.25 in polar solvents with interconversion occurring in the millisecond timescale.[37] Each isomer has distinct terminal-carbonyl absorption bands in the infrared thus providing kinetic information in a structure-specific manner. Upon absorption of a 400-nm photon, both isomers undergo photocleavage of the metal-metal bond to generate two solvent-caged monomers.[38-40] By monitoring the transient-DVE bleach recovery associated with the *trans* and *gauche* conformations, we were able to conclude that rebinding exclusively favors the *trans* isomer.[36] The study highlighted structurally sensitivity as one of the main strengths of vibrational spectroscopy, which is usually not afforded by electronic spectroscopy. This geminate recombination reaction will be used to test and compare t-DVE and TA as described in the next section.

Theoretical Models

Several different theoretical approaches to computing a non-linear infrared spectrum of a given molecular system have been developed (See Ref. 41 and references therein). In this work, we use the standard perturbative approach in which the polarization giving rise to the signal is computed as a convolution between the system's optical response function, $S^{(3)}(t_1,t_2,t_3)$, and the applied laser fields.

$$P^{(3)}(t) = \int_0^\infty dt_3 \int_0^\infty dt_2 \int_0^\infty dt_1 S^{(3)}(t_1,t_2,t_3) E_3(t-t_3) E_2(t-t_3-t_2) E_1(t-t_3-t_2-t_1) \qquad (1)$$

To simulate the experimental transient DVE data presented below, we start with a third-order optical response function for a one-dimensional anharmonic oscillator in the molecular frame so that contributions due to orientational relaxation are neglected. The modeling is done within the context of Redfield theory with a phenomenological dephasing rate.[42] The main input parameters are the oscillator strengths for the lowest two transitions, V_{10} and V_{21}, and the transition frequencies, ω_{10} , and ω_{21}. The relaxation parameters represent the decays of diagonal (populations, Γ_{jj}) and off-diagonal elements (coherences, Γ_{ij}, $i \neq j$) of the density matrix, and the latter determine the widths of the peaks.

$$R_1(t_1,t_2,t_3) = |V_{10}|^4\, e^{+(i\omega_{10}-\Gamma_{10})t_3} e^{-\Gamma_{11}t_2} e^{-(i\omega_{10}+\Gamma_{10})t_1} + |V_{21}|^2 |V_{10}|^2\, e^{+(i\omega_{21}-\Gamma_{21})t_3} e^{-\Gamma_{11}t_2} e^{-(i\omega_{10}+\Gamma_{10})t_1}$$

$$R_2(t_1,t_2,t_3) = |V_{10}|^4\, e^{+(i\omega_{10}-\Gamma_{10})t_3} e^{-\Gamma_{11}t_2} e^{+(i\omega_{10}-\Gamma_{10})t_1} + |V_{10}|^2 |V_{21}|^2\, e^{+(i\omega_{21}-\Gamma_{21})t_3} e^{-\Gamma_{11}t_2} e^{+(i\omega_{10}-\Gamma_{10})t_1}$$

$$R_3(t_1,t_2,t_3) = |V_{10}|^4\, e^{+(i\omega_{10}-\Gamma_{10})t_3} e^{+(i\omega_{10}-\Gamma_{10})t_1} + |V_{10}|^2 |V_{12}|^2\, e^{+(i\omega_{21}-\Gamma_{21})t_3} e^{+(i\omega_{20}-\Gamma_{20})t_2} e^{+(i\omega_{10}-\Gamma_{10})t_1} \quad (2)$$

$$R_4(t_1,t_2,t_3) = |V_{10}|^4\, e^{+(i\omega_{10}-\Gamma_{10})t_3} e^{-(i\omega_{10}+\Gamma_{10})t_1} + |V_{10}|^2 |V_{12}|^2\, e^{+(i\omega_{10}-\Gamma_{10})t_3} e^{-(i\omega_{20}+\Gamma_{20})t_2} e^{-(i\omega_{10}+\Gamma_{10})t_1}$$

In the case of 2DIR spectroscopy, the rephasing (R) and non-rephasing (NR) contributions to the spectrum are computed as follows:

$$S_{NR} = Re\int_0^\infty dt_3 e^{i\omega_3 t_3} \int_0^\infty dt_1 e^{i\omega_1 t_1} \left[R_1 + R_4\right] \quad (3)$$

$$S_R = Re\int_0^\infty dt_3 e^{i\omega_3 t_3} \int_0^\infty dt_1 e^{i\omega_1 t_1} \left[R_2 + R_3\right] \quad (4)$$

It is important to note that as third-order processes, 2DIR and vibrational echo spectroscopy can only access first and second excited vibrational levels when starting in the ground state. In the present model, we set the anharmonicity $(\omega_{01} - \omega_{12})$ to 10 cm^{-1}, a typical value for terminal CO stretching modes in metal carbonyls and we also assume harmonic scaling of the transition dipole moments. To compute a homodyne-detected DVE signal spectrum from the above equations one sets t_1 and t_2 to zero and computes the modulus square polarization in the frequency domain:

$$P^{(3)}_{DVE}(t) = \int_0^\infty dt_3 S^{(3)} E_3(t-t_3) E_2(t-t_3) E_1(t-t_3) \quad (5)$$

$$I_{DVE}(\omega) \propto \left| \int_0^\infty e^{i\omega t} P^{(3)}_{DVE}(t) dt \right|^2 \quad (6)$$

To obtain a transient-DVE difference spectrum, two signals are generated corresponding to the equilibrium and non-equilibrium concentrations of molecules, and the difference in signal intensity is computed. Here we are principally concerned with the transient-DVE signal arising from the depletion of the parent species (described below), and ignore the photoproduct response since it does not overlap the parent. The present model

only includes the signal arising from the parent molecules, but it can be easily extended to treat a mixture of different molecules, such as other isomers and the photoproducts, including their equilibrium and non-equilibrium populations by simply adding multiple response functions with different sets of parameters. In the above equations, the induced polarization scales linearly with respect to the number of oscillators (molecules), and the signal intensity scales with the square of the number of molecules. This nonlinear scaling makes the extraction of kinetic information from a t-DVE experiment somewhat cumbersome compared to a transient absorption measurement where the signal intensity scales linearly with respect to the number of oscillators. In the next section we derive the kinetic equations for analyzing t-DVE traces and explore the implications of making simplifications in the data analysis.

The absorption spectrum can similarly be computed from the linear response function, $J(t)$, where

$$J^{(1)}(t) = |V_{10}|^2 \, e^{-(i\omega_{10}+\Gamma_{10})t} \tag{7}$$

Which leads to the first-order induced polarization $P^{(1)}(t)$:

$$P^{(1)}(t) = \int_0^\infty J^{(1)} E_t(t-\tau)\, d\tau \tag{8}$$

Note that since, within the current treatment, linear spectroscopy can only access the first-excited state, the optical response of an (an)harmonic oscillator is identical to that of a two-level system.

The detected infrared pulse spectrum (after passing through the sample) can be computed as an interference between the radiated field, $E_{induced}$, arising from the induced linear polarization[43] and probe pulse field itself.

$$I_{Abs}(\omega) = \left| \int_0^\infty \left[E_{Induced}(t) - E_t(t) \right] e^{i\omega t} dt \right|^2 \tag{9}$$

To gain a better understanding of the experimental measurements outlined below, we use these models to compute the transient absorption and transient DVE signals as a function of the number of oscillators, or concentration of molecules, and explore the signal-to-noise

ratio dependence of the computed signals on the laser and detector noise. The time-dependent difference TA and t-DVE traces (Figure 2.6) are simulated by generating signals corresponding to two different populations—pumped and unpumped—at various delays after the phototrigger. The evolution of the transient population after the UV excitation is modeled using a single-exponential function with values that closely match the experimental conditions: 10% excitation fraction, 18 ps recombination lifetime, and 50% rebinding ratio.

Experimental Methods and Results

The ultrafast optical setup has been described in detail elsewhere.[44, 45] In brief, an 800-nm Ti:Sapphire regenerative amplifier (Spectra Physics Spitfire Pro) pumps a BBO-based dual-OPA system which is then used to generate mid-IR in GaSe by difference frequency generation between the OPA signal and idler. The First OPA/DFG setup is used to generate pump pulses E_1 and E_2 whereas the second setup generates E_3 and E_t. The last beam E_t is used for alignment and acts as the probe in transient absorption measurements. A measurement of the IR pulse fluctuations shows that these fluctuations (Gaussian white noise) on the two OPA/DFG setups are essentially uncorrelated. Given that the same white light source is used to seed both OPAs, the lack of correlation in their outputs suggests that fluctuations in the white light are irrelevant, indicating that the non-linear OPA process is being saturated. The IR beams are arranged in a box geometry and the signal spectrum is detected by upconversion into the visible with a 300-ps highly-chirped pulse derived from the amplifier output before compression.[46] The visible spectrum is detected using 20 rows (vertically binned) of a 1340-by-100-pixel CCD detector attached to a conventional grating spectrometer. Chirped-pulse upconversion allows us to use a silicon-based detector, and thus affords improved detection sensitivity and lower noise levels. Part of the 800-nm amplifier output is frequency-doubled in a 0.4-mm BBO crystal to obtain a 400-nm phototrigger pulse. The UV pulse is chopped at half the laser repetition rate of 1 kHz, and the UV-IR delay is scanned continuously while the signal spectrum (absorption or DVE) is measured at the laser repetition rate. The difference signal is computed at varying delays using an integration window of 100 pulses, giving an effective UV-IR time resolution of ~500 fs.

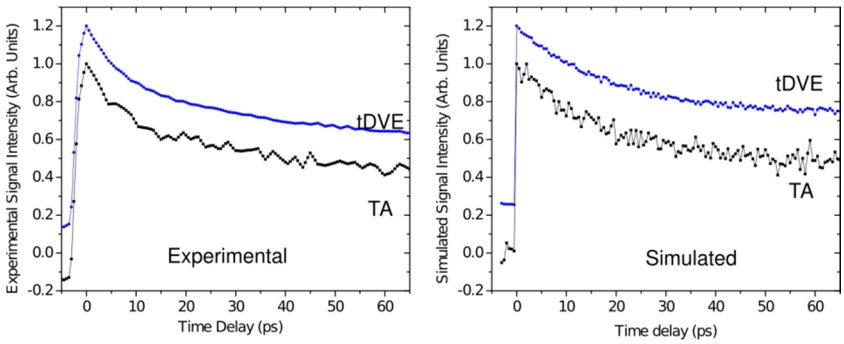

Figure 2.6: Experimental (left) and simulated (right) transient DVE and transient absorption traces. The experimental traces were collected back-to-back under identical conditions, and the simulated plots were obtained using the same laser noise and excitation ratios for both curves. The experimental curves are obtained by averaging 1000 laser shots (10 x 100-shot window) per point, or a total data acquisition time of approximately 300 seconds. The two curves are offset for clarity.

The test molecule used for the experiments is cyclopentadienylmolybdenum(II) tricarbonyl dimer, a complex which upon excitation at 400-nm undergoes metal-metal bond cleavage to generate solvent-caged monomer radicals.[38] This particular molecule is chosen because of the large non-linear signal inherent to metal carbonyls and because the in-cage recombination to cage escape ratio is large, making it an ideal test case for comparing the kinetics measured with t-DVE and TA. The sample solution in ethyl acetate is flowed in a 200-μm path length flow-cell equipped with 2 mm calcium fluoride windows using a peristaltic pump. In addition, the sample cell is mechanically moved to minimize scattering caused by the accumulation of a photoproduct on the cell windows. The solute concentration is adjusted to yield a ~50% transmittance at the main infrared absorption band at 1958 cm^{-1} , which corresponds to a concentration of approximately 2.6 mM. The corresponding extinction coefficients for the two transitions are 1437 m^2/mole and 800 m^2/mole at 400 nm and at 1958 cm^{-1} respectively. The optical density of the sample at 400-nm is ~0.4, and the UV energy is adjusted to yield an excitation fraction of approximately 0.1 (ratio of excited to ground-state molecules following absorption of the UV pulse). About 50% of the radicals undergo geminate recombination inside the solvent cage with a time constant of ~16 ps and the rest diffuse into the bulk solution.[36] To monitor the cage-recombination kinetics, an absorption peak at 1958 cm^{-1} corresponding to the dimer is monitored as a function of time-delay after ultraviolet excitation. This peak exhibits a bleach upon absorption of 400-nm light as the population of dimer molecules is depleted; a bleach recovery is observed as the product molecules (monomers) recombine to repopulate the

parent states. To obtain a kinetic trace (Figure 2.6) the t-DVE or TA signals are integrated over the width of the peak.

Estimation of Signal-to-noise Ratios

Transient-DVE is a background free experiment; therefore the signal-to-noise ratio (SNR) is significantly improved in comparison with transient absorption. The noise percentage for t-DVE measurements will depend mainly on the laser fluctuations, signal intensity, and the excitation fraction. Assuming that the experiments are carried out in the regime where the signal intensity is large enough so that the detector noise can be neglected, and also assuming negligible fluctuations in the trigger pulse, the SNR for a single pair of shots, or adjacent pulses in the pulse train, can be estimated from the IR pulse fluctuations. As shown in equation 10 below, the intensity of the DVE signal is proportional to the square of the three incoming fields:

$$I_{DVE} \propto (E_1 E_2 E_3)^2 \tag{10}$$

This allows us to compute the fluctuations in the t-DVE signal from the laser intensity fluctuations. In the analysis below we assume that fields E_1 and E_2 have perfectly correlated noise fluctuations and that field E_3 has independent fluctuations as the first two pulses are generated by the same OPA/DFG setup whereas the third pulse is generated by a second OPA/DFG. We also assume that all three pulses have the same amplitude noise percentage (NP) fluctuations corresponding to Gaussian white-noise, denoted σ. In our experimental setup a typical value for NP of the shot-to-shot amplitude fluctuations is $(\sigma / I) = 0.7\%$. The percentage intensity fluctuations of the DVE signal intensity can be computed from the simple equations used to describe the propagation of error in experimental measurements:

$$\sigma_{I_{DVE}} = 2\sqrt{(2\sigma)^2 + \sigma^2} = \sqrt{20}\sigma \tag{11}$$

The noise percentage for a single pulse-pair difference DVE ($\Delta I_{DVE} = I_{DVE,Pumped} - I_{DVE,Unpumped}$) can be computed as follows:

$$\sigma_{\Delta I_{DVE}} = \frac{\sqrt{(\sigma_{I_{DVE}} I_{DVE,Pumped})^2 + (\sigma_{I_{DVE}} I_{DVE,Unpumped})^2}}{I_{DVE,Unpumped} - I_{DVE,Pumped}} \tag{12}$$

$$\sigma_{\Delta I_{DVE}} = \frac{\sigma_{I_{DVE}} \sqrt{20\left[\left(1-\kappa_{exc}\right)^4 + 1\right]}}{1-\left(1-\kappa_{exc}\right)^2} \tag{13}$$

In the above equation, κ_{exc} represents the fraction of molecules excited by the trigger pulse. To obtain a simple form of the next equation, we now assume zero correlation in the fluctuations between the difference DVE and the DVE signal itself. This assumption gives an upper limit for the noise estimate:

$$\sigma_{tDVE} \approx \sqrt{\sigma^2_{\Delta I_{DVE}} + \sigma^2_{I_{DVE}}} \tag{14}$$

Using typical values for the present experiment: $(\sigma / I) = 0.7\%$, and a $\kappa_{exc} = 10\%$, gives a Gaussian noise width of ~1.6% with a 100-pulse-pair integration window.

We estimate the noise percentage for transient absorption. We can estimate the noise obtained from subtracting two subsequent laser shots using the following relation:

$$\sigma_{Diff} = \frac{\sqrt{(I_{Pump}\sigma_{Pump})^2 + (I_{Probe}\sigma_{Probe})^2}}{I_{Pump} - I_{Probe}} \tag{15}$$

In the above equations we assume that there is no correlation between the pulse difference and the normalizing probe pulse. Since the error added by normalizing is negligible compared to the error of the difference between two shots, a good estimate in the error can be obtained from inputting our parameters into equation 15.

$$\sigma_{TA} \approx 2\sigma \frac{\sqrt{(1 - A\kappa_{exc})^2 + 1}}{A\kappa_{exc}} \tag{16}$$

Once again, κ_{exc} represents the fraction of molecules excited by the phototrigger, and A corresponds to the fraction of light absorbed by the sample at the frequency of interest.

Similar to tDVE, the TA difference signal is calculated as $\left[A_{pumped} - A_{unpumped} \right] / A_{unpumped}$. The calculated noise-percentage using the same values as above is ~3.9%. From these results we can observe that, under the same experimental conditions, the amount of signal averaging required to obtain the same signal-to-noise ratio with TA as obtained with t-DVE is approximately six times greater assuming a square-root dependence on the number of measurements.

The observation that a higher order spectroscopy method offers signal-to-noise ratio advantages over lower-order approaches is not new, and forms the basis for interest in using coherent anti-Stokes Raman spectroscopy (CARS) instead of spontaneous Raman spectroscopy. Under conditions that correspond to typical spectroscopic applications, such as high laser pulse intensity and high oscillator number density, CARS clearly offers significant advantages over incoherent Raman spectroscopy.[47, 48] On the other hand, when pulse energy is low—as is required to avoid cell death and tissue damage—and number density is low, Raman actually offers superior signal amplitude and thus enhanced signal-to-noise ratio since the method is linear in the incident intensity. [47]

Extracting Kinetics from t-DVE Experiments

In this section we derive the equations used for analyzing the transient-DVE signal as a function of the time delay following the phototrigger (t). Consider a general reaction of the type:

$$A \underset{k_{rec}}{\overset{h\upsilon}{\rightleftarrows}} B \xrightarrow{k_{esc}} C \tag{17}$$

The following equations are derived assuming that the quantity of interest corresponds to the concentration of species **A**. These equations can be easily modified to represent the quantities of species **B** or to accommodate other types of reactions. The ratio of equilibrium to transient concentration of **A** as a function of time after the excitation pulse is described using the following equation:

$$\phi(t) = 1 - \left[\kappa_{exc} \left(\phi_{rec} e^{-t/\mathrm{T}} - \phi_{rec} + 1 \right) \right] \tag{18}$$

Where κ_{exc} is the excitation fraction (the fraction of molecules excited by the pump pulse), T is the observed rate of recovery of **A** and ϕ_{rec} can be considered a recombination "quantum yield", and it is expressed as:

$$\phi_{rec} = \frac{k_{rec}}{k_{rec} + k_{esc}} \tag{19}$$

Since the DVE intensity is proportional to the square of the number of oscillators at a given frequency, (e.g. number of reactant or product molecules, in this particular case reactant molecules) the transient signal can be calculated as follows:

$$I_{tDVE}(t) = \frac{I_{pumped} - I_{unpumped}}{I_{unpumped}} = \phi(t)^2 - 1 \tag{20}$$

Substituting $\phi(t)$ into the above equation yields the following relation:

$$I_{tDVE}(t) = \left[\kappa_{exc} e^{-2t/T}\right]\left[e^{t/T}\left(\phi_{rec} - 1\right) - \phi_{rec}\right]\left[e^{-t/T}\left(\kappa_{exc}(\phi_{rec} - 1) + 2\right) - \kappa_{exc}\phi_{rec}\right] \tag{21}$$

Equation 21 represents the t-DVE signal difference in terms of the excitation fraction, the recombination ratio and the reaction time constant, though fitting an experimentally obtained curve to this equation may be non-trivial despite the monoexponential underlying kinetics. As seen below, the curves show largely monoexponential behavior, and can be adequately fit to a single exponential curve under many experimentally-relevant conditions. Figure 2.7 and Figure 2.8 below show the percent error in time constant, T, and recombination ratio, ϕ_{rec}, extracted from a single-exponential fit to generated t-DVE curves. The plots show that the smallest fitting errors are achieved using low excitation ratios, and that under these conditions, the errors are small enough that they may be within the normal experimental error. A special case of equation 21 can be obtained when the recombination ratio is unity: $\phi_{rec} = 1$. This case applies to a wide range of photophysical reactions where the system cycles on the same timescale as the experiment.

$$I_{tDVE,\phi_{rec}=1} = \kappa_{exc} e^{-2t/T}\left(-2\,\mathrm{e}^{t/T} + \kappa_{exc}\right) \tag{22}.$$

Although this relation is simpler than the equation for the general case (21), a double-exponential is still required to fit the data. The errors in the recombination time constant obtained by fitting to a single-exponential for this case are also shown in Figure 2.7. The plot shows that these errors can vary between 5 and 20% depending on the fraction of molecules excited by the pump pulse.

Discussion

In the present experiment we monitor the repopulation of parent molecules using the two described probing techniques. To ensure consistency, both experiments were collected consecutively with no realignment of the optical setup. The experimental traces (Figure 2.6) show an initial transient-signal arising at zero-time and recovering to approximately 50% of the initial value. The onset of the signal is limited by the experimental time-resolution of ~500 fs which is given by the size of the integration window (100 shots). A greater time resolution can be achieved using the more standard approach of stepping the UV delay and collecting t-DVE spectra at the various delays. A comparison between the experimental and calculated t-DVE and TA traces (Figure 2.6) shows that the signal-to-noise ratios are successfully reproduced using our models. The figures also clearly show that the signal-to-noise is much higher in the t-DVE measurements.

In addition to the signal-to-noise ratio differences it is important to discuss the issue of detection noise. Transient-DVE, a background-free measurement, has an inherent advantage over TA since the signal level can be largely adjusted so that the full dynamic range of the detector is used. Therefore, an improved signal-to-noise ratio and lower averaging times can be realized by this method. Also, unlike TA, small spectral shifts in the laser pulses, do not cause large distortions of the background in the difference spectrum. A change in the background as a result of pulse fluctuations can pose a problem when trying to monitor the amplitude of the different features in the spectrum. Many of the limitations of TA outlined here can be overcome by detecting a reference pulse at every laser shot in a dual-detection system as is implemented in many experimental cases. Naturally, this requires multiple detector arrays and a slightly more complicated optical setup and similar to TA, the signal-to-noise ratio in t-DVE can be greatly improved by referencing. As t-DVE is a background-free signal, small spectral shifts of the Gaussian pump pulses do not have a

significant effect on the signal amplitude, and the main source of noise remains the shot-to-shot pulse amplitude fluctuations. Therefore, the signal-to-noise in t-DVE can be greatly improved by detecting the integrated pump pulse intensities with a single-channel detector, and normalizing each spectrum by the pump amplitude. It is also important to point out that the present signal-to-noise ratio comparison is carried out on a strongly infrared-active terminal carbonyl stretching mode, where the DVE signal can be made to span the full dynamic range of the detector. Therefore, in the models presented, only the laser fluctuations are considered to be a source of measurement noise. Other sources of noise such as detector dark counts, digitization and shot-noise may need to be explicitly considered when measuring weaker transitions.

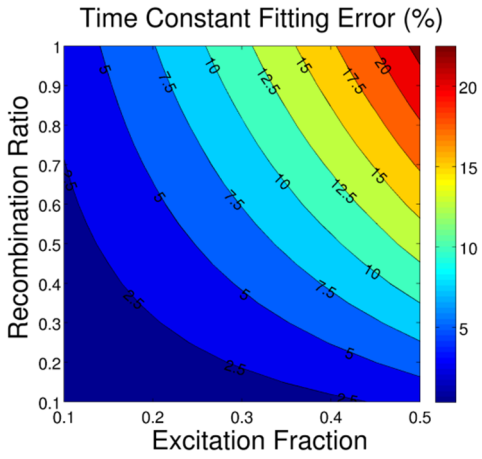

Figure 2.7: Error in the recombination time constant obtained by fitting Equation 21 to a single exponential. Small excitation fraction and low recombination rates are favorable to obtain smaller fitting errors.

In principle t-DVE spectra feature narrower peaks than TA since, due to the four-field interactions, the signal field amplitude for ground-to-first-excited-state transitions scales with the fourth power of the transition dipole moment. However, several contributions from anharmonic states may actually broaden the peaks. The DVE signal contains contributions from excited-state transitions, which have similar line widths, similar intensities, and appear slightly red-shifted with respect to the fundamental transitions as a result of anharmonicity. Although they provide additional information about the system Hamiltonian, these excited-state transitions and combination-bands can contribute to broader line-shapes in t-DVE

compared to TA. If the anharmonicity is large enough compared to the peak widths, the narrower features may be extracted by fitting the DVE

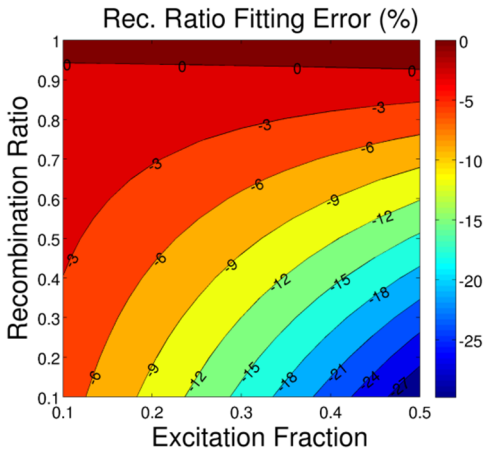

Figure 2.8: Error in the recombination ratio obtained by fitting Equation 21 to a single exponential with an offset.

line shapes. Since the DVE is a projection of the 2D spectrum, cross peaks in the 2D spectrum can appear in the DVE signal in different ways. Cross peaks that arise from excitation and emission in the same manifold, such as the cross peaks between two different modes (q_1 and q_2, for example), largely serve to amplify the DVE spectrum since they appear at detection frequencies matching the diagonal peaks. Cross peaks that are explicitly due to anharmonicity—either diagonal (i.e. q_1^3) overtones or off-diagonal (i.e. $q_1 q_2^2$) combination bands—broaden the DVE spectrum since they contribute signal amplitude at frequencies that are different from the diagonal features. In addition to broadening the lineshapes, these anharmonic contributions may complicate the interpretation of the DVE spectrum, however since the DVE signal can be reconstructed from a 2DIR spectrum, the latter can be used to directly interpret all the peaks in the DVE spectrum. In many systems, the photoexcitation process deposits enough energy into the molecule to significantly raise its temperature, thus leading to broader features at early times.[31, 45] Transient-DVE is sensitive to small changes in the molecular structure through the anharmonic couplings and thus it would likely make a sensitive probe of temperature. The effects of dynamics on linear and non-linear spectral lineshapes have been successfully modeled using frequency maps combined with molecular dynamics simulations.[49-52] Recently, Tokmakoff and coworkers have employed DVE

spectroscopy to study the unfolding of a protein triggered by a temperature-jump.[22, 23] Their interpretation of the transient-DVE data is aided by the 2DIR spectrum of the same system. Finally, the non-linear intensity scaling with respect to the spectra of the infrared pulses serves to localize the DVE signal in frequency, making TA a better choice for exploring the spectroscopic landscape, followed by DVE "zooms" in specific regions of interest.

The increased sensitivity and lower noise levels in t-DVE come at the cost of more complicated extraction of kinetic data from the experiment. The monoexponential fitting procedure, as shown in Figure 2.7, shows that the error in recovering the underlying monoexponential rate constant is small as long as the fraction of excited molecules remains small. The actual errors remain within a few percent as long as the excitation fraction remains less than 10%. Equation 21 shows that the observed signal-decay curve is a biexponential where the two exponentials have opposite sign, therefore a single-exponential fit always gives an upper limit for the underlying kinetic rate of the reaction. Multiexponential kinetics may further complicate the extraction of lifetimes from t-DVE and would likely require partial knowledge of the reaction along with numerical modeling of the data, a problem which is not present in TA spectroscopy. The plot in Figure 2.8 also shows that the offset in the single-exponential fit is a lower limit for the actual recombination ratio. In this context it is important to report the actual geminate rebinding time constant of cyclopentadienylmolybdenum(II) tricarbonyl dimer of 16.18$\pm$0.67 ps (TA) 16.08$\pm$0.38 (t-DVE) and the rebinding ratio of 0.496$\pm$0.08 (TA) 0.51$\pm$0.04 (t-DVE) obtained by fitting a single exponential to the experimental curves in Figure 2.6. We would like to point out that these values replace our previously reported time constant of 31 ps in an earlier publication,[36] where the measured lifetime of 15.6 ps was doubled based on a simplistic consideration of the population dependence of t-DVE.

One final matter that should be discussed in the present context is the issue of orientational relaxation. Transient-DVE, similar to transient-2DIR, is a fifth order non-linear experiment; but since the three pulses are time-coincident, the simpler third-order formalism can be used to analyze the results.[53] This simplification is clearly not valid for transient-2DIR spectroscopy where the full set of fifth-order tensor elements must be taken into consideration.[54] However, it is important to keep in mind that the contribution from orientational relaxation is not identical to that for TA due to the fact that t-DVE is a non-

linear probe, thus altering the dependence on the number of oscillators as well as the transition dipole moments involved. The equations provided above for analyzing the signal decay kinetics can be slightly modified to analyze orientational contributions to the t-DVE signal, though such a treatment is beyond the scope of this work. Additional information relating to the molecular Hamiltonian of the transient species, such as the relative orientation of the transition dipoles, can be obtained from a transient-DVE experiment by controlling the polarization of the three probe pulses.[54]

Concluding Remarks

We have compared two different spectroscopic techniques used for obtaining kinetic information on non-equilibrium systems: transient-DVE and transient absorption spectroscopy. We have shown that transient-DVE offers improved signal-to-noise ratios over transient absorption while offering additional structural information which can be related to the molecular Hamiltonian. The results also show that t-DVE can provide reasonably high signal-to-noise ratios while avoiding the need for detecting a reference spectrum at every laser shot. Although the equations associated with modeling the kinetics using a non-linear probe can become cumbersome, single-exponential fitting of the transient data produces rather accurate estimates of the kinetics, especially under low excitation conditions.

In addition to serving as probe of molecular kinetics, t-DVE can be directly related to transient-2DIR experiments by a simple projection on to the detection axis; so it may be possible to extract much of the information content in transient-2DIR using this simpler technique, which may prove useful in situations where collecting a full 2DIR of a transient species may not be feasible. Alternatively, one could extract structural information and assign the spectrum using transient-2DIR spectra at a few time delays and measure the kinetics using t-DVE. Although the t-DVE experiment requires a more complicated optical setup, transient-DVE may become an attractive complement to TA as has already been demonstrated in studies of temperature-jump protein folding[29,33] and ultrafast photochemistry.[34]

2.4 Ultrabroadband Detection of an Infrared Continuum

Unlike conventional Fourier-transform spectroscopy, ultrafast mid-infrared spectroscopy has been limited to small spectral windows of widths typically <500 cm^{-1}, where only a small set of nearby vibrations can be measured simultaneously.[55] Ideally, ultrafast spectroscopy with IR pulses should be able to access the entire 500–4000 cm^{-1} spectral region, providing maximum structural and dynamical information. Two constraints limit the spectral bandwidth of IR generation and detection. Firstly, conventional implementations rely on optical parametric amplification (OPA) followed by difference frequency generation (DFG) to produce mid-IR pulses, and are limited in bandwidth by phase matching.[56] Secondly, direct multichannel infrared detection is carried out using mercury-cadmium-telluride (MCT) detector arrays that suffer from low pixel count, reduced sensitivity, and high cost compared to their silicon-based counterparts for visible detection. A state-of-the-art MCT detector features only 128 pixels.

Broadband sources of THz and mid-infrared radiation through plasma generation in air have been recently demonstrated.[24-28] In particular, Petersen and Tokmakoff implemented a new infrared continuum source for sub-100 fs pulses spanning <400 cm^{-1} to >3000 cm^{-1} by simultaneously focusing three high-intensity pulses centered at 800, 400 and 267 nm in air.[29] Though the complete mechanism of the IR continuum generation is not yet well understood, the process has been described in terms of optical rectification[24, 25] in collisional plasma.[57] Until now the efficient detection of such a continuum source has remained a challenge. In this letter we describe a straightforward apparatus for ultrabroadband mid-IR generation and detection based on chirped-pulse upconversion[46, 58] (CPU), whereby starting with 100-fs 800-nm pulses, we can achieve a nearly 1000 cm^{-1}detected bandwidth with 1 cm^{-1} spectral resolution over most of the mid-infrared (1600 to 4100 cm^{-1}).

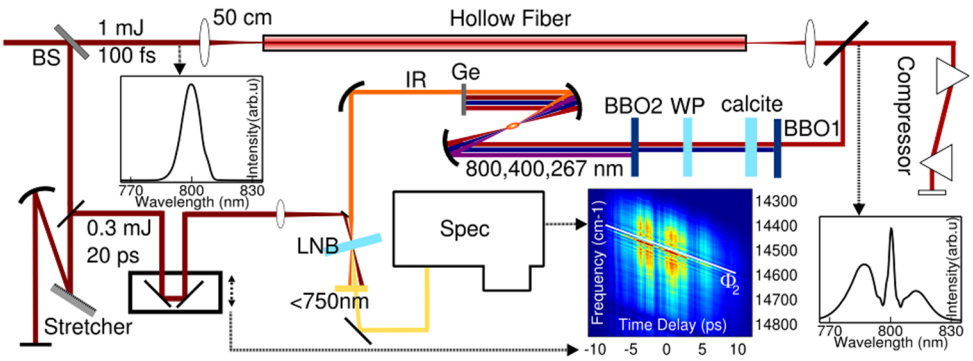

Figure 2.9: Infrared continuum generation and upconversion setup. Spectra corresponding to the 800-nm pulses before and after the hollow fiber are shown for comparison. A spectrogram of the upconverted IR as a function of the IR-800 delay shows the second order spectral phase of the 800-nm chirped pulse.

The optical setup is illustrated in Figure 2.9. Pulses derived from a 100-fs 2mJ Ti:sapphire amplifier (Spectra-Physics Spitfire Pro) are split in a 50:50 ratio. One half is used for IR generation while the other half is used for upconversion. Since the bandwidth of the IR continuum is dictated by the bandwidth of the source, we spectrally broaden the 800-nm pulse via self-phase modulation in argon.[59] 1mJ 800-nm pulses are focused using a f=50-cm lens into a 125μm hollow-core fused silica fiber (FemtolasersOA219) placed inside a pressurized chamber. The 400 μJ fiber output is collimated to a diameter of 5mm and recompressed using a pair of fused silica Brewster prisms. Typically, 40 fs full-width-at-half-maximum (FWHM) compressed pulses are obtained with 0.75 atm of Ar and a 234 cm tip-to-tip prism pair distance. The compressed pulses are sent through an in-line second and third harmonic generation setup.[60] Second harmonic pulses are generated by type I phase matching in a 0.4 mm β-barium borate (BBO) crystal, followed by a calcite plate (Eksma 225-2112) to compensate the group delay of the entire setup (83 fs BBO + 451 fs waveplate +220 fs BBO). Next, a dual-band λ/2 waveplate (Eksma 466-4211) rotates the 800-nm polarization to coincide with the 400-nm polarization. Finally, type I sum-frequency generation in a 0.4 mm BBO generates the 267 nm third harmonic. The three pulses are focused into air using a spherical dielectric mirror with a 10 cm radius (Layertec 100600). A bright ~0.5-mm filament is observed at the focus, and the IR continuum intensity correlates well with the brightness of the filament. A 12 cm radius aluminum-coated spherical mirror collimates the light and a 1-mm Ge window filters out the UV and visible light. The IR is then refocused to a ~1 mm spot using a 12 cm spherical gold-coated mirror. The total IR

output is measured and optimized by placing a single channel MCT detector (IR Associates MCT-20-1.0) at the focus; after attenuation by an OD=0.3 neutral density filter the IR power is still sufficient to saturate the detector. A sample of $Mn_2(CO)_{10}$ in cyclohexane, provides narrow absorption bands in the carbonyl stretching region (~2000 cm^{-1}) to calibrate the detection axis, test the phase correction procedure, and evaluate the effective spectral resolution of the upconversion. The remaining 1 mJ of 800-nm laser output is sent through a grating stretcher constructed from a 1200 grooves/mm grating (Spectrogon 9800-2840). Finally, the ~15-ps chirped pulses (350 μJ) are mixed with the IR continuum in a type-I SFG arrangement using a wedged 0.3-to-0.8-mm MgO(5%):$LiNbO_3$ (LNB) crystal. The leftover 800-nm is filtered out by a 750-nm shortpass filter, and sent to a conventional visible spectrometer equipped with a 1340-by-100 pixel CCD detector (Pixis, Princeton Instruments) that may be operated in a mode can record 1340-pixel spectra at 1 kHz. Unless focused, the upconverted visible light (~650 nm) cannot be seen by the naked eye, thus a small 4° angle between the IR and 800-nm beams ensures that the upconverted light will be practically collinear with the 800-nm beam which facilitates its initial alignment into the spectrometer.

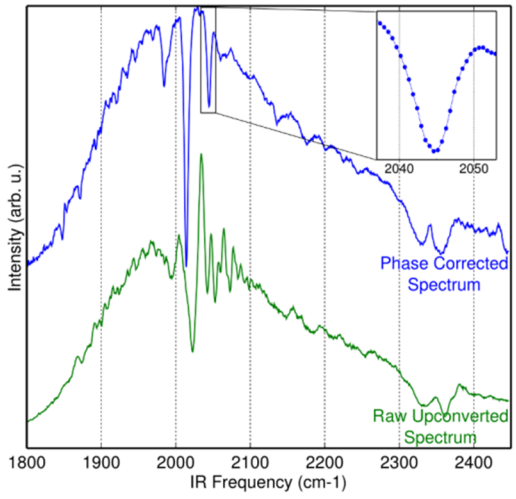

Figure 2.10: Upconverted IR continuum. The absorption lines at 1983, 2013, and 2045 cm^{-1} correspond to carbonyl stretches in of in $Mn_2(CO)_{10}$, the remaining absorption lines are from atmospheric water and carbon dioxide. The inset shows the large number of points measured by upconversion. The spectra in are collected with an integration time of 100 ms.

The IR source is particularly stable; the measured shot-to-shot noise percentage (standard deviation/mean) of the IR continuum is 2.0% (upconverted) or 3.1% (MCT),

which compares well with a 0.7% shot-to-shot noise in our OPA-DFG narrowband IR generation setup pumped by the same laser. In terms of the total IR bandwidth, we were able to upconvert frequencies between 1600 and 4100 cm^{-1}, indicating that the continuum spans the entire mid-IR region. The low-frequency limit is due to IR absorption in LNB and can be circumvented using other nonlinear media. To measure the continuum generation efficiency in different gases, N_2, CO_2, and Ar were flowed from a nozzle placed 2 mm below the plasma filament. The IR intensity increase relative to that in air measured using the MCT is as follows: 7% (N_2), 17%(CO_2), and 24% (Ar). We measured the bandwidth changes by simultaneously upconverting two IR regions centered at 1646 (type I) and 3114 (type II) cm^{-1} in a single LNB crystal. The high-to-low frequency intensity ratios are 1.1 (N_2), 2.0 (CO_2), 2.2 (Ar) normalized to a 1.0 ratio in air, suggesting that increasingly polarizable gases can enhance the generated IR intensity at the high-frequency region, consistent with recent THz generation studies.[61]

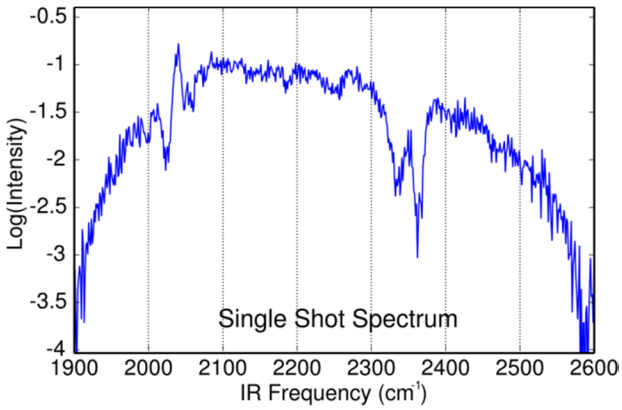

Figure 2.11: Single-shot upconverted IR spectrum (not phase corrected). The peaks near 2350 cm-1 correspond to absorption by atmospheric carbon dioxide.

A frequency-resolved cross-correlation between the IR and upconverting pulses measures the instantaneous frequency and amplitude of the chirped pulse (CP). Since no optical realignment is required, the chirp characterization can be performed *in situ* by scanning the time delay between the two pulses. When no attempt is made to remove the cross-phase modulation imparted by the chirped pulse, the resulting spectrum is convolved with the bandwidth present during overlap with the mid-IR pulse. Here, the continuum pulse is measured to have a temporal width of 58 fs FWHM by cross-correlation (SFG) with a transform limited 100-fs 800-nm pulse. Thus, the uncorrected CPU spectral convolution is

0.5 cm^{-1} given the CP has FWHM bandwidth and a duration of 130-cm^{-1} and 15 ps, respectively. By comparison, upconversion with a transform-limited 15 ps Gaussian pulse would be convolved with 1.1 cm^{-1}. In addition to the spectral convolution, the second order phase of the CP modulates the phase of the upconverted IR pulse and causes severe distortions when narrow absorption lines are present. Correcting for these distortions and recovering the original lineshapes is straightforward.[62, 63] In brief, a power spectrum is Fourier-transformed into the time domain where the antisymmetrized second order phase, $exp(-[i \times sign(t)]t^2/\Phi_2)$, is divided out and the spectrum is inverse Fourier-transformed back into the frequency domain. The phase can be recovered from the cross-correlation by extracting the value of the upconverted frequencies as a function the CP-IR delay (see spectrogram in Figure 2.9).The first order phase, or absolute IR-CP delay, is not precisely known, therefore there is an ambiguity in the absolute frequency. This can be corrected by shifting the frequency axis to reproduce the known transition frequencies of a reference sample. Raw upconverted and corresponding phase-corrected spectra are shown in Figure 2.10. The narrow peaks of $Mn_2(CO)_{10}$ (6.5 cm^{-1} FWHM) are recovered by the phase correction procedure with no loss of spectral resolution. Given a chirped pulse long enough to match the longest free-induction decays (narrowest transitions), the spectral resolution is only determined by how accurately the second-order phase can be measured. Although upconversion can also be implemented using a narrowband pulse, from a practical perspective the chirped-pulse upconversion method efficiently uses all the light available, whereas to attain a 1 cm^{-1} narrowband pulse starting from a 130-cm^{-1} 100-fs pulse, >99 % of the light must be discarded through spectral filtering. This is an important advantage of the CPU method. Finally, another advantage of upconversion over direct IR detection in its ability simultaneously detect a full octave of IR bandwidth, whereas overlapping diffraction orders from the grating would prevent direct detection in the infrared unless additional filters are placed after the grating.

Signal intensity versus bandwidth is the central tradeoff within CPU: a thin upconversion crystal will support a broader bandwidth, but with less conversion efficiency, and thus a low-noise detector is essential to achieving ultrabroadband upconversion. To measure the signal-to-noise ratio and detection limit of the setup we collected single-shot spectra (Figure 2.11). Near the most intense region (~2200 cm^{-1}), the detector noise to signal

intensity ratio is 1.3%(~10^{-2} OD), a value comparable to the shot-to-shot fluctuations. A high pixel density, (~2 pixels/cm^{-1}), means a low-pass filter can be applied to further reduce the noise without significant loss of spectral resolution.

In conclusion, we have demonstrated a new ultrabroadband generation and detection method based on chirped pulse upconversion that spans the complete mid-infrared region. The detection bandwidth is only limited by the thickness of the nonlinear crystal and the spectrometer noise. We believe that the developments presented here will find immediate applications in transient absorption and multidimensional infrared spectroscopy.

References

1. C. R. Baiz, R. McCanne, and K. J. Kubarych, "Structurally selective geminate rebinding dynamics of solvent-caged radicals studied with nonequilibrium infrared echo spectroscopy," Journal of the American Chemical Society **131**(38), 13590-13591 (2009).

2. J. Bredenbeck, J. Helbing, K. Nienhaus, G. U. Nienhaus, and P. Hamm, "Protein ligand migration mapped by nonequilibrium 2D-IR exchange spectroscopy," Proceedings of the National Academy of Sciences of the United States of America **104**(36), 14243-14248 (2007).

3. J. R. Zheng, K. W. Kwak, J. Xie, and M. D. Fayer, "Ultrafast carbon-carbon single-bond rotational isomerization in room-temperature solution," Science **313**(5795), 1951-1955 (2006).

4. Z. Ganim, K. C. Jones, and A. Tokmakoff, "Insulin dimer dissociation and unfolding revealed by amide I two-dimensional infrared spectroscopy," Physical Chemistry Chemical Physics **12**(14), 3579-3588 (2010).

5. S. H. Shim, R. Gupta, Y. L. Ling, D. B. Strasfeld, D. P. Raleigh, and M. T. Zanni, "Two-dimensional IR spectroscopy and isotope labeling defines the pathway of amyloid formation with residue-specific resolution," Proceedings of the National Academy of Sciences of the United States of America **106**(16), 6614-6619 (2009).

6. K. Wynne and R. M. Hochstrasser, "The Theory of Ultrafast Vibrational Spectroscopy," Chemical Physics **193**(3), 211-236 (1995).

7. S. Woutersen, U. Emmerichs, and H. J. Bakker, "Femtosecond mid-IR pump-probe spectroscopy of liquid water: Evidence for a two-component structure," Science **278**(5338), 658-660 (1997).

8. H. J. Bakker, S. Woutersen, and H. K. Nienhuys, "Reorientational motion and hydrogen-bond stretching dynamics in liquid water," Chemical Physics **258**(2-3), 233-245 (2000).

9. M. Cho, "Coherent Two-Dimensional Optical Spectroscopy," Chemical Reviews **108**, 1331-1418 (2008).

10. M. D. Fayer, "Dynamics of Liquids, Molecules, and Proteins Measured with Ultrafast 2D IR Vibrational Echo Chemical Exchange Spectroscopy," Annual Review of Physical Chemistry **60**(1), 21 (2009).

11. J. P. Oglivie and K. J. Kubarych, "Chapter 5 Multidimensional Electronic and Vibrational Spectroscopy: An Ultrafast Probe of Molecular Relaxation and Reaction Dynamics," Advances In Atomic, Molecular, and Optical Physics **57**, 249-321 (2009).

12. P. Hamm, M. H. Lim, and R. M. Hochstrasser, "Structure of the amide I band of peptides measured by femtosecond nonlinear-infrared spectroscopy," Journal of Physical Chemistry B **102**(31), 6123-6138 (1998).

13. C. R. Baiz, P. L. McRobbie, N. K. Preketes, K. J. Kubarych, and E. Geva, "Two-Dimensional Infrared Spectroscopy of Dimanganese Decacarbonyl and Its Photoproducts: An Ab Initio Study," The Journal of Physical Chemistry A **113**(35), 9617-9623 (2009).

14. C. R. Baiz, P. L. McRobbie, J. M. Anna, E. Geva, and K. J. Kubarych, "Two-Dimensional Infrared Spectroscopy of Metal Carbonyls," Accounts of Chemical Research **42**(9), 1395-1404 (2009).

15. A. M. Moran, J. Dreyer, and S. Mukamel, "Ab initio simulation of the two-dimensional vibrational spectrum of dicarbonylacetylacetonato rhodium(I)," The Journal of Chemical Physics **118**(3), 1347-1355 (2003).

16. N. Demirdoven, M. Khalil, O. Golonzka, and A. Tokmakoff, "Correlation effects in the two-dimensional vibrational spectroscopy of coupled vibrations," Journal of Physical Chemistry A **105**(34), 8025-8030 (2001).

17. N. Demirdoven, M. Khalil, and A. Tokmakoff, "Correlated vibrational dynamics revealed by two-dimensional infrared spectroscopy," Physical Review Letters **89**(23), 237401 (2002).

18. M. Khalil, N. Demirdoven, and A. Tokmakoff, "Coherent 2D IR spectroscopy: Molecular structure and dynamics in solution," Journal of Physical Chemistry A **107**(27), 5258-5279 (2003).

19. J. Bredenbeck, J. Helbing, C. Kolano, and P. Hamm, "Ultrafast 2D-IR Spectroscopy of transient species," Chemphyschem **8**(12), 1747-1756 (2007).

20. P. Hamm, J. Helbing, and J. Bredenbeck, "Two-dimensional infrared spectroscopy of photoswitchable peptides," Annual Review of Physical Chemistry **59**, 291-317 (2008).

21. M. J. Nee, C. R. Baiz, J. M. Anna, R. McCanne, and K. J. Kubarych, "Multilevel vibrational coherence transfer andwavepacket dynamics probed with

multidimensional IR spectroscopy," Journal of Chemical Physics **129**(8) 048503 (2008).

22. Adam W. Smith and A. Tokmakoff, "Probing Local Structural Events in beta-Hairpin Unfolding with Transient Nonlinear Infrared Spectroscopy," Angewandte Chemie International Edition **46**(42), 7984-7987 (2007).

23. H. S. Chung, M. Khalil, and A. Tokmakoff, "Nonlinear infrared spectroscopy of protein conformational change during thermal unfolding," Journal of Physical Chemistry B **108**(39), 15332-15342 (2004).

24. D. J. Cook and R. M. Hochstrasser, "Intense terahertz pulses by four-wave rectification in air," Optics Letters **25**(16), 1210-1212 (2000).

25. T. Fuji and T. Suzuki, "Generation of sub-two-cycle mid-infrared pulses by four-wave mixing through filamentation in air," Optics Letters **32**(22), 3330-3332 (2007).

26. M. D. Thomson, V. Blank, and H. G. Roskos, "Terahertz white-light pulses from an air plasma photo-induced by incommensurate two-color optical fields," Optics Express **18**(22), 23173-23182 (2010).

27. J. L. Liu, J. M. Dai, S. L. Chin, and X. C. Zhang, "Broadband terahertz wave remote sensing using coherent manipulation of fluorescence from asymmetrically ionized gases," Nature Photonics **4**(9), 627-631 (2010).

28. A. A. Silaev, M. Y. Ryabikin, and N. V. Vvedenskii, "Strong-field phenomena caused by ultrashort laser pulses: Effective one- and two-dimensional quantum-mechanical descriptions," Physical Review A **82**(3), - (2010).

29. P. B. Petersen and A. Tokmakoff, "Source for ultrafast continuum infrared and terahertz radiation," Optics Letters **35**(12), 1962-1964 (2010).

30. M. J. Tauber, R. A. Mathies, X. Y. Chen, and S. E. Bradforth, "Flowing liquid sample jet for resonance Raman and ultrafast optical spectroscopy," Review of Scientific Instruments **74**(11), 4958-4960 (2003).

31. D. A. Steinhurst, A. P. Baronavski, and J. C. Owrutsky, "Transient infrared spectroscopy of Mn-2(CO)(10) with 400 nm excitation," Chemical Physics Letters **361**(5-6), 513-519 (2002).

32. K. D. Rector, D. Zimdars, and M. D. Fayer, "Vibrational echo spectroscopy: Spectral selectivity from vibrational coherence," Journal of Chemical Physics **109**(13), 5455-5465 (1998).

33. W. Xiong, J. E. Laaser, P. Paoprasert, R. A. Franking, R. J. Hamers, P. Gopalan, and M. T. Zanni, "Transient 2D IR Spectroscopy of Charge Injection in Dye-Sensitized Nanocrystalline Thin Films," Journal of the American Chemical Society **131**(50), 18040-18041 (2009).

34. V. Cervetto, J. Helbing, J. Bredenbeck, and P. Hamm, "Double-resonance versus pulsed Fourier transform two-dimensional infrared spectroscopy: An experimental and theoretical comparison," Journal of Chemical Physics **121**(12), 5935-5942 (2004).

35. K. C. Jones, Z. Ganim, and A. Tokmakoff, "Heterodyne-Detected Dispersed Vibrational Echo Spectroscopy," Journal of Physical Chemistry A **113**(51), 14060-14066 (2009).

36. C. R. Baiz, R. McCanne, and K. J. Kubarych, "Structurally Selective Geminate Rebinding Dynamics of Solvent-Caged Radicals Studied with Nonequilibrium Infrared Echo Spectroscopy," Journal of the American Chemical Society **131**(38), 13590-13591 (2009).

37. J. C. Linehan, C. R. Yonker, R. S. Addleman, S. T. Autrey, J. T. Bays, T. E. Bitterwolf, and J. L. Daschbach, "Solvent study of the kinetics of molybdenum radical self-termination," Organometallics **20**(3), 401-407 (2001).

38. T. E. Bitterwolf, "Mechanisms and intermediates in the photochemistry of M-2(CO)(6)(eta(5)-C5H5)(2), where M = Cr, Mo and W, and their ring-coupled analogs," Coordination Chemistry Reviews **211**, 235-254 (2001).

39. A. B. Oelkers, L. F. Scatena, and D. R. Tyler, "Femtosecond pump-probe transient absorption study of the photolysis of [Cp ' Mo(CO)(3)](2) (Cp ' = eta(5)-C5H4CH3): Role of translational and rotational diffusion in the radical cage effect," Journal of Physical Chemistry A **111**(25), 5353-5360 (2007).

40. A. B. Oelkers, E. J. Schutte, and D. R. Tyler, "Solvent cage effects: the influence of radical mass and volume on the recombination dynamics of radical cage pairs generated by photolysis of [CpCH2CH2N(CH3)C(O)(CH2)(n)CH3Mo(CO)(3)](2) (n=3, 8, 13, 18) (Cp = eta(5)-C5H4) complexes," Photochemical & Photobiological Sciences **7**(2), 228-234 (2008).

41. Y. Tanimura and A. Ishizaki, "Modeling, Calculating, and Analyzing Multidimensional Vibrational Spectroscopies," Accounts of Chemical Research **42**(9), 1270-1279 (2009).

42. S. Mukamel, *Principles of nonlinear optical spectroscopy*, Oxford series in optical and imaging sciences 6 (Oxford University Press, New York, 1995), pp. xviii, 543 p.

43. The radiated field is proportional to the induced polarization. A full derivation if these equations is given in: S. Mukamel Principles of Nonlinear Optical Spectroscopy, Oxford University Press, (1995)

44. C. Baiz, M. Nee, R. McCanne, and K. Kubarych, "Ultrafast nonequilibrium Fourier-transform two-dimensional infrared spectroscopy," Optics Letters **33**(21), 2533-2535 (2008).

45. C. R. Baiz, R. McCanne, M. J. Nee, and K. J. Kubarych, "Orientational Dynamics of Transient Molecules Measured by Nonequilibrium Two-Dimensional Infrared Spectroscopy," The Journal of Physical Chemistry A **113**(31), 8907-8916 (2009).

46. M. J. Nee, R. McCanne, K. J. Kubarych, and M. Joffre, "Two-dimensional infrared spectroscopy detected by chirped pulse upconversion," Optics Letters **32**(6), 713-715 (2007).

47. M. Cui, B. R. Bachler, and J. P. Ogilvie, "Comparing coherent and spontaneous Raman scattering under biological imaging conditions," Optics Letters **34**(6), 773-775 (2009).

48. G. I. Petrov, R. Arora, V. V. Yakovlev, X. Wang, A. V. Sokolov, and M. O. Scully, "Comparison of coherent and spontaneous Raman microspectroscopies for noninvasive detection of single bacterial endospores," Proceedings of the National Academy of Sciences of the United States of America **104**(19), 7776-7779 (2007).

49. K.-I. Oh, J.-H. Choi, J.-H. Lee, J.-B. Han, H. Lee, and M. Cho, "Nitrile and thiocyanate IR probes: Molecular dynamics simulation studies," Journal of Chemical Physics **128**(15), 154504-154510 (2008).

50. J. Asbury, T. Steinel, C. Stromberg, S. Corcelli, C. Lawrence, J. Skinner, and M. Fayer, "Water dynamics: Vibrational echo correlation spectroscopy and comparison to molecular dynamics simulations," Journal of Physical Chemistry A **108**(7), 1107-1119 (2004).

51. S. A. Corcelli, C. P. Lawrence, and J. L. Skinner, "Combined electronic structure/molecular dynamics approach for ultrafast infrared spectroscopy of dilute HOD in liquid H2O and D2O," Journal of Chemical Physics **120**(17), 8107-8117 (2004).

52. B. A. Lindquist, K. E. Furse, and S. A. Corcelli, "Nitrile groups as vibrational probes of biomolecular structure and dynamics: an overview," Physical Chemistry Chemical Physics **11**(37), 8119-8132 (2009).

53. A. Tokmakoff, "Orientational correlation functions and polarization selectivity for nonlinear spectroscopy of isotropic media .1. Third order," Journal of Chemical Physics **105**(1), 1-12 (1996).

54. J. Bredenbeck, J. Helbing, and P. Hamm, "Transient two-dimensional infrared spectroscopy: Exploring the polarization dependence," Journal of Chemical Physics **121**(12), 5943-5957 (2004).

55. M. Cho, *Two-dimensional optical spectroscopy* (CRC Press, Boca Raton, 2009).

56. R. A. Kaindl, M. Wurm, K. Reimann, P. Hamm, A. M. Weiner, and M. Woerner, "Generation, shaping, and characterization of intense femtosecond pulses tunable from 3 to 20 mu m," Journal of the Optical Society of America B-Optical Physics **17**(12), 2086-2094 (2000).

57. J. Penano, P. Sprangle, B. Hafizi, D. Gordon, and P. Serafim, "Terahertz generation in plasmas using two-color laser pulses" Physical Review E **81**(2) 026407 (2010).

58. K. J. Kubarych, M. Joffre, A. Moore, N. Belabas, and D. M. Jonas, "Mid-infrared electric field characterization using a visible charge-coupled-device-based spectrometer," Optics Letters **30**(10), 1228-1230 (2005).

59. M. Nisoli, S. DeSilvestri, and O. Svelto, "Generation of high energy 10 fs pulses by a new pulse compression technique," Applied Physics Letters **68**(20), 2793-2795 (1996).

60. H. Enqvist, "A setup for efficient frequency tripling of high-power femtosecond laser pulses.," Lund Reports on Atomic Physics **330**(2004).

61. G. Rodriguez and G. L. Dakovski, "Scaling behavior of ultrafast two-color terahertz generation in plasma gas targets: energy and pressure dependence," Optics Express **18**(14), 15130-15143 (2010).

62. K. F. Lee, P. Nuernberger, A. Bonvalet, and M. Joffre, "Removing cross-phase modulation from midinfrared chirped-pulse upconversion spectra," Optics Express **17**(21), 18738-18744 (2009).

63. J. M. Anna, M. J. Nee, C. R. Baiz, R. McCanne, and K. J. Kubarych, "Measuring absorptive two-dimensional infrared spectra using chirped-pulse upconversion detection,"Journal of the Optical Society of America B **27**(3), 382-393 (2010).

Chapter 3

Ultrafast Condensed-Phase Chemical Dynamics: The solute's Response

The work presented in this chapter has been published in the following three papers:

1. C.R. Baiz, R. McCanne, M.J. Nee, and K.J. Kubarych, "*Orientational Dynamics of Transient Molecules Measured by Nonequilibrium Two-Dimensional Infrared Spectroscopy*", The Journal of Physical Chemistry A, **113** (31), 8907-8916, 2009.
2. C.R. Baiz, R. McCanne, and K.J. Kubarych, "*Structurally Selective Geminate Rebinding Dynamics of Solvent-Caged Radicals Studied with Nonequilibrium Infrared Echo Spectroscopy"* , Journal of the American Chemical Society, **131** (38), 13590-13591, 2009
3. C.R. Baiz, R. McCanne, and K.J. Kubarych, *"Structurally-Sensitive Rebinding Dynamics of Solvent-Caged Radical Pairs: Exploring the Viscosity Dependence"* , Proceedings of International Conference on Ultrafast Phenomena XV, In Press (2011)

3.1 Introduction

Two-dimensional infrared (2DIR) spectroscopy enables the observation of molecular dynamics such as vibrational energy transfer, spectral diffusion, or ultrafast chemical exchange by using the system's vibrational modes as local probes of molecular

microensembles.[1, 2] 2DIR also provides time-resolved structural information by measuring the normal mode anharmonicities and couplings which are directly linked to the underlying vibrational Hamiltonian. Recently, non-equilibrium variants of 2DIR, where the system is optically perturbed before or during the measurement, have been used to investigate phototriggered reactions including metal-to-ligand charge transfer,[3] disulfide bond breaking,[4] and metal-metal bond photodissociation reactions.[5, 6]

These two-dimensional experiments build upon more traditional techniques such as one-dimensional pump-probe measurements which continue to successfully reveal new information on the dynamics of chemical systems under non-equilibrium conditions. For example, the mechanisms for reorientational dynamics and resonant energy transfer in liquid water have been revealed by polarization-resolved infrared pump-probe spectroscopy.[7, 8] Similar experiments have investigated the orientational dynamics of carbon monoxide following photodissociation from a heme host in hemoglobin[9] and myoglobin.[10] It was found that upon dissociation, the ligand finds specific docking sites within the heme pocket where it remains for several nanoseconds, suggesting the existence of an energy barrier for the recombination process. Recently, these results were further expanded upon by mapping the photoinduced ligand migration to the docking sites and the subsequent interconversion between the distinct conformations in myoglobin by triggered-exchange 2DIR spectroscopy.[11] Here we measure the orientational dynamics of a transient radical species via transient 2DIR spectroscopy. It is important to emphasize the key difference between the molecular information provided by transient-2DIR in comparison to established one-dimensional anisotropy measurements: A typical UV-pump/IR-probe anisotropy experiment, such as the one described above, reports on the orientational correlation of the transition dipole moment of a photoproduct IR transition with respect to the excited electronic transition dipole moment of the initial state. The orientational information contained in transient-2DIR reports on the self-correlation of the photoproduct species at different delays following photodissociation. For sufficiently long delays between the photolysis pulse and the 2DIR probe there is no correlation at all between the photodissociation and the photoproduct transition dipole moments. Thus, this new technique probes the changing dynamics of transient species itself en route to thermodynamic equilibrium.

Non-equilibrium classical dynamics simulations have been successful in modeling solute to solvent vibrational energy relaxation in multiple systems, and the theory of classical and semiclassical energy relaxation is well-established within this context.[12-16] In a recent paper, Backus and coworkers[17] used non-equilibrium molecular dynamics (MD) simulations to model vibrational energy transport among isotope-labeled carbonyl modes in a short peptide. Carbonyl vibrations were excited either directly in the IR or by UV excitation of an azobenzene chromophore attached one of the peptide's termini where the excess electronic energy subsequently relaxes into the vibrational modes. Though transient absorption results show that the rate of transport is slower when exciting the chromophore, the rate obtained from MD simulations is insensitive to the type of excitation. The MD results agreed well with the low-energy excitation experiments, but yielded rates that were too fast in the case of UV excitation.

Metal Carbonyls The photochemistry of $Mn_2(CO)_{10}$ has been the focus of numerous studies mainly aimed at understanding the excited state reaction pathways and subsequent energy relaxation processes.[18-31] Two dissociation pathways have been demonstrated: excitation at 400 nm primarily cleaves the Mn-Mn bond, producing 2 $\cdot Mn(CO)_5$ radicals, whereas excitation at 342 nm dissociates one carbonyl ligand to yield $Mn_2(CO)_9$.[25, 29] In both cases the bond energy is substantially less than the excitation energy, causing the products to remain in a vibrationally hot state after photodissociation.

Steinhurst *et al.*[29] measured the 1982 cm^{-1} absorption lineshape narrowing of $Mn(CO)_5$ photoproducts with excitation at 400 nm using time-resolved infrared spectroscopy and found the narrowing lifetime in cyclohexane to be 44.7 $\pm$17.4 ps. The results also showed that the narrowing lifetime is shorter in polar solvents due to stronger solute-solvent interactions, an effect also observed in photodissociation of other metal carbonyls.[18] Although a detailed discussion of temperature-dependent absorption linewidths was not presented, the authors concluded that this narrowing lifetime provided a lower limit for the vibrational cooling of the product molecules as they did not observe any contribution to the absorption from anharmonic transitions. Other related studies have reported similar rates for low frequency mode relaxation in similar metal carbonyls.[18, 32, 33] The UV-pump/visible-probe measurements of Zhang *et al.*[31] found the relaxation of $Mn(CO)_5$

following photolysis at 295 nm to exhibit biexponential behavior with a ~15 ps fast component and a ~180 ps slow decay. The authors attributed the fast component to intramolecular vibrational relaxation of the CO modes through low frequency modes of the molecule, and the slow component was ascribed to ultimate relaxation to the solvent. Although these previous studies have provided significant insight into the photochemistry of $Mn_2(CO)_{10}$, a full understanding requires the characterization of excited-state lifetimes and quantum yields, as well as geminate rebinding rates and mechanisms.

3.2 Orientational Dynamics of Transient Species in Solution

In this section we report our measurements of orientational relaxation rates of $Mn(CO)_5$ as a function of the time delay after photodissociation as obtained by transient-2DIR spectroscopy. The response function underlying the 2DIR spectrum includes the same orientational dynamics typically probed using absorption anisotropy, and due to the separation of timescales, we are able to extract the orientational component of the transient 2DIR spectra. We use the measured orientational lifetimes to determine the system-solvent energy dissipation rate (cooling) after photodissociation. These experiments create conditions unique to non-equilibrium phenomena where, due to weak solute-solvent coupling, the temperature of the solute increases following photodissociation while the solvation shell remains at nearly a constant temperature. Orientational relaxation rates are used as a molecular thermometer which indirectly report on the excitation of the low-frequency modes. Similar ultrafast methods, such as IR-Raman spectroscopy, have also been useful in providing mode-specific populations in various non-equilibrium systems.[34-36] To further elucidate the dynamics of $Mn(CO)_5$ transient species, classical dynamics simulations are used in modeling temperature relaxation and orientational lifetimes, and temperature dependence of transient-absorption lineshape modeled using an anharmonic description based on vibrational perturbation theory.

Orientational Diffusion

The rate of orientational relaxation is commonly written in the context of Debye-Stokes-Einstein theory. Within this framework, the orientational correlation time is

expressed in terms of the solvent viscosity η, the specific volume of the molecules v_s, and the temperature *(T)* as

$$\tau_R = \frac{C\eta v_s}{k_B T} \tag{1}$$

where k_B is Boltzmann's constant and *C* is an empirical constant. If the transition dipoles are assumed to be invariant with respect to the bath degrees of freedom, as in the Condon limit, the molecular reorientational time can be approximated as the dipole-dipole correlation time of a single vibrational transition, as the angle between the transition dipoles and the molecular axis are invariant with time. It is important to note the inverse temperature dependence of the correlation function; below we provide a discussion of measured temperature-dependent orientational dynamics and, using this relationship, we extract the cooling rate of the transient $Mn(CO)_5$ species following photoexcitation.

It is well known that the infrared pump-probe anisotropy *r(t)* for an individual vibrational transition can be written as a function of the dipole-dipole time correlation function.[37, 38]

$$r(t) = \frac{I_{\parallel}(t) - I_{\perp}(t)}{I_{\parallel}(t) + 2I_{\perp}(t)} \tag{2}$$

In the above equation $I_{\parallel}(t)$ and $I_{\perp}(t)$ represent the pump-probe intensity measured with parallel and perpendicular relative polarizations. These two contributions can also be written as

$$\begin{aligned} I_{\parallel}(t) &= \left[\tfrac{1}{3} + \tfrac{4}{15} C_2(t)\right] P(t) \\ I_{\perp}(t) &= \left[\tfrac{1}{3} - \tfrac{2}{15} C_2(t)\right] P(t) \end{aligned} \tag{3}$$

where *P(t)* is the population of the excited state and $C_2(t)$ is the second Legendre polynomial of the dipole-dipole time correlation function averaged over all the initial configurations. The orientational contribution to the anisotropy decay, obtained by combining Equations 2 and 3, is written in terms of the dipole-dipole correlation function as:

$$r(t) = \tfrac{2}{5} C_2(t)$$
$$C_2(t) = \left\langle P_2\left[\vec{\mu}(0)\cdot\vec{\mu}(t)\right]\right\rangle \quad (4)$$

The orientational contribution to the 2DIR signal in the zzzz-polarization geometry is similarly expressed as a function dipole-dipole correlation function:[39]

$$Y_{zzzz}(t_1,t_2,t_3) = \tfrac{1}{9}\left(\left[C_1(t_1)C_1(t_3)\right]\left[1+\tfrac{4}{5}C_2(t_2)\right]\right) \quad (5)$$

From the above relation, we observe that the orientational contribution to the waiting time dependence of the 2D signal is the same as for the one-dimensional anisotropy. The orientational equations for transient-2DIR spectroscopy, a fifth-order experiment, are significantly more complex as the UV pulse pre-selects a sub ensemble of the molecules.[40, 41] However, in our experiments, the time between the UV and IR pulses is at least 40 ps, and since the orientational lifetime of the photoproducts is ~10 ps (see below), the 2DIR experiment is essentially done on an isotropic ensemble. This clear separation of time scales allows us to apply the simpler third-order version of the orientational equations outlined above.

Ultrafast Spectroscopy

The non-equilibrium time-domain 2DIR spectrometer has been described in detail elsewhere.[42] Briefly, mid-infrared pulses (2 μJ, 100 fs), centered at 2000 cm^{-1} with ~100 cm^{-1} FWHM bandwidth are generated using a dual-optical parametric amplifier/difference frequency generation setup pumped by a regeneratively-amplified Ti:Sapphire laser. The mid-IR pulses are split into, k_1, k_2, k_3, tracer, and reference beams. The UV pulses (>30 μJ, ~100 fs) are obtained by frequency-doubling ~200 μJ of the laser output in a 0.4-mm BBO crystal and stretched to ~400 fs using a 10-cm fused silica block to minimize multiphoton interactions with the sample. An interferometrically-stable wire-guided jet[43] is used to refresh the sample volume between laser shots. The UV beam is mechanically chopped with a 50% duty cycle synchronized to the 1-kHz amplifier repetition frequency. To collect a transient 2DIR spectrum, the delay of the first IR pulse (k_1) is scanned continuously and the heterodyned rephasing signal is upconverted into the visible using a highly chirped pulse (FWHM = 160 ps) centered at 800 nm[44] and detected at the laser repetition rate in a

spectrometer using a silicon-based CCD detector. The collected time-domain data are deinterlaced into separate interferograms corresponding to pumped (UV on) and unpumped (UV off), and are processed separately. The final difference 2D spectrum is computed in the frequency domain by subtracting the unpumped from the pumped absolute value rephasing spectra. To measure the photoproduct relaxation rates we collected transient-2DIR spectra at different t_2 delay times, between 0 and 20 ps using fifty steps spaced such that the relaxation is more densely sampled at the beginning of the exponential decay. These experiments were repeated at six different UV-IR time delays ranging from 40 to 300 ps; 120 transient-2DIR spectra were collected in total. Errors arising from laser drift and long-time instabilities of the liquid jet were minimized by randomizing the order in which the spectra were acquired.

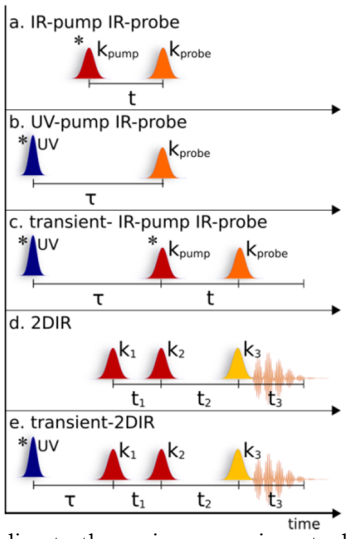

Figure 3.1: Pulse sequences corresponding to the various experiments described throughout this chapter. The blue pulse represents the UV phototrigger pulse, the red pulses represent IR pump pulses, k1 and k2, in 2DIR experiments, orange corresponds to the tracer pulse, used in one-dimensional pump-probe experiments, and the yellow pulses correspond to k3 used in the two-dimensional experiments. The pulses marked with a star are mechanically chopped during the experiment.

UV-pump/IR-probe spectra were collected by measuring the differential transmission of the tracer pulse while chopping the UV and IR pump pulses respectively and blocking all the other beams. Equilibrium IR-pump/IR-probe measurements used to obtain anisotropy decays of the parent molecules were collected by recording the differential probe transmission at two polarization configurations while chopping k_1 and blocking all the other beams. Similarly, transient-pump-probe spectra were obtained by combining the UV and IR pump beams, chopping the UV at 500 Hz and the IR at 250 Hz and recording the tracer

transmission at the laser repetition frequency of 1 kHz. Experimental pulse sequences are shown in Figure 3.1. $Mn_2(CO)_{10}$ solutions (6 mM) were prepared using spectrophotometric grade cyclohexane. This concentration produces an optical density of ~0.30 at the $Mn_2(CO)_{10}$ main absorption peak (2013 cm^{-1}) with a ~200 μm path length in the liquid jet. All chemicals were purchased from Sigma-Aldrich and were used without further purification.

Non-equilibrium Molecular Dynamic Simulations

The cyclohexane solvent was modeled using the all-atom general AMBER force field[45, 46] and atomic charges were assigned *ab-initio* using the restrained electrostatic potential (RESP) scheme[47, 48] computed with Gaussian 03.[49] The metal carbonyl force fields were parameterized using harmonic potentials and Mulliken atomic charges derived from density functional theory (DFT) with B3LYP/6-31+G(d). One molecule of $Mn_2(CO)_{10}$ was placed in a cubic box containing 507 solvent molecules. The system was energy-minimized and equilibrated for 1 ns with 1 fs integration steps at 298 K and 1 bar using a Berendsen thermostat.[50] The simulations were performed using the leapfrog algorithm as implemented in GROMACS, long-range electrostatic interactions were treated using the particle-mesh Ewald method, the non-bonded neighbor lists were updated every 10 integration steps and the interaction cutoff was set to 1.0 nm. After equilibration, a 2 ns $Mn_2(CO)_{10}$ production trajectory was generated under the same simulation conditions. The same procedure was used to generate a 2-ns equilibrium trajectory for $Mn(CO)_5$. From the 2-ns trajectory for $Mn(CO)_5$, 50 independent conformations were obtained as starting points for the non-equilibrium simulations. The quantum description of vibrational energy redistribution is quite complex. For example, the energy distribution ratios among the modes could be obtained by propagating the full quantum anharmonic Hamiltonian. However, since the simulations are classical in nature, and thus would not be able to accurately capture the effects of vibrational energy transfer,[17] it would be wasteful to compute the full quantum mechanical energy distribution ratios as an input to the classical simulations. As an approximation, the photolysis reaction and subsequent energy redistribution were simulated by scaling the velocities of all the atoms in $Mn(CO)_5$ to account for the excess energy that remains after dissociation. At each starting conformation, the equilibrium kinetic energy was

computed, and all the atoms velocities in $Mn(CO)_5$ were scaled by a factor that yielded a final kinetic energy equal to the equilibrium energy plus excess excitation energy: The Mn-Mn bond energy is estimated to be 12600 cm^{-1},[20] which leaves 12400 cm^{-1} of excess energy after photodissociation with 400 nm excitation. Using the DFT-derived heat capacity, the temperature of $Mn(CO)_5$ immediately following photodissociation is predicted to be 664 K. The non-equilibrium NVE trajectories were run for 100 ps using integration steps of 0.2 fs and atom positions and velocities were collected every 10 fs for analysis. From these trajectories, the temperature of the molecule and the solvation shell (nearby cyclohexane molecules) were computed. Dipole-dipole time correlation functions for the parent molecules and photoproducts were also computed from the 2-ns equilibrium simulations. All simulations were performed using the GROMACS 3.3 package of programs.[51]

Theoretical Lineshapes

To simulate the temperature-dependent absorption linewidth of $Mn(CO)_5$ we employ an anharmonic description based on a previous model by Hamm et al.[52] which accounts for the thermal excitation of low-frequency (bath) modes and their effect on the frequency of the CO stretch mode of interest. We begin by computing a set of third- and semidiagonal fourth-order anharmonic force constants for all the modes using standard electronic structure methods, (B3LYP, LANL2DZ on Mn, 6-31G(d) on C and O). These anharmonic force constants are obtained by displacing the molecular geometry along the normal modes and computing the change in harmonic frequencies between the equilibrium and displaced geometries.[53, 54] The anharmonic coupling constants, X_{ii} and X_{ik}, which represent the shift in frequency of mode k given that mode i is excited, are computed using second-order vibrational perturbation theory (VPT2). The computation of anharmonic coupling constants from electronic structure methods via VPT2 is well-established and the procedure is described in detail elsewhere.[55, 56] It is important to note that the described DFT/VPT2 procedure successfully reproduces the experimentally-measured carbonyl anharmonicities in $Mn_2(CO)_{10}$ therefore justifying its use in this work.[57] A temperature-dependent absorption lineshape $A_k(\omega)$ of the carbonyl stretching mode of interest k is written as:

$$A_k(\omega) = v_k + \sum_{i \neq k} \sum_{n_i} Q^{-1} \exp\left(-n_i v_i / kT\right) \exp\left(-[\omega - v_k - n_i X_{ik}]^2 / \sigma^2\right) \quad (6)$$

The first exponential inside the sum represents the thermal probability that a bath mode *i* will be in the n^{th} excited state at temperature *T* with a normalization factor $Q(T)$, the second term is a Gaussian function centered at a frequency shifted from the fundamental by $n_i X_{ik}$. In the above equation ν_i represents the fundamental transition of mode *i* in the anharmonic description, computed by:

$$v_k = \omega_k + 2X_{kk} + \tfrac{1}{2} \sum_i X_{ik} \quad (7)$$

where ω_k is the harmonic frequency of mode *k*, and X_{kk} and X_{ik} are the anharmonic coupling constants described above. A full set of coupling constants along with the harmonic and anharmonic frequencies for $Mn(CO)_5$ is given below. It is important to note that in our model the high frequency mode *k* remains in the ground state, an approximation that only applies to systems where the mode of interest has negligible thermal population. In the above expression for $A_k(\omega)$ the first summation is over all the bath modes, in our case we define the bath modes as all the normal modes with frequencies lower than the lowest frequency terminal CO stretch. We explicitly exclude the solvent degrees of freedom due to the very weak coupling, manifested in the long vibrational lifetime. The second summation in Eq. 6 is over all excitations of these modes, from a practical perspective we found that including 10 excitations is sufficient to converge the results at a temperature of 600 K or below.

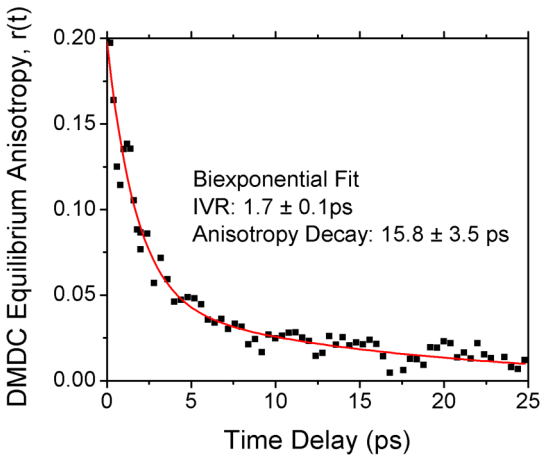

Figure 3.2: $Mn_2(CO)_{10}$ equilibrium anisotropy obtained by measuring IR-pump/IR-probe differential absorption of the 2013 cm^{-1} transition in the parallel and perpendicular polarization geometries. The initial fast decay is due to IVR and the slower decay represents the orientational relaxation of the equilibrium species. The initial value of 0.2 is attributed to the fact that the probed frequency corresponds to two degenerate CO stretching modes with perpendicular transition dipole moments.

Experimental and Simulation Results

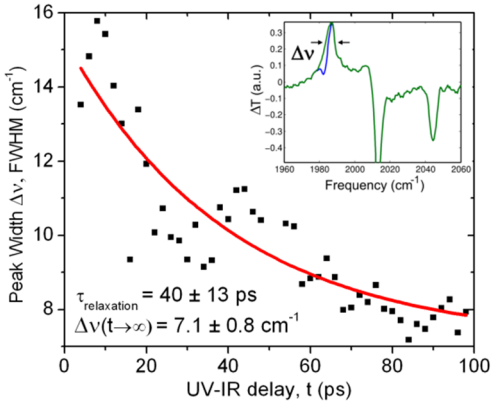

Figure 3.3: Transient peak widths obtained from one-dimensional UV-pump/IR-probe transient absorption experiments with a single-exponential fit. The inset shows transient absorption spectrum at long UV-IR delay (100 ps) after bleach substraction. The green and blue curves represent the transient absorption before and after bleach subtraction near 1982 cm^{-1} respectively (see text for details).

Equilibrium Anisotropy Equilibrium IR-pump/IR-probe anisotropy measurements, shown in Figure 3.2, report directly on the orientational relaxation lifetime of the parent molecule, $Mn_2(CO)_{10}$. The transient absorption anisotropy shown for the central 2013 cm^{-1} band exhibits biexponential behavior with a fast component of ~600 fs caused by rapid

randomization of energy among the carbonyl modes (IVR), and a slower component due to the orientational relaxation. This measured relaxation lifetime of 15.8 ± 3.5 ps can be directly compared to the calculated MD lifetimes as shown below.

UV-Pump/IR-Probe

The broad bandwidth of the induced photoproduct absorption observed in the one-dimensional UV-IR transient spectra has previously been attributed to the population of low-frequency modes (heating) in the photoproduct by the excess energy remaining after photodissociation. To obtain a system-to-solvent energy transfer lifetime (cooling), we measure the absorption linewidth in UV/IR transient absorption spectra collected from 10 to 100 ps delay at 2 ps steps as shown in **Error! Reference source not found.**. The overlapping bleach is removed by fitting the 1982 cm^{-1} feature in a single long-delay pump-probe spectrum to two Gaussian functions, one positive and one negative, and then subtracting the negative Gaussian from all the other pump-probe spectra. After removing the bleach in each spectrum, the photoproduct transient peak centered near 1982 cm^{-1} is fit to a single Gaussian function. The full-width-at-half-maximum of the Gaussian fits are plotted (**Error! Reference source not found.**) as a function of the UV-IR time delay and the data is fit to a single exponential. This procedure yields a relaxation lifetime of $Mn(CO)_5$ in cyclohexane of 40±13 ps which is in excellent agreement with the previously published lifetime of 44±17 ps.[29] The data also shows that the linewidth remains broad at long UV-IR time delays (see discussion below). Additionally, the $Mn_2(CO)_{10}$ bleaches do not recover within the timescale of the experiment (200 ps). Previous experiments[29] also reported an instrument response limited onset of the bleach and the absence of bleach recovery even at 500 ps after photoexcitation; Dougherty *et al*[18] reported a bleach recovery in the 5-400 μs regime in $Rh(CO)_2(acac)$ suggesting that non-geminate recombination is a diffusion limited process.

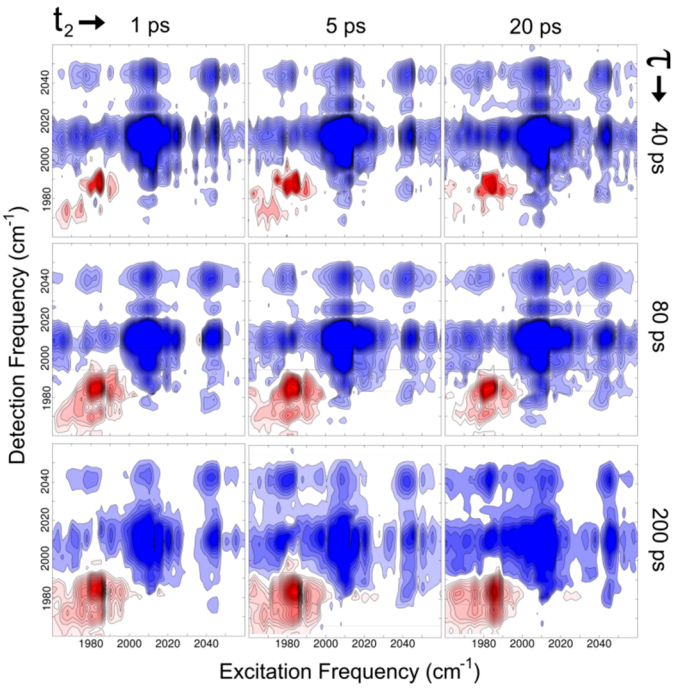

Figure 3.4: Transient-2DIR spectra of $Mn_2(CO)_{10}$ obtained at different waiting times (t_2) and multiple UV-2DIR delays (τ) (See Figure 3.1). The negative features, shown in blue, represent the bleaches corresponding to depletion of parent $Mn_2(CO)_{10}$ molecules and the red feature, (lower left) represents the absorption due to the transient $Mn(CO)_5$ radical species. The transient signal is initially weak and becomes stronger as the photoproduct molecules reach the final equilibrium temperature. Contour spacing is normalized to the maximum signal difference and contours that are smaller than 2% or larger than 40 % of the total bleach amplitude are removed for clarity.

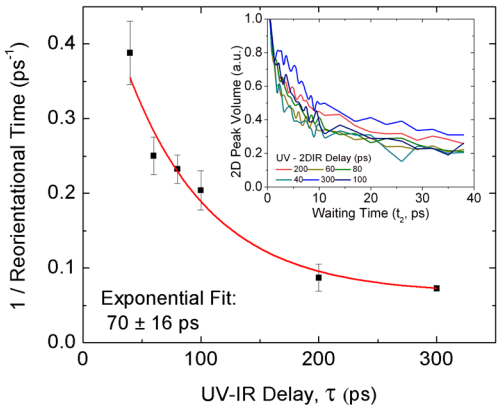

Figure 3.5: $Mn(CO)_5$ reorientational time constants as a function of the UV-2DIR time delay, τ, obtained from the integrated transient peak volumes as a function of the 2DIR waiting time, t_2. The solid curve is a single-exponential curve fit to the data showing a decay time of 70±16 ps. This exponential represents the cooling of the molecules after photoexcitation. Additional information about the fitting process and a representative fit is provided in the supplementary information.

Transient-2DIR The equilibrium absolute-value rephasing 2DIR spectrum of $Mn_2(CO)_{10}$, described in detail elsewhere,[44] exhibits nine main peaks, diagonal peaks at 1983, 2013, and 2045 cm^{-1}, and six cross-peaks which correspond to Liouville paths involving light interactions with different vibrational modes during the infrared excitation and detection times. As the waiting time t_2 is increased these off-diagonal peaks oscillate at the difference frequency between the corresponding diagonal modes. The transient-2DIR spectra (Figure 3.4) show bleaches as a result of depletion of parent molecules and a transient peak centered near [ω_1=1982, ω_3=1982 cm^{-1}] due to the nascent photoproduct molecules. The 2D lineshape of this peak is somewhat distorted due to spectral overlap with the low-frequency diagonal bleach. In order to minimize these distortions, the IR pulses were tuned to the high-frequency region of the spectrum so as to decrease contributions from low-frequency bleaches. Similar to the previously reported 1D transient absorption spectra,[29] this transient 2D peak is initially broad and becomes narrower with increasing UV-IR time delay due in part to vibrational cooling. Three different processes contribute to the signal decay along t_2, intramolecular vibrational redistribution, orientational relaxation and vibrational relaxation. The different timescales for these three processes allows for clean isolation of the orientational contribution as discussed below. Relaxation rate constants are obtained by integrating the volume of the entire transient 2D peak (red features in Figure 3.4) for each value of t_2 and fitting the t_2 decay to a single exponential. In order to reduce the errors arising from the exponential fitting of the relaxation data, the integrated peak volume is low-pass Fourier filtered and is fit starting at t_2 = 2 ps to remove the contribution from the rapid initial decay (τ~600 fs) which arises from intramolecular vibrational redistribution. The filtering also removes any errors due to coherent oscillations of the overlapping parent peaks observed at small waiting times.[58] Although the decay constants obtained from the curve fitting may still contain errors that arise from vibrational energy relaxation or the fitting procedure itself, we expect these errors to be similar for all the curves as the same procedure is applied to all the decay curves. The relative change in the relaxation rates as a function of the UV-IR delay should therefore be reliable. The Debye-Stokes-Einstein relationship makes it possible to obtain an effective temperature decay from the set of orientational relaxation curves. The orientational rate constant (inverse decay time) is directly proportional to the temperature of the system allowing the direct mapping of the UV-IR time delay axis to a molecular temperature axis. It is important to note that as verified by the simulation study

discussed below, in this experiment the temperature and viscosity of the solvent remain at their equilibrium values; the only variable is the temperature of the solute molecules. The relaxation rate constants plotted as a function of the UV-IR delay along with the temperature decay are shown **Error! Reference source not found.**.

Transient UV-Pump/IR-Pump-IR-Probe

The transient UV-pump/IR-pump-IR-probe spectra, shown in Figure 3.6, can be best understood as two IR-pump/IR-probe spectra with and without the presence of nonequilibrium photoproducts in solution. The negative-going bleaches observed correspond to the depletion of ground vibrational state molecules caused by the IR pump with the corresponding anharmonically-shifted increase due to excited state absorption (ESA). The UV pump causes a depletion of parent molecules and generates photoproduct molecules, which, aside from the induced photoproduct, yield a similar ground-state bleach (GSB) and ESA signal. In the IR/IR experiments, two processes contribute to the GSB signal, the depletion of ground state molecules and the stimulated emission from the populated excited states. The broad 1982 cm^{-1} peak in the UV-pumped spectrum is caused by the overlapping contributions of both the parent and daughter species. To remove these contributions, the difference between the two pump-probe spectra is computed. The data shows that the ESA of the photoproducts directly overlaps the GSB from the parent molecules. In principle, the same orientational relaxation information contained in the transient-2DIR experiments is present in the transient-pump-probe data (see equation 3), however, spectral overlap between the low-frequency bleach and transient peak along with a low signal-to-noise ratio prevented the extraction of reliable orientational relaxation lifetimes from these data. Pump-probe and 2DIR signals arise from the same light-matter interactions and thus contain similar information. One advantage of 2DIR over one-dimensional pump-probe relies in the fact that the 2DIR signal is emitted in a background-free direction, whereas in pump-probe the signal is emitted in the same direction as the probe beam. In which case, to avoid saturating the detector, the probe beam must be weak. Because intensity of the signal is proportional to the intensity of the pump and probe pulses, in the pump-probe experiments the signal is usually weaker and additional signal averaging is required to obtain reliable data. In addition, comparing the transient-pump-probe and transient-2DIR

spectra it is possible to observe that the photoproduct peak height is larger with respect to the bleaches, and better isolated in the 2DIR data, making the extraction of orientational relaxation rates possible.

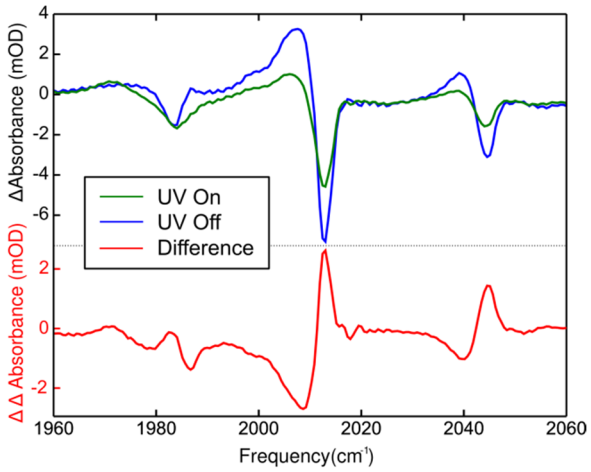

Figure 3.6: IR-pump/IR-probe spectra obtained with (green) and without (blue) the UV pump. The pumped (UV on) spectrum shows smaller changes at 2045 and 2013 cm^{-1} due to the depletion of parent molecules and shows a comparable bleach intensity at 1982 cm^{-1} because of the absorption of the new transient species generated by the UV phototrigger. The difference (UV on – UV off, red) spectrum clearly shows the increase in signal near 1982 cm^{-1} due to the photoproducts.

MD Simulations

A plot of temperature versus time, as shown in Figure 3.7, is obtained from the MD simulations, indicating that adding 12400 cm^{-1} of excess kinetic energy causes an initial temperature of ~760K, in reasonable agreement with the result predicted via the DFT-derived heat capacity. It is well known that the classical heat capacity of a molecule is larger than the quantum heat capacity, thus one would expect the MD simulations to show a smaller increase in temperature than the increase calculated using the DFT heat capacity. The similarity arises because dihedral angles are not specifically parameterized in the classical force field and thus these low-frequency vibrations, which may have a large contribution to the heat capacity, are not present in the classical simulations. A biexponential curve is needed to accurately fit the temperature data, giving a fast component of ~480 fs and a slower component of 8.01 ps. The slower component is attributed to energy relaxation to the solvent (cooling). To further elucidate the energy relaxation process, we computed the temperature of the solvation shell, and found it to remain constant near the equilibrium value of 298K, indicating that the heat diffusion within the solvent is an efficient process. In

addition, we simulated the photodissociation reaction by simply removing the Mn-Mn bond from the force field and scaling the velocities of the atoms but observed that the two $Mn(CO)_5$ molecules formed stable dimers in every computed nonequilibrium trajectory. The temperature decay time of the dimers (8.94 ps) is similar to that of the monomers, suggesting that the molecule-solvent interactions remain mostly unaffected.

Simulated Equilibrium Orientational Relaxation

Orientational relaxation curves were obtained from the equilibrium and non-equilibrium trajectories by fixing the molecular axis along one of the equatorial carbonyl bonds and computing a time autocorrelation of the vector dot product trajectory. The second Legendre polynomial of this autocorrelation function is directly proportional to the orientational contribution to the anisotropy, as well as the 2DIR waiting-time decays as noted in Equations 4 and 5. Orientational relaxation curves for the parent molecule obtained from the MD simulations (Figure 3.8) show single exponential behavior with a lifetime of 18.2 ps. The photoproduct exhibits a biexponential relaxation that is likely due to the two $Mn(CO)_5$ dimer structures. However, the two exponentials have nearly equal amplitude, and the decay curve is adequately fit with a single exponential, allowing direct comparison with the 2DIR experimental decay curves. The temperature-dependence of the orientational relaxation constants was not computed from the simulations because to achieve this, either the entire simulation box would need to be heated to a higher temperature or the solute and solvent would have to be simulated under different thermostats, neither of which reproduces the experimental conditions.

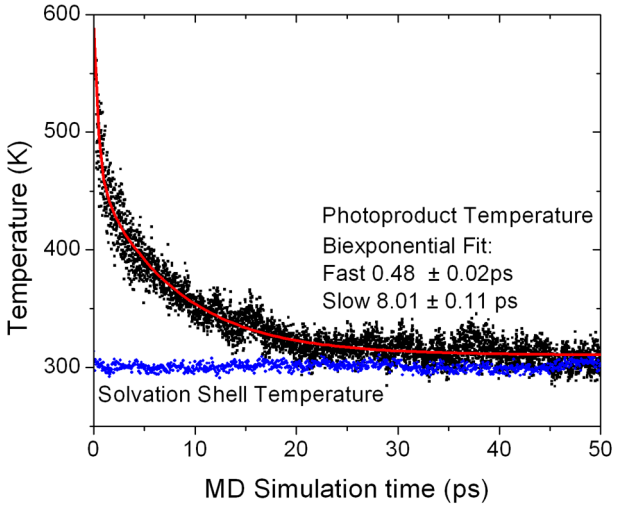

Figure 3.7: Temperature of the $Mn(CO)_5$ species following photodissociation obtained from the non-equilibrium MD simulations using an average of 50 non-equilibrium trajectories. The temperature of the solvation shell, which remains near the equilibrium value, was obtained by identifying the six nearest cyclohexane molecules at each MD step and computing their average temperature.

Table 3.1: Summary of the orientational relaxation constants obtained from experiment and from the molecular dynamics (MD) simulations

Method	Orientational	Cooling Rate (ps)	Species
Equilibrium Anisotropy	15.8 ± 3.5		$Mn_2(CO)_{10}$
UV-pump/IR-probe		44 ± 17 (lower limit)	$Mn(CO)_5$
Transient-2DIR	13.7 ± 0.7 (τ = 300ps)	70 ± 16	$Mn(CO)_5$
Equilibrium MD	18.2		$Mn_2(CO)_{10}$
Equilibrium MD	11.7		$Mn(CO)_5$
Non-Equilibrium MD		8.0	$Mn(CO)_5$

Discussion

Orientational Relaxation

Table 3.1 summarizes the orientational relaxation and cooling rates obtained from experiment and MD simulations. The 2DIR signal decay along the waiting time is characterized by three main contributions with substantially distinct timescales: intramolecular vibrational relaxation (~1 ps), orientational diffusion[59] (~5-10 ps), and vibrational energy relaxation to the solvent (~100 ps). The separation of these timescales

enables isolation of the orientational contribution to the transient 2DIR signal by fitting the overall signal decays as described above. The decay times range from 2.5 to 10 ps, consistent with the transient IR-pump/IR-probe anisotropy measurements of the parent molecules, where we observe a similar reorientation timescale showing that these decays are indeed due to orientational dynamics.

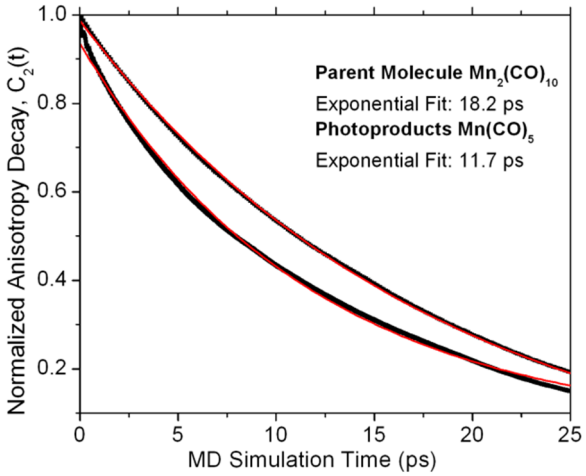

Figure 3.8: Orientational relaxation contribution to the anisotropy and 2DIR signal decays computed from the MD simulation via the dipole-dipole time correlation (black) function along with their exponential fit (red). The curve corresponding to the photoproduct was obtained from MD data collected from the 2-ns equilibrium (NPT) trajectory.

The key experimental observation of this work is that the orientational relaxation times are dependent on the UV-2DIR waiting time. It is a unique feature of the additional temporal and spectral correlation made possible by nonlinear 2D spectroscopy that reorientation of a transient species can be directly observed in the time domain. Previous experiments have suggested that initial molecular reorganization of metal carbonyl photoproducts likely occurs on an ultrafast timescale.[30] Therefore by the time of our first 2DIR measurement (40 ps) the molecules should be largely at equilibrium in this regard. It is also known, from the long CO vibrational lifetimes (~100 ps) and narrow infrared transitions observed in metal carbonyls in non-polar solvents (3-5 cm^{-1} in $Mn_2(CO)_{10}$), that the system-solvent interactions are weak and thus the molecules are largely isolated from the solvent. Therefore, it is expected that the process of heat transfer between the molecule and

the solvent should be slow with a timescale comparable to that of vibrational energy relaxation.

The observed evolution in the orientational relaxation as the UV-2DIR delay is then due to temperature effects. Orientational diffusion occurs faster when the molecules are in a hot state and slower as the molecules reach the final equilibrium temperature. Due to weak system-solvent interactions, the solvent remains at a constant temperature, as indicated by the molecular dynamics simulations, and therefore the viscosity of the liquid is properly regarded as remaining constant. This scenario is in contrast to other ultrafast temperature dependent relaxation experiments where the solvent and the molecules are in thermal equilibrium, thus solvent viscosity changes and changes in the material density can significantly influence the measurements and should be explicitly included in the data analysis.[60, 61]

To further elucidate the effects of orientational relaxation on the 2DIR waiting-time signal decay, we analyze the results obtained from molecular dynamics simulations. The simulated photoproduct orientational decay of 13.4 ps is in excellent agreement with the experimental values at long time-delays of 11.7 ps. In the equilibrium case, the simulations predict a slightly longer decay lifetime of 18.2 ps in which is also in agreement with the experimental value of 15.8 ps measured in the anisotropy experiment (Figure 3.2). However, such good agreement is likely a coincidence as we do not expect the MD simulations to quantitatively reproduce the experimental values. The similarity in relaxation rates for the $Mn_2(CO)_{10}$ and $Mn(CO)_5$ molecules arise from the similar forces experienced by both species in the simulations. It is also observed that the $Mn(CO)_5$ orientational decay is biexponential in nature (Figure 3.8), an effect attributed to fact that $Mn(CO)_5$ is a symmetric top. The decay is, nonetheless, adequately fit with a single exponential function, and it is unlikely that this behavior would be observed experimentally as an extremely high signal-to-noise ratio would be required.

Based on the observed changes in orientational lifetime as a function of UV-2DIR time delay, we are now in a position to apply Debye-Stokes-Einstein (DSE) theory and directly correlate the differences in orientational relaxation rates to the temperature of the molecule. The main underlying assumption that allows us to obtain a cooling rate from DSE

theory is that the molecular degrees of freedom of the solute are completely equilibrated; the energy is partitioned among all the degrees of freedom and a single temperature can be used to describe the system. This is a reasonable assumption since it is likely that collisions with the solvent would rapidly partition the energy among all degrees of freedom in the system, particularly given that the 2DIR measurements are preformed starting at 40 ps after the photoreaction. The understanding of these temperature-dependent orientational relaxation rates is rather intuitive; part of the excess excitation energy is channeled into the low-frequency vibrational and rotational modes of the molecule, causing an increase in the collision rate with the solvent and thus increasing the rate of orientational diffusion. Next we discuss the cooling rates based on the evidence from one-dimensional pump-probe, transient-2DIR and the MD simulations.

Temperature Decay

The time-dependence of the one-dimensional UV-IR transient absorption line narrowing (**Error! Reference source not found.**) provides a lower limit of 44±17 ps for vibrational cooling. Our data is also in agreement with the results of Steinhurst et al.,[29] in that no anharmonic CO transitions are present after photodissociation, indicating that the excess energy is largely deposited into the low-frequency modes of the molecule. Although a general quantum mechanical treatment that rigorously describes the temperature dependence of absorption lineshapes remains a challenge, the basic assumption is that the absorption width, caused by population of the low-frequency modes, is proportional to the non-equilibrium temperature of the molecules as it is described by our anharmonic model above. The measured orientational rates from transient-2DIR, which by Debye-Stokes-Einstein theory are proportional to temperature, should be a more accurate reporter of the molecular temperature. These values show a temperature relaxation of 70±16 ps, which is a reasonable value given the large amount of evidence for weak system-solvent interactions in non-polar solvents. It is a natural extension of the present work to consider solvents with varying polarity, polarizability, viscosity and thermal conductivity to determine the relative importance of these parameters in promoting microscopic, nonequilibrium temperature relaxation. For the present study, the nonpolar solvent cyclohexane was chosen as it results in a particularly clearly-resolved IR spectrum.

A photoproduct cooling rate is also obtained from the molecular dynamics simulations. Analysis of the photoproduct temperature decay yields a value of 8.01 ps, which is about an order of magnitude faster than experiment. The disparity with experiment is likely due to larger system-solvent interactions present in the MD simulations coupled with solvent molecular diffusion that was found to be roughly half the experimental value. Despite of the numerical disparity, however, we measure the temperature of the instantaneous solvation shell and observe that it indeed remains near the equilibrium value. This fast energy dissipation away from the solvation shell can occur by either fast energy transfer among the molecules or by rapid exchange of solvent molecules between the solvation shell and the bulk solvent. To answer this question, we performed a similar non-equilibrium simulation, using identical MD parameters, except the temperature of a single *solvent* molecule was increased by adding kinetic energy (uniformly scaling all the atom velocities). Monitoring the temperature relaxation back to the equilibrium value revealed a time constant of 5.3 ps, similar to that of the $Mn(CO)_5$ photoproducts. A solvent self diffusion constant of $1.14\pm0.03\times10^{-5}$ cm^2/s is obtained from the velocity-velocity autocorrelation function. This value is smaller than the experimental value of 2.09×10^{-5} cm^2/s,[62] suggesting that the very fast heat transfer is not mediated by motional diffusion, but rather intermolecular energy transfer whose rate is over estimated by the simulation. A temperature decay timescale on the order of 5 ps is consistent with a simple comparison to the experimental thermal conductivity k_{th} of cyclohexane (0.123 W/m•K). The thermal conductance g_{th} is defined as the amount of heat transferred per second over a distance L across an area A for each degree difference of temperature:[63]

$$g_{th} = \frac{Ak_{th}\Delta T}{L} \tag{8}$$

Assuming a solute radius of 3 Å and length of 10 Å, it would take 5.9 ps for 148 kJ/mol of energy to transfer from a single cyclohexane molecule heated 300 K above its surroundings. Although the length is somewhat arbitrary, it is reasonable to assume that the transfer of energy 1 nm away from a solute is sufficiently dissipated. It would appear that the MD simulation captures the heat transfer of the pure solvent, but fails to adequately reproduce the heterogeneous heat transfer of the hot photoproduct to solution. In a classical system, the rate of vibrational energy relaxation is proportional to force-force

autocorrelation function of the solvent molecules onto a specific normal mode of the solute.[13] The fast rate of relaxation observed in our simulations likely arises from an overestimation of the solute-solvent interactions (friction, etc). Since force fields are generally calibrated under in equilibrium conditions, the refinement of these force fields and their use under non-equilibrium conditions warrants further investigation.

Inhomogeneous Lineshapes

The inhomogeneous absorption linewidths computed via vibrational perturbation theory (Figure 3.9) are approximately 20% of the experimental absorption width, and they are largely invariant with respect to temperature. From the peak-width fit (**Error! Reference source not found.**) it is observed that the equilibrium absorption width of $Mn(CO)_5$ is 7.1 ± 0.8 cm^{-1} a value that is slightly larger than the 5.8 cm^{-1} width of the 2013 cm^{-1} peak of the parent. The experimental data was collected at 100 ps UV/IR delay which means that the $Mn(CO)_5$ molecules are in thermal equilibrium with the solvent (~300K) and so the broadness of the CO absorption is likely not due to temperature effects. This failure in reproducing the experimental width could arise from several origins: Firstly, it may be possible that VPT2 does not accurately reproduce the coupling between the carbonyl and low-frequency modes of the molecule; since VPT2 successfully reproduces the anharmonic overtone shifts of the CO modes in $Mn_2(CO)_{10}$ [57] it is possible that this procedure underestimates the coupling to the low-frequency modes while overestimating the coupling among the CO modes. Secondly, given the radical nature of the molecule, it may be possible that interactions with the solvent distort the molecular geometry lifting the degeneracy of the two 1982 cm^{-1} carbonyl modes, thus giving an inherently broader lineshape. Evidence for solvent complexation has been found in similar metal carbonyl radicals such as $W(CO)_5$ and $Cr(CO)_5$ from transient absorption measurements in n-hexane.[64] We anticipate improvements in experimental sensitivity and in modeling transient spectra will enable detailed comparisons with these explanations, especially if it becomes possible to directly observe spectral diffusion of an inhomogeneously broadened photoproduct.

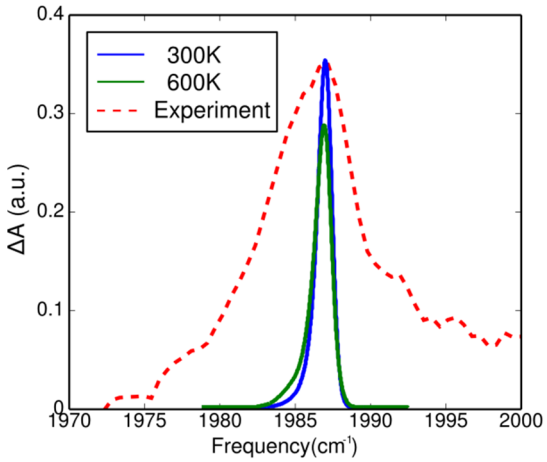

Figure 3.9: Computed inhomogeneous lineshape of the $Mn(CO)_5$ carbonyl transition at 300K and 600K. The experimental UV/IR transient absorption at 100 ps time delay after subtraction of the overlapping bleach is shown in dashed lines for comparison. The center frequency of the simulated peaks was shifted to match the transient absorption frequency.

Conclusion and Outlook

In conclusion, 400 nm excitation of $Mn_2(CO)_{10}$ triggers the homolytic cleavage of the Mn-Mn bond producing $Mn(CO)_5$ radicals in solution. The excess photon energy is dissipated into the low frequency modes of the molecules, causing a temperature increase which in turn affects orientational diffusion rates of the photoproduct. These orientational rates serve as a molecular thermometer, which allow the extraction of a cooling rate for the transient species after photoreaction. While the MD simulations confirm some experimental results such as the orientational timescales, significant questions remain with respect to the simulated cooling rates. Anharmonic linewidth calculations show that temperature alone cannot account for the broad absorption lineshape in $Mn(CO)_5$ and other effects may contribute to inhomogeneous broadening. It is also likely that this first-principles approach may require further testing and validation in systems whose dynamics are better understood.

This work presents an experimental and theoretical study of the temperature-dependent dynamics of transient species in solution, illustrating the capabilities of transient-2DIR spectroscopy as a powerful technique to provide dynamical information beyond one-dimensional transient absorption experiments. We have directly measured the orientational lifetime of a transient species as a function of waiting time after the photoreaction as well as the vibrational cooling rate and absorption linewidths as a function of transient, effective temperature. Molecular dynamics simulations provided further insight into reorientational

lifetimes and vibrational cooling from a molecular perspective and allowed the results to be directly compared to experiment. The temperature dependence of the absorption linewidths was treated using an anharmonic model based on vibrational perturbation theory using *ab-initio* derived force constants. The lack of agreement between the modeling results and experimental absorption width warrants further testing and validation of the perturbation approach in systems with well-characterized dynamics. Although 2DIR spectra include rich spectral and dynamical information, they alone cannot provide a molecular level picture. Classical MD simulations have been successful in helping to explain equilibrium 2DIR spectra, even those of the complex dynamics in liquid water. This work suggests, however, that the transient dynamics probed by non-equilibrium multidimensional methods pose a challenge to existing simulation methods.

In summary, we presented a unified ultrafast experimental and theoretical approach to understanding the non-equilibrium dynamics of $Mn(CO)_5$ following photodissociation. Future experimental work will elucidate the role of solvent polarity, polarizability and viscosity in determining the temperature decay and orientational relaxation rates for both photoproducts of $Mn_2(CO)_{10}$.

3.3 Geminate Rebinding Dynamics of Solvent-Caged Radical Pairs

As two reacting partners approach, kinetic control of intermediate formation and asymmetric branching ratios are governed by subtle interactions that pose significant challenges to experiment and theory. Understanding geminate recombination reactions has been of paramount importance in developing a full mechanistic view of bimolecular processes including ligand rebinding after photodissociation in heme proteins[10] and radical pair rebinding in a solvent cage.[65-67] More generally, bimolecular reaction dynamics are driven by and are sensitive to both the details of interpair interactions and the complex role of the surrounding solvent, protein or surface. This communication reports the direct observation—using ultrafast transient nonlinear infrared spectroscopy—of non-equilibrium structural selectivity, thus providing a model for asymmetric chemical reaction dynamics in solution.

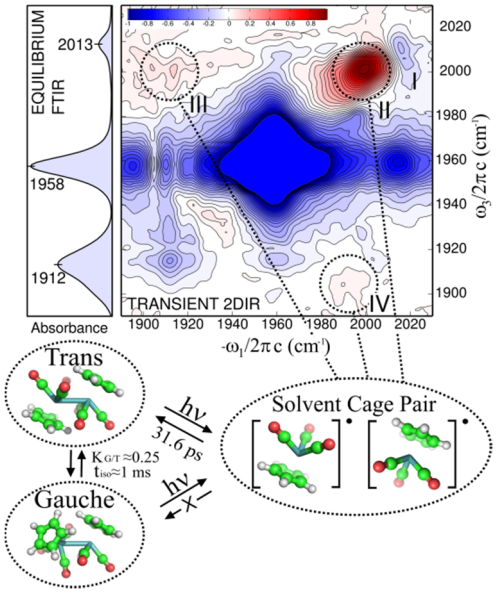

Figure 3.10: Reaction scheme and transient-2DIR spectrum of $[CpMo(CO)_3]_2$ in ethyl acetate at zero waiting time and a UV/IR delay of 5 ps. The red features (circled) are due to the photoproduct radicals.

Cyclopentadienylmolybdenum(II) tricarbonyl dimer is a dimetal carbonyl complex that exists in two different isomeric forms in polar solvents, *trans* and *gauche* (Figure 3.10), which slowly exchange on a millisecond timescale.[68] The relative ratios of the two isomers depend on the solvent polarity; the *trans* isomer predominates in non-polar liquids, whereas polar liquids support both isomers.[69] Similar to other dimetal carbonyl complexes, 400-nm photoexcitation induces a σ–σ* transition, leading to homolytic cleavage of the metal-metal bond, generating $[CpMo(CO)_3]$ radicals.[70] Bimolecular recombination of these radicals typically shows biexponential behavior, with a fast picosecond component attributed to rebinding inside the solvent cage, and a slow, microsecond component due to diffusion in the bulk solution.[68] Recent ultrafast transient absorption studies in the ultraviolet and visible have examined the fast geminate recombination process. The effects of the size and mass of the radicals on the recombination dynamics, as well as the nature of the solvent have been extensively studied, and the experimental results have been modeled in terms of solvent-caged radical pairs.[65-67] In contrast to electronic spectroscopy, transient IR spectroscopy affords structural specificity, thus offering valuable insight into the rebinding processes lacking in electronic spectroscopy. We present our results on the geminate recombination process obtained using non-equilibrium three-pulse photon echo spectroscopy to monitor the picosecond bleach recovery of infrared bands assigned to the *trans* and *gauche* isomers in a

polar solvent. To the best of our knowledge, this is the first ultrafast spectroscopic study of a geminate rebinding reaction using multidimensional infrared spectroscopy.[71, 72] Interpretation of the recombination process is facilitated by computing the potential energy along the Mo–Mo bond and rotation angle using electronic structure methods.

Detailed descriptions of the experimental methods are given in previous chapters. Briefly, equilibrium 2DIR spectra of $[CpMo(CO)_3]_2$ in ethyl acetate were collected using a Fourier-transform 2DIR setup. *UV-pump/2DIR-probe*: Transient-2DIR spectra were collected by applying a 400-nm UV pulse to cleave the Mo–Mo bond before the 2DIR measurement.[42, 73] *UV-pump/DVE-probe*: Transient dispersed vibrational echo (DVE) signals were collected by time-overlapping all three infrared pulses and measuring the homodyne echo spectrum with and without the UV pulse. The transient-DVE measurement is a projection of the transient 2DIR spectrum, but benefits from a much faster acquisition time. A full potential energy surface along the Mo–Mo bond distance and the orientation angle that connects the *trans* and *gauche* configurations was computed using electronic structure methods.

2DIR Peak Assignment

The absorption spectrum in ethyl acetate (Figure 3.11) shows three main peaks centered at 1913, 1958, and 2013 cm^{-1}. The two low-frequency peaks have contributions from the *trans* and *gauche* conformations whereas the 2013 cm^{-1} peak is only due the to *gauche* conformation. It has been previously observed that in non-polar solvents, where only the *trans* conformation is favored, that the high frequency peak is not present and the low frequency peaks become narrower. Thus it was predicted that the two isomers would have overlapping transitions near 1913 and 1958 cm^{-1}. This assignment is confirmed by the equilibrium 2DIR spectrum shown in Figure 3.11 The spectrum shows cross peaks between all three main diagonal peaks, at zero waiting time, the only possible route to cross peaks is a common ground-state between the transitions, therefore, in addition to the high-frequency transition, the *gauche* isomer has transitions that overlap those of the *trans* isomer. This simple peak assignment is one clear example of the inherent structure-specific spectral information provided by 2DIR spectroscopy.

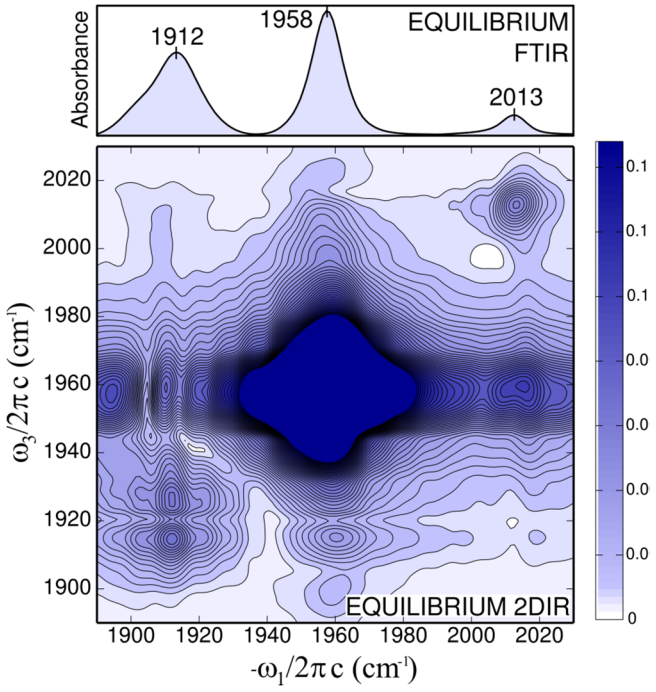

Figure 3.11: (top) Absorption spectrum of $[CpMo(CO)_3]_2$ in ethyl acetate. (bottom) Absolute value rephasing 2DIR spectrum measured with all-parallel polarizations at zero waiting time. The spectrum shows cross-peaks between all three main peaks.

Temperature-dependent absorption spectra

Absorption spectral were collected using a standard Fourier-transform infrared spectrometer. The sample solution was flowed using a flow-cell equipped with a 100 μm spacer. While flowing continuously, the solution was slowly cooled by placing the reservoir in an acetone/dry-ice bath and FTIR spectra were recorded between -7 and 27 °C. The equilibrium constant was obtained by monitoring the ratio of the center peak at 1958 cm^{-1} (*trans* + *gauche*), to the high frequency 2013 cm^{-1} (*gauche* only). Since the two isomers have overlapping transitions, *ab-initio* derived molar absorptivities were used for calculating the equilibrium constants from the measured FTIR spectra. A van 't Hoff plot (Figure 3.12) reveals a $\Delta H=3.16\pm0.94$ kJ mol^{-1} and $\Delta S=-24.5\pm0.94$ J mol^{-1} K^{-1}.

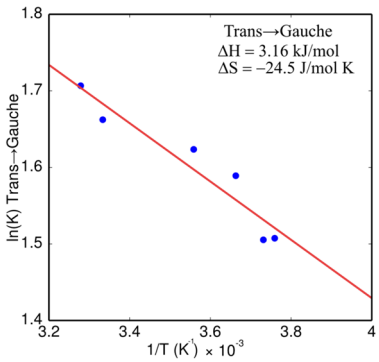

Figure 3.12: Plot of 1/T versus ln(K) for *trans*-to-*gauche* isomerization reaction of [CpMo(CO)3]2 in ethyl acetate.

Computational Methods and Models

Electronic-structure computations of the potential energy surface along the Mo-Mo bond and rotation angle of each monomer were carried out using unrestricted Hartree-Fock theory. This method was chosen over density functional theory as it provides a better description of long-range interactions. A mixed basis set using LanL2DZ[74] on the metal centers and a 6-31G(d) basis on the remaining atoms was used. A harmonic vibrational analysis on the equilibrium geometries confirmed that these are stationary points. Starting from the equilibrium geometry in the *trans* conformation, a potential energy surface was obtained by computing single-point energies at seven values along the metal-metal bond, and twelve angles from *trans* (0^o) to *cis* (90^o). Since Hartree-Fock results tend to grossly overestimate energies in comparison with experiment, all the computed energies were scaled by an empirical factor of 0.62. This factor was obtained by comparing the computed to the experimental ΔH of isomerization. Since the reaction coordinate for isomerization at the equilibrium bond distance is likely more complicated than a simple rotation of one of the monomers around the metal-metal bond, the potential energy surface was computed starting at 0.5 Angstroms up to 2.2 from the equilibrium bond distance. All electronic-structure computations were carried out using the Gaussian 03 program.[49]

Optimized UHF energies and parameters are shown in Table 3.2 below. The raw electronic structure results show an isomerization energy of 5.01 kJ/mol, a factor of 1/0.62 (i.e. 1.6) higher than the experimental value. A high-level density functional theory analysis of all the stable isomers in $[CpMo(CO)_3]_2$ has been recently reported in the literature.[75]

Table 3.2: Optimized UHF energies and selected geometry parameters.

UHF Energies			
	Trans	*Gauche*	Difference
Energy (a.u.)	-1194.693175	-1194.691233	5.01 kJ/mol
ZPE (a.u)	0.234704	0.234408	
Entropy (J/mol K)	709.19218	713.27577	4.08 J/ mol K
Selected UHF Geometry Parameters			
Mo-Mo Distance (Angstroms)	3.413	3.352	
Mo_2-Mo_1-C_1 Angle (Deg)	132.51	129.214	
C_1-Mo_1-Mo_2-C_2 Dihedral (Deg)	180.0	105.72	
C_1-O_1 Distance (Angstroms)	1.1281	1.16	

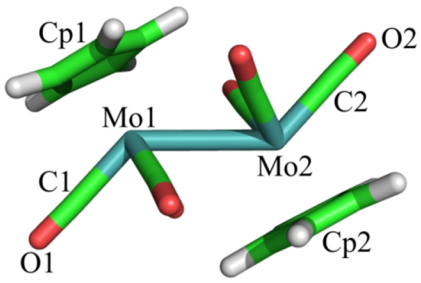

Figure 3.13: Optimized geometry of the trans isomer showing selected atom labels.

Results and Discussion

The transient-2DIR spectrum (Figure 3.10) shows three main diagonal bleaches with corresponding cross peaks and a large diagonal positive peak centered near 1995 cm^{-1}. In this case, cross peaks in the spectrum appear because the transitions share a common ground-state (i.e. reside on the same molecule). Similar to one-dimensional transient-absorption spectroscopy, the bleaches arise from the depletion of parent molecules, and the positive peaks are due to the nascent product species. The high-frequency positive peak (**II**), slightly distorted due to spectral overlap with the 2013 cm^{-1} bleach (**I**), has been assigned to the 17-electron $CpMo(CO)_3$ radical species, obtained by photocleavage of the metal-metal bond. A low-frequency peak centered near 1912 cm^{-1} has also been observed in infrared transient absorption experiments, however due the experimental detection bandwidth in our experiments we are not able to observe this peak on the diagonal. The positive features **III**

and **IV** correspond to a cross peak between the high-frequency and low-frequency peaks, indicating that both transitions arise from the product molecule.

The rebinding was tracked using UV-pump/DVE-probe, where the recovery bleaches of the peaks at 1958 and 2013 cm^{-1} was measured as a function of the UV-IR delay as shown in Figure 3.16. The bleach onset is instrument-limited, in agreement with previous experiments. The 1958 cm^{-1} peak is observed to recover with a time constant of 15.8±0.5 ps, whereas the high-frequency peak corresponding to the *gauche* isomer does not recover significantly in the timescale of the experiment. These observations are clear indications that the geminate rebinding process favors exclusively the *trans* isomer. UV-pump/IR-probe transient absorption (TA) experiments (not shown) yielded a 27±5 ps bleach recovery rate (further discussion provided in Chapter 2). The background-free detected DVE signal greatly improves the experimental signal-to-noise ratio over TA, while providing enhanced spectral resolution.[76] Previous TA studies using 515-nm-pump/400-nm-probe reported a rebinding time constant of 5.9 ps in cyclohexane,[6] which is markedly more rapid than what is observed in ethyl acetate. The recombination efficiency, which describes the number of molecules that undergo geminate recombination inside the solvent cage, can be computed from the exponential fit to the DVE bleach recovery. Our extracted value of 32% is in agreement with previous results of 30% (*n*-hexane)[77] and 48% (Cp' derivative in cyclohexane),[78] and we further expect the recombination efficiency to depend on solvent viscosity and polarity as well as the size and mass of the radicals.

The diffusive *trans*/*gauche* recombination ratios of $[(n\text{-butylCp})Mo(CO)_3]_2$ in various solvents have been measured using microsecond time-resolved absorption spectroscopy.[68] These ratios are observed to be highly dependent on the solvent polarity and viscosity, with viscous non-polar solvents significantly favoring the *trans* configuration (15:1 ratio in n-heptane). The studies also measured the *gauche*-to-*trans* isomerization rate constants and found these to be on the order of $k_{G\text{-}T} = 1.1\times10^3$ (s^{-1}) at 283 K. Because of the slow exchange kinetics compared to the timescale of our experiments (50 ps), the *gauche* and *trans* populations can be considered static with exchange only occurring via bond cleavage/recombination (i.e. via the photochemical reaction). A separate study has reported that the *gauche* isomer is significantly favored in the diffusion-limited recombination of $[CpMo(CO)_3]_2$.[77] These two results are somewhat conflicting with those of

$[(n\text{-butylCp})Mo(CO)_3]_2$ as it is not expected that slightly modifying the Cp ligand would significantly affect these ratios. Therefore a careful study of the nature of the aromatic ligand on the diffusive recombination ratio may lead to a reinterpretation of these experimental results. Although our measurements are on the solvent-caged radical pairs and on a vastly different timescale, they show that the *trans* isomer is greatly favored in polar solvents. Detailed studies on cage escape rates and recombination efficiencies have been reported in the literature.[66, 67] These studies were carried out using transient absorption in the visible with a 515-nm pump. The results indicate that the recombination efficiency can vary widely from 10% to 90% and is proportional to $mass^{1/2}radius^{-2}$ for different substituted Cp ligands.

Oelkers and coworkers have measured the solvent-caged radical rebinding rate constants for $[CpMo(CO)_3]_2$ in several solvents using transient absorption spectroscopy with a 515-nm pump and 400-nm probe.[65] The values obtained range from 3.5 ps in pentane to 8.0 ps in 1-propanol. These rebinding rates are significantly faster than the results measured in our 400-nm pump/DVE-probe experiments. In an attempt to understand this difference in rebinding rates we repeated the transient-DVE experiments by monitoring the bleach recovery of the 1958 cm^{-1} parent peak in n-hexane using the 400-nm pump as well as a 515-nm pump to directly compare the results with those of Oelkers et al. The measured rebinding curves (shown in Figure 3.14 below) exhibit decay times of 19.3±0.6 and 16.5±0.5 ps corresponding to rebinding rate constants of 38.6±1.2 and 33.0±1.0 ps for 400-nm and 515-nm pump respectively, much greater than the 5.6±1 ps measured by Oelkers et al. In an attempt to understand this difference we have also successfully reproduced their experimental transient-absorption results obtaining a value of 4.6±0.5 ps in n-hexane. Although the actual rebinding rate constants are not the central topic of investigation and do not directly determine the main conclusion of this work, this discrepancy certainly warrants further investigation. It is also worth noting that the choice of pump wavelength has a measurable but slight, effect on the rebinding rates. This evidence suggests that the two different excited states may lead to different dissociative potentials.

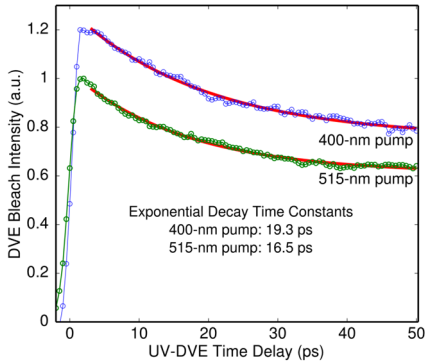

Figure 3.14: Transient DVE bleach recoveries of the 1958 cm^{-1} of $[CpMo(CO)_3]_2$ in n-hexane along with the respective single-exponential fits. The rebinding rates were measured using two different pump wavelengths. The two curves are offset for clarity.

Finally, another important issue that should be discussed in this context is the orientational relaxation of the monomers. The basic question is: How long in time do the monomers retain a memory of their pre-cleavage conformation? The orientational correlation time constants of the monomers inside the solvent cage have been carefully measured in various non-polar solvents by Oelkers and coworkers.[65] These time constants were found to depend linearly on the viscosity of the solvent. The solvent used for our experiments has a viscosity of 0.423 cP at 298 K,[79] so according to their results, one would predict an orientational relaxation time of approximately 6 ps. This measurement, combined with our measured recombination time constant of 16.2 ps, indicates that the radical caged-pairs start out completely randomized in the orientational coordinate before rebinding. In ethyl acetate, we do not observe significant recombination into the *gauche* isomer, an observation which, when combined with the computed PES, suggests that orientational energy landscape "steers" the molecules towards the more stable *trans* conformation.

The dependence of the solvent viscosity on the recombination rate is measured using mixtures of n-hexane and squalane as shown in Figure 3.15. The data shows no dependence, within error, on the solvent viscosity, indicating that radical pairs are somewhat isolated within the solvent cage and that in-cage diffusion is largely independent of the bulk solvent viscosity. If the cage-escape process is diffusion controlled, one expects that a higher viscosity solvent will lead to a higher recombination efficiency. This assumption is indeed correct, the data shows a higher recombination efficiency in high-viscosity mixtures: 58% in

n-hexane (η=0.3 cP) versus 71% in a 80:20 mixture of squalane to n-hexane (η=8 cP); in agreement with previous transient visible absorption measurements.

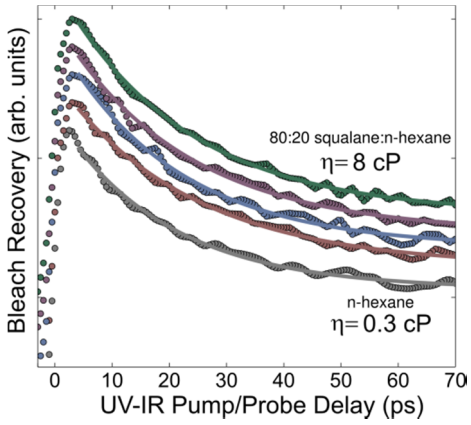

Figure 3.15: Viscosity dependence of the rebinding rates in non-polar solvents. A mixture of squalane and n-hexane was used to modulate the viscosity from 0.4 cP to 8 cP. The solid curves are single-exponential fits to the data. The curves are offset for clarity.

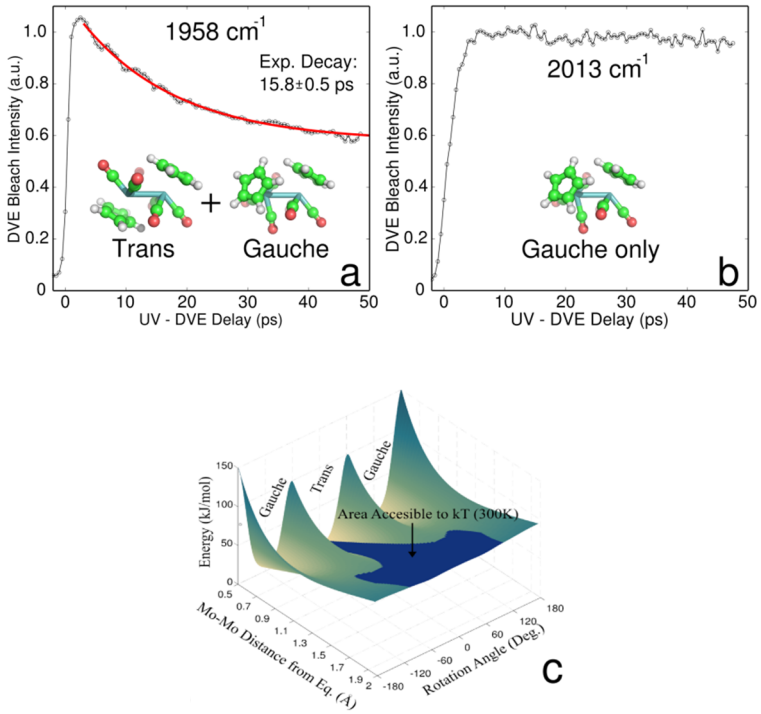

Figure 3.16: Transient DVE bleach recovery, due to geminate rebinding of the radical fragments, at the 1958 cm^{-1} (a) corresponding to the *trans* and *gauche* conformations and 2013 cm^{-1} (b) corresponding to the *gauche* isomer. The red curve represents a single-exponential fit to the data. The insets show the chemical structures of the *trans* and *gauche* conformations obtained from electronic structure computations. (c) Potential energy surface (PES) computed along the Mo-Mo bond and the orientation angle. The blue area shows the range of angles accessible by the system at each point along the bond coordinate.

A molecular-level interpretation of the experimental results is aided by the *ab-initio* energy surface for the reaction shown in Figure 3.16. This plot shows the potential energy as a function of the bond distance and orientation angle about the Mo–Mo bond. Multiple observations can be made from this figure: *1*. The geminate rebinding is a barrierless process for both isomers, and thus the timescale for recombination is likely dominated by the diffusion of the fragments inside the solvent cage, and not necessarily by the potential itself. *2*. The large torsional energy barrier to isomerization remains high even at metal-metal bond distances far from the equilibrium configuration, indicating that the rebinding process pre-selects a specific isomer channel long before reaching the equilibrium bond distance. *3*. The blue area shows the orientational angle-coordinate space thermally accessible (at 300 K) from the minimum energy at each point in the metal-metal bond distance coordinate. The preferred channel for recombination is clearly the one leading to the *trans* configuration, in agreement with the experimental observations. This is a kinetic effect where the molecules are "steered" towards the *trans* conformation as they approach each other.

The computed PES shows the thermally accessible area at 300K along the Mo-Mo bond rotation coordinate at each point in the Mo-Mo distance coordinate. Since the molecules have a large excess energy after photodissociation with vibrational cooling occurring in the same timescale as the experiment it is unlikely that the molecules are in full thermal equilibrium during the rebinding process. The temperature of the $CpMo(CO)_3$ radicals after photodissociation can be estimated from the initial photon energy, bond energy, and the ab-initio heat capacity.[75] This temperature is estimated to be 750K, a significant increase from the equilibrium temperature of 300K. Evidence for rapid vibrational cooling, however, can be found in the absorption linewidths of the photoproduct peaks. In metal carbonyls, excitation of the low-frequency modes of the molecule, due to a temperature increase, causes the high-frequency peaks to broaden due to anharmonic coupling in the vibrational Hamiltonian.[29, 80] Measuring the absorption linewidth as a function of UV-IR time delay in $CpMo(CO)_3$ we observe that the linewidths remain narrow even at short delays after photodissociation, which is direct evidence for rapid vibrational cooling. This is not surprising since the photoproduct molecules have a large number of low-frequency modes that can efficiently transfer energy to the solvent by resonantly

coupling to the solvent modes. We expect that future modeling of this reaction will include temperature effects as well as properly modeling the excited-state potentials.

Conclusion

In conclusion, the photochemistry of $[CpMo(CO)_3]_2$ was studied using equilibrium and non-equilibrium 2DIR spectroscopy and transient IR echo spectroscopy with particular attention to the fast rebinding of the radicals following photodissociation. The experimental data support the conclusion that fast geminate rebinding specifically favors the *trans* isomer over the slightly higher-energy *gauche* isomer. A molecular level picture of the branching is supported by the *ab-initio* derived potential energy surface. These results highlight the promise of ultrafast nonlinear vibrational spectroscopy to elucidate complex many-body reaction dynamics that underlie asymmetric chemical processes central to catalysis and mechanistic determination.

References

1. M. Cho, "Coherent Two-Dimensional Optical Spectroscopy," Chemical Reviews **108**, 1331-1418 (2008).

2. P. Hamm, M. H. Lim, and R. M. Hochstrasser, "Structure of the amide I band of peptides measured by femtosecond nonlinear-infrared spectroscopy," Journal of Physical Chemistry B **102**(31), 6123-6138 (1998).

3. J. Bredenbeck, J. Helbing, and P. Hamm, "Labeling vibrations by light: Ultrafast transient 2D-IR spectroscopy tracks vibrational modes during photoinduced charge transfer," Journal of the American Chemical Society **126**(4), 990-991 (2004).

4. C. Kolano, J. Helbing, G. Bucher, W. Sander, and P. Hamm, "Intramolecular disulfide bridges as a phototrigger to monitor the dynamics of small cyclic peptides," Journal of Physical Chemistry B **111**, 11297-11302 (2007).

5. C. Baiz, M. Nee, R. McCanne, and K. Kubarych, "Ultrafast nonequilibrium Fourier-transform two-dimensional infrared spectroscopy," Optics Letters **33**(21), 2533-2535 (2008).

6. A. I. Stewart, R. Kania, G. M. Greetham, I. P. Clark, M. Towrie, A. W. Parker, and N. T. Hunt, " Investigating the vibrational dynamics of a 17e(-) metallocarbonyl intermediate using ultrafast two dimensional infrared spectroscopy" Physical Chemistry Chemical Physics, **12**(5) 1051(2010).

7. H. J. Bakker, S. Woutersen, and H. K. Nienhuys, "Reorientational motion and hydrogen-bond stretching dynamics in liquid water," Chemical Physics **258**(2-3), 233-245 (2000).

8. S. Woutersen and H. J. Bakker, "Resonant intermolecular transfer of vibrational energy in liquid water," Nature **402**(6761), 507-509 (1999).

9. P. A. Anfinrud, C. Han, and R. M. Hochstrasser, "Direct Observations of Ligand Dynamics in Hemoglobin by Subpicosecond Infrared-Spectroscopy," Proceedings of the National Academy of Sciences of the United States of America **86**(21), 8387-8391 (1989).

10. M. H. Lim, T. A. Jackson, and P. A. Anfinrud, "Ultrafast rotation and trapping of carbon monoxide dissociated from myoglobin," Nature Structural Biology **4**(3), 209-214 (1997).

11. J. Bredenbeck, J. Helbing, K. Nienhaus, G. U. Nienhaus, and P. Hamm, "Protein ligand migration mapped by nonequilibrium 2D-IR exchange spectroscopy," Proceedings of the National Academy of Sciences of the United States of America **104**(36), 14243-14248 (2007).

12. C. B. Harris, D. E. Smith, and D. J. Russell, "Vibrational-Relaxation of Diatomic-Molecules in Liquids," Chemical Reviews **90**(3), 481-488 (1990).

13. J. Chesnoy and G. M. Gale, "Vibrational-Energy Relaxation in Liquids," Annales De Physique **9**(6), 893-949 (1984).

14. S. A. Adelman and R. H. Stote, "Theory of Vibrational-Energy Relaxation in Liquids - Construction of the Generalized Langevin Equation for Solute Vibrational Dynamics in Monatomic Solvents," Journal of Chemical Physics **88**(7), 4397-4414 (1988).

15. R. M. Whitnell, K. R. Wilson, and J. T. Hynes, "Vibrational-Relaxation of a Dipolar Molecule in Water," Journal of Chemical Physics **96**(7), 5354-5369 (1992).

16. R. M. Whitnell, K. R. Wilson, and J. T. Hynes, "Fast Vibrational-Relaxation for a Dipolar Molecule in a Polar-Solvent," Journal of Physical Chemistry **94**(24), 8625-8628 (1990).

17. E. H. G. Backus, P. H. Nguyen, V. Botan, R. Pfister, A. Moretto, M. Crisma, C. Toniolo, G. Stock, and P. Hamm, "Energy transport in peptide helices: A comparison between high- and low-energy excitations," Journal of Physical Chemistry B **112**(30), 9091-9099 (2008).

18. T. P. Dougherty, W. T. Grubbs, and E. J. Heilweil, "Photochemistry of Rh(CO)2(acetylacetonate) and Related Metal Dicarbonyls Studied by Ultrafast Infrared Spectroscopy," Journal of Physical Chemistry **98**(38), 9396-9399 (1994).

19. R. Herrick, S. and T. Brown, L. , "Flash photolytic investigation of photoinduced carbon monoxide dissociation from dinuclear manganese carbonyl compounds," Inorganic Chemistry **23**(26), 4550-4553 (1984).

20. J. L. Hughey, C. P. Anderson, and T. J. Meyer, "Photochemistry of Mn2(CO)10," Journal of Organometallic Chemistry **125**(2), C49-C52-C49-C52 (1977).

21. T. Kobayashi, H. Ohtani, H. Noda, S. Teratani, H. Yamazaki, and K. Yasufuku, "Excitation wavelength dependence of photodissociation and the secondary laser pulse photolysis of dimanganese decacarbonyl," Organometallics **5**(1), 110-113 (1986).

22. M. Lee and C. B. Harris, "Ultrafast studies of transition metal carbonyl reactions in the condensed phase. Solvation of coordinatively unsaturated pentacarbonyls," Journal of the American Chemical Society **111**(24), 8963-8965 (1989).

23. R. A. Levenson and H. B. Gray, "Electronic structure of compounds containing metal-metal bonds. Decacarbonyldimetal and related complexes," Journal of the American Chemical Society **97**(21), 6042-6047 (1975).

24. T. J. Meyer and J. V. Caspar, "Photochemistry of metal-metal bonds," Chemical Reviews **85**(3), 187-218 (1985).

25. J. C. Owrutsky and A. P. Baronavski, "Ultrafast infrared study of the ultraviolet photodissociation of Mn2(CO)10," The Journal of Chemical Physics **105**(22), 9864-9873 (1996).

26. A. Rosa, G. Ricciardi, E. J. Baerends, and D. J. Stufkens, "Density Functional Study of the Photodissociation of Mn2(CO)10," Inorganic Chemistry **35**(10), 2886-2897 (1996).

27. L. J. Rothberg, N. J. Cooper, K. S. Peters, and V. Vaida, "Picosecond dynamics of solution-phase photofragmentation of dimanganese decacarbonyl [Mn2(CO)10]," Journal of the American Chemical Society **104**(12), 3536-3537 (1982).

28. T. A. Seder, S. P. Church, and E. Weitz, "Photodissociation pathways and recombination kinetics for gas-phase dimanganese decacarbonyl," Journal of the American Chemical Society **108**(24), 7518-7524 (1986).

29. D. A. Steinhurst, A. P. Baronavski, and J. C. Owrutsky, "Transient infrared spectroscopy of Mn-2(CO)(10) with 400 nm excitation," Chemical Physics Letters **361**(5-6), 513-519 (2002).

30. A. Waldman, S. Ruhman, S. Shaik, and G. N. Sastry, "Coherent photochemistry in solution - Impulsive photoselective photolysis of Mn2(CO)10," Chemical Physics Letters **230**(1-2), 110-116 (1994).

31. J. Z. Zhang and C. B. Harris, "Photodissociation dynamics of Mn[sub 2](CO)[sub 10] in solution on ultrafast time scales," The Journal of Chemical Physics **95**(6), 4024-4032 (1991).

32. T. P. Dougherty and E. J. Heilweil, "Transient infrared spectroscopy of (eta [sup 5] - C[sub 5] H[sub 5])Co(CO)[sub 2] photoproduct reactions in hydrocarbon solutions," The Journal of Chemical Physics **100**(5), 4006-4009 (1994).

33. M. W. George, T. P. Dougherty, and E. J. Heilweil, "UV Photochemistry of [CpFe(CO)2]2 Studied by Picosecond Time-Resolved Infrared Spectroscopy," Journal of Physical Chemistry **100**(1), 201-206 (1996).

34. Z. H. Wang, A. Pakoulev, and D. D. Dlott, "Watching vibrational energy transfer in liquids with atomic spatial resolution," Science **296**(5576), 2201-2203 (2002).

35. J. C. Deak, L. K. Iwaki, and D. D. Dlott, "Vibrational energy redistribution in polyatomic liquids: Ultrafast IR-Raman spectroscopy of acetonitrile," Journal of Physical Chemistry A **102**(42), 8193-8201 (1998).

36. D. D. Dlott, "Vibrational energy redistribution in polyatomic liquids: 3D infrared-Raman spectroscopy," Chemical Physics **266**(2-3), 149-166 (2001).

37. T. Tao, "Time-Dependent Fluorescence Depolarization and Brownian Rotational Diffusion Coefficients of Macromolecules," Biopolymers **8**(5), 609-& (1969).

38. B. Berne and R. Pecora, *Dynamic Light Scattering: With Applications to Chemistry, Biology, and Physics* (Dover Publications, 2000).

39. A. Tokmakoff, "Orientational correlation functions and polarization selectivity for nonlinear spectroscopy of isotropic media .1. Third order," Journal of Chemical Physics **105**(1), 1-12 (1996).

40. J. Bredenbeck, J. Helbing, and P. Hamm, "Transient two-dimensional infrared spectroscopy: Exploring the polarization dependence," The Journal of Chemical Physics **121**(12), 5943-5957 (2004).

41. A. Tokmakoff, "Orientational correlation functions and polarization selectivity for nonlinear spectroscopy of isotropic media. II. Fifth order," The Journal of Chemical Physics **105**(1), 13-21 (1996).

42. C. R. Baiz, M. J. Nee, R. McCanne, and K. J. Kubarych, "Ultrafast nonequilibrium Fourier-transform two-dimensional infrared spectroscopy," Optics Letters **33**(21), 2533--2535 (2008).

43. M. J. Tauber, R. A. Mathies, X. Y. Chen, and S. E. Bradforth, "Flowing liquid sample jet for resonance Raman and ultrafast optical spectroscopy," Review of Scientific Instruments **74**(11), 4958-4960 (2003).

44. M. J. Nee, R. McCanne, K. J. Kubarych, and M. Joffre, "Two-dimensional infrared spectroscopy detected by chirped pulse upconversion," Optics Letters **32**(6), 713-715 (2007).

45. J. Wang, W. Wang, P. A. Kollman, and D. A. Case, "Automatic atom type and bond type perception in molecular mechanical calculations," Journal of Molecular Graphics and Modeling **25**(2), 247-260 (2006).

46. J. Wang, R. M. Wolf, J. W. Caldwell , P. A. Kollman, and D. A. Case, "Development and testing of a general amber force field," Journal of Computational Chemistry **25**(9), 1157-1174 (2004).

47. C. I. Bayly, P. Cieplak, W. D. Cornell, and P. A. Kollman, "A Well-Behaved Electrostatic Potential Based Method Using Charge Restraints for Deriving Atomic Charges - the Resp Model," Journal of Physical Chemistry **97**(40), 10269-10280 (1993).

48. U. C. Singh and P. A. Kollman, "An approach to computing electrostatic charges for molecules," Journal of Computational Chemistry **5**(2), 129-145 (1984).

49. M. J. Frisch, G. W. Trucks , H. B. Schlegel , G. E. Scuseria , M. A. Robb, J. R. Cheeseman, J. A. Montgomery Jr., T. Vreven, K. N. Kudin, J. C. Burant, J. M. Millam, S. S. Iyengar, J. Tomasi, V. Barone, B. Mennucci, M. Cossi, G. Scalmani, N. Rega , G. A. Petersson , H. Nakatsuji , M. Hada , M. Ehara , K. Toyota , R. Fukuda , J. Hasegawa , M. Ishida , T. Nakajima , Y. Honda , O. Kitao , H. Nakai , M. Klene , J. E. X. Li , H. P. Knox , Hratchian , J. B. Cross , V. Bakken , C. Adamo , J. Jaramillo , R. Gomperts , R. E. Stratmann , O. Yazyev , A. J. Austin , R. Cammi , C. Pomelli , J. W. Ochterski , P. Y. Ayala , K. Morokuma , G. A. Voth , P. Salvador , J. J. Dannenberg , V. G. Zakrzewski , S. Dapprich , A. D. Daniels , M. C. Strain , O. Farkas , D. K. Malick , A. D. Rabuck , K. Raghavachari , J. B. Foresman , J. V. Ortiz , Q. Cui , A. G. Baboul , S. Clifford , J. Cioslowski , B. B. Stefanov , G. Liu , A. Liashenko , P. Piskorz , I. Komaromi , R. L. Martin , D. J. Fox , T. Keith , M. A. Al-Laham , C. Y. Peng , A. Nanayakkara , M. Challacombe , P. M. W. Gill , B. Johnson , W. Chen , M. W. Wong , C. Gonzalez , and J. A. Pople, Gaussian 03, Gaussian, Inc., Wallingford CT, 2004.

50. H. J. C. Berendsen, J. P. M. Postma, W. F. van Gunsteren, A. DiNola, and J. R. Haak, "Molecular dynamics with coupling to an external bath," Journal of Chemical Physics **81**(8), 3684-3690 (1984).

51. E. L. David Van Der Spoel, Berk Hess, Gerrit Groenhof, Alan E. Mark, Herman J. C. Berendsen, "GROMACS: Fast, flexible, and free," Journal of Computational Chemistry **26**(16), 1701-1718 (2005).

52. P. Hamm, S. M. Ohline, and W. Zinth, "Vibrational cooling after ultrafast photoisomerization of azobenzene measured by femtosecond infrared spectroscopy," Journal of Chemical Physics **106**(2), 519-529 (1997).

53. W. Schneider and W. Thiel, "Anharmonic force fields from analytic second derivatives: Method and application to methyl bromide," Chemical Physics Letters **157**(4), 367-373 (1989).

54. S. Dressler and W. Thiel, "Anharmonic force fields from density functional theory," Chemical Physics Letters **273**(1-2), 71-78 (1997).

55. V. Barone, "Anharmonic vibrational properties by a fully automated second-order perturbative approach," The Journal of Chemical Physics **122**(1), 014108-014110 (2005).

56. S. Califano, *Vibrational states* (John Wiley and Sons, London, 1976).

57. C. R. Baiz, P. L. McRobbie, J. Anna, E. Geva, and K. J. Kubarych, "Two-Dimensional Infrared Spectroscopy of Metal Carbonyls," Accounts of Chemical Research **42**(9) 1395 (2009) .

58. M. Nee, C. Baiz, J. Anna, R. McCanne, and K. Kubarych, "Multilevel vibrational coherence transfer and wavepacket dynamics probed with multidimensional IR spectroscopy," Journal of Chemical Physics **129**(8), 084503 (2008).

59. G. M. Sando, Q. Zhong, and J. C. Owrutsky, "Vibrational and rotational dynamics of cyanoferrates in solution," The Journal of Chemical Physics **121**(5), 2158-2168 (2004).

60. S. Woutersen, U. Emmerichs, H. K. Nienhuys, and H. J. Bakker, "Anomalous temperature dependence of vibrational lifetimes in water and ice," Physical Review Letters **81**(5), 1106-1109 (1998).

61. P. Moore, A. Tokmakoff, T. Keyes, and M. D. Fayer, "The low frequency density of states and vibrational population dynamics of polyatomic molecules in liquids," The Journal of Chemical Physics **103**(9), 3325-3334 (1995).

62. S. A. Sanni, C. J. D. Fell, and H. P. Hutchinson, Journal of Chemical Engineering Data (16), 424 (1971).

63. R. Berman, *Thermal Conduction in Solids*, Oxford Studies in Physics (Clarendon Press, 1976).

64. T. P. Dougherty and E. J. Heilweil, "Ultrafast transient infrared absorption studies of M(CO)6 (M = Cr, Mo or W) photoproducts in n-hexane solution," Chemical Physics Letters **227**(1-2), 19-25 (1994).

65. A. B. Oelkers, L. F. Scatena, and D. R. Tyler, "Femtosecond pump-probe transient absorption study of the photolysis of [Cp ' Mo(CO)(3)](2) (Cp ' = eta(5)-C5H4CH3): Role of translational and rotational diffusion in the radical cage effect," Journal of Physical Chemistry A **111**(25), 5353-5360 (2007).

66. A. B. Oelkers, E. J. Schutte, and D. R. Tyler, "Solvent cage effects: the influence of radical mass and volume on the recombination dynamics of radical cage pairs generated by photolysis of [CpCH2CH2N(CH3)C(O)(CH2)(n)CH3Mo(CO)(3)](2) (n=3, 8, 13, 18) (Cp = eta(5)-C5H4) complexes," Photochemical & Photobiological Sciences **7**(2), 228-234 (2008).

67. A. B. Oelkers and D. R. Tyler, "Radical cage effects: A method for measuring recombination efficiencies of secondary geminate radical cage pairs using pump-probe transient absorption methods," Photochemical & Photobiological Sciences **7**(11), 1386 - 1390-1386 - 1390 (2008).

68. J. C. Linehan, C. R. Yonker, R. S. Addleman, S. T. Autrey, J. T. Bays, T. E. Bitterwolf, and J. L. Daschbach, "Solvent study of the kinetics of molybdenum radical self-termination," Organometallics **20**(3), 401-407 (2001).

69. R. Adams and F. Cotton, "Structural and Dynamic Properties of Dicyclopentadienylcarbonylmolybdenum in Various Solvents," Inorganica Chimica Acta **7**(1), 153-156 (1972).

70. T. E. Bitterwolf, "Mechanisms and intermediates in the photochemistry of M-2(CO)(6)(eta(5)-C5H5)(2), where M = Cr, Mo and W, and their ring-coupled analogs," Coordination Chemistry Reviews **211**, 235-254 (2001).

71. M. Cho, "Coherent Two-Dimensional Optical Spectroscopy," Chemical Reviews **108**(4), 1331-1418 (2008).

72. M. Cho, *Two-dimensional optical spectroscopy* (CRC Press, Boca Raton, 2009)

73. C. R. Baiz, P. L. McRobbie, J. M. Anna, E. Geva, and K. J. Kubarych, "Two-Dimensional Infrared Spectroscopy of Metal Carbonyls," Accounts of Chemical Research **42**(9), 1395-1404 (2009).

74. P. J. Hay and W. R. Wadt, "Ab initio effective core potentials for molecular calculations. Potentials for the transition metal atoms Sc to Hg," The Journal of Chemical Physics **82**(1), 270-283 (1985).

75. X. Zhang, Q. s. Li, M. Ge, Y. Xie, R. B. King, and H. F. Schaefer, "Binuclear Cyclopentadienylmolybdenum Carbonyl Derivatives:Where is the Missing ModMo Double-Bonded Species Cp2Mo2(CO)5," Organometallics **28**, 2818 - 2829 (2009).

76. Adam W. Smith and A. Tokmakoff, "Probing Local Structural Events in beta-Hairpin Unfolding with Transient Nonlinear Infrared Spectroscopy," Angewandte Chemie International Edition **46**(42), 7984-7987 (2007).

77. J. Peters, M. W. George, and J. J. Turner, "Photochemistry of [Cpmo(Co)(3)](2) - Direct-Detection and Kinetics of the Radical Cpmo(Co)(3) in N-Heptane Solution at Room-Temperature by Fast Time-Resolved Infrared-Spectroscopy," Organometallics **14**(3), 1503-1506 (1995).

78. J. L. Male, B. E. Lindfors, K. J. Covert, and D. R. Tyler, "The effect of radical size and mass on the cage recombination efficiency of photochemically generated radical cage pairs," Journal of the American Chemical Society **120**(50), 13176-13186 (1998).

79. D. R. Lide, *CRC handbook of chemistry and physics: A ready-reference book of chemical and physical data* (CRC press, 2004).

80. C. R. Baiz, R. McCanne, M. J. Nee, and K. J. Kubarych, "Orientational Dynamics of Transient Molecules Measured by Nonequilibrium Two-Dimensional Infrared Spectroscopy," The Journal of Physical Chemistry A **113**(31), 8907-8916 (2009).

Chapter 4

Ultrafast Condensed-Phase Chemical Dynamics: The solvent's Response

The work presented in this chapter has been published in the following two papers:

1. C.R. Baiz, K.J. Kubarych, "*Ultrafast Vibrational Stark-Effect Spectroscopy: Exploring Charge-Transfer Reactions by Directly Monitoring the Solvation Shell Response"* , Journal of the American Chemical Society, **132** (37), 12784-12785, 2010
2. C.R. Baiz, K.J. Kubarych, *"Vibrational Stark-Effect Spectroscopy: Measuring the Solvent Response in Ultrafast Charge-transfer Reactions"* , Proceedings of International Conference on Ultrafast Phenomena XV, In Press (2011)

4.1 Introduction

Charge transfer reactions—ubiquitous in chemistry and biology—present particular experimental and theoretical challenges due to the strong coupling to the environment, such as a liquid, polymer, or a protein. These reactions are especially sensitive to structural rearrangements of the solvent, as the energy fluctuations of the donor and acceptor states ultimately determine the coordinate as well as the rate of the reaction, thus separating the molecular response from the solvent degrees of freedom can be difficult.[1,2] In this chapter we present a new approach that leverages recent advances in ultrafast spectroscopy to directly probe the solvent response during a phototriggered intramolecular charge-transfer reaction. Using a three-component system comprised of a dye, Betaine-30 (Figure 4.1), surrounded by a polarizable and strongly infrared-active solvation shell (Na^+SCN^-) all embedded within a supporting solvent (ethyl acetate), we demonstrate that it is possible to

track ultrafast charge transfer by monitoring the infrared response of the nearest solvent molecules.

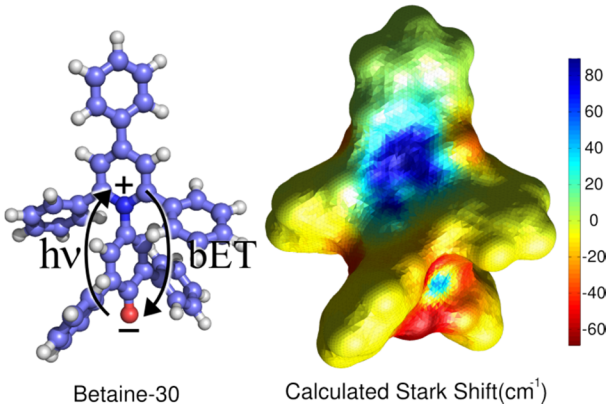

Figure 4.1: (left) Molecular structure of Betaine-30 in the ground-state electronic configuration showing the positive and negative charges on the oxygen and nitrogen atoms. The arrows represent the phototriggered charge transfer and back electron transfer (bET) reactions. (right) Stark map of NaSCN frequency shifts (in cm^{-1}) at the solvent-accessible surface of Betaine-30.

A key feature of our work is that by probing the first solvation shell, the transient measurements interrogate only those solvent molecules that respond to and guide the charge transfer reaction. The essential physical interaction which enables the spectroscopic observation of the electronic excitation is a dynamic vibrational Stark effect[3-5] (VSE) that shifts the nearest solvent vibrations by a few wavenumbers in response to the changing electric field caused by the reaction, effectively shining a light on the charge transfer process. An added advantage of the dynamic VSE method lies in the fact that Stark tuning rates, or frequency shifts as a function of field strength, can be near-quantitatively calculated using standard electronic-structure methods,[5] thus turning each solvent vibration into a structure-sensitive dynamical probe of the electrostatic potential. Alternative methods rely on detecting differences in low-frequency Raman spectra of the solvent,[6-8] and although these transient measurements have yielded much insight into charge-transfer reactions in solution, they typically lack the chemical specificity of a resonant infrared probe.

The main challenge associated with probing the solvent during a charge transfer reaction—an experiment first attempted by Hochstrasser and coworkers[9]—arises from the large difference in the ratio of solute to solvent molecules, causing a significant mismatch in the absorption at the UV/Vis and IR wavelengths. In typical solutions, dyes are present at

the level of several mM, while the solvent is four to five orders of magnitude higher in concentration. To circumvent this problem we have implemented a three-component system consisting of two strongly-interacting highly polar components, a chromophore and spectroscopic solvent, surrounded by a less polar supporting solvent. In such a construct it is necessary to establish that the NaSCN actually solvates the dye molecule. Measurements of the shift in absorption maximum of Betaine-30, a solvatochromic dye often used as an indicator of solvent polarity,[10] in the presence of NaSCN provide strong evidence that NaSCN interacts with the chromophore as discussed next.

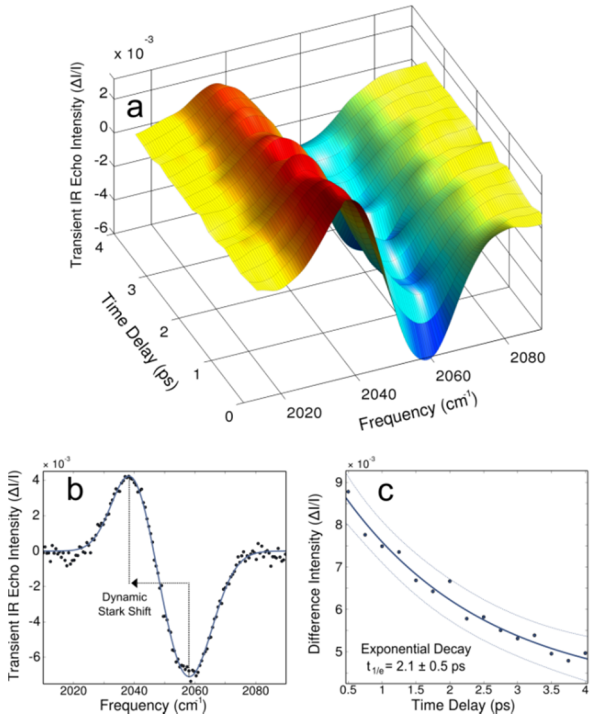

Figure 4.2: (a)Vibrational Stark-effect spectra of the thiocyanate C≡N stretch at various delays after excitation of Betaine-30. (b) Single VSE spectrum at zero time delay with a dual-Gaussian fit (solid line) showing the 19 cm^{-1} red-shift of the solvent C≡N stretching frequency induced by the change in electrostatic environment. (c) VSE difference amplitude (induced signal – bleach) versus delay after excitation with a single-exponential fit (solid line) and 95% confidence bounds (dashed). The Betaine-30 and NaSCN concentrations are 2 and 50 mM respectively.

4.2 Vibrational Stark-Effect Spectroscopy: Experiments and Models

Ultrafast Spectroscopy

The optical setups for measuring equilibrium two-dimensional infrared (2DIR) and transient dispersed vibrational echo are described in detail elsewhere.[11-14] Transient infrared echo spectroscopy offers key experimental advantages over transient infrared absorption, namely background-free detection and improved signal-to-noise ratios without referencing, but the information content is largely similar.[15] In brief, three infrared pulses (~2000cm^{-1}, 100 fs, 1μJ) are arranged in a box geometry at the sample position, and the vibrational echo signal is detected with a CCD-based spectrometer by upconversion to the visible.[11] Further improvement of the signal-to-noise ratio was achieved by adding a slight time delay (<400 fs) between the first and second IR pulses to increase the intensity of the photon-echo signal. This naturally lowers the time-resolution of the measurement. However a transient-DVE (t_1=t_2=0) spectrum shows the same signal decay as the photon echo measurements. An equilibrium 2DIR spectrum is obtained by heterodyning the echo signal with an extra pulse to recover the amplitude and phase of the emitted field while the delay between the two pulses is scanned. The two-stage non-collinear optical parametric amplifier (NOPA) delivers (5.4 μJ, ~100 fs) pulses centered at the absorption maximum of Betaine-30 (580 nm). The difference signal is computed as the normalized difference between the NOPA pump-on and pump-off signals:

$$\Delta I_{DVE}(t_1, t_2 = 0, \omega_3, \tau) = \frac{I_{DVE,Pump} - I_{DVE,\mathrm{Pr}obe}}{I_{DVE,\mathrm{Pr}obe}}$$

Experiments were carried out in the parallel and perpendicular Visible-IR polarization geometries (see discussion below). A solution of Betaine-30 and NaSCN in ethyl acetate was flowed using a 200 μm path-length flow cell equipped with CaF_2 windows. The concentrations were adjusted to obtain a ~20% and ~50% transmittance at the IR and visible wavelengths respectively. The dispersed echo signal corresponding to the C≡N stretch in thiocyanate was measured as a function of the time delay (τ) after electronic excitation of Betaine-30. Using these experimental parameters it is possible to estimate the number of Betaine-30 molecules excited by the pump pulses. Assuming a 200 μm focus size for the pump and probe beams, we estimate a 0.1% excitation fraction (10^{12} photons absorbed/pulse, 10^{15} dye molecules in sample volume). This means that 1 out of every 1000 Betaine-30 molecules get excited by the pump pulses. Given that the transient signal is about 5 x 10^{-3}, this indicates that the number of NaSCN molecules that respond to Betaine-30

excitation is between 1 and 10, consistent with a single solvation shell. The intensity of the transient-DVE signal remained linear with respect to the NOPA power over the range used in the experiments.

Electronic-Structure Models

The geometry of Betaine-30 was optimized using standard Hartree-Fock theory with a 6-31G(d) basis set as implemented in Gaussian 03.[16] Starting from this geometry, the solvent-accessible surface was calculated using the Conolly[17] algorithm as implemented in PyMol.[18] The respective ground and excited state atomic charges, of Maroncelli and Mente,[19] were used to calculate the difference electric field at various points within the surface. A Stark tuning rate of 0.7 $cm^{-1}/(MV/cm)$—corresponding to covalently bonded thiocyanate—was used to compute the frequency shifts shown in Figure 4.1.[4, 5] With a larger polarizability, we expect the tuning rate for ionic NaSCN to be slightly higher. It is also important to point out that the present model only accounts for the initial redistribution of charge into the Franck-Condon surface and not the excited-state dynamics.

The Stark shift corresponds to the projection along the vibrational coordinate of the change in electric field, but because the actual orientation of NaSCN relative to Betaine-30 is not yet fully known, in this model we chose to compute the *maximum* Stark shift at each point on the surface. This was done by computing the magnitude of the electric field at the solvent accessible surface. Thus the map provides upper and lower limits for the expected shifts and is consistent with the experimental observations. Future simulations will combine the Stark map with nonequilibrium molecular dynamics and attempt to reproduce the experimental Stark lineshapes.

From the absorption shifts, the polarity of this unusual solvation environment can be estimated to be similar to that of butanol. Betaine-30 features a decrease in dipole moment[10] as well as significant geometric rearrangements upon photoexcitation into the lowest excited singlet state. The ultrafast radiationless return to the ground-state[20] (<5 ps) indicates rapid dynamics following excitation as well as large solvation energies,[21, 22] making this an ideal system to study with dynamic VSE spectroscopy. A discussion of the

equilibrium vibrational structure of NaSCN along with a two-dimensional spectrum is included below.

4.3 Stark-effect Spectroscopy: Measuring the Solvent Response

Nonequilibrium structural and dynamical information can be extracted from the lineshapes and time evolution of the transient spectra respectively (Figure 4.2). The bleach at 2058 cm^{-1} and the positive Stark-shifted peak at 2039 cm^{-1} arise from a local change in electric field at the positions of the nearby solvent molecules induced by the dipole moment change of the chromophore upon optical excitation. The observed 19 cm^{-1} red-shift can be used to map the electric field change induced by the reaction. The Stark tuning rate of SCN is ~0.7 cm^{-1}/(MV/cm),[4] thus a shift of 19 cm^{-1} represents a change in electric field of approximately 27 MV/cm. To obtain a molecular-level interpretation of the results we computed the expected Stark shifts of the NaSCN molecules in the first solvation shell. The procedure is straightforward, starting with the Betaine-30 ground and excited-state atomic charges[19] we computed the difference in electric field (excited–ground) at the solvent-accessible surface of the dye; a map of the C≡N frequency shifts at the surface is then calculated using the NaSCN Stark tuning rate.[12] Though the Stark shifts are orientation dependent, as a first approximation we compute the maximum magnitude of the shift at various points within the surface. The results (Figure 4.1) show that molecules lying near the nitrogen or oxygen atoms shift by as much as 80 cm^{-1}, but molecules near the phenyl rings only shift by ~20 cm^{-1} or less, in general agreement with the experimental observations. The change in electric field can be thought of as adding an extra inhomogeneity into the system, thus randomly oriented solvent molecules, would not show an overall shift but only a broadening of the C≡N stretch band. The experimental red-shift thus indicates a degree of alignment between the chromophore and solvent molecules. Polarization-sensitive VSE experiments also suggest that the dye and NaSCN molecules are somewhat aligned. Finally, our simple ab-initio model highlights one of the main advantages of dynamic VSE spectroscopy, namely the ability to semi-quantitatively predict the Stark shifts from first principles. The Stark map can be further combined with classical dynamics simulations to

test the intermolecular interactions and underlying nonequilibrium dynamics that give rise to the observed spectra.

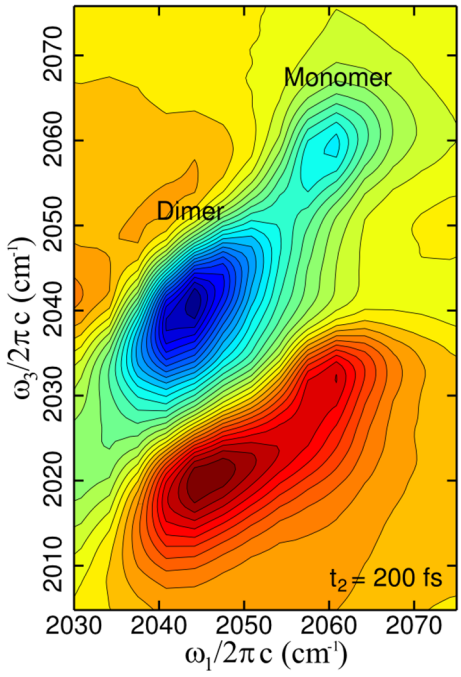

Figure 4.3: Absorptive two-dimensional infrared spectrum of NaSCN in the C≡N stretching region.

In general, the time evolution of the Stark lineshapes reports on the excited-state dynamics of the chromophore/solvent system and can be related to more traditional solvation measurements such as transient absorption or dynamic Stokes shifts. The amplitude of the Stark spectra immediately following photoexcitation (Figure 4.2) shows a single exponential decay with a time-constant of 2.1±0.5 ps^{-1}. The decay can be attributed to the back electron transfer (bET) reaction that returns Betaine-30 to its ground-state electronic configuration. In full agreement with our results, transient absorption measurements also suggested a bET rate of <5 ps^{-1} in polar solvents.[20, 23, 24] Orientational relaxation and vibrational energy transfer to the solvent may also contribute to the signal decay but these processes are generally slower as discussed next. To minimize the contributions from these processes only the short-delay data (<4ps) was analyzed. Future experiments will be aimed at probing both the impulsive and the diffusive solvent orientational contributions to the overall solvation of the charge-transfer state.

Equilibrium Vibrational Structure of NaSCN

In semi-polar solvents, such as ethyl acetate or tetrahydrofuran, sodium thiocyanate exists as an equilibrium mixture of two different species: contact-pair monomers $Na^+[NCS]^-$, and contact-pair dimers $(Na^+[NCS]^-)_2$ with C≡N stretch fundamentals centered at 2056 and 2043 cm^{-1} respectively.[25] The 2DIR spectrum (Figure 4.3) shows two negative peaks along the ($\omega_1 = \omega_3$) diagonal with the corresponding red-shifted anharmonic peaks. The diagonal peaks correspond to the vibrational transition from the ground to the first excited state (ω_{01}), whereas the anharmonic peaks involve transitions between the first and second excited states (ω_{21}). Interestingly, the vibrational anharmonicities ($\Delta = \omega_{01} - \omega_{21}$) of the monomers ($\Delta = 28$ cm^{-1}) and dimers ($\Delta = 20$ cm^{-1}) are very different. This result is consistent to the anharmonicity of other excitonic monomer/dimer systems such as acetic acid where the anharmonicity of the dimer is smaller than that of the monomer.[26] The absence of cross peaks between the two species indicates that chemical exchange occurs on a slower timescale than the experiment. The 2D spectrum also exhibits elongation along the diagonal, indicating a degree of inhomogeneous broadening attributable to microscopically distinct, though constantly fluctuating, environments. This inhomogeneity is responsible for the temporal shift in the maximum of the photon echo signal used to probe the non-equilibrium charge transfer.

The photon echo spectrum is the square of the projection of the 2DIR spectrum along the detection axis ω_3. Due to the spectral overlap between the anharmonicities and fundamentals of the two species, the peaks are not resolved in the transient-echo measurements as shown in the main text. Because 2DIR spreads the spectral information onto two frequency axes, the NaSCN peaks are cleanly resolved in the two-dimensional spectra. Clearly there would be considerably more spectral detail in a transient 2D spectrum, but the changes in the spectral amplitude due to the charge transfer-induced Stark shift are very small and will require substantial increases in sensitivity to extract using transient 2D spectroscopy.

Interpretation of Vibrational Stark-Effect Data

The interpretation of the VSE data along with the theoretical model is based on the observations listed below. Based on the experimental data available we believe that all these statements are correct and we discuss each one in more detail below. *1*. NaSCN forms a single solvation shell around Betaine-30 consisting of only a few molecules. *2*. There is a certain degree of alignment of the NaSCN molecules relative to the dye. *3*. The observed lineshapes are due to a Stark shift of the C≡N stretch upon excitation of the dye. *4*. Vibrational cooling does not play a significant role in the lineshapes or the observed dynamics. *5*. Diffusive orientational relaxation does not occur on the timescale of the experiment.

NaSCN Solvation of Betaine-30

Betaine-30 exhibits negative solvatochromic behavior—the absorption maximum of the lowest excited state shifts to shorter wavelengths with increasing solvent polarity. In pure ethyl acetate, the absorption maximum appears at 738 nm, and upon addition of NaSCN (50 mM) the maximum shifts to 580 nm. Using the ET-30 solvatochromic scale,[10] the polarity of the NaSCN solvation environment is measured to be 49.3 kcal/mol, similar to that of that of pure butanol (49.7 kcal/mol). The relative permittivity of pure ethyl acetate is 6.08, and that of butanol is 17.84,[27] indicating that the NaSCN solvation environment is significantly more polar than the supporting solvent. Interestingly, the polarity of pure molten salts, as measured using the ET-30 scale,[28] ranges between 40 and 60 kcal/mol indicating that the NaSCN contact pair solvation environment may have a similar polarity as pure molten NaSCN. Typical NaSCN and Betaine-30 concentrations used for the present experiments are ~50 mM and ~2 mM respectively, giving a mole-ratio of 25:1. Naturally, NaSCN molecules in the first solvation shell of Betaine-30 and those in the bulk solvent should be expected to be in chemical equilibrium. As described above, we estimate the number of molecules of NaSCN responding to excitation of a single Betaine-30 molecule to be approximately between 1 and 10, consistent with the idea of a single NaSCN solvation shell around the dye.

Structure of the Betaine-30/NaSCN

Figure 4.2 shows that the induced signal is red-shifted with respect to the bleach. This indicates a certain degree of alignment between the NaSCN molecules and the change in electric field. If the molecules were randomly aligned, no net shift would be observed. Our vibrational Stark-effect (VSE) measurements (Figure 4.2) only probed time delays up to 4 ps after excitation. In general the solvent response involves a fast inertial reorientation and a much longer "diffusive" relaxation.[29, 30] Interestingly, the bleach signal is centered at 2060 cm^{-1} suggesting that most of the NaSCN near Betaine-30 are contact-pair monomers. This is consistent with previous studies that suggest in polar environments the contact-pair monomers are favored over the dimers.[25]

To further elucidate the structure and dynamics of the Betaine-30/NaSCN complex, we measured the anisotropy of the Stark signal by rotating the polarization of the visible pump pulses with respect to the three infrared pulses. The overall lineshape of the Stark signal is preserved under the two different polarization conditions but the amplitude of the signal at 0.5 ps after excitation is 40% smaller in the perpendicular polarization geometry with respect to the parallel geometry. The signal decay under the two polarization conditions is very similar (~2 ps^{-1}) but we were not able to differentiate the two decay constants due to the intrinsically low signal to noise ratio in the data. The anisotropy data along with the red-shift of the VSE signal provide substantial evidence that in our case the relative orientation between Betaine-30 and NaSCN seems to be somewhat rigid, but without the aid of dynamics simulations the actual angle between the transition dipole vectors of Betaine-30 and NaSCN is difficult to determine as the tensor representing the local changes in electric field may not necessarily coincide with the changes in overall dipole of the molecule.

Orientational Dynamics and Energy Transfer

Our vibrational Stark-effect (VSE) measurements (Figure 4.2) only probed time delays up to 4 ps after excitation. In general the solvent response involves a fast inertial reorientation and a much longer "diffusive" relaxation.[29, 30] The equilibrium diffusive orientational relaxation of magnesium thiocyanate in water was recently measured to be ~40 ps[31], suggesting that this process remains significantly slower than the timescale of our experiments. The time dependence of the VSE spectrum collected at different polarization geometries should provide information on the nonequilibrium orientational dynamics of the

NaSCN molecules in the first solvation shell as they respond to the change in electrostatic environment.

Finally, the back electron transfer (bET) process deposits a large amount of energy into the Franck-Condon active modes of Betaine-30. This excess energy is then distributed among the low-frequency modes of the dye by vibrational relaxation before finally being transferred to the first solvation shell. We expect that this process should also have an effect our vibrational Stark spectrum. Thermalization within the intramolecular degrees of freedom of Betaine-30 occurs in the ~10 ps range.[32] Because energy transfer to the solvent is expected to be slower, especially when there is no available resonant transfer pathway, this process should not contribute significantly to the initial decay of the VSE signal (~2 ps).

4.4 Conclusion

In conclusion, the vibrational Stark-effect measurements demonstrated here have the potential to elucidate nonequilibrium dynamics in charge-transfer processes where a clean separation of system and bath consisting of molecule and solvent may not be applicable because the solvent fluctuations guide the reaction which in turn causes a further response in the solvent. This general method may be used to characterize charge-transfer reactions from the solvent's perspective in many chemical and biological processes. Dynamic modeling methods should provide a microscopic interpretation of the observed Stark lineshapes.

References

1. P. J. Rossky and J. D. Simon, "Dynamics of Chemical Processes in Polar-Solvents," Nature 370(6487), 263-269 (1994).

2. P. Barbara, T. Meyer, and M. Ratner, "Contemporary issues in electron transfer research," Journal of Physical Chemistry 100(31), 13148-13168 (1996).

3. S. G. Boxer, "Stark Realities," Journal of Physical Chemistry B 113(10), 2972-2983 (2009).

4. I. T. Suydam and S. G. Boxer, "Vibrational Stark effects calibrate the sensitivity of vibrational probes for electric fields in proteins," Biochemistry 42(41), 12050-12055 (2003).

5. S. H. Brewer and S. Franzen, "A quantitative theory and computational approach for the vibrational Stark effect," Journal of Chemical Physics 119(2), 851-858 (2003).

6. A. M. Moran, S. Park, and N. F. Scherer, "Polarizability response spectroscopy: Formalism and simulation of ultrafast dynamics in solvation," Chemical Physics 341(1-3), 344-356 (2007).

7. S. J. Schmidtke, D. F. Underwood, and D. A. Blank, "Following the solvent directly during ultrafast excited state proton transfer," Journal of the American Chemical Society 126(28), 8620-8621 (2004).

8. S. J. Schmidtke, D. F. Underwood, and D. A. Blank, "Probing excited-state dynamics and intramolecular proton transfer in 1-acylaminoanthraquinones via the intermolecular solvent response," Journal of Physical Chemistry A 109(32), 7033-7045 (2005).

9. T. Q. Lian, Y. Kholodenko, and R. M. Hochstrasser, "Infrared Probe of the Solvent Response to Ultrafast Solvation Processes," Journal of Physical Chemistry 99(9), 2546-2551 (1995).

10. C. Reichardt, "Solvatochromic Dyes as Solvent Polarity Indicators," Chemical Reviews 94(8), 2319-2358 (1994).

11. M. J. Nee, R. McCanne, K. J. Kubarych, and M. Joffre, "Two-dimensional infrared spectroscopy detected by chirped pulse upconversion," Optics Letters 32(6), 713-715 (2007).

12. C. R. Baiz, R. McCanne, and K. J. Kubarych, "Structurally Selective Geminate Rebinding Dynamics of Solvent-Caged Radicals Studied with Nonequilibrium Infrared Echo Spectroscopy," Journal of the American Chemical Society 131(38), 13590-13591 (2009).

13. C. Baiz, M. Nee, R. McCanne, and K. Kubarych, "Ultrafast nonequilibrium Fourier-transform two-dimensional infrared spectroscopy," Optics Letters 33(21), 2533-2535 (2008).

14. J. M. Anna, M. J. Nee, C. R. Baiz, R. McCanne, and K. J. Kubarych, "Measuring absorptive two-dimensional infrared spectra using chirped-pulse upconversion detection," Journal of the Optical Society of America B 27(3), 382-393 (2010).

15. C. R. Baiz, R. McCanne, and K. J. Kubarych, "Transient vibrational echo versus transient absorption spectroscopy: A direct experimental and theoretical comparison" Applied Spectroscopy, 64(9) 1037 (2010).

16. M. J. Frisch, G. W. Trucks , H. B. Schlegel , G. E. Scuseria , M. A. Robb, J. R. Cheeseman, J. A. Montgomery Jr., T. Vreven, K. N. Kudin, J. C. Burant, J. M. Millam, S. S. Iyengar, J. Tomasi, V. Barone, B. Mennucci, M. Cossi, G. Scalmani, N. Rega , G. A. Petersson , H. Nakatsuji , M. Hada , M. Ehara , K. Toyota , R. Fukuda , J. Hasegawa , M. Ishida , T. Nakajima , Y. Honda , O. Kitao , H. Nakai , M. Klene , J. E. X. Li , H. P. Knox , Hratchian , J. B. Cross , V. Bakken , C. Adamo , J. Jaramillo , R. Gomperts , R. E. Stratmann , O. Yazyev , A. J. Austin , R. Cammi , C. Pomelli , J. W. Ochterski , P. Y. Ayala , K. Morokuma , G. A. Voth , P. Salvador , J. J. Dannenberg , V. G. Zakrzewski , S. Dapprich , A. D. Daniels , M. C. Strain , O.

Farkas , D. K. Malick , A. D. Rabuck , K. Raghavachari , J. B. Foresman , J. V. Ortiz , Q. Cui , A. G. Baboul , S. Clifford , J. Cioslowski , B. B. Stefanov , G. Liu , A. Liashenko , P. Piskorz , I. Komaromi , R. L. Martin , D. J. Fox , T. Keith , M. A. Al-Laham , C. Y. Peng , A. Nanayakkara , M. Challacombe , P. M. W. Gill , B. Johnson , W. Chen , M. W. Wong , C. Gonzalez , and J. A. Pople, Gaussian 03, Gaussian, Inc., Wallingford CT, 2004.

17. M. Connolly, "Solvent-accessible surfaces of proteins and nucleic acids," Science 221(4612), 709-713 (1983).

18. L. Schrödinger, The PyMOL Molecular Graphics System, Version 1.2r1, 2010.

19. S. R. Mente and M. Maroncelli, "Computer simulations of the solvatochromism of betaine-30," Journal of Physical Chemistry B 103(36), 7704-7719 (1999).

20. S. A. Kovalenko, N. Eilers-Konig, T. A. Senyushkina, and N. P. Ernsting, "Charge transfer and solvation of betaine-30 in polar solvents - A femtosecond broadband transient absorption study," Journal of Physical Chemistry A 105(20), 4834-4843 (2001).

21. V. Kharlanov and W. Rettig, "Experimental and Theoretical Study of Excited-State Structure and Relaxation Processes of Betaine-30 and of Pyridinium Model Compounds," Journal of Physical Chemistry A 113(40), 10693-10703 (2009).

22. T. Ishida and P. J. Rossky, "Consequences of strong coupling between solvation and electronic structure in the excited state of a betaine dye," Journal of Physical Chemistry B 112(36), 11353-11360 (2008).

23. G. C. Walker, E. Akesson, A. E. Johnson, N. E. Levinger, and P. F. Barbara, "Interplay of Solvent Motion and Vibrational-Excitation in Electron-Transfer Kinetics - Experiment and Theory," Journal of Physical Chemistry 96(9), 3728-3736 (1992).

24. M. C. Beard, G. M. Turner, and C. A. Schmuttenmaer, "Measuring intramolecular charge transfer via coherent generation of THz radiation," Journal of Physical Chemistry A 106(6), 878-883 (2002).

25. P. Firman, M. Xu, E. M. Eyring, and S. Petrucci, "Thermodynamics of Dimerization of Nascn in Some Acyclic Polyethers Studied by Infrared-Spectroscopy," Journal of Physical Chemistry 96(21), 8631-8639 (1992).

26. M. Lim and R. M. Hochstrasser, "Unusual vibrational dynamics of the acetic acid dimer," Journal of Chemical Physics 115(16), 7629-7643 (2001).

27. D. R. Lide, CRC handbook of chemistry and physics: A ready-reference book of chemical and physical data (CRC press, 2004).

28. W. B. Harrod and N. J. Pienta, "Solvent polarity scales. 1. Determination of ET-30 and pi* values for phosphonium and ammonium melts," Journal of Physical Organic Chemistry 3(8), 534-544 (1990).

29. M. Maroncelli, "Computer simulations of solvation dynamics in acetonitrile," The Journal of Chemical Physics 94(3), 2084-2103 (1991).

30. M. Maroncelli, "The dynamics of solvation in polar liquids," Journal of Molecular Liquids 57, 1-37 (1993).

31. S. Park, M. Ji, and K. J. Gaffney, "Ligand Exchange Dynamics in Aqueous Solution Studied with 2DIR Spectroscopy," The Journal of Physical Chemistry B 114(19), 6693-6702 (2010).

32. W. Werncke, S. Wachsmann-Hogiu, J. Dreyer, A. I. Vodchits, and T. Elsaesser, "Ultrafast Intramolecular Electron Transfer Studied by Picosecond and Stationary Raman Spectroscopy," Bulletin of the Chemical Society of Japan 75(5), 1049-1055 (2002).

Chapter 5

Anharmonic Vibrational Structure of Metal Carbonyls: Ab-initio models

The work presented in this chapter has been published in the following paper:

1. C.R. Baiz, P.L. McRobbie, N.K. Preketes, K.J. Kubarych, and E. Geva, "Two-dimensional infrared spectroscopy of dimanganese decacarbonyl and its photoproducts: An *ab-initio* study", Journal of Physical Chemistry A, **113**(35), 9617-9623, (2009).

5.1 Introduction

Over the last decade, two-dimensional infrared (2DIR) spectroscopy has established itself as a powerful probe of molecular structure and dynamics.[1-3] Structural information is typically obtained from the spectral peak positions and intensities, while dynamical information can be obtained from the lineshapes and the dependence of the 2D spectra on the waiting time between the pump and the probe pulses. The recent introduction of nonequilibrium 2DIR spectroscopy has also made it possible to use 2DIR spectroscopy in order to probe nonequilibrium dynamics triggered by electronic photoexcitation.[4-6]

Metal-carbonyl complexes have proven to be useful benchmark systems for 2DIR spectroscopy.[7-11] In particular, the measurement and analysis of the 2DIR spectrum of the coupled symmetrical and anti-symmetrical carbonyl stretch modes in $Rh(CO)_2C_5H_7O_2$ (RDC) have led to many important insights regarding how anharmonicity, mode-mode coupling, the tensorial nature of optical response and rotational relaxation affect 2DIR

spectra.[12-14] The interpretation of the spectra relied originally on simple models with empirically fitted parameters. Such an intuitive approach is tractable in a system like RDC because it can be modeled in terms of only two coupled anharmonic modes and using a relatively small number of empirical parameters. However, the empirical nature of the models employed and the fact that they relied on uncontrollable approximations made it desirable to develop a more general *ab initio* modeling approach. Indeed, an *ab initio* approach to modeling 2DIR spectra , which relies on input obtained from electronic structure calculations has been recently demonstrated with considerable success on several polyatomic systems, including RDC.[11, 15-21] More specifically, Moran and coworkers[11] have recently produced a 2DIR spectrum of RDC by computing the two-dimensional anharmonic potential energy surface in terms of the carbonyl stretch coordinates up to fourth-order via DFT and numerically diagonalizing the corresponding Hamiltonian. The computed 2DIR spectrum was found to be in reasonable agreement with the experimental one obtained by Tokmakoff and co-workers.[7, 10] Most importantly, their work has revealed that fourth-order force constants can have a significant effect on the spectral features, even though the experimental 2DIR spectrum was originally fit to a model that ignored them. While the empirical and theoretical approaches mentioned above appear to be adequate for a small system like RDC they become impractical as the size of the system is increased. More specifically, in a system like $Mn_2(CO)_{10}$ one would need to employ hundreds of fitting parameters and the resulting parameter set is not likely to be unique. It should also be noted that the effective dimensionality of the system may not be determined by the number of IR active modes since IR-inactive modes may also affect the spectra if they are strongly coupled to the IR-active ones.

In this chapter we present an *ab initio* approach for calculating 2DIR spectra of the carbonyl stretch modes in $Mn_2(CO)_{10}$ and its photoproducts $Mn(CO)_5$ and $Mn_2(CO)_9$ (see Figure 5.1). The choice of system is motivated by the availability of equilibrium 2DIR spectra for $Mn_2(CO)_{10}$ and the difficulty of measuring the equilibrium 2DIR spectra of its relatively unstable photoproducts. It should be noted that with 10 (4 active and 6 inactive), 5 (3 active and 2 inactive) and 9 (all active) highly delocalized CO stretch modes in $Mn_2(CO)_{10}$, $Mn(CO)_5$ and $Mn_2(CO)_9$, respectively, this system is considerably more challenging than RDC (which only involve 2 active modes).

The UV photolysis of $Mn_2(CO)_{10}$ has been extensively studied, both theoretically[22-29] and experimentally, in the gas phase,[30-32] liquid solution[33-39] and low-temperature matrices.[40-43] It is well established that the two primary photochemical events that take place are: (1) Homolytic cleavage of the Mn-Mn bond to form the square pyramidal $Mn(CO)_5$; (2) CO ligand dissociation to form $Mn_2(CO)_9$ whose structure involves a bridging carbonyl across the Mn-Mn bond. The fact that $Mn_2(CO)_{10}$, $Mn(CO)_5$ and $Mn_2(CO)_9$ have distinctly different IR spectra has turned time-resolved IR spectroscopy into a powerful tool for studying photodissociation in this system.[37] The photodissociation reaction is believed to involve a singlet-singlet $\sigma_{Mn-Mn} \rightarrow \sigma^*_{Mn-Mn}$ and $3d_{Mn} \rightarrow \sigma^*_{Mn-Mn}$ photoexcitations, followed by inter-system crossing to the corresponding dissociative triplet states.[28] The calculation of the equilibrium 2DIR spectra of $Mn_2(CO)_{10}$, $Mn(CO)_5$ and $Mn_2(CO)_9$ therefore constitutes an important first step towards understanding the spectral signature of the photodissociation process as measured via optical-pump/2DIR-probe techniques. The main challenges involved in computing the 2DIR spectra of $Mn_2(CO)_{10}$ and its photoproducts include: (1) The small spectral shifts that require high accuracy in order to be resolved, (2) The relatively large number of CO stretches; (3) The fact that the state-to-state transition dipole moments are oriented along different directions, which makes it necessary to account for the tensorial nature of optical response; (4) The relatively strong coupling between the active and inactive CO stretch modes.

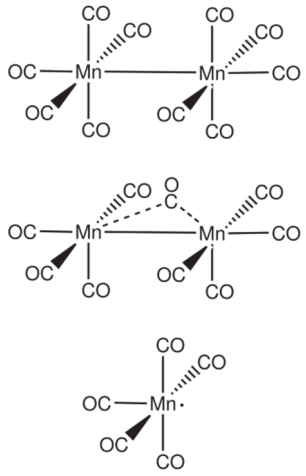

Figure 5.1: Chemical structure of dimanganese decacarbonyl [$Mn_2(CO)_{10}$] and two photoproducts dimanganese nonacarbonyl [$Mn_2(CO)_9$] and manganese pentacarbonyl [$Mn(CO)_5$].

Normal-Mode Anharmonic Vibrational Hamiltonian

The anharmonic Hamiltonian up to fourth-order in terms of the normal mode coordinates is given by:

$$H = \tfrac{1}{2}\sum_i \phi_{ii}(q_i^2 + p_i^2) + \tfrac{1}{6}\sum_{ijk}\phi_{ijk}q_i q_j q_k + \tfrac{1}{24}\sum_{ijkk}\phi_{ijkk}q_i q_j q_k^2 \quad (1)$$

Third-order force constants, ϕ_{ijk}, and semi-diagonal fourth-order force constants, ϕ_{ijkk}, were calculated in terms of the normal-mode coordinates via a finite displacement method [44, 45] Off-diagonal fourth-order force constants of the type ϕ_{ijkl} have been observed to lead to very small shifts of the energy levels (~1 cm^{-1}) and are therefore neglected.[46] More specifically, the second derivatives of the potential energy with respect to the normal mode coordinates $\phi_{ij} = \partial^2 U / \partial q_i \partial q_j$ were calculated at the equilibrium geometry, as well as at geometries slightly displaced relative to it. The displaced configurations were obtained by shifting the atoms relative to their equilibrium positions along all 3N-6 normal-mode coordinates in the positive and negative directions. For a given displacement Δq_k along *k-th* mode coordinate, the third-order force constant is given by:

$$\phi_{ijk} = \left[\frac{\partial^3 U}{\partial q_i \partial q_j \partial q_k}\right]_{\mathbf{q}=0} = \frac{\phi_{ij}^{+} - \phi_{ij}^{-}}{2\Delta q_k} \quad (2)$$

Where ϕ_{ij}^{+} and ϕ_{ij}^{-} represent the second-order force constants at the positively and negatively displaced geometries respectively. Similarly, the semi-diagonal fourth-order force constants are given by:

$$\phi_{ijkk} = \left[\frac{\partial^4 U}{\partial q_i \partial q_j \partial q_k^2}\right]_{\mathbf{q}=0} = \frac{\phi_{ij}^{+} + \phi_{ij}^{-} - 2\phi_{ij}^{0}}{2(\Delta q_k)^2} \quad (3)$$

Where $\phi_{ij}^{0} \equiv \phi_{ii}^{0}\delta(i,j)$ is the second-order constant at the equilibrium geometry. The most straightforward approach to obtaining the stationary wavefunctions and energy levels of the Hamiltonian in Eq. (1) associated with the fundamental and overtone transitions is by direct

diagonalizion. This approach works well for a system where the number of modes of interest is small, such as RDC. However, since the size of the Hamiltonian matrix grows exponentially with respect to the number of modes, direct diagonalization becomes unfeasible for a system with more than a few modes. One way of avoiding direct diagonalization is by using second-order vibrational-perturbation theory (VPT2) which is based on using the harmonic stationary states and energy levels as the zero order approximation and assuming that the anharmonicities can be treated as small perturbations.[47-50] Assuming that the harmonic transition dipole moments are sufficiently accurate, one can combine them with the anharmonic transition frequencies obtained via VPT2, thereby giving rise to a feasible route for computing spectra of systems like $Mn_2(CO)_{10}$ that have a large number of modes.

Ab-initio Methods

Molecular geometries were optimized with DFT. The choices of density functional and basis sets were guided by previously reported calculations of anharmonic vibrational frequencies in small molecules.[50-52] The results reported in the present study were obtained using Becke's 1988 exchange functional[53] and Perdew's 1986 correlation functional[54] (BP86) with a LanL2DZ pseudopotential[55] basis on Manganese and 6-31G(d) basis on the Carbon and Oxygen atoms. This particular choice of density functionals and basis sets was found to give the best agreement with experiment, such that the computed frequencies are within ~1% of the experimental values (see Table 5.1). We have also found that a tight optimization threshold was required in order to obtain reliable third- and fourth-order force constants. Thus, optimization convergences needed to be set to 10^{-6} hartrees/bohr of maximum gradient and the SCF convergence to 10^{-10} hartrees. Frequency analyses were carried out at the equilibrium and 6N-11 displaced geometries. All Cartesian geometry optimizations and second-derivative matrix computations were carried out using Q-Chem 3.1.[56]

The displacement along the normal modes, Δq, was set to 0.03, after tests indicated that the force constants are independent of the displacement for values between 0.01-0.03. It should be noted that the displacement should be small enough so that higher order terms do not contribute significantly, yet large enough so as to minimize numerical errors arising from the SCF procedure. It is also important to emphasize that although the harmonic frequencies

may contain systematic errors that arise from using DFT, it is reasonable to expect these errors to be the same at the equilibrium and displaced configurations and therefore to cancel out and yield accurate third- and fourth-order force constants. [57]

Anharmonic energy levels were computed via the standard VPT2 method using the full set (third- and fourth-order) of force constants. The VPT2 calculation was also repeated using subsets of the force constants, in order to investigate the importance of contributions from fourth-order force constants relative to those from third-order ones, and the importance of contributions from photoactive modes relative to photoinactive ones. It should be pointed out that the VPT2 anharmonic method is currently implemented in many popular electronic structure packages. However, these packages will only perform the perturbation using the full set of force constants. Thus, applying VPT2 to models involving subsets of the force constants and modes require us to write our own code.

For the sake of benchmarking, it was desirable to compare the VPT2 results to results obtained via direct diagonalization. To this end, we have computed anharmonic energy levels and wavefunctions for all five CO stretches of $Mn(CO)_5$ obtained using the full vibrational Hamiltonian. Using this procedure, it was necessary to increase the size of the harmonic basis until convergence of the anharmonic energy levels was reached. For example, in the case of $Mn(CO)_5$ the number of basis functions per mode needed to converge the first- and second-excited energy levels is 7; with a total of $7^5 = 16807$ basis functions. To minimize memory requirements the Hamiltonian was stored as a sparse matrix and the lowest 30 eigenvalues and eigenvectors were computed iteratively via the Arnoldi method as implemented in the ARPACK subroutine library.[58] Note that this iterative method is equivalent to numerically diagonalizing the Hamitonian matrix, thus in the following section we use both terms interchangeably.

5.2 Results and Discussion

In Table 5.1 we present a comparison of the harmonic and VPT2-based anharmonic fundamental frequencies with the corresponding experimental values for $Mn_2(CO)_{10}$, $Mn(CO)_5$ and $Mn_2(CO)_9$. The harmonic frequencies are found to be in good agreement with the experimental values for all three molecules. The anharmonic frequencies are shifted down by ~10-60 cm^{-1} below the experimental values and do not preserve the relative

ordering of the frequencies. This behavior of DFT/VPT2 has been previously observed in other molecules[50, 59] and can be attributed to Fermi or other type of resonances between the carbonyl modes and low-frequency modes or inaccuracies brought about by the use of DFT as well as the fact that such effects as solvent shifts have not been accounted for. In the case of our metal carbonyl molecules, the CO modes are isolated in frequency and the coupling to the lower frequency modes is small, therefore we avoid errors arising from Fermi resonances by performing the perturbation on the CO modes only. This approach, however may not work in other systems where the modes may be more highly coupled and not as well isolated in frequency. Nevertheless, as we will see below, the actual values of the anharmonic shifts, rather than the absolute value of the fundamental frequencies, are still reproduced rather well with this approach when using the full set of force constants. One may, therefore, adopt a strategy that combines the *harmonic* fundamental frequencies, which happen to be in excellent agreement with experiment, with *anharmonic* shifts obtained via VPT2.

Table 5.1: Experimental, harmonic, and anharmonic (via VPT2) fundamental transition frequencies for $Mn_2(CO)_{10}$ and its photoproducts (in cm^{-1}). The experimental frequencies were obtained from: a. Raman scattering in light petroleum,[60] b. FTIR in n-hexane, c. transient absorption in cyclohexane ,[30] d. transient absorption in cyclohexane.[37]

	$Mn_2(CO)_{10}$			$Mn_2(CO)_9$			$Mn(CO)_5$		
Mode	**Exp.**	**Harmonic**	**VPT2**	**Exp.**	**Harmonic**	**VPT2**	**Exp.**	**Harmonic**	**VPT2**
1	1981[a]	1972.5	1912.2	1760[c]	1786.9	1752.9	--	1981.1	1952.5
2	1981[a]	1972.5	1909.9	1966[c]	1968.8	1934.3	1982[d]	1985.6	1956.9
3	1983[b]	1980.6	1964.1	--	1979.2	1949.2	1982[d]	1985.6	1956.1
4	1997[a]	1990.7	1985.5	1994[c]	1987.5	1839.7	--	2000.5	1970.6
5	2014[b]	2004.8	1939.6	2006[c]	1994.5	1984.1	--	2080.0	2047.9
6	2014[b]	2004.9	1937.4	--	2007.6	1974.8			
7	2024[a]	2005.6	1960.3	2020[c]	2008.4	1979.0			
8	2024[a]	2008.6	1921.4	2058[c]	2040.1	1993.8			
9	2044[b]	2035.6	1993.6	--	2085.6	2044.3			
10	2116[a]	2097.0	2039.4						

In Table 5.2 we report the diagonal anharmonic shifts obtained for $Mn_2(CO)_{10}$ via VPT2. The entries in the second and third columns of this table correspond to the anharmonic shifts obtained by applying VPT2 to a model that includes all 3N-6 vibrational modes, using either only the third-order force constants or the third-order and fourth-order force constants, respectively. The fourth-order force constants are seen to affect the anharmonic shifts significantly. Similar results obtained for RDC by Moran *et al*[41] using a full

diagonalization of a two-mode Hamiltonian have also demonstrated the importance of including higher than third-order force constants. Thus, our results reinforce the view that the fact that an experimental 2DIR spectrum can be fitted to a model that only accounts for third-order anharmonicities, does not exclude the possibility that higher-order force constants are important, particularly in cases where *ab-initio* calculations suggest that this is the case.[7]

The fourth column of Table 5.2 shows the anharmonic shifts obtained by applying VPT2 to a model that only includes the ten CO stretch modes. The similarity between those results and the results obtained for an all-mode model (second column) indicates that the CO stretch modes are essentially decoupled from the other vibrational modes of the complex. This is not surprising since the CO stretch modes are largely isolated in frequency, so that coupling to other lower frequency

Table 5.2: The diagonal anharmonic shifts, $\Delta = \omega_{0\to1} - \omega_{1\to2}$ for $Mn_2(CO)_{10}$, in cm^{-1} , as obtained using VPT2. A positive anharmonic shift means that the excited-state absorption peak appears at lower frequency than the ground-state bleach. A comparison is made for frequencies where the perturbation includes all modes (columns 2 & 3), only CO modes (column 4), and only the IR active CO modes (column 5). The second and third columns also show the anharmonicities obtained by using third- and fourth order force constants and only the third-order force constants, respectively. Experimental values are obtained from fits to transient absorption spectra.

	All Modes		**CO Modes**	**IR Active CO Modes**	**Experimental.**
	3rd & 4th Order	**3rd Order Only**	**3rd & 4th Order**	**3rd & 4th Order**	
1	5.2	10.2	4.3	--	--
2	5.3	10.2	4.3	--	--
3	6.5	12.8	5.4	-6.3	8.3
4	9.7	19.1	8.0	--	--
5	5.5	10.3	4.5	-4.7	6.5
6	5.5	10.3	4.5	-4.7	6.5
7	3.9	7.4	3.0	--	--
8	4.6	7.6	3.7	--	--
9	3.2	5.3	2.5	-2.1	4.4
10	3.4	5.0	2.6	--	--

modes is expected to be weak compared to the coupling among these CO stretch modes. The fifth column of Table 5.2 shows the anharmonic shifts obtained by applying VPT2 to a model that only includes the four photoactive CO stretch modes. A comparison to the results in the fourth column clearly reveals that neglecting the coupling between the

photoactive and photoinactive CO stretch modes leads to qualitatively incorrect results. More specifically, the sign of the anharmonic shifts is reversed, so that the overtone frequencies become larger than the fundamental frequencies.

Comparison to the experimental results (column 6) reveal that a minimal model must include at least all ten CO stretches, whether photoactive or not, and account for anharmonic force constants at least up to fourth order. It is important to note that with such small anharmonic shifts, one cannot expect quantitative agreement with experiment. However, the fact that the trends and orders of magnitude are in reasonable agreement with experiment is quite encouraging.

The experimental 2DIR spectrum of $Mn_2(CO)_{10}$ has been analyzed in detail in a previous paper.[61] In brief, the spectrum shows three main peaks along the diagonal with cross peaks between all transitions. The three peaks correspond to four transitions at 1983, 2014, 2014 and 2045 cm^{-1} with B_2, E_1, E_1 and B_2 symmetry respectively. The transition dipole moments associated with the B modes are parallel to the Mn-Mn axis whereas those associated with the degenerate E-modes are oriented perpendicular to each other and to the Mn-Mn axis. The experimental techniques used to measure multidimensional IR spectra have been thoroughly documented elsewhere and are therefore not discussed here.[9, 61-63]

The absolute value rephasing 2DIR spectra in the zzzz polarization geometry are compared to the corresponding experimental spectra in Figure 5.2. The spectra were calculated using the VPT2-based anharmonic frequencies (fundamentals, overtones and combination states), computed using all third- and fourth-order force constants involving all 10 CO stretch modes. The harmonic transition dipole moments were used since excellent agreement is observed when comparing the computed and experimental linear absorption spectra. Optical response functions were calculated via SPECTRON,[64] within the framework of Redfield theory, using a phenomenological homogeneous width ($\Gamma = 2\ cm^{-1}$). The general qualitative agreement with experiment is satisfactory, considering the fact that no scaling factors were used. The two spectra show that, in the case of the absolute value rephasing 2DIR spectrum, the anharmonic peaks are buried underneath the fundamental peaks.

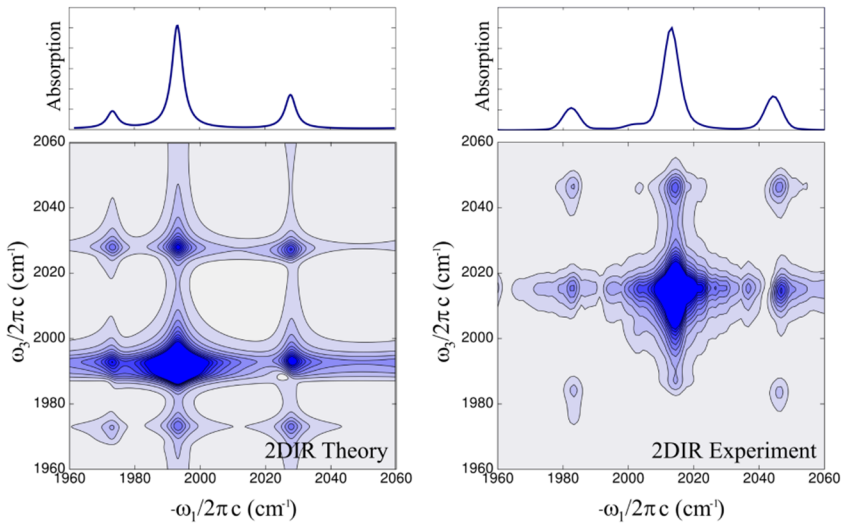

Figure 5.2: (left) Theoretical absorption (upper traces) and absolute-value rephasing 2DIR spectra of $Mn_2(CO)_{10}$ using the VPT2 frequencies (Table 5.2, column 4) and diagonal anharmonicities. No empirical frequency scaling is used. (right) Experimental absorption and Fourier-transform absolute-value rephasing 2DIR spectra of $Mn_2(CO)_{10}$ in cyclohexane measured in the zzzz polarization geometry at zero waiting time. Contours larger than 20% of the total amplitude are omitted for clarity.

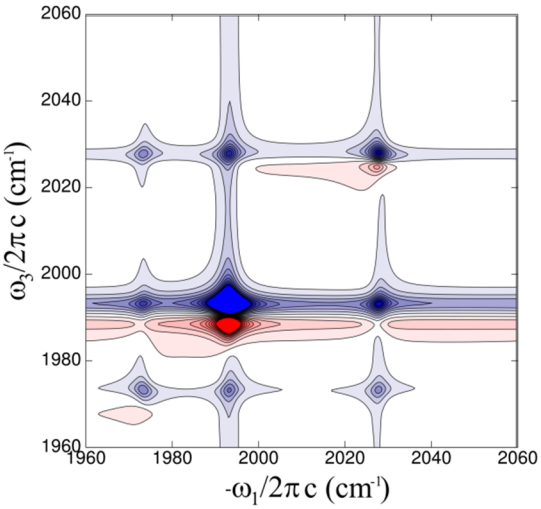

Figure 5.3: Theoretical absorptive 2DIR spectrum of $Mn_2(CO)_{10}$ at zero waiting time computed in the zzzz polarization geometry. Red contours correspond to positive peaks whereas negative contours represent negative peaks. Contours larger than 20% of the maximum amplitude are omitted.

The calculated absorptive 2DIR spectrum of $Mn_2(CO)_{10}$ is shown in Figure 5.3. In this case, it is predicted that the off-diagonal anharmonic peaks, which correspond to Liouiville paths that involve two-quantum combination states, would be resolved. It should

be noted that the additional peak present in the experimental absorption and absolute value rephasing 2DIR spectra at 2002 cm^{-1} is due to natural ^{13}C isotope present in the molecule.[62] A single ^{13}C substitution on an axial carbonyl splits the 2013 cm^{-1} mode into two modes centered at 2013 cm^{-1} and 2002 cm^{-1}. Hence cross peaks are observed in the 2DIR spectrum between these two diagonal transitions. Finally, Figure 5.2 also shows that the computed oscillator strengths are also in good agreement with experiment.

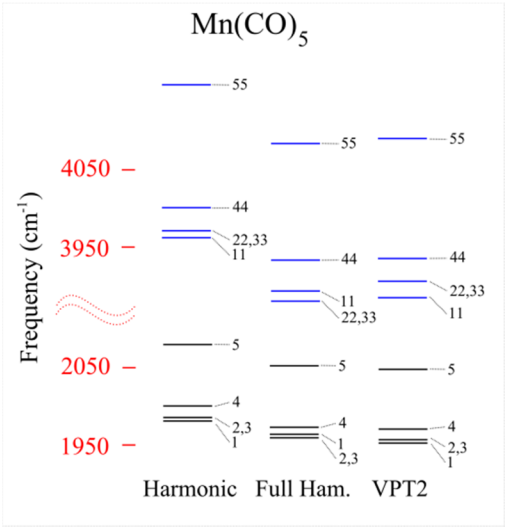

Figure 5.4: Comparison between the three methods for the one- and two-quanta energy levels of $[Mn(CO)_5]$. The energy levels represented in this diagram is also shown on Table 5.3.

Next, we compare the VPT2 results with results obtained via a direct diagonalization in the case of $Mn(CO)_5$ (see Table 5.3). Due to the computational expense involved in generating, storing and diagonalizing the vibrational Hamiltonian, it was not possible to perform a similar comparison in the cases of $Mn_2(CO)_{10}$ or $Mn_2(CO)_9$. The agreement between the frequencies obtained with VPT2 and numerical diagonalization validates the perturbation treatment. The second part of Table 5.3 shows the same comparison within a model that only includes the two degenerate photoactive CO stretch modes. Once again, the VPT2 and numerical diagonalization energy levels are observed to be in excellent agreement; both yielding negative anharmonic shifts. As discussed above, these negative anharmonicities are not qualitatively correct compared to experiment, however, the results show that VPT2 is still able to produce reliable frequencies, in comparison to numerical diagonalization using a reduced set of force constants. In addition, these observations once again underscore the

fact that all the strongly coupled modes— either photoactive or not—must be explicitly included in order to reproduce the experimental spectra.

Table 5.3: Comparison of the $Mn(CO)_5$ energy levels obtained by computation of the Hamiltonian eigenvalues (Full Ham.) and those obtained by VPT2. Fundamentals, overtones and a few selected combination (Comb.) bands are shown. The anharmonic shifts ($\Delta = \omega_{0\to 1} - \omega_{1\to 2}$) correspond to the difference between two-quantum transitions and twice the fundamental transitions. To simplify notation we denote the state by the number of excitations within each corresponding mode $|n_1 n_2 n_3 n_4 n_5\rangle \equiv n_i$ for singly excited states and $|n_1 n_2 n_3 n_4 n_5\rangle \equiv n_i n_j$ for doubly excited states ($i = j$ for overtones, $i \neq j$ for combination). For example, $1 = |10000\rangle$, $11 = |20000\rangle$, $34 = |00110\rangle$, etc. The information contained in the upper portion of this table is shown graphically as energy level diagrams in Figure 4.

$Mn(CO)_5$ - All CO Modes				
State (Harmonic)	**Full Ham.**		**VPT2**	
1 (1981.1)	1956.9		1952.5	
2 (1985.6)	1952.4		1956.9	
3 (1985.6)	1952.4		1956.1	
4 (2000.5)	1966.0		1970.6	
5 (2080.0)	2045.5		2047.9	
Overtones		**Δ**		**Δ**
11	3893.2	20.6	3884.6	20.4
22	3880.1	24.6	3905.8	8.0
33	3880.1	24.6	3904.2	8.0
44	3933.2	-1.1	3935.3	6.0
55	4084.0	7.0	4090.5	5.3
Comb.				
32	3876.6	28.2	3904.1	8.8
24	3883.4	35.0	3915.0	12.5
31	3912.9	-3.6	3907.7	0.9
41	3923.6	-0.6	3922.2	1.0
53	3987.3	10.6	3992.5	11.5
51	3994.2	8.3	3993.7	6.7
$Mn(CO)_5$ - IR Active Modes Only				
State	**Full Ham.**		**VPT2**	
2	1996.3		1999.8	
3	1996.3		1999.8	
Overtones		**Δ**		**Δ**
22	4001.6	-8.9	4008.8	-9.2
33	4003.1	-10.4	4008.7	-9.1
Comb.				
23	3994.2	-1.5	4009.6	-10.0

Table 5.4 shows the fundamental and diagonal overtone transition frequencies of the CO stretches in $Mn_2(CO)_9$ as obtained via VPT2. In the second and third column we show the results obtained based on a model that included all 3N-6 vibrational modes of the

molecule, while in the fourth and fifth columns we show results obtained based on a model that only included the 9 CO stretch modes. Interestingly, in this case the results of the two calculations are considerably different. In particular, in the large deviation by more than 100 cm^{-1} in the case of mode 4 is indicative of significant coupling between this CO stretch and lower frequency modes. The table also shows that the anharmonic shift of mode 1 (27.2 cm^{-1}), is larger than the rest. This can be attributed to the fact that this mode corresponds to the stretching of the bridging carbonyl, which is expected to be more anharmonic due to the fact that it is simultaneously bonded to both metal centers.

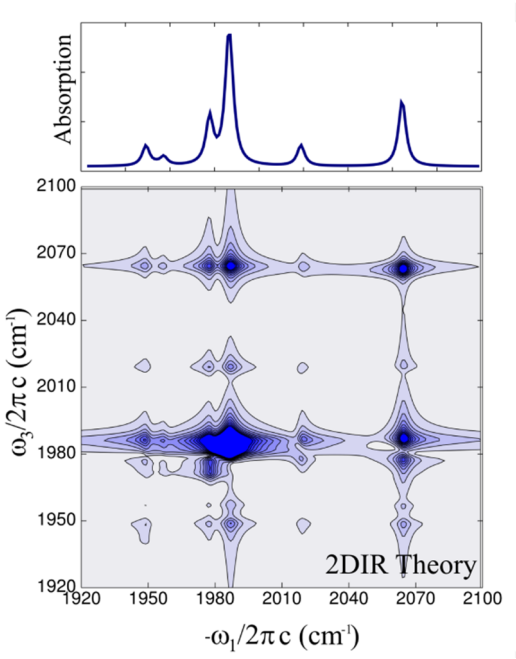

Figure 5.5: Theoretical absorption (upper trace) and absolute-value rephasing 2DIR spectra of $Mn_2(CO)_9$ at zero waiting time computed in the zzzz polarization geometry using the VPT2 anharmonic frequencies and harmonic transition dipole moments. Contours larger than 20% of the total amplitude are omitted for clarity.

Theoretical one-dimensional (1D) and 2D IR spectra of $Mn_2(CO)_9$ (zzzz polarization geometry) are shown in Figure 5.5. At present only a transient absorption spectrum of this species is available in the literature.[34] The harmonic and VPT2 frequencies for $Mn_2(CO)_9$, shown in Table 5.1, are in reasonable agreement with the experimental values. The measurement of nonequilibrium 2DIR spectra of $Mn_2(CO)_9$ is currently underway in our laboratory. Given the good agreement between experiment and theory in the case of

$Mn_2(CO)_{10}$ we expect that the computed spectrum for $Mn_2(CO)_9$ also provides a reliable depiction of the actual spectra of this species.

Table 5.4: VTP2 frequencies for $Mn_2(CO)_9$ in cm^{-1} along with overtones and anharmonic shifts $\Delta = 2\omega_{0\to1} - \omega_{1\to2}$ computed using the full set of force constants (all modes) and a reduced set of force constants involving only the carbonyl stretching modes.

	$Mn_2(CO)_9$ - VPT2 All Modes			**$Mn_2(CO)_9$ - VPT2 CO Modes Only**		
Mode (Harmonic)	**Fundamental**	**Overtone**	**Δ**	**Fundamental**	**Overtone**	**Δ**
1 (1786.9)	1752.9	3478.6	27.2	1769.8	3520.9	18.6
2 (1934.2)	1934.3	3857.0	11.6	1949.2	3888.9	9.5
3 (1979.2)	1949.2	3892.0	6.4	1957.2	3909.0	5.4
4 (1987.5)	1839.7	3665.2	14.2	1953.8	3895.9	11.8
5 (1994.5)	1984.1	3959.3	8.9	1977.8	3948.5	7.1
6 (2007.6)	1974.8	3943.8	5.9	1987.6	3970.4	4.8
7 (2008.4)	1979.0	3951.6	6.5	1986.4	3967.5	5.3
8 (2040.1)	1993.8	3983.8	3.8	2018.9	4034.8	2.9
9 (2085.6)	2044.3	4085.0	3.6	2064.4	4126.0	2.8

5.3 Conclusion and Outlook

In this study, we have explored the use of a methodology that combines ab-initio DFT (BP86/LanL2DZ) calculations with VPT2 in order to compute the experimentally relevant 1D and 2D spectra of $Mn_2(CO)_{10}$ and its photoproducts $Mn(CO)_5$ and $Mn_2(CO)_9$. We have demonstrated that predictive self-consistent treatment must account for higher than third-order anharmonic force constants and include all highly-coupled modes, regardless on weather or not they are photoactive. In the case of metal carbonyls, this modeling implied accounting for at least fourth-order anharmonic force constants and including at least all CO stretch modes. We have also demonstrated the accuracy of VPT2 by benchmarking it against results obtained via direct diagonalization in the case of $Mn(CO)_5$.

Further motivation for future modeling of $Mn(CO)_5$ arises from recent nonequilibrium 2DIR experiments which have provided evidence for solute-solvent complexes.[39] Solvent complexation may distort the molecular geometry causing the dark modes to become active; an effect which would be captured by the modeling methods presented here. These effects may be captured by using continuum solvent models in the electronic structure computations or by explicitly adding a small number of nearby solvent molecules to the solute. In addition, cross-peaks in 2DIR spectra are sensitive to vibrational

energy-transfer among the vibrational modes, which in turn is directly mediated by through-bond anharmonic coupling and spatial overlap of the wavefunctions.[65, 66] Since energy transfer may likely involve IR inactive modes, modeling of these energy relaxation measurements would require knowledge of all the coupling constants.

Finally, it should be noted that although fourth-order force constants impact 2DIR spectra, higher order nonlinear spectroscopies are expected to be even more sensitive to it. In this context, it is interesting to note that several fifth-order infrared experiments have been reported recently, either under equilibrium[67] or nonequilibrium conditions.[63, 68] As peak assignments are likely to be even more challenging in this case, one expects that electronic structure methods of the type described herein will prove useful for the interpretation of these experiments.

References

1. M. Cho, "Coherent Two-Dimensional Optical Spectroscopy," Chemical Reviews **108**, 1331-1418 (2008).

2. J. Zheng, K. Kwak, and M. Fayer, "Ultrafast 2D IR vibrational echo spectroscopy," Accounts of Chemical Research **40**(1), 75-83 (2007).

3. S. Mukamel, "Multidimensional Femtosecond Correlation Spectroscopies of Electronic and Vibrational Excitations," Annual Review of Physical Chemistry **51**(1), 691 (2000).

4. P. Hamm, J. Helbing, and J. Bredenbeck, "Two-dimensional infrared spectroscopy of photoswitchable peptides," Annual Review of Physical Chemistry **59**, 291-317 (2008).

5. C. Kolano, J. Helbing, M. Kozinski, W. Sander, and P. Hamm, "Watching hydrogen-bond dynamics in a beta-turn by transient two-dimensional infrared spectroscopy," Nature **444**(7118), 469-472 (2006).

6. E. R. Andresen and P. Hamm, "Site-Specific Difference 2D-IR Spectroscopy of Bacteriorhodopsin," The Journal of Physical Chemistry B **113**(18), 6520-6527 (2009).

7. M. Khalil, N. Demirdoven, and A. Tokmakoff, "Coherent 2D IR spectroscopy: Molecular structure and dynamics in solution," Journal of Physical Chemistry A **107**(27), 5258-5279 (2003).

8. K. A. Merchant, D. E. Thompson, and M. D. Fayer, "Two-Dimensional Time-Frequency Ultrafast Infrared Vibrational Echo Spectroscopy," Physical Review Letters **86**(17), 3899 (2001).

9. M. J. Nee, R. McCanne, K. J. Kubarych, and M. Joffre, "Two-dimensional infrared spectroscopy detected by chirped pulse upconversion," Optics Letters **32**(6), 713-715 (2007).

10. O. Golonzka, M. Khalil, N. Demirdoven, and A. Tokmakoff, "Coupling and orientation between anharmonic vibrations characterized with two-dimensional infrared vibrational echo spectroscopy," Journal of Chemical Physics **115**(23), 10814-10828 (2001).

11. A. M. Moran, J. Dreyer, and S. Mukamel, "Ab initio simulation of the two-dimensional vibrational spectrum of dicarbonylacetylacetonato rhodium(I)," Journal of Chemical Physics **118**(3), 1347-1355 (2003).

12. J. Sung and R. J. Silbey, "Four wave mixing spectroscopy for a multilevel system," Journal of Chemical Physics **115**(20), 9266-9287 (2001).

13. A. Tokmakoff, "Orientational correlation functions and polarization selectivity for nonlinear spectroscopy of isotropic media .1. Third order," Journal of Chemical Physics **105**(1), 1-12 (1996).

14. R. M. Hochstrasser, "Two-dimensional IR-spectroscopy: polarization anisotropy effects," Chemical Physics **266**(2-3), 273-284 (2001).

15. K. Heyne, N. Huse, J. Dreyer, E. T. J. Nibbering, T. Elsaesser, and S. Mukamel, "Coherent low-frequency motions of hydrogen bonded acetic acid dimers in the liquid phase," Journal of Chemical Physics **121**, 902-902 (2004).

16. T. Hayashi and S. Mukamel, "Multidimensional Infrared Signatures of Intramolecular Hydrogen Bonding in Malonaldehyde," Journal of Physical Chemistry A **107**(43), 9113-9131 (2003).

17. T. Hayashi, T. l. C. Jansen, W. Zhuang, and S. Mukamel, "Collective solvent coordinates for the infrared spectrum of HOD in D2O based on an ab initio electrostatic map," Journal of Physical Chemistry A **109**(1), 64 - 82-64 - 82 (2005).

18. J. Dreyer, "Density functional theory simulations of two-dimensional infrared spectra for hydrogen-bonded acetic acid dimers," International Journal of Quantum Chemistry **104**(5), 782-793 (2005).

19. K. Park, M. Cho, S. Hahn, and D. Kim, "Two-dimensional vibrational spectroscopy. II. Ab initio calculation of the coherent 2D infrared response function of CHCl[sub 3] and comparison with the 2D Raman response function," Journal of Chemical Physics **111**(9), 4131-4139 (1999).

20. J. Wang, "Ab Initio-Based All-Mode Two-Dimensional Infrared Spectroscopy of a Sugar Molecule," Journal of Physical Chemistry B **111**(31), 9193-9196 (2007).

21. K. Kwak, S. Cha, M. Cho, and J. C. Wright, "Vibrational interactions of acetonitrile: Doubly vibrationally resonant IR--IR--visible four-wave-mixing spectroscopy," Journal of Chemical Physics **117**(12), 5675-5687 (2002).

22. D. A. Brown, W. J. Chambers, Fitzpatr.Nj, and Rawlinso.Rm, "Molecular Orbital Theory of Organometallic Compounds .12. Nature of Metal-Metal Bonding in Some Binuclear Metal Carbonyls," Journal of the Chemical Society A -Inorganic Physical Theoretical (5), 720-& (1971).

23. M. Elian and R. Hoffmann, "Bonding Capabilities of Transition-Metal Carbonyl Fragments," Inorganic Chemistry **14**(5), 1058-1076 (1975).

24. H. Nakatsuji, M. Hada, and A. Kawashima, "Electronic-Structures of Dative Metal Metal Bonds - Abinitio Molecular-Orbital Calculations of (Oc)5os-M(Co)5 (M = W, Cr) in Comparison with (Oc)5m-M(Co)5 (M = Re, Mn)," Inorganic Chemistry **31**(10), 1740-1744 (1992).

25. E. Folga and T. Ziegler, "A Density-Functional Study on the Strength of the Metal Bonds in Co2(Co)8 and Mn2(Co)10 and the Metal Hydrogen and Metal-Carbon Bonds in R-Mn(Co)5 and R-Co(Co)4," Journal of the American Chemical Society **115**(12), 5169-5176 (1993).

26. A. Rosa, G. Ricciardi, E. J. Baerends, and D. J. Stufkens, "Density-Functional Study of Ground and Excited-States of Mn-2(Co)(10)," Inorganic Chemistry **34**(13), 3425-3432 (1995).

27. S. J. A. van Gisbergen, J. A. Groeneveld, A. Rosa, J. G. Snijders, and E. J. Baerends, "Excitation energies for transition metal compounds from time-dependent density functional theory. Applications to MnO4-, Ni(CO)(4), and Mn-2(CO)(10)," Journal of Physical Chemistry A **103**(34), 6835-6844 (1999).

28. O. Kuhn, M. R. D. Hachey, M. M. Rohmer, and C. Daniel, "A CASSCF/CASPT2 study of the low-lying excited states of Mn-2(CO)(10)," Chemical Physics Letters **322**(3-4), 199-206 (2000).

29. C. Daniel, "Electronic spectroscopy and photoreactivity in transition metal complexes," Coordination Chemistry Reviews **238**, 143-166 (2003).

30. T. A. Seder, S. P. Church, and E. Weitz, "Photodissociation pathways and recombination kinetics for gas-phase dimanganese decacarbonyl," Journal of the American Chemical Society **108**(24), 7518-7524 (1986).

31. A. Marquez, J. F. Sanz, M. Gelize, and A. Dargelos, "The Vacuum Ultraviolet-Spectrum of [Mn2(Co)10]," Journal of Organometallic Chemistry **434**(2), 235-240 (1992).

32. S. K. Kim, S. Pedersen, and A. H. Zewail, "Femtochemistry of Organometallics - Dynamics of Metal-Metal and Metal-Ligand Bond-Cleavage in M(2)(Co)(10)," Chemical Physics Letters **233**(5-6), 500-508 (1995).

33. L. J. Rothberg, N. J. Cooper, K. S. Peters, and V. Vaida, "Picosecond dynamics of solution-phase photofragmentation of dimanganese decacarbonyl [Mn2(CO)10]," Journal of the American Chemical Society **104**(12), 3536-3537 (1982).

34. S. P. Church, H. Hermann, F. W. Grevels, and K. Schaffner, "The Primary Photoproducts of Mn2(Co)10 - Direct I.R. Observation and Decay Kinetics of Mn(Co)5 and Mn2(Co)9 in Hydrocarbon Solution at Room-Temperature," Journal of the Chemical Society-Chemical Communications (12), 785-786 (1984).

35. J. Z. Zhang and C. B. Harris, "Photodissociation dynamics of Mn[sub 2](CO)[sub 10] in solution on ultrafast time scales," The Journal of Chemical Physics **95**(6), 4024-4032 (1991).

36. A. Waldman, S. Ruhman, S. Shaik, and G. N. Sastry, "Coherent photochemistry in solution - Impulsive photoselective photolysis of Mn2(CO)10," Chemical Physics Letters **230**(1-2), 110-116 (1994).

37. D. A. Steinhurst, A. P. Baronavski, and J. C. Owrutsky, "Transient infrared spectroscopy of Mn-2(CO)(10) with 400 nm excitation," Chemical Physics Letters **361**(5-6), 513-519 (2002).

38. J. Owrutsky and A. Baronavski, "Ultrafast infrared study of the ultraviolet photodissociation of Mn-2(CO)(10)," Journal of Chemical Physics **105**(22), 9864-9873 (1996).

39. C. R. Baiz, R. McCanne, M. J. Nee, and K. J. Kubarych, "Orientational dynamics of transient molecules measured by non-equilibrium two-dimensional infrared spectroscopy," Journal of Physical Chemistry A **113**(31) 8907(2009).

40. I. R. Dunkin, P. Harter, and C. J. Shields, "Recognition of a Semibridging Carbonyl Group in Mn2(Co)9 from Plane-Polarized Photolysis of Mn2(Co)10 in Ar Matrices at 12-K," Journal of the American Chemical Society **106**(23), 7248-7249 (1984).

41. A. F. Hepp and M. S. Wrighton, "Relative Importance of Metal Metal Bond Scission and Loss of Carbon-Monoxide from Photo-Excited Dimanganese Decacarbonyl - Spectroscopic Detection of a Coordinatively Unsaturated, Co-Bridged Dinuclear Species in Low-Temperature Alkane Matrices," Journal of the American Chemical Society **105**(18), 5934-5935 (1983).

42. M. Martin, B. Rees, and A. Mitschler, "Bonding in a Binuclear Metal-Carbonyl - Experimental Charge-Density in Mn-2(Co)10," Acta Crystallographica Section B-Structural Science **38**(JAN), 6-15 (1982).

43. S. P. Church, M. Poliakoff, J. A. Timney, and J. J. Turner, "Synthesis and Characterization of the Pentacarbonylmanganese(O) Radical, Mn(Co)5, in Low-Temperature Matrices," Journal of the American Chemical Society **103**(25), 7515-7520 (1981).

44. W. Schneider and W. Thiel, "Anharmonic force fields from analytic second derivatives: Method and application to methyl bromide," Chemical Physics Letters **157**(4), 367-373 (1989).

45. S. Dressler and W. Thiel, "Anharmonic force fields from density functional theory," Chemical Physics Letters **273**(1-2), 71-78 (1997).

46. C. Lin, A. Gilbert, and P. Gill, "Calculating molecular vibrational spectra beyond the harmonic approximation," Theoretical Chemistry Accounts: Theory, Computation, and Modeling (Theoretica Chimica Acta) **120**(1), 23-35 (2008).

47. S. Califano, *Vibrational states* (John Wiley and Sons, London, 1976).

48. V. Barone, "Anharmonic vibrational properties by a fully automated second-order perturbative approach," Journal of Chemical Physics **122**(1), 014108-014110 (2005).

49. V. Barone, "Vibrational zero-point energies and thermodynamic functions beyond the harmonic approximation," Journal of Chemical Physics **120**(7), 3059-3065 (2004).

50. J. Neugebauer and B. A. Hess, "Fundamental vibrational frequencies of small polyatomic molecules from density-functional calculations and vibrational perturbation theory," Journal of Chemical Physics **118**(16), 7215-7225 (2003).

51. Boese A.D, K. W., and M. J. M. L., "Assessment of various density functionals and basis sets for the calculation of molecular anharmonic force fields," (2005), pp. 830-845.

52. A. D. Boese, W. Klopper, and J. M. L. Martin, "Anharmonic force fields and thermodynamic functions using density functional theory," (Taylor & Francis, 2005), pp. 863 - 876.

53. A. D. Becke, "Density-functional exchange-energy approximation with correct asymptotic behavior," Physical Review A **38**(6), 3098 (1988).

54. J. P. Perdew, "Density-functional approximation for the correlation energy of the inhomogeneous electron gas," Physical Review B **33**(12), 8822 (1986).

55. P. J. Hay and W. R. Wadt, "Ab initio effective core potentials for molecular calculations. Potentials for the transition metal atoms Sc to Hg," Journal of Chemical Physics **82**(1), 270-283 (1985).

56. Y. Shao, L. Molnar, Y. Jung, J. Kussmann, C. Ochsenfeld, S. Brown, A. Gilbert, L. Slipchenko, S. Levchenko, D. O'Neill, R. DiStasio, R. Lochan, T. Wang, G. Beran, N. Besley, J. Herbert, C. Lin, T. Van Voorhis, S. Chien, A. Sodt, R. Steele, V. Rassolov, P. Maslen, P. Korambath, R. Adamson, B. Austin, J. Baker, E. Byrd, H. Dachsel, R. Doerksen, A. Dreuw, B. Dunietz, A. Dutoi, T. Furlani, S. Gwaltney, A. Heyden, S. Hirata, C. Hsu, G. Kedziora, R. Khalliulin, P. Klunzinger, A. Lee, M. Lee, W. Liang, I. Lotan, N. Nair, B. Peters, E. Proynov, P. Pieniazek, Y. Rhee, J. Ritchie, E. Rosta, C. Sherrill, A. Simmonett, J. Subotnik, H. Woodcock, W. Zhang, A. Bell, A. Chakraborty, D. Chipman, F. Keil, A. Warshel, W. Hehre, H. Schaefer, J. Kong, A. Krylov, P. Gill, and M. Head-Gordon, "Advances in methods and algorithms in a modern quantum chemistry program package," Physical Chemistry Chemical Physics **8**(27), 3172-3191 (2006).

57. P. Hamm and S. Woutersen, "Coupling of the Amide I Modes of the Glycine Dipeptide," Bulletin of the Chemical Society of Japan **75**(5), 985-988 (2002).

58. R. B. Lehoucq, D. C. Sorensen, and C. Yang, ARPACK Users Guide: Solution of Large Scale Eigenvalue Problems by Implicitly Restarted Arnoldi Methods, 1997.

59. A. D. Boese and J. M. L. Martin, "Vibrational Spectra of the Azabenzenes Revisited: Anharmonic Force Fields," The Journal of Physical Chemistry A **108**(15), 3085-3096 (2004).

60. D. M. Adams, M. A. Hooper, and A. Squire, "A Raman spectroscopic study of dimanganese and dirhenium decacarbonyls," Journal of the Chemical Society A, 71-77 (1971).

61. M. Nee, C. Baiz, J. Anna, R. McCanne, and K. Kubarych, "Multilevel vibrational coherence transfer and wavepacket dynamics probed with multidimensional IR spectroscopy," Journal of Chemical Physics **129**(8), 084503 (2008).

62. C. R. Baiz, P. L. McRobbie, J. M. Anna, E. Geva, and K. J. Kubarych, "Two-Dimensional Infrared Spectroscopy of Metal Carbonyls," Accounts of Chemical Research **42**(9), 1395-1404 (2009)

63. C. Baiz, M. Nee, R. McCanne, and K. Kubarych, "Ultrafast nonequilibrium Fourier-transform two-dimensional infrared spectroscopy," Optics Letters **33**(21), 2533-2535 (2008).

64. W. Zhuang, D. Abramavicius, T. Hayashi, and S. Mukamel, "Simulation Protocols for Coherent Femtosecond Vibrational Spectra of Peptides," The Journal of Physical Chemistry B **110**(7), 3362-3374 (2006).

65. S. R. G. Naraharisetty, V. M. Kasyanenko, and I. V. Rubtsov, "Bond connectivity measured via relaxation-assisted two-dimensional infrared spectroscopy," Journal of Chemical Physics **128**(10)(2008).

66. D. V. Kurochkin, S. R. G. Naraharisetty, and I. V. Rubtsov, "A relaxation-assisted 2D IR spectroscopy method," Proceedings of the National Academy of Sciences of the United States of America **104**(36), 14209-14214 (2007).

67. F. Ding and M. T. Zanni, "Heterodyned 3D IR spectroscopy," Chemical Physics **341**(1-3), 95-105 (2007).

68. J. Bredenbeck, J. Helbing, and P. Hamm, "Labeling vibrations by light: Ultrafast transient 2D-IR spectroscopy tracks vibrational modes during photoinduced charge transfer," Journal of the American Chemical Society **126**(4), 990-991 (2004).

Chapter 6

Ultrafast Vibrational Dynamics: Modeling 2DIR Signatures of Coherence-Transfer

The work presented in this chapter has been published in the following paper:

1. C.R. Baiz, K.J. Kubarych and E. Geva "*Molecular Theory and Simulation of Coherence Transfer in Metal Carbonyls and Its Signature on Multidimensional Infrared Spectra* , The Journal of Physical Chemistry B, In press (2011)

6.1 Introduction

Coherent multidimensional infrared spectroscopy has recently become a powerful technique for unraveling structure-dynamics relationships in many complex systems with femtosecond time resolution.[1-10] Similar to multidimensional NMR spectroscopy,[11] detailed molecular information is most often derived from models that map structures to frequencies and the quality of the specific model largely determines the amount of molecular information that can be extracted from the experiment. [12-16] The ability of multidimensional NMR to provide atomistically detailed structural information in large biomolecules emerges from the fact that nuclear spin resonances and spin-spin couplings can be predicted quantitatively from standard models, providing the structure-frequency map needed to translate the experimental data into chemical structures.[17] Similarly, the most insightful two-dimensional infrared (2DIR) experiments to date use complex models in order to obtain

information on the molecular structure and dynamics underlying the spectra. For example, 2DIR studies of peptides in the amide-I region rely on a combination of molecular dynamics simulations, high-quality ab-initio frequency maps and vibrational coupling schemes to extract protein structures from the measured spectra. [18-24]

Although frequency maps have proven successful in reproducing the experimental lineshapes, two-dimensional spectra also contain information on such processes as coherence-to-coherence transfer[25, 26] or relaxation to dark states, for which reliable microscopic models remain underdeveloped. As a result, the analysis of these processes is often based on phenomenological and somewhat oversimplified models that contain a limited amount of information on the underlying molecular picture. It is therefore important to construct a theoretical framework to account for the aforementioned processes based on an explicit description of molecular structure and dynamics.

Over the last ten years, metal carbonyls have been established as useful benchmark systems for 2DIR spectroscopy.[27-38] Their rich vibrational structure, narrow lineshapes, and large oscillator strengths make metal carbonyls ideal molecules for testing different aspects of 2DIR spectroscopy, such as intramolecular vibrational redistribution (IVR), where populations are transferred among high-frequency vibrational states within the molecule, or vibrational energy relaxation (VER), where the energy is lost to the bath or low frequency modes of the molecule. In addition, newer experiments have been able to directly test coherence-coherence coupling (coherence transfer), where a coherence created between two eigenstates by a laser pulse is spontaneously transferred to a different coherence of similar frequency but involving a new eigenstate or pair of eigenstates. One system in particular $Rh(CO)_2C_5H_7O_2$ (RDC) has provided important insights on the effect of anharmonic coupling coefficients,[28, 39] and coherence transfer [25, 39-41] on multidimensional spectra. The interpretation of the results, however, relied on fitting the data to phenomenological models which lacked molecular detail. Furthermore, as the number of fitting parameters grows rapidly with the number of modes, phenomenological models become impractical for most systems, which unlike RDC would typically have more than two modes.

Within this context, recent effort has been directed towards developing a general electronic-structure-based framework for calculating anharmonic frequencies and oscillator

strengths, which can be compared directly to experiment.[35, 36, 42] It is important to note that although the 2DIR experiment only probes the bright (i.e. IR active) modes directly, it was found necessary to include the dark (i.e. IR inactive) modes which remain strongly coupled and turn out to have a significant effect on the transition frequencies and dipole moments (see Chapter 5). Here we attempt to develop a new and complimentary general framework aimed at providing a molecularly-detailed description of solvent-induced dynamical effects such as dephasing, population relaxation, coherence-to-coherence transfer and population-to-coherence transfer. The development of such a framework is motivated in part by recent 2DIR measurements of the carbonyl stretching modes of dimanganese decacarbonyl, ($Mn_2(CO)_{10}$; DMDC) wherever direct signatures of coherence transfer were observed in the spectra.[26] The strong infrared transitions and weakly interacting cyclohexane solvent allowed for the observation of long-lived coherences between singly-excited states as well as dual-frequency oscillations of certain 2D cross peaks along the waiting time. The latter observation was, to the best of our knowledge, the first unambiguous evidence for low-frequency coherence transfer in vibrational systems. It is worth pointing out that RDC only has two carbonyl stretching modes and two states in the singly excited band, and thus only one low-frequency coherence. The observation of coupling between coherences within the singly excited band requires a system consisting of at least three distinct energy levels, which is the case for DMDC. In this section we present a theoretical and computational modeling approach based on a Markovian quantum master equation, which, in addition to the coherence and population relaxation terms, also accounts for coherence-to-coherence transfer as well as coherence-to-population and population-to-coherence transfer.

Importantly, our approach does not rely on empirical, adjustable parameters: we obtain the transition frequencies and dipole moments from electronic-structure calculations and employ explicit expressions for the relaxation matrix elements in terms of solvent force correlation functions, which are in turn obtained from molecular dynamics simulations. We subsequently use the model to explore the vibrational spectroscopy of $Mn_2(CO)_{10}$ with particular attention to the effects of coherence transfer and coherence-population coupling on the spectra as well as investigate the effect of strongly coupled dark modes on the lineshapes and waiting-time dependence of the 2D peaks.

The remainder of this chapter is organized as follows: In section II we describe the molecular Hamiltonian and derive the quantum master equation. In section III we derive explicit expressions for the system-bath coupling. In sections IV and V we provide a treatment of the field-matter coupling and outline the procedure for computing multidimensional spectra. In section VI we provide the specific simulation parameters, and in sections VII and VIII we discuss the simulations results for $Mn_2(CO)_{10}$ and compare them to experiment. Finally in section IX we summarize the results and provide an outlook towards future uses of the model.

6.2 Theoretical Methods and Models

I. Excitonic vibrational Hamiltonian and quantum master equation

In this section we develop the theoretical framework for modeling coherence transfer in a multi-mode system. For the sake of concreteness, the theory is developed in the context of the 2DIR spectroscopy of the 10-carbonyl system $Mn_2(CO)_{10}$ (Figure 6.1) in the terminal C≡O stretching region. However, it should be noted that the methodologies described herein can be extended in a straightforward manner to other molecular systems.

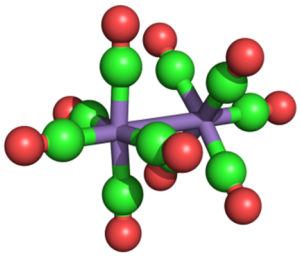

Figure 6.1: Equilibrium structure of dimanganese decacarbonyl ($Mn_2(CO)_{10}$, DMDC), the green and red atoms represent carbon and oxygen respectively.

We start by writing the overall system Hamiltonian in a system-bath form:

$$\hat{H} = \hat{H}_S + \hat{H}_B + \hat{H}_{BS} \tag{1}$$

The system Hamiltonian, $\hat{H}_S$, corresponds to the *anharmonic* vibrational Hamiltonian of the C≡O stretches in DMDC:

$$\hat{H}_S = \sum_{j=0}^{n_1-1}\left(\hbar\omega_{10} + \varepsilon_{1j}\right)\left|1j\right\rangle\left\langle 1j\right| + \sum_{j=0}^{n_2-1}\left(\hbar\omega_{20} + \varepsilon_{2j}\right)\left|2j\right\rangle\left\langle 2j\right| \quad (1)$$

Where $\left|\alpha j\right\rangle$ represents the j-th state in the α-th band, and α=0, 1, 2 represent the ground, singly-excited, and doubly-excited states respectively. Since the model is developed within the context of two-dimensional spectroscopy, only the singly- and doubly-excited states are considered as these are the only states that are accessed experimentally. The ground state is denoted by $\left|00\right\rangle$ and its energy is assumed to coincide with the origin. n_1 is the number of C≡O stretch modes, where it should be understood that all C≡O stretches need to be included, whether photoactive or not (n_1=10 in the case of DMDC). n_1 is also the number of states in the "singly-excited" band. The overall number of "doubly-excited" states is $n_2 = n_1(n_1+1)/2$ (55 in the case of DMDC). Importantly, the "singly-excited" and "doubly-excited" states correspond to eigenfunctions of the anharmonic vibrational Hamiltonian, and as such include contributions from harmonic states with higher occupancy. We also assume that the energy levels within the α-th band are ordered in the following manner: $\varepsilon_{\alpha 0} \le \varepsilon_{\alpha 1} \le \varepsilon_{\alpha 2} \le \ldots$. The transition frequencies and dipole moments are calculated from electronic structure methods. Indeed, we have recently shown that these can be obtained in the case of DMDC by combining density functional theory with vibrational perturbation theory.[35,36] Alternatively, if known, the experimental frequencies and anharmonicities may be used. It should be noted that in a system like DMDC, the intra-band transitions range from 0 to 135 cm^{-1} whereas the inter-band transition frequency is ~2000 cm^{-1}. Thus, at room temperature, one can assume that

$$\varepsilon_{\alpha j} \le k_B T << \hbar\omega_{\alpha\beta} \quad (1)$$

The bath Hamiltonian, $\hat{H}_B$, corresponds to the solvent degrees of freedom, and will remain undetermined for the time being. Finally, the system-bath coupling, $\hat{H}_{BS}$, in its most general form, is given by:

$$\hat{H}_{BS} = |00\rangle \hat{\Lambda}_{00,00} \langle 00| + \sum_{j=1}^{n_1-1}\sum_{k=1}^{n_1-1} |1j\rangle \hat{\Lambda}_{1j,1k} \langle 1k| + \sum_{j=1}^{n_2-1}\sum_{k=1}^{n_2-1} |2j\rangle \hat{\Lambda}_{2j,2k} \langle 2k|$$
$$+ \sum_{j=1}^{n_1-1} \left[|00\rangle \hat{\Lambda}_{00,1j} \langle 1j| + |1j\rangle \hat{\Lambda}_{1j,00} \langle 00| \right] + \sum_{k=1}^{n_2-1} \left[|00\rangle \hat{\Lambda}_{00,2k} \langle 2k| + |2k\rangle \hat{\Lambda}_{2k,00} \langle 00| \right] \quad (1)$$
$$+ \sum_{j=1}^{n_1-1}\sum_{k=1}^{n_2-1} \left[|1j\rangle \hat{\Lambda}_{1j,2k} \langle 2k| + |2k\rangle \hat{\Lambda}_{2k,1j} \langle 1j| \right]$$

Here, $\left\{ \hat{\Lambda}_{\alpha j,\beta k} \right\}$ are the, yet to be explicitly specified, bath operators. Since the energy of the bath, $Tr_B \left[\hat{H}_{BS} \hat{\rho}_B^{eq} \right]$, is constant, it can be assumed without loss of generality, that $Tr_B \left[\hat{H}_{BS} \hat{\rho}_B^{eq} \right] \equiv \left\langle \hat{H}_{BS} \right\rangle_B = 0$, which implies that

$$Tr_B \left[\hat{\Lambda}_{\alpha j,\beta k} \hat{\rho}_B^{eq} \right] \equiv \left\langle \hat{\Lambda}_{\alpha j,\beta k} \right\rangle_B = 0 \quad \text{for all } \alpha j, \beta k \quad (1)$$

Here $\hat{\rho}_B^{eq}$ represents the equilibrium density matrix of the bath. More specifically, if $\left\langle \hat{H}_{BS} \right\rangle_B \neq 0$, then we can always redefine $\hat{H}_S$ and $\hat{H}_{BS}$ as $\hat{H}_S + \left\langle \hat{H}_{BS} \right\rangle_B$ and $\hat{H}_{BS} - \left\langle \hat{H}_{BS} \right\rangle_B$, respectively, so that $\left\langle \hat{H}_{BS} \right\rangle_B = 0$. In other words, $\left\langle \hat{H}_{BS} \right\rangle_B$ corresponds to a static solvent shift, and therefore it is equivalent to redefining the frequency origin.

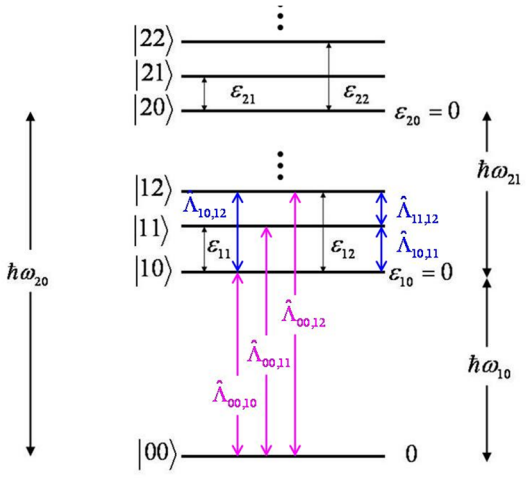

Figure 6.2: A schematic view of the system energy level diagram and some of the bath operators associated with various transitions. It should be noted that the inter-band and intra-band transitions are marked in blue and pink, respectively, and that the bath-operators associated with the inter-band transitions (pink) are neglected here. See Figure 6.3 for a schematic view of the density matrix.

Noting that $\hat{\Lambda}_{\alpha j,\beta k}$ is the bath operator that couples to the system operator $|\alpha j\rangle\langle\beta k|$ and assuming that that the bath is weakly coupled to the system, energy conservation dictates that $\hat{\Lambda}_{\alpha j,\beta k}$ induces an energy change in the bath which is comparable to $|E_{\alpha j} - E_{\beta k}|$. The fact that all modes that are close to resonance with the photoactive transitions are included in the system Hamiltonian then implies that the system-bath interactions are of the non-resonant type. Thus, the bath can exchange no more than $\sim k_B T$ with the system. Since inter-band energy gaps are much larger than $k_B T$ (see Eq. (1)), one can neglect the inter-band system-bath coupling terms in Eq. (1), thereby considerably simplifying the system-bath coupling equation:

$$\hat{H}_{BS} = |00\rangle \hat{\Lambda}_{00,00} \langle 00| + \sum_{j=1}^{n_1-1}\sum_{k=1}^{n_1-1} |1j\rangle \hat{\Lambda}_{1j,1k} \langle 1k| + \sum_{j=1}^{n_2-1}\sum_{k=1}^{n_2-1} |2j\rangle \hat{\Lambda}_{2j,2k} \langle 2k| \tag{1}$$

In what follows, we will refer to this approximation as the *intra-band coupling approximation* (IntraCA).

Next, assuming that the system starts out at thermal equilibrium, $\hbar\omega_{10} >> k_B T$ implies that the initial state of the overall system is given by the following density operator:

$$\hat{\rho}(0) = \hat{\rho}_B^{eq} \otimes |00\rangle\langle 00| \equiv \hat{\rho}_B^{eq} \otimes \hat{\sigma}(0). \tag{1}$$

Here, $\hat{\rho}_B^{eq} = e^{-\beta \hat{H}_B} \Big/ Tr\left[e^{-\beta \hat{H}_B}\right]$, where $\beta = 1/k_B T$ is the free bath thermal equilibrium density operator and $\hat{\sigma}(t) = Tr_B\left[\hat{\rho}(t)\right]$ is the reduced density operator of the system. In practice it is convenient to represent $\hat{\sigma}(t)$ as a matrix in the basis of the system eigenfunctions, $\{|\alpha j\rangle\}$. In what follows we will refer to the diagonal elements, $\{\sigma_{\alpha j,\alpha j}(t)\}$, and off-diagonal elements $\{\sigma_{\alpha j,\beta k}(t)\}$, as *populations* and *coherences*, respectively. We will also distinguish between *intra-band coherences*, $\{\sigma_{\alpha j,\alpha k}(t)\}$, and *inter-band coherences*, $\{\sigma_{\alpha j,\beta k}(t)\}$ (where $\alpha \neq \beta$).

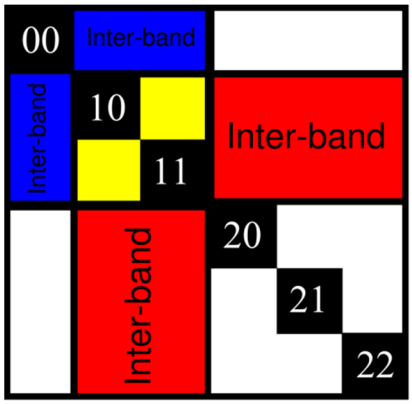

Figure 6.3: A schematic view of populations, inter-band (blue, red) and intra-band (yellow) coherence blocks in the density matrix. The intra-band coherences within the second manifold levels are inaccessible in 2DIR experiments, and thus are not shown.

The reduced dynamics of the system $\hat{\sigma}(t)$ are described by a quantum master equation (QME) which can be derived in the limit of weak system-bath coupling by assuming Markovity (i.e. that the time scale for system relaxation is slower than the relevant bath correlation times).[43-67] The resulting QMEs for the populations, intra-band and inter-band coherences are given below:

$$\begin{aligned}\frac{d}{dt}\sigma_{\alpha j,\alpha j}(t) &= -\sum_{m\neq j} k_{\alpha m\leftarrow\alpha j}\sigma_{\alpha j,\alpha j}(t) + \sum_{m\neq j} k_{\alpha j\leftarrow\alpha m}\sigma_{\alpha m,\alpha m}(t) \\ &- \sum_{m\neq j,n} \Gamma_{\alpha j,\alpha n;\alpha n,\alpha m}\left(\omega_{\alpha m,\alpha n}\right)\sigma_{\alpha m,\alpha j}(t) - \sum_{m\neq j,n} \Gamma^{*}_{\alpha j,\alpha n;\alpha n,\alpha m}\left(\omega_{\alpha m,\alpha n}\right)\sigma_{\alpha j,\alpha m}(t) \\ &+ \sum_{m\neq n} \Gamma_{\alpha n,\alpha j;\alpha j,\alpha m}\left(\omega_{\alpha m,\alpha j}\right)\sigma_{\alpha m,\alpha n}(t) + \sum_{m\neq n} \Gamma^{*}_{\alpha n,\alpha j;\alpha j,\alpha m}\left(\omega_{\alpha m,\alpha j}\right)\sigma_{\alpha n,\alpha m}(t)\end{aligned} \tag{2}$$

$$\frac{d}{dt}\sigma_{\alpha j,\alpha k}(t) = -\left\{\begin{array}{l} i\omega_{\alpha j,\alpha k}\sigma_{\alpha j,\alpha k}(t) + \sum_{n\neq j}\Gamma_{\alpha j,\alpha n;\alpha n,\alpha j}\left(\omega_{\alpha j,\alpha n}\right) + \sum_{m\neq k}\Gamma^{*}_{\alpha k,\alpha m;\alpha m,\alpha k}\left(\omega_{\alpha k,\alpha m}\right) \\ +\Gamma_{\alpha j,\alpha j;\alpha j,\alpha j}\left(0\right) + \Gamma^{*}_{\alpha k,\alpha k;\alpha k,\alpha k}\left(0\right) - \Gamma_{\alpha k,\alpha k;\alpha j,\alpha j}\left(0\right) - \Gamma^{*}_{\alpha j,\alpha j;\alpha k,\alpha k}\left(0\right) \end{array}\right\}\sigma_{\alpha j,\alpha k}(t)$$
$$- \sum_{m\neq(j,k)}\left[\sum_{n}\Gamma_{\alpha j,\alpha n;\alpha n,\alpha m}\left(\omega_{\alpha m,\alpha n}\right)\right]\sigma_{\alpha m,\alpha k}(t) - \sum_{m\neq(j,k)}\left[\sum_{n}\Gamma^{*}_{\alpha k,\alpha n;\alpha n,\alpha m}\left(\omega_{\alpha m,\alpha n}\right)\right]\sigma_{\alpha j,\alpha m}(t)$$
$$+ \sum_{m\neq n,m\neq j,n\neq k}\Gamma_{\alpha n,\alpha k;\alpha j,\alpha m}\left(\omega_{\alpha m,\alpha j}\right)\sigma_{\alpha m,\alpha n}(t) + \sum_{m\neq n,m\neq j,n\neq k}\Gamma^{*}_{\alpha m,\alpha j;\alpha k,\alpha n}\left(\omega_{\alpha n,\alpha k}\right)\sigma_{\alpha m,\alpha n}(t)$$
$$-\left[\sum_{n}\Gamma_{\alpha j,\alpha n;\alpha n,\alpha k}\left(\omega_{\alpha k,\alpha n}\right)\right]\sigma_{\alpha k,\alpha k}(t) - \left[\sum_{m}\Gamma^{*}_{\alpha k,\alpha m;\alpha m,\alpha j}\left(\omega_{\alpha j,\alpha m}\right)\right]\sigma_{\alpha j,\alpha j}(t)$$
$$+ \sum_{m\neq(j,k)}\Gamma_{\alpha m,\alpha k;\alpha j,\alpha m}\left(\omega_{\alpha m,\alpha j}\right)\sigma_{\alpha m,\alpha m}(t) + \sum_{m\neq(j,k)}\Gamma^{*}_{\alpha m,\alpha j;\alpha k,\alpha m}\left(\omega_{\alpha m,\alpha k}\right)\sigma_{\alpha m,\alpha m}(t)$$

(3)

$$\frac{d}{dt}\sigma_{\alpha j,\beta k}(t) = -\left\{\begin{array}{l} i\omega_{\alpha j,\beta k} + \sum_{n\neq j}\Gamma_{\alpha j,\alpha n;\alpha n,\alpha j}\left(\omega_{\alpha j,\alpha n}\right) + \sum_{n\neq k}\Gamma^{*}_{\beta k,\beta n;\beta n,\beta k}\left(\omega_{\beta k,\beta n}\right) \\ +\Gamma_{\alpha j,\alpha j;\alpha j,\alpha j}\left(0\right) + \Gamma^{*}_{\beta k,\beta k;\beta k,\beta k}\left(0\right) - \Gamma_{\beta k,\beta k;\alpha j,\alpha j}\left(0\right) - \Gamma^{*}_{\alpha j,\alpha j;\beta k,\beta k}\left(0\right) \end{array}\right\}\sigma_{\alpha j,\beta k}(t)$$
$$-\sum_{m\neq j}\left[\sum_{n}\Gamma_{\alpha j,\alpha n;\alpha n,\alpha m}\left(\omega_{\alpha m,\alpha n}\right)\right]\sigma_{\alpha m,\beta k}(t) - \sum_{m\neq k}\left[\sum_{n}\Gamma^{*}_{\beta k,\beta n;\beta n,\beta m}\left(\omega_{\beta m,\beta n}\right)\right]\sigma_{\alpha j,\beta m}(t)$$
$$+ \sum_{m\neq j,n\neq k}\Gamma_{\beta n,\beta k;\alpha j,\alpha m}\left(\omega_{\alpha m,\alpha j}\right)\sigma_{\alpha m,\beta n}(t) + \sum_{m\neq j,n\neq k}\Gamma^{*}_{\alpha m,\alpha j;\beta k,\beta n}\left(\omega_{\beta n,\beta k}\right)\sigma_{\alpha m,\beta n}(t)$$

(4)

Here,

$$\Gamma_{\alpha j,\alpha k;\beta m,\beta n}\left(\omega\right) = \frac{1}{\hbar^{2}}\int_{0}^{\infty} d\tau e^{i\omega\tau} C_{\alpha j,\alpha k;\beta m,\beta n}\left(\tau\right) \tag{4}$$

where $\left\{C_{\alpha j,\alpha k;\beta m,\beta n}\left(\tau\right)\right\}$ are free-bath quantum-mechanical correlation functions,

$$C_{\alpha j,\alpha k;\beta m,\beta n}\left(\tau\right) = Tr_{B}\left[\hat{\rho}_{B}^{eq} e^{iH_{B}\tau/\hbar}\hat{\Lambda}_{\alpha j,\alpha k} e^{-iH_{B}\tau/\hbar}\hat{\Lambda}_{\beta m,\beta n}\right] \equiv \left\langle \hat{\Lambda}_{\alpha j,\alpha k}\left(\tau\right)\hat{\Lambda}_{\beta m,\beta n}\right\rangle_{B} \tag{4}$$

and

$$k_{\alpha m\leftarrow\alpha j} = 2\,\mathrm{Re}\left[\Gamma_{\alpha j,\alpha m;\alpha m,\alpha j}\left(\omega_{\alpha j,\alpha m}\right)\right] \tag{5}$$

are intra-band population relaxation rate constants. It should be noted that within our model, inter-band population relaxation is assumed infinitely slow, due to the IntraCA. However, it is also important to note that population transfer between bright and dark modes is accounted for and is expected to be the dominant mechanism for population relaxation.

Importantly, the QMEs (Eqs. (2)-(4)) were derived without neglecting terms that couple between coherences and populations as well as terms that couple between different coherences. The latter terms, in turn, lead to *coherence transfer*. Note that these couplings are bath induced. Within the IntraCA, populations are only coupled to intra-band coherences and intra-band coherences are not coupled to inter-band coherences. Thus, the coherence transfer terms can be further classified as *intra-band* or *inter-band coherence transfer*, depending on the type of coherences that are coupled (see Figure 6.4).

II. System-bath coupling

In practice, one needs to know the bath operators that couple to the system in order to describe its dynamics as described by the QMEs, Eq. (2)-(4). To this end, we note that the Hamiltonian of the overall system is generally given by

$$H\left(\mathbf{q},\mathbf{p},\mathbf{Q},\mathbf{P}\right)=H_S^0(\mathbf{q},\mathbf{p})+T(\mathbf{P})+V_0(\mathbf{Q})+V_1(\mathbf{q},\mathbf{Q}) \tag{6}$$

Here, $\mathbf{Q}=\left(Q_1,...,Q_N\right)$ are the bath coordinates and $\mathbf{q}=\left(q_1,...,q_{n_1}\right)$ are the normal mode coordinates, $\mathbf{P}=\left(P_1,...,P_N\right)$ and $\mathbf{p}=\left(p_1,...,p_{n_1}\right)$ are the corresponding conjugate momenta, $H_S^0(\mathbf{q},\mathbf{p})$ is the gas phase vibrational Hamiltonian, $T(\mathbf{P})$ is the bath kinetic energy, $V_0(\mathbf{Q})$ is the free bath potential energy (i.e. solvent-solvent interactions), and $V_1(\mathbf{q},\mathbf{Q})$ represent the interactions between the bath and the system (i.e. solvent-solute interactions). It should be noted that the explicit functional form of $V_0(\mathbf{Q})$ and $V_1\left(\mathbf{q},\mathbf{Q}\right)$ depend on the force fields governing solvent-solvent and solvent-solute interactions which are system specific.

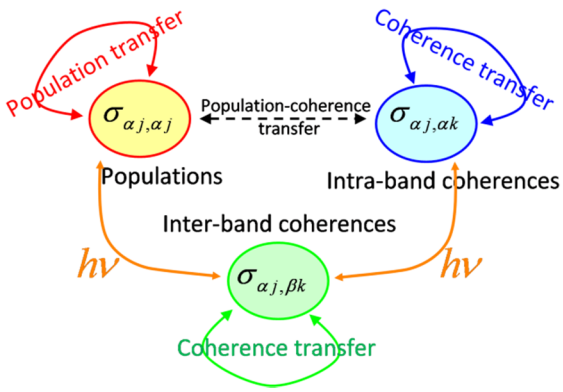

Figure 6.4: A schematic representation of the vibrational dynamics captured by the model. Inter-band coherences are decoupled from intra-band coherences and populations. Intra-band coherences are coupled to populations. The light-matter interactions couple populations and intra-band coherences to inter-band coherences.

Since the displacement along the normal mode coordinates is expected to be relatively small in a molecule like DMDC, one can approximate $V_1(\mathbf{q},\mathbf{Q})$ by its expansion to first order in the normal mode coordinates:

$$V_1(\mathbf{q},\mathbf{Q}) = V_1(\mathbf{Q},0) + \sum_{l=1}^{n_1}\left[\frac{\partial V_1}{\partial q_l}\right]_{\mathbf{q}=0} q_l + \cdots \equiv V_1(\mathbf{Q},\mathbf{0}) - \sum_{l=1}^{n_1} F_l(\mathbf{Q})\, q_l + \cdots \tag{6}$$

Here, $F_l(\mathbf{Q})$ is the force exerted by the bath on the l-th normal mode.

Since $V_1(\mathbf{Q},\mathbf{0})$ is a bath operator, it can be included in the potential energy part of the bath Hamiltonian, so that

$$H_B(\mathbf{Q},\mathbf{P}) = T(\mathbf{P}) + V_0(\mathbf{Q}) + V_1(\mathbf{0},\mathbf{Q}) \tag{7}$$

It is also convenient to define the free bath thermal average of the force $F_l(\mathbf{Q})$:

$$\left\langle F_l(\mathbf{Q})\right\rangle_B = \frac{Tr\left[F_l(\hat{\mathbf{Q}})\exp\left(-\beta\hat{H}_B\right)\right]}{Tr\left[\exp\left(-\beta\hat{H}_B\right)\right]} \tag{8}$$

so that the system Hamiltonian and the system-bath coupling can be defined as follows:

$$H_S(\mathbf{q},\mathbf{p}) = H_S^0(\mathbf{q},\mathbf{p}) - \sum_{l=1}^{n_1} \left\langle F_l(\mathbf{Q}) \right\rangle_B q_l \tag{9}$$

$$H_{BS} = -\sum_{l=1}^{n_1} \left(F_l(\mathbf{Q}) - \left\langle F_l(\mathbf{Q}) \right\rangle_B \right) q_l \equiv -\sum_{l=1}^{n_1} \delta F_l(\mathbf{Q}) q_l \tag{10}$$

Writing H_{BS} in terms of the eigenfunctions of $\widehat{H}_S$ and only accounting for intra-band coupling we obtain (see Eq.(1)):

$$\hat{H}_{BS} = |00\rangle \left[\sum_{l=1}^{n_1} q_{l;00,00} \delta F_l(\mathbf{Q}) \right] \langle 00| + \sum_{j=0}^{n_1-1} |1j\rangle \left[\sum_{l=1}^{n_1} q_{l;1j,1j} \delta F_l(\mathbf{Q}) \right] \langle 1j| + \sum_{j=1}^{n_2-1} |2j\rangle \left[\sum_{l=1}^{n_1} q_{l;2j,2j} \delta F_l(\mathbf{Q}) \right] \langle 2j|$$
$$+ \sum_{j\neq k}^{n_1-1} |1j\rangle \left[\sum_{l=1}^{n_1} q_{l;1j,1k} \delta F_l(\mathbf{Q}) \right] \langle 1k| + \sum_{j\neq k}^{n_2-1} |2j\rangle \left[\sum_{l=1}^{n_1} q_{l;2j,2k} \delta F_l(\mathbf{Q}) \right] \langle 2k| \tag{10}$$

where

$$q_{l;\alpha j,\alpha k} = \langle \alpha j | q_l | \alpha k \rangle \tag{11}$$

It should be noted that $q_{l;\alpha j,\alpha k} = 0$ if the vibrational Hamiltonian is assumed harmonic, i.e. within the normal mode approximation. Thus, within the treatment of the system-bath coupling as linear in the normal mode coordinates, one needs to use the anharmonic vibrational Hamiltonian in order to account for relaxation.

According to Eq. (10) one can identify the bath operators that couple to the system as so:

$$\Lambda_{00,00} = \sum_{l=1}^{n_1} q_{l;00,00} \delta F_l(\mathbf{Q}) \;\; ; \;\; \Lambda_{1j,1j} = \sum_{l=1}^{n_1} q_{l;1j,1j} \delta F_l(\mathbf{Q}) \;\; ; \;\; \Lambda_{2j,2j} = \sum_{l=1}^{n_1} q_{l;2j,2j} \delta F_l(\mathbf{Q})$$
$$\Lambda_{1j,1k} = \sum_{l=1}^{n_1} q_{l;1j,1k} \delta F_l(\mathbf{Q}) \;\; ; \;\; \Lambda_{2j,2k} = \sum_{l=1}^{n_1} q_{l;2j,2k} \delta F_l(\mathbf{Q}) \tag{11}$$

The corresponding bath correlation functions then assume the following form:

$$\left\langle \Lambda_{\alpha j,\alpha k}(t) \Lambda_{\beta m,\beta n} \right\rangle = \sum_{l,l'=1}^{n_1} q_{l;\alpha j,\alpha k} q_{l';\beta m,\beta n} \left\langle \delta F_l(t) \delta F_{l'} \right\rangle \tag{11}$$

In principle, if the force fields for the solvent-solute interactions are known, then the forces $\{F_l\}$ can be obtained explicitly. Furthermore, due to the IntraCA, $\{\Gamma_{\alpha j,\alpha k;\beta m,\beta n}(\omega)\}$ only need to be calculated at frequencies which are comparable to or smaller than $k_B T/\hbar$ (see Eq. (4)). Thus, the corresponding correlation functions, $\{C_{\alpha j,\alpha k;\beta m,\beta n}(\tau)\}$, can be obtained from classical MD simulations where the solute and solvent are treated as rigid molecules. The classical approximation naturally assumes that the solvent dynamics are independent of the solute vibrational state. This is a standard assumption made when using a QME approach and is undoubtedly justified in the case of weak system solvent coupling. Quantum correction factors have been used to model vibrational energy relaxation involving transitions greater than kT, since our model only accounts for energy redistribution within the states of the same manifold, where the gaps are than smaller than kT, quantum correction factors are not necessary.

Alternatively, one can use the above formulation in order to reduce the number of adjustable fitting parameters. To this end, we can assume that

$$\langle \delta F_l(t)\delta F_{l'}\rangle \approx \delta(l,l')C_{FF}(t) \tag{11}$$

Eq. (11) relies on the assumption that the forces on different normal modes are uncorrelated but have the same autocorrelation function (which can be justified in a molecule like DMDC where the CO stretch normal modes are highly delocalized, see Section VII). Applying this assumption to Eq. (11) then yields:

$$\langle \Lambda_{\alpha j,\alpha k}(t)\Lambda_{\beta m,\beta n}\rangle = \left[\sum_{l=1}^{n_1} q_{l;\alpha j,\alpha k} q_{l;\beta m,\beta n}\right] C_{FF}(t) \equiv A_{\alpha j,\alpha k;\beta m,\beta n} C_{FF}(t) \tag{11}$$

The coefficients $\{A_{\alpha j,\alpha k;\beta m,\beta n}\}$ can then be calculated explicitly provided that the eigenfunctions of the anharmonic vibrational Hamiltonian are known. The spectral density that corresponds to $C_{FF}(t)$ can be obtained as:

$$\int_0^\infty d\tau e^{i\omega\tau} C_{FF}(\tau) \approx \mathrm{Re}\int_0^\infty d\tau e^{i\omega\tau} C_{FF}(\tau) = \frac{1}{2}\int_{-\infty}^{\infty} d\tau e^{i\omega\tau} C_{FF}(\tau) \equiv \frac{1}{2}\tilde{C}_{FF}(\omega)$$
$$= \frac{2}{1+e^{-\beta\hbar\omega}}\tilde{C}^{S}_{FF}(\omega) \approx \frac{2}{1+e^{-\beta\hbar\omega}}\tilde{C}^{cl}_{FF}(\omega) \tag{11}$$

The first approximation, $\int_0^\infty d\tau e^{i\omega\tau} C_{FF}(\tau) \approx \mathrm{Re}\int_0^\infty d\tau e^{i\omega\tau} C_{FF}(\tau)$, is based on assuming that the imaginary part can be neglected; the fourth equality, $\frac{1}{2}\tilde{C}_{FF}(\omega) = \frac{2}{1+e^{-\beta\hbar\omega}}\tilde{C}^{S}_{FF}(\omega)$, is based on an identity that relates the Fourier transform of $C_{FF}(\tau)$, i.e. $\tilde{C}_{FF}(\omega)$, with that of $\mathrm{Re}C_{FF}(\tau)$, i.e. $\tilde{C}^{S}_{FF}(\omega)$; the fifth equality is based on assuming that the real part of the force correlation function, $\mathrm{Re}C_{FF}(\tau)$, can be approximated by the classical force correlation function, $C^{cl}_{FF}(\tau)$. It should be noted that this procedure assures that detailed balance is satisfied within the band:

$$\frac{\tilde{C}_{FF}(\omega)}{\tilde{C}_{FF}(-\omega)} = \frac{1+e^{\beta\hbar\omega}}{1+e^{-\beta\hbar\omega}} = e^{\beta\hbar\omega} \tag{11}$$

Since the intra-band transitions are small compared to kT, using a classical correlation functions is justified. Substituting Eqs. (11) and (11) into Eq. (4) then yields the following general expression for the relaxation coefficients that appear in the QMEs. Eqs. (2)-(4):

$$\Gamma_{\alpha j,\alpha k;\beta m,\beta n}(\omega) = \frac{2A_{\alpha j,\alpha k;\beta m,\beta n}}{\hbar^2}\frac{1}{1+e^{-\beta\hbar\omega}}\tilde{C}^{cl}_{FF}(\omega) \approx \frac{2A_{\alpha j,\alpha k;\beta m,\beta n}}{\hbar^2}\frac{1}{1+e^{-\beta\hbar\omega}}\tilde{C}^{cl}_{FF}(0) \tag{11}$$

The last approximation in Eq. (11) is based on the assumption that $\tilde{C}^{cl}_{FF}(\omega)$ can be assumed to be constant on the relatively narrow range of intra-band transition frequencies. Thus, we are left with a single parameter, namely $\tilde{C}^{cl}_{FF}(0)$, which can either be obtained from molecular dynamics simulations or from fitting to experiment.

Further insight can be obtained by considering the expressions for some of the relaxation coefficients that can be obtained based on Eq. (11). For example, the population relaxation rate constants can be shown to be given by

$$k_{\alpha m\leftarrow\alpha j}=2\,\mathrm{Re}\left[\Gamma_{\alpha j,\alpha m;\alpha m,\alpha j}\left(\omega_{\alpha j,\alpha m}\right)\right]\approx\frac{4}{\hbar^2}\sum_{l=1}^{n_1}q_{l;\alpha j,\alpha m}^2\frac{1}{1+e^{-\beta\hbar\omega_{\alpha j,\alpha m}}}\tilde{C}_{FF}^{cl}\left(0\right) \tag{11}$$

and are seen to depend solely on the off-diagonal matrix elements of q_l. The latter are expected to be small compared to the diagonal ones, which is consistent with the observation that population relaxation is slower compared to pure dephasing despite of the fact that $\beta\hbar\omega_{\alpha j,\alpha m}<1$.

Next, consider the inter-band and intra-band pure dephasing rate constants:

$$\begin{aligned}\left(\frac{1}{T_2^*}\right)_{\alpha j,\beta k}&\equiv\Gamma_{\alpha j,\alpha j;\alpha j,\alpha j}\left(0\right)+\Gamma_{\beta k,\beta k;\beta k,\beta k}^*\left(0\right)-\Gamma_{\beta k,\beta k;\alpha j,\alpha j}\left(0\right)-\Gamma_{\alpha j,\alpha j;\beta k,\beta k}^*\left(0\right)\\&\approx\frac{1}{\hbar^2}\sum_{l=1}^{n_1}\left[q_{l;\alpha j,\alpha j}-q_{l;\beta k,\beta k}\right]^2\tilde{C}_{FF}^{cl}\left(0\right)\end{aligned} \tag{11}$$

$$\begin{aligned}\left(\frac{1}{T_2^*}\right)_{\alpha j,\alpha k}&=\Gamma_{\alpha j,\alpha j;\alpha j,\alpha j}\left(0\right)+\Gamma_{\alpha k,\alpha k;\alpha k,\alpha k}^*\left(0\right)-\Gamma_{\alpha k,\alpha k;\alpha j,\alpha j}\left(0\right)-\Gamma_{\alpha j,\alpha j;\alpha k,\alpha k}^*\left(0\right)\\&=\frac{1}{\hbar^2}\sum_{l=1}^{n_1}\left[q_{l;\alpha j,\alpha j}-q_{l;\alpha k,\alpha k}\right]^2\tilde{C}_{FF}^{cl}\left(0\right)\end{aligned} \tag{11}$$

It should be noted that the inter-band pure dephasing rate constant relies on the difference between the diagonal elements of q_l in different bands, thereby making it rather sensitive to anharmonicities. In contrast, the intra-band pure dephasing rate constant rely on the difference between the diagonal elements of q_l within the same band, and can therefore be expected to be significantly slower.

The inter-band and intra-band coherence transfer terms and the population-coherence transfer terms can be shown to involve both diagonal and off-diagonal matrix elements of q_l. More specifically, the matrix elements appear as pair products where either

both members in the pair are off-diagonal or one is diagonal and one is not. In practice, we have observed that the diagonal elements are larger. Thus, a reasonable approximation can be based on neglecting the terms that involve two off-diagonals:

$$\left[\frac{d}{dt}\sigma_{\alpha j,\beta k}(t)\right]_{coh-coh} \approx$$
$$-\frac{2\tilde{C}_{FF}^{cl}(0)}{\hbar^2}\left\{\begin{array}{l}\sum_{m\neq j}\sum_{l=1}^{n_1}\left[\frac{1}{1+e^{-\beta\hbar\omega_{\alpha m,\alpha j}}}q_{l;\alpha j,\alpha j}q_{l;\alpha j,\alpha m}+\frac{1}{2}q_{l;\alpha j,\alpha m}q_{l;\alpha m,\alpha m}\right]\sigma_{\alpha m,\beta k}(t) \\ +\sum_{m\neq k}\sum_{l=1}^{n_1}\left(\frac{1}{1+e^{-\beta\hbar\omega_{\beta m,\beta k}}}q_{l;\beta k,\beta k}q_{l;\beta k,\beta m}+\frac{1}{2}q_{l;\beta k,\beta m}q_{l;\beta m,\beta m}\right)\sigma_{\alpha j,\beta m}(t)\end{array}\right\} \quad (11)$$

$$\left[\frac{d}{dt}\sigma_{\alpha j,\alpha k}(t)\right]_{\text{coh-coh}} \approx -\frac{1}{\hbar^2}\tilde{C}_{FF}^{cl}(0)\sum_{m\neq(j,k)}\sum_{l=1}^{n_1}\left\{q_{l;\alpha j,\alpha m}q_{l,\alpha m,\alpha m}\sigma_{\alpha m,\alpha k}(t)+q_{l;\alpha k,\alpha m}q_{l,\alpha m,\alpha m}\sigma_{\alpha j,\alpha m}(t)\right\} \quad (11)$$

$$\left[\frac{d}{dt}\sigma_{\alpha j,\alpha k}(t)\right]_{coh-pop}$$
$$\approx -\frac{2\tilde{C}_{FF}^{cl}(0)}{\hbar^2}\left\{\begin{array}{l}\left[\frac{1}{1+e^{-\beta\hbar\omega_{\alpha k,\alpha j}}}q_{l;\alpha j,\alpha j}q_{l;\alpha j,\alpha k}+\frac{1}{2}q_{l;\alpha j,\alpha k}q_{l;\alpha k,\alpha k}\right]\sigma_{\alpha k,\alpha k}(t) \\ +\left[\frac{1}{2}q_{l;\alpha k,\alpha j}q_{l;\alpha j,\alpha j}+\frac{1}{1+e^{-\beta\hbar\omega_{\alpha j,\alpha k}}}q_{l;\alpha k,\alpha k}q_{l;\alpha k,\alpha j}\right]\sigma_{\alpha j,\alpha j}(t)\end{array}\right\} \quad (11)$$

III. Field-matter interaction

The interaction of the system with the laser is treated perturbatively. The interaction Hamiltonian is assumed to be given by:

$$W(t) = -\hat{\vec{V}}\cdot\vec{E}(t)\cos\left[\omega t-\vec{k}\cdot\vec{r}\right] \quad (11)$$

where $\vec{E}(t)$, $\vec{k}$ and ω are the envelope, wave vector and leading frequency of the driving field and $\hat{\vec{V}}$ is the dipole moment vector operator. It is assumed that the bandwidth of the laser overlaps with the fundamental transition (ground state to the first-excited band) and overtone transition (first-excited band to the second-excited band). Thus, within the rotating wave approximation (RWA):[68-70]

$$\hat{W}(t) = -\frac{\hbar}{2} e^{i\omega t - i\vec{k}\cdot\vec{r}} \left[\sum_{j=0}^{n_1-1} \chi_{00,1j}(t) |00\rangle\langle 1j| + \sum_{j=0}^{n_1-1} \sum_{k=0}^{n_2-1} \chi_{1j,2k}(t) |1j\rangle\langle 2k| \right]$$
$$-\frac{\hbar}{2} e^{-i\omega t + i\vec{k}\cdot\vec{r}} \left[\sum_{j=0}^{n_1-1} \chi_{1j,00}(t) |1j\rangle\langle 00| + \sum_{j=0}^{n_1-1} \sum_{k=0}^{n_2-1} \chi_{2k,1j}(t) |2k\rangle\langle 1j| \right] \quad (11)$$

Here,

$$\hbar\chi_{\alpha j,\beta k}(t) = \vec{V}_{\alpha j,\beta k} \cdot \vec{E}(t) = \sum_b V_{\alpha j,\beta k,b} E_b(t) = \sum_b \hbar\chi_{\alpha j,\beta k,b}(t) \quad (12)$$

where $\left\{ \vec{V}_{\alpha i,\beta j} = \left(V_{\alpha i,\beta j,x}, V_{\alpha i,\beta j,y}, V_{\alpha i,\beta j,z} \right) \right\}$ are the transition dipole moments which are assumed to be constant vectors (the Condon approximation). Dark transitions can be included by setting the corresponding transition dipole moments to zero, $\vec{V}_{\alpha i,\beta j} = 0$.

In order to eliminate rapidly oscillating terms, it is desirable to calculate the system's optical response in the *rotating frame*. To this end, we define the density operator in the rotating frame picture as follows:

$$\tilde{\sigma}(t) = e^{iH_{rot}t/\hbar} \hat{\sigma}(t) e^{-iH_{rot}t/\hbar} \quad (12)$$

where

$$\hat{H}_{rot} = \hbar\omega \sum_{j=0}^{n_1-1} |1j\rangle\langle 1j| + 2\hbar\omega \sum_{j=0}^{n_2-1} |2j\rangle\langle 2j| \quad (12)$$

As a result:

$$\sigma_{\alpha j,\beta k}(t) = e^{-i\omega_{\alpha\beta}^{rot} t} \tilde{\sigma}_{\alpha j,\beta k}(t) \Leftrightarrow \tilde{\sigma}_{\alpha j,\beta k}(t) = e^{i\omega_{\alpha\beta}^{rot} t} \sigma_{\alpha j,\beta k}(t) \quad (12)$$

where $\omega_{\alpha\alpha}^{rot} = 0, \omega_{10}^{rot} = -\omega_{01}^{rot} = \omega_{21}^{rot} = -\omega_{12}^{rot} = \omega, \omega_{20}^{rot} = -\omega_{02}^{rot} = 2\omega$. It is important to note that the populations and intraband coherences are invariant to the transformation to the rotating frame and that only inter-band coherences ($\alpha \neq \beta$) change as a result of it.

Next we consider the effect on the system of an interaction with a light pulse which is short on the time scale of the system relaxation. Under these conditions, relaxation dynamics can

be neglected during the period of the pulse. Assuming for the sake of simplicity, that the pulse has a square profile, such that:

$$\chi_{\alpha j,\beta k}(t)=\begin{cases}\chi_{\alpha j,\beta k} & \text{during pulse}\\ 0 & \text{otherwise}\end{cases} \tag{12}$$

one can describe the dynamics during the short time period when the pulse is on by equation of motion in the rotating frame:

$$\frac{d}{dt}\tilde{\sigma}(t)=-\frac{i}{\hbar}\left[\widetilde{H},\tilde{\sigma}(t)\right] \tag{12}$$

where,

$$\tilde{H}=\sum_{j=0}^{n_1-1}\Delta_{1j}|1j\rangle\langle 1j|+\sum_{j=0}^{n_2-1}\Delta_{2j}|2j\rangle\langle 2j|-\frac{\hbar}{2}e^{-i\vec{k}\cdot\vec{r}}\left[\sum_{j=0}^{n_1-1}\chi_{00,1j}|00\rangle\langle 1j|+\sum_{j=0}^{n_1-1}\sum_{k=0}^{n_2-1}\chi_{1j,2k}|1j\rangle\langle 2k|\right]$$
$$-\frac{\hbar}{2}e^{i\vec{k}\cdot\vec{r}}\left[\sum_{j=0}^{n_1-1}\chi_{1j,00}|1j\rangle\langle 00|+\sum_{j=0}^{n_1-1}\sum_{k=0}^{n_2-1}\chi_{2k,1j}|2k\rangle\langle 1j|\right] \tag{12}$$

Here, $\Delta_{\alpha j}=\omega_{\alpha 0}+\varepsilon_{\alpha j}-\alpha\omega$ is the detuning. Assuming resonance, $|\Delta_{\alpha j}|\ll|\chi_{\alpha j,\beta k}|$, the rotating-frame interaction Hamiltonian can be further simplified to become:

$$\tilde{H}=-\frac{\hbar}{2}e^{-i\vec{k}\cdot\vec{r}}\left[\sum_{j=0}^{n_1-1}\chi_{00,1j}|00\rangle\langle 1j|+\sum_{j=0}^{n_1-1}\sum_{k=0}^{n_2-1}\chi_{1j,2k}|1j\rangle\langle 2k|\right]$$
$$-\frac{\hbar}{2}e^{i\vec{k}\cdot\vec{r}}\left[\sum_{j=0}^{n_1-1}\chi_{1j,00}|1j\rangle\langle 00|+\sum_{j=0}^{n_1-1}\sum_{k=0}^{n_2-1}\chi_{2k,1j}|2k\rangle\langle 1j|\right] \tag{12}$$

Furthermore, in the limit of weak field-matter interaction, one can treat the latter perturbatively, so that the evolution (in the rotating frame) during a pulse of length τ_p is given by:

$$\exp\left[-\frac{i}{\hbar}\tilde{H}\tau_p\right]=1-\frac{i}{\hbar}\tilde{H}\tau_p=1+\frac{i}{2}e^{-i\vec{k}\cdot\vec{r}}\hat{\Omega}^{-}+\frac{i}{2}e^{i\vec{k}\cdot\vec{r}}\hat{\Omega}^{+} \tag{12}$$

where

$$\hat{\Omega}^{-} = \sum_b \hat{\Omega}_b^{-} = \tau_p \sum_b \left[\sum_{j=0}^{n_1-1} \chi_{00,1j,b} |00\rangle\langle 1j| + \sum_{j=0}^{n_1-1} \sum_{k=0}^{n_2-1} \chi_{1j,2k,b} |1j\rangle\langle 2k| \right]$$
$$\hat{\Omega}^{+} = \sum_b \hat{\Omega}_b^{+} = \tau_p \sum_b \left[\sum_{j=0}^{n_1-1} \chi_{1j,00,b} |1j\rangle\langle 00| + \sum_{j=0}^{n_1-1} \sum_{k=0}^{n_2-1} \chi_{2k,1j,b} |2k\rangle\langle 1j| \right] \quad (12)$$

Finally, we note that the field-free evolution in the rotating frame can be described by Eqs. (2)-(4), except for the fact that $\omega_{\alpha j,\beta k}$ needs to be replaced by

$$\Delta_{\alpha j,\beta k} = \omega_{\alpha j,\beta k} - \omega_{\alpha\beta}^{rot} \quad (13)$$

IV. Rephasing and nonrephasing signals

Let $\mathbf{k}_\alpha, \mathbf{k}_\beta, \mathbf{k}_\gamma$ be the wave vectors of the first (α), second (β) and third (γ) pulses, respectively. Let the time intervals between pulses α and β be t_1, and between pulses β and γ be t_2. Let t_3 be the time interval between pulse γ and detection. The rephasing and nonrephasing signals are defined as the signal fields measured in the directions $\mathbf{k}_r = -\mathbf{k}_\alpha + \mathbf{k}_\beta + \mathbf{k}_\gamma$ and $\mathbf{k}_{nr} = \mathbf{k}_\alpha - \mathbf{k}_\beta + \mathbf{k}_\gamma$, respectively. These signals can then be calculated based on the algorithm described below.

We start out with the system at equilibrium ($t = 0_-$ implies prior to the first pulse while $t = 0_+$ implies right after the first pulse):

$$\tilde{\sigma}(0_-) = |00\rangle\langle 00| \quad (13)$$

The interaction with the b_α component (b_α =x,y,z) of the first pulse (pulse α) can then be described by:

$$\tilde{\sigma}(0_+) = \left[1 + \frac{i}{2} e^{-i\mathbf{k}_\alpha \cdot \mathbf{r}} \hat{\Omega}_{b_\alpha}^{-} + \frac{i}{2} e^{i\mathbf{k}_\alpha \cdot \mathbf{r}} \hat{\Omega}_{b_\alpha}^{+} \right] \tilde{\sigma}(0_-) \left[1 - \frac{i}{2} e^{-i\mathbf{k}_\alpha \cdot \mathbf{r}} \hat{\Omega}_{b_\alpha}^{-} - \frac{i}{2} e^{i\mathbf{k}_\alpha \cdot \mathbf{r}} \hat{\Omega}_{b_\alpha}^{+} \right] \quad (13)$$

This product can be broken into 9 terms. However, we are only interested in the terms that contribute to the rephasing and nonrephasing signals. Since the *rephasing signal* is along the

wave vector $\mathbf{k}_r = -\mathbf{k}_\alpha + \mathbf{k}_\beta + \mathbf{k}_\gamma$, only the following two terms that go as $e^{-i\mathbf{k}_\alpha \cdot \mathbf{r}}$, out of the nine, contribute to it:

$$\tilde{\sigma}(0_+) \xrightarrow{\text{rephasing}} \frac{i}{2} e^{-i\mathbf{k}_\alpha \cdot \mathbf{r}} \left[\hat{\Omega}^-_{b_\alpha} \tilde{\sigma}(0_-) - \tilde{\sigma}(0_-) \hat{\Omega}^-_{b_\alpha} \right] \tag{13}$$

Similarly, for the *nonrephasing signal*, which is along $\mathbf{k}_{nr} = \mathbf{k}_\alpha - \mathbf{k}_\beta + \mathbf{k}_\gamma$, only the following two terms that go as $e^{i\mathbf{k}_\alpha \cdot \mathbf{r}}$ contribute to it:

$$\tilde{\sigma}(0_+) \xrightarrow{\text{nonrephasing}} \frac{i}{2} e^{i\mathbf{k}_\alpha \cdot \mathbf{r}} \left[\hat{\Omega}^+_{b_\alpha} \tilde{\sigma}(0_-) - \tilde{\sigma}(0_-) \hat{\Omega}^+_{b_\alpha} \right] \tag{13}$$

In the next step, the field-free evolution between pulses α and β is obtained by solving the QMEs, Eqs. (2)-(4), in the rotating frame. More specifically, by writing the QME for $\tilde{\sigma}_{\alpha j,\beta k}(t)$ in the following way,

$$\frac{d}{dt} \tilde{\sigma}_{\alpha j,\beta k}(t) = -i\Delta_{\alpha j,\beta k} \tilde{\sigma}_{\alpha j,\beta k}(t) - \sum_{\gamma m,\delta n} \mathbf{R}_{\alpha j,\beta k;\gamma m,\delta n} \tilde{\sigma}_{\gamma m,\delta n}(t) \tag{13}$$

where $\left\{ \mathbf{R}_{\alpha j,\beta k;\gamma m,\delta n} \right\}$ stand for the relaxation coefficients given explicitly in Eqs. (2)-(4), it can be easily shown that:

$$\vec{\tilde{\sigma}}(t_{1-}) = \exp(-i\boldsymbol{\Delta} t_1) \exp(-\mathbf{R} t_1) \vec{\tilde{\sigma}}(0_+) \tag{13}$$

Here, $\boldsymbol{\Delta}$ is the diagonal matrix detuning matrix:

$$\boldsymbol{\Delta} = \begin{pmatrix} 0 & 0 & 0 & \cdots \\ 0 & \Delta_{10,00} & 0 & \cdots \\ 0 & 0 & \Delta_{11,00} & \cdots \\ \vdots & \vdots & \vdots & \ddots \end{pmatrix} \tag{13}$$

and $\exp(-\mathbf{R}t_1)$ can be obtained by numerical diagonalization of the $\mathbf{R}$ matrix.

The interaction with the b_β component of the second pulse is treated similarly to that of the first pulse. In the case of rephasing ($\mathbf{k}_r = -\mathbf{k}_\alpha + \mathbf{k}_\beta + \mathbf{k}_\gamma$), only the two terms as $e^{i\mathbf{k}_\beta \cdot \mathbf{r}}$ contribute:

$$\tilde{\sigma}\left(t_{1+}\right) \xrightarrow{\text{rephasing}} \frac{i}{2} e^{i\mathbf{k}_\beta \cdot \mathbf{r}} \left[\hat{\Omega}^{+}_{b_\beta} \tilde{\sigma}\left(t_1\right) - \tilde{\sigma}\left(t_1\right) \hat{\Omega}^{+}_{b_\beta} \right] \tag{13}$$

Similarly, for the *nonrephasing signal* ($\mathbf{k}_{nr} = \mathbf{k}_\alpha - \mathbf{k}_\beta + \mathbf{k}_\gamma$) only the two terms like $e^{-i\mathbf{k}_\beta \cdot \mathbf{r}}$ contribute:

$$\tilde{\sigma}\left(t_{1+}\right) \xrightarrow{\text{nonrephasing}} \frac{i}{2} e^{-i\mathbf{k}_\beta \cdot \mathbf{r}} \left[\hat{\Omega}^{-}_{b_\beta} \tilde{\sigma}\left(t_{1-}\right) - \tilde{\sigma}\left(t_{1-}\right) \hat{\Omega}^{-}_{b_\beta} \right] \tag{13}$$

The field-free time evolution between pulses β and γ is then obtained similarly to that between pulses α and β

$$\vec{\tilde{\sigma}}\left(t_1 + t_{2-}\right) = \exp\left(-i\boldsymbol{\Delta} t_2\right) \exp\left(-\mathbf{R} t_2\right) \vec{\tilde{\sigma}}\left(t_{1+}\right) \tag{13}$$

This is followed by the interaction with the b_γ component of the third pulse which is treated similarly to that of the first and second pulses. In this case, both rephasing ($\mathbf{k}_r = -\mathbf{k}_\alpha + \mathbf{k}_\beta + \mathbf{k}_\gamma$) and nonrephasing ($\mathbf{k}_{nr} = \mathbf{k}_\alpha - \mathbf{k}_\beta + \mathbf{k}_\gamma$) signals go as $e^{i\mathbf{k}_c \cdot \mathbf{r}}$, so that the following two terms contribute:

$$\tilde{\sigma}\left(t_1 + t_{2+}\right) \xrightarrow[\text{nonrephasing}]{\text{rephasing}} \frac{i}{2} e^{i\mathbf{k}_\gamma \cdot \mathbf{r}} \left[\hat{\Omega}^{+}_{b_\gamma} \tilde{\sigma}\left(t_1 + t_{2-}\right) - \tilde{\sigma}\left(t_1 + t_{2-}\right) \hat{\Omega}^{+}_{b_\gamma} \right] \tag{13}$$

Finally, heterodyne-detection of the signal with polarization along b_δ corresponds to measuring the following expectation value:

$$\left\langle \hat{W}_{b_\delta} \right\rangle (t_1+t_2+t_3) = Tr\left[\hat{\sigma}(t_1+t_2+t_3)\hat{W}_{b_\delta}\right] = Tr\left[e^{-iH_{rot}(t_1+t_2+t_3)/\hbar}\tilde{\sigma}(t_1+t_2+t_3)e^{iH_{rot}(t_1+t_2+t_3)/\hbar}\hat{W}_{b_\delta}\right]$$
$$= Tr\left[\tilde{\sigma}(t_1+t_2+t_3)e^{iH_{rot}(t_1+t_2+t_3)/\hbar}\hat{W}_{b_\delta}e^{-iH_{rot}(t_1+t_2+t_3)/\hbar}\right]$$
$$\propto \left[\sum_{j=0}^{n_1-1} V_{00,1j,b_\delta}\tilde{\sigma}_{1j,00}(t_1+t_2+t_3) + \sum_{j=0}^{n_1-1}\sum_{k=0}^{n_2-1} V_{1j,2k,b_\delta}\tilde{\sigma}_{2k,1j}(t_1+t_2+t_3)\right] \quad (13)$$

Steps 1-8 need to be repeated for different values of (t_1, t_2, t_3) as well as for the $3^4 = 81$ possible tensor elements and orientational averaging need to be performed in order to get the lab-frame spectrum of one's choice (XXXX, XYXY, etc).

6.3 Numerical Simulations

V. Ab initio calculation of the model parameters

The required input parameters include the transition energies and dipole moments, the normal-mode coordinate displacement elements, the classical force-force time correlation functions, and the laser frequency and polarization. Aside from the choice of electronic structure method and MD force fields, our approach is free of adjustable phenomenological parameters. Below we describe how each of these inputs was obtained for $Mn_2(CO)_{10}$.

The fundamental transition frequencies ω_{1j} (Equation (1), Table 6.1) were obtained from infrared absorption and Raman scattering experiments of $Mn_2(CO)_{10}$ in non-polar solvents. We chose to use the experimental frequencies so as to compare the results directly with experiment (see below). Overtone and combination-band anharmonicities (ε_{2j}) are set to 10 cm^{-1}, a value that agrees well with the 2DIR experimental data for transitions between IR active states. Since the modes are highly delocalized, we expect the anharmonicities of the dark states to remain similar to those of the IR active ones. Alternatively, second-order vibrational perturbation theory (VPT2) can be used to obtain the transition frequencies for the first- and second-manifold states. We have recently shown that VPT2 gives excellent agreement with experiment for the case $Mn_2(CO)_{10}$ and its two photoproducts $Mn_2(CO)_9$ and $Mn(CO)_5$ (see Ref 35 for full details). The transition dipole moments were obtained from a

harmonic analysis of $Mn_2(CO)_{10}$ using a Hessian derived from density functional theory. Electronic structure calculations were carried out using the Becke 1986 exchange and Perdew correlation functionals (BP86)[71, 72] combined with a LANL2DZ pseudopotential basis[73] on the Mn atoms and a 6-31G(d) basis on the remaining atoms. The optimization gradient convergence was set to 10^{-6} hartree/bohr and the SCF convergences were set to 10^{-10} hartree.

In order to obtain the $q_{l;\alpha j,\alpha k}$ elements of the transport coefficients, the full anharmonic Hamiltonian for the system needs to be diagonalized. The Hamiltonian, which includes third (ϕ_{ijk}) and semi-diagonal fourth order (ϕ_{ijkk}) force constants, was obtained by finite differentiation (see Chapter 5). Briefly, the molecule was displaced along each normal mode in the positive and negative directions and a Hessian was computed for each structure, the difference between the frequencies at the equilibrium and displaced geometries is directly related to the higher order force constants. Once these force constants are known, writing the molecular Hamiltonian is straightforward:

$$H = \tfrac{1}{2}\sum_i \phi_{ii}(q_i^2 + p_i^2) + \tfrac{1}{6}\sum_{ijk} \phi_{ijk} q_i q_j q_k + \tfrac{1}{24}\sum_{ijkk} \phi_{ijkk} q_i q_j q_k^2 \qquad (14)$$

Diagonalizing the 10-oscillator anharmonic Hamiltonian to obtain the wavefunctions remains computationally challenging. To converge the eigenfunctions and energies, a minimum of approximately 7 basis functions per oscillator is needed, within a ten mode system, such as in the present model, the total number of basis functions needed would be 7^{10} or approximately 280 million functions. Although the matrices are sparse, this is beyond the memory capacity of modern computers.

In the present case we include six modes in the Hamiltonian, four IR active modes and two dark modes (Table 1 modes 2 and 8). The Hamiltonian matrix is diagonalized, and the eigenvectors are used to calculate the $q_{l;\alpha j,\alpha k}$ matrix elements to be used in calculating the transport coefficients (Equation (11)). We observe that the diagonal elements ($q_{l;\alpha j,\alpha j}$) which lead to pure dephasing of the inter-band coherences are approximately an order of magnitude larger than the off-diagonal elements ($q_{l;\alpha j,\alpha k;j\neq k}$) which lead to coherence

transfer and population relaxation. We also observe that the elements depend mostly on the third order force constants, as the fourth order force constants have little effect on the final value of the displacement elements.

Table 6.1: Experimental transition frequencies for the ground-to-first-manifold transitions of $Mn_2(CO)_{10}$ obtained from a. infrared absorption[35] and b. Raman scattering[74] in nonpolar solvents, along with the anharmonicities for the infrared active states (bold) obtained from transient infrared absorption experiments.[35]

Mode	Experiment	
	$\omega_{1j}+\varepsilon_{1j}(cm^{-1})$	$\varepsilon_{2j}(cm^{-1})$
1	1981[a]	
2	1981[a]	
3	1983[b]	-11
4	1997[a]	
5	2014[b]	-13
6	2014[b]	-13
7	2024[a]	
8	2024[a]	
9	2044[b]	-15
10	2116[a]	

The force-force time correlation functions were obtained from a two-nanosecond molecular dynamics simulation of Mn_2CO_{10} in cyclohexane. The general Amber force field[75] was used to model the solvent and a custom force field was developed for Mn_2CO_{10},[76] all bonds were kept rigid using the SHAKE algorithm.[77] The equilibration and production trajectories were run within the Canonical ensemble (NVT) at 300 K. All MD simulations were carried out using the GROMACS 4.0.5 package of programs.[78] The eigenvectors of the C≡O Hamiltonian in a local-mode basis were used to project the Cartesian forces onto the normal modes of $Mn_2(CO)_{10}$.

The laser polarization was set to [x,y,z] = $[\sqrt{3},\sqrt{3},\sqrt{3}]$ and the center laser frequency was set to 2000 cm^{-1}. In our case the laser is assumed to have infinite spectral bandwidth; the pulse envelope can be straightforwardly implemented by modulating the transition dipole moments to include a resonance overlap term for each transition. The density matrix was propagated for 15 ps along t_1 and t_3 while stepping the value of t_2 from 0.1 to 40 ps in 0.1 ps steps. All the simulations were carried out in the body-fixed molecular frame. In order to simplify the program, reduce the number of loops and avoid coding errors, the eight-index

relaxation terms $\Gamma_{\alpha j,\alpha k;\beta m,\beta n}$ were stored in a standard query language (SQL)-like database and the sums were done by extracting the values through database queries.

6.4 Results and Discussion

VI. Simulation results: system-bath coupling

Figure 6.5 shows the value of the force-force correlation function at $\tau = 0$, $\tilde{C}_{FF}^{cl}(0)$, along the four IR active normal mode coordinates of $Mn_2(CO)_{10}$ and an average correlation function obtained from the molecular dynamics simulations. The diagonal elements along the four normal modes are similar, indicating that the system-solvent interactions are the same for all the modes; this is expected since the modes are highly delocalized. Off-diagonal cross correlations are much smaller than the diagonal autocorrelations, indicating that the force fluctuations along the different modes are essentially uncorrelated. An exponential fit to the average time correlation function over the ten modes gives a decay time constant of 62 fs. The inset shows the frequency-domain behavior of the average correlation function over the 0-135 cm^{-1} range of intraband transitions. The correlation function varies within approximately a factor of three over this range, but for simplicity we assume that the value remains constant. Similar force fluctuations are observed for all ten normal modes regardless of IR activity.

To simplify the calculation of the relaxation coefficients, based on the molecular dynamics results we make the following two approximations: *1.* The autocorrelation functions are the same for all modes and the cross correlations are zero. *2.* The corresponding spectral densities are constant with respect to the frequency gaps between different modes. This allows us to use the simpler form of the system-bath coupling expression as shown in Equation (11).

The $q_{\alpha j,\alpha k}$ elements obtained from the diagonalization of the ab-initio anharmonic Hamiltonian are shown in Figure 6.6. As discussed above, it is presently not possible to include all ten modes, and thus six modes, four infrared active and two dark, were included in the Hamiltonian. The diagonal elements, which lead to pure dephasing, have, on average, higher amplitude than the off-diagonal elements, which lead to coherence transfer.

Consequently, coherence transfer rates are on average slower than the corresponding parent dephasing rates (see Eqs. (3) and (4)).

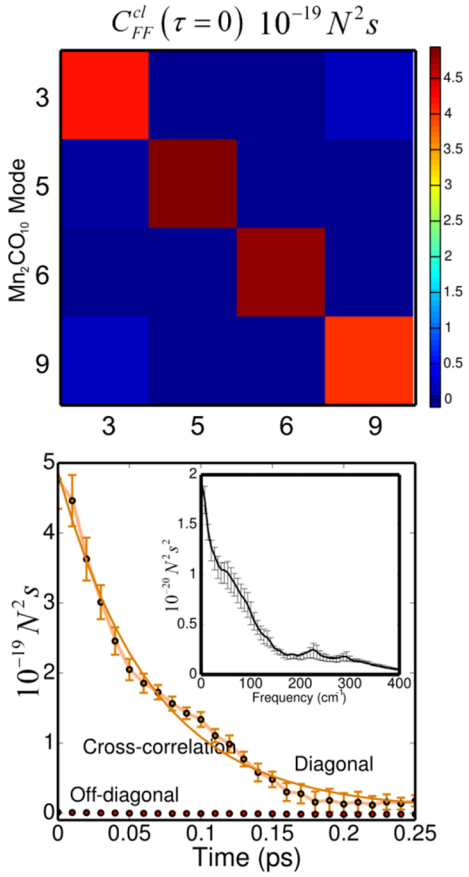

Figure 6.5: (top) Classical force-force time-correlation functions along the four IR active modes of Mn2(CO)10 at . The diagonal terms represent the self-correlation whereas the off-diagonal terms represent the cross-correlations. (bottom) Average diagonal and off-diagonal correlation functions corresponding to the ten modes of Mn2(CO)10 along with a single exponential fit to the diagonal decay. The figure shows that the force along different normal modes remains uncorrelated whereas, on average, the self-correlation decays with a time constant of 62 fs^{-1}. The inset shows the correlation function in the frequency domain obtained by Fourier transforming time-domain function from 0 to 1.5 ps. In both plots the error bars correspond to one standard deviation within the ten-mode average.

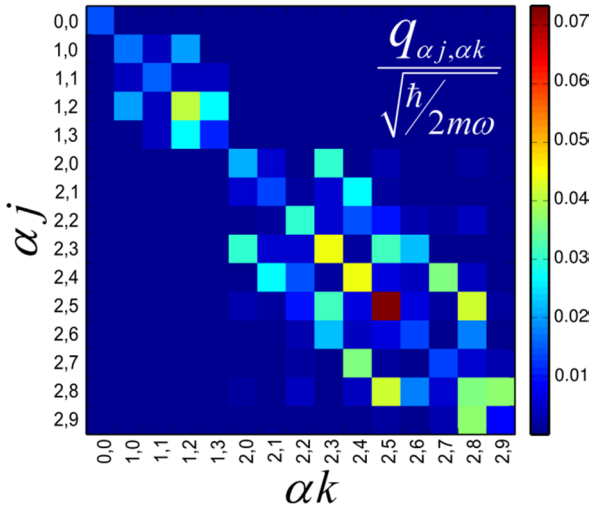

Figure 6.6: Matrix elements corresponding to the anharmonic intra-band transitions. The figure shows the sum of the absolute values over all oscillators dimensionless units: $\sum_l \left| q_{l;\alpha j,\alpha k} \right|$. The first block corresponds to the singly excited states, whereas the second block contains overtones and combination bands.

VII. Discussion of the simulation results

Three different models were devised to test the effect of dark modes on the relaxation and coherence transfer rates. The simplest model (a) contains the four IR active modes of $Mn_2(CO)_{10}$ as shown in Table 6.1; the second model (b) has five modes, four IR active and a single dark mode (mode2, 1981 cm^{-1}); the last model (c) contains four IR active and two dark modes (modes 2 and 7, 1981 and 2014 cm^{-1}). The coupling between the IR active and dark modes is similar for all the dark modes, so the two modes were simply chosen as representative dark modes. It is worth mentioning that the elements of the q matrix are somewhat dependent on the specific modes included in the Hamiltonian, leading to slightly different relaxation rates when different dark modes are included, but the overall trends described below are independent of the specific dark modes included in the simulation.

a. Relaxation rates and two dimensional infrared spectra

Table 6.2 shows the inter-band dephasing time constants (inverse rate) for coherences involving the ground and one-quantum states as well as the population relaxation constants corresponding to the first manifold states for the three model systems. Several

observations can be made from these data. Firstly, the relaxation rates approximately double upon addition of a single dark mode and double again upon addition of the second dark mode. For example, the dephasing times for the coherence involving mode 3 (1983 cm^{-1}) decreases from 12.8 to 5.6 to 3.5 ps as the number of dark modes increases from zero to two. Numerically, this arises from the increase in the number of terms included the system-bath coupling equation (Equation 25) with increasing number of dark modes. The additional dark modes can thus be thought of as an effective strongly coupled "intramolecular bath" that can accelerate the rates of dephasing for the IR active modes. Secondly, it can be observed that coherences and populations involving dark modes generally decay faster than those involving IR active modes. This phenomenon is observed when including different sets of dark modes but it is not clear why these modes should dephase faster since, aside from their transition dipole moments, the dark modes behave similarly to the IR active modes. Unfortunately it is difficult to test this prediction as the dark modes cannot be resonantly probed with infrared spectroscopy. Thirdly, the dephasing and population relaxation rates for the different modes vary over a large range. For example, the population relaxation corresponding to mode five is significantly slower than mode four in all three models. At first this may seem surprising given that that the two modes share the same symmetry and are indeed degenerate. However, in the full ten-mode molecular Hamiltonian, the dark modes at 1981 and 2024 cm^{-1} also have degenerate counterparts, we expect each degenerate mode to be coupled differently to other degenerate modes depending on the specific symmetry and the number of local sites shared. Including one mode from each pair of dark modes in the simulation is what causes the observed differences in the dephasing rates for the degenerate IR active modes. These issues could be avoided by diagonalizing the full Hamiltonian (see above discussion).

Intra-band coherences show similar trends as inter-band coherences, namely the relaxation time constants become faster as additional dark modes are included in the Hamiltonian. Table 6.3 shows the relaxation time constants for coherences involving states within the first manifold, these are the only intra-band coherences that can be accessed with resonant third order experiments such as 2DIR photon echo spectroscopy. Addition of a single dark mode roughly doubles the dephasing time constant. This is consistent with the interpretation of the trends seen in the inter-band coherence rate constants. Figure 6.9

shows the populations, intra-band coherences, and coherence-population coupling rate constants. Diagonal elements, corresponding to pure dephasing and population relaxation, remain larger than the off-diagonal elements corresponding to coherence transfer and population transfer. These results are at odds with the model of Tokmakoff and coworkers, where phenomenological fitting of the peak amplitudes along the waiting time to a Redfield model suggested that in a two-carbonyl system ($Rh(CO)_2C_5H_7O_2$, RDC), the intra-band coherence transfer rate remains very fast (0.35 ps^{-1}) whereas the diagonal dephasing is much slower (10 ps^{-1}).[25] An extra peak appearing below the diagonal in the RDC spectrum was interpreted as evidence for coherence transfer as there are no Liouville paths that lead excitation and detection at those particular frequencies in the rephasing spectrum. There is a possibility that the spectrum at zero waiting time has contributions from intramolecular vibrational redistribution (IVR) between the two first-manifold states of RDC. For example, the experimental laser pulses have a finite width of ~100 fs, IVR could thus give rise to the extra peak even at "zero" time delay. Using the 3 ps^{-1} IVR rate reported in the paper, we should expect 3.2% of the excitation being transferred within the first 100 fs; thus pathways involving IVR between the two one-quantum states should not be discarded, even at zero waiting time. These effects could make the extracted coherence transfer rates appear somewhat faster than their actual values.

Figure 6.7 and Figure 6.8 show the simulated and experimental 2DIR spectra $Mn_2(CO)_{10}$ respectively. Overall the simulations are in good agreement with experiment; the extra peaks observed in the experimental spectrum (i.e. peak 8) are due to naturally occurring isotopologues, containing a single ^{13}CO substitution. Simulated two dimensional spectra for the three model systems show that as extra modes are included, the 2D peaks become broadened. This is due to the faster dephasing of the inter-band coherences observed in models (b) and (c). In a 2D spectrum, the diagonal peaks and corresponding cross peaks involve coherences between the ground and first-manifold states during the excitation and detection times. The peaks appearing below the diagonal, and corresponding cross peaks, involve coherences between the first- and second-manifold states during the detection time. These peaks contain information about the two-quanta states, and are commonly referred to as "anharmonic" peaks. The anharmonic peaks remain broader than the fundamental peaks, indicating that first-to-second-manifold coherences dephase faster than the ground-to-first-

manifold coherences. Two-quanta states exhibit greater anharmonic behavior than the one-quantum states as they sample a larger region of the anharmonic potential (see Figure 6.6). The different widths observed for the three diagonal peaks are due to the fact that the dephasing rates for the different modes can be quite different (see above discussion). The corresponding cross peaks also exhibit different widths along the excitation and detection axes depending on the widths of the parent peaks.

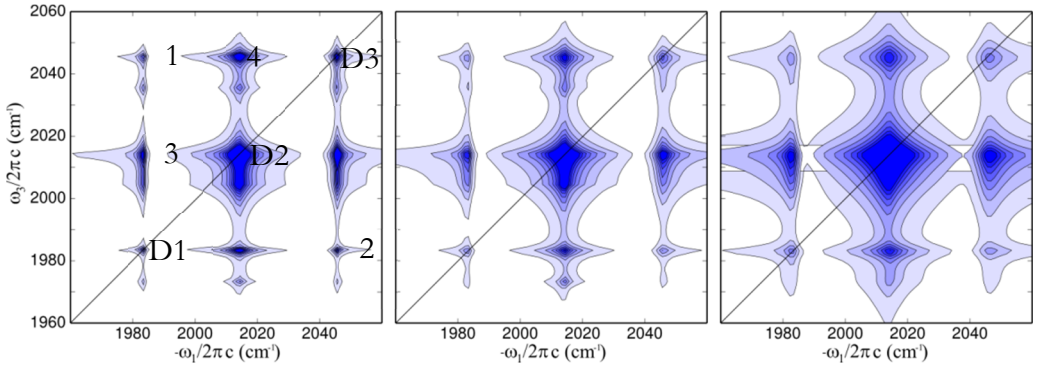

Figure 6.7: Absolute value rephasing spectra of $Mn_2(CO)_{10}$ calculated using three different models: (a)four IR active modes (left); (b) five modes, four IR active plus one dark mode (center); and six modes, four IR active plus two dark modes (right). The figure shows how the peaks become broadened as dark modes are included in the model. The peaks below the diagonal correspond to inter-band coherences involving the first and second manifolds during the detection time t_3. The waiting time dynamics of cross peaks labeled 1-4 are shown in Figure 6.10 and Figure 6.11 below, and the three diagonal peaks labeled D1-D3 shown in Figure 6.13. See text for full details.

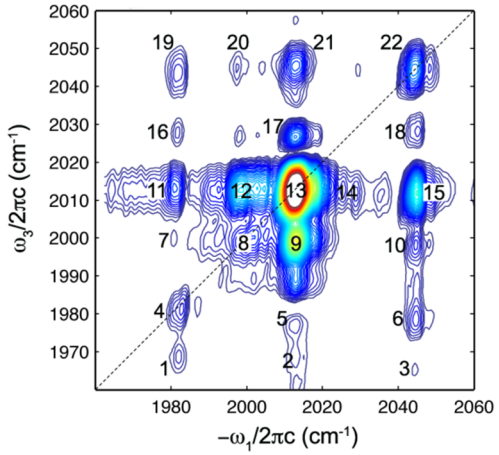

Figure 6.8: Experimental absolute-value rephasing spectrum of $Mn_2(CO)_{10}$ in cyclohexane. Adapted with permission from Nee, M., Baiz, C., Anna, J., McCanne, R., and Kubarych, K., J Chem Phys 129, 084503.(2008). Copyright 2008 American Institute of Physics.

Table 6.2: Inter-band dephasing time constants (ps) for the ground-to-first-manifold coherences and population relaxation rates for the first-manifold states calculated for the three models (a-c).

	Inter-band			Population (1j,1j;1j1j)		
Mode	**4 IR**	**+ 1**	**+ 2**	**4 IR**	**+ 1**	**+ 2**
1981		1.6	1.0		1.3	0.7
1983	12.6	5.8	3.5	6.4	2.9	1.8
2015	5.2	5.2	2.7	104.1	71.2	2.7
2015	2.7	1.5	1.0	2.3	1.0	0.6
2024			0.6			0.4
2045	6.4	3.2	1.7	3.3	1.6	0.9

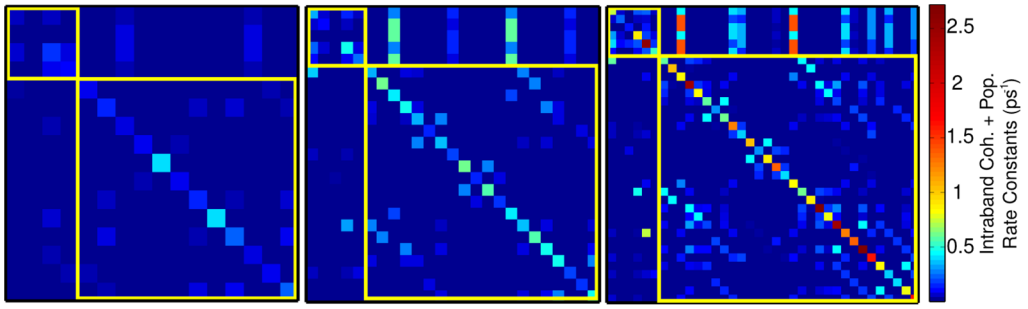

Figure 6.9: Relaxation and transfer rate constants (ps^{-1}) for the populations (small square box in upper left corner) intra-band coherences (large square box in lower right corner) along with the population-coherence coupling constants (off-diagonal blocks). The three matrices from left to right correspond to the three, four, and five mode models respectively. To allow for direct comparison of the rates, all the models are plotted using the same color scale shown on the right.

b. Vibrational dynamics along the waiting time: Coherence transfer and coherence-population coupling

The dynamics of the peaks along the waiting time (t_2) are dictated by the dynamics of the populations and intra-band coherences. Population transfer causes an overall decay of the peak amplitudes whereas intra-band coherences account for the oscillations observed along the waiting time. In the absence of coherence transfer, rephasing and non-rephasing spectra show oscillations of the off-diagonal and diagonal peaks respectively. In this section, we focus on the oscillations of the off-diagonal peaks present in the absolute-value rephasing spectra, as these can be directly compared to experiment.[26] To test the spectral signatures of particular couplings between states (coherence-coherence, coherence-population, etc), we 'switch off/on' the respective contributions by setting the particular rates in the relaxation

matrix to either zero, or their respective values obtained from the system-bath coupling equations.

Table 6.3: Intra-band dephasing time constants (ps) for the first-manifold coherences. The three models are described in the text. Similar to the inter-band coherences and population relaxation rates, faster dephasing is observed when a larger number of dark modes is included.

Intra-band Dephasing (1j,1k;1j,1k)				
		4 IR Active	**+ 1 Dark**	**+ 2 Dark**
1981	1983		1.3	0.8
1981	2015		0.8	0.6
1981	2015		1.1	0.6
1981	**2024**			0.4
1981	2045		1.0	0.6
1983	**1981**		1.3	0.8
1983	2015	3.3	2.5	1.5
1983	2015	2.4	1.2	0.8
1983	**2024**			0.5
1983	2045	4.2	2.0	1.2
2015	**1981**		0.8	0.6
2015	1983	3.3	2.5	1.5
2015	2015	1.1	0.9	0.6
2015	**2024**			0.5
2015	2045	3.3	2.1	1.1
2015	**1981**		1.1	0.6
2015	1983	2.4	1.2	0.8
2015	2015	1.1	0.9	0.6
2015	**2024**			0.4
2015	2045	1.8	1.0	0.6
2024	**1981**			0.4
2024	1983			0.5
2024	2015			0.5
2024	2015			0.4
2024	2045			0.5
2045	**1981**		1.0	0.6
2045	1983	4.2	2.0	1.2
2045	2015	3.3	2.1	1.1
2045	2015	1.8	1.0	0.6
2045	**2024**			0.5

Four cross peaks, labeled 1-4 in Figure 6.7 are selected for analysis of the amplitude along the waiting time. In the absence of off-diagonal coherence-coherence and coherence-population couplings peaks 1 and 2 oscillate at 62 cm^{-1}, the frequency corresponding to the difference between the two parent peaks (1983-2045 cm^{-1}), and peaks 3 and 4 oscillate at a frequency of 32 cm^{-1} which is similarly given by the diagonal frequencies (2013-2045 cm^{-1}). Figure 6.10 and Figure 6.11 show the waiting-time peak oscillations for a selected set of 2D peaks together with the corresponding frequency-domain plots. In order to focus solely on the coherence dynamics, all the population-population couplings were set to zero.

Population transfer gives rise to an overall decay of the peaks but does not induce additional oscillations.

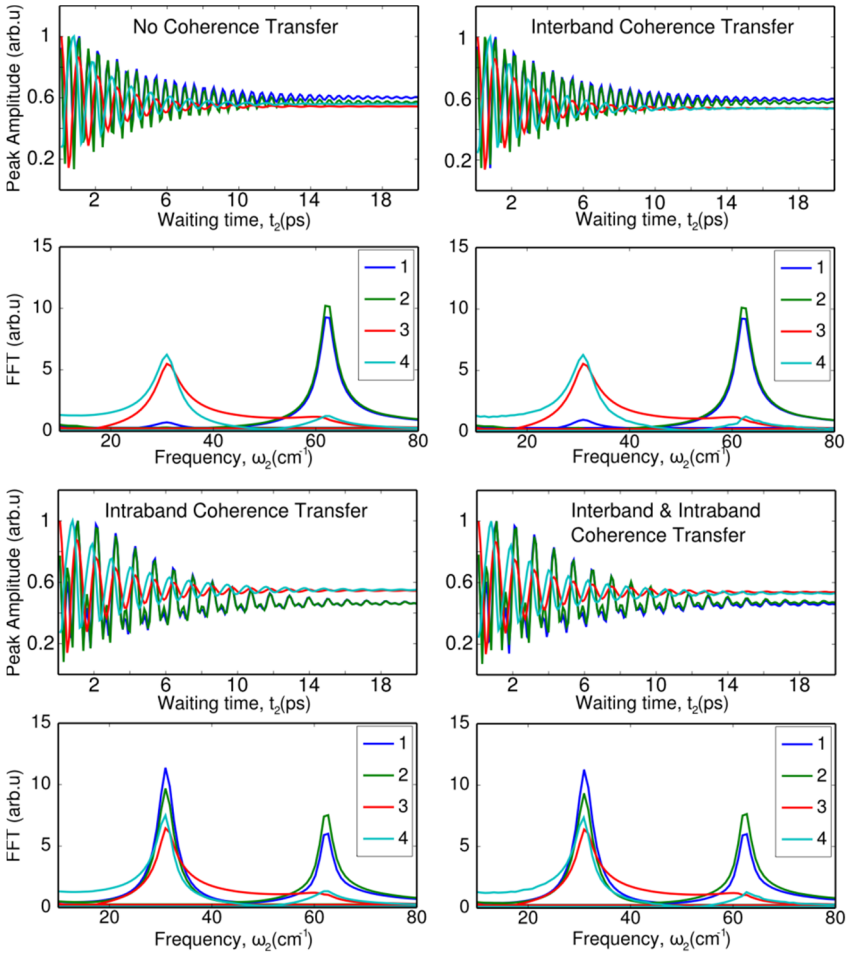

Figure 6.10: Amplitude oscillations along the waiting time corresponding to the peaks labeled 1-4 in Figure 6.7. All the plots were obtained using the model which only includes the four IR active modes of $Mn_2(CO)_{10}$. Each panel shows a plot of the peak oscillations along the waiting time (t_2, ps) with the corresponding Fourier-transforms below (ω_2, cm^{-1}). Spectra were calculated at waiting times ranging from 0 to 40 ps in 0.1 ps intervals, but for clarity the oscillations are only plotted out to 20 ps. To compare the different peak dynamics, the maximum amplitude for each peak is normalized to a value of one. Population-population coupling terms, which lead to an overall decay of the peaks, were set to zero in order to better observe the coherences. In addition to inter-band and intra-band coherence relaxation, the four different simulations show the oscillations when including: (a) only diagonal dephasing, (b) dephasing and inter-band coherence-coherence coupling, (c) dephasing and intra-band coherence-coherence coupling, and (d) dephasing, inter-band and intra-band coherence-coherence coupling as indicated within each individual plot.

Several observations can be made from the simulation results: *1.* The diagonal dephasing rate is similar for all the intra-band coherences, as evidenced by the similar decay rate of the oscillations for the different peaks. Intra-band dephasing rates are shown in Table

6.1 and discussed above. *2.* Inter-band coherence-coherence coupling does not have any significant effect on the oscillations of the peaks along the waiting time. This is not surprising since the peak oscillations are caused by intra-band coherences excited during t_2, and inter-band coherences are only excited during t_1 and t_3. *3.* Intra-band coherence-coherence coupling (coherence transfer) causes peaks 1 and 2 to oscillate at two different frequencies 32 cm^{-1} and 62 cm^{-1}, corresponding to the difference in energy between the three one-quantum levels in the system. In addition, the peaks oscillating at 62 cm^{-1} only show minimal amplitude at 32 cm^{-1}. These results are in good agreement with experiment and are discussed in detail below. *4.* Inter-band coherence-coherence coupling has, once again, no effect on the peak oscillations in the presence of intra-band coupling. We can thus conclude that the dual-frequency oscillation of the peaks is due solely to inter-band coherence transfer. *5.* Coherence-population coupling (Figure 6.11) does not have a significant effect on the oscillation frequencies of the peaks but it does affect the overall peak amplitude ratios.

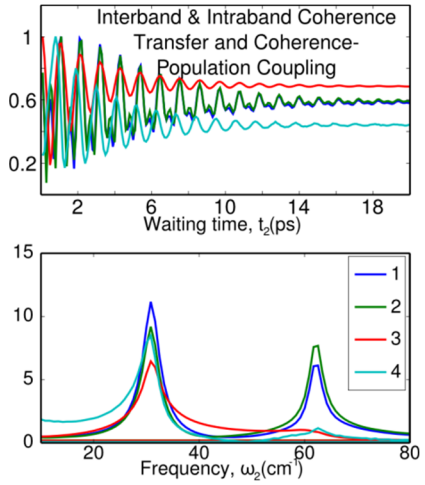

Figure 6.11: Peak amplitude oscillations along the waiting time calculated including coherence-coherence and coherence-population coupling terms. See Figure 6.10 for full description.

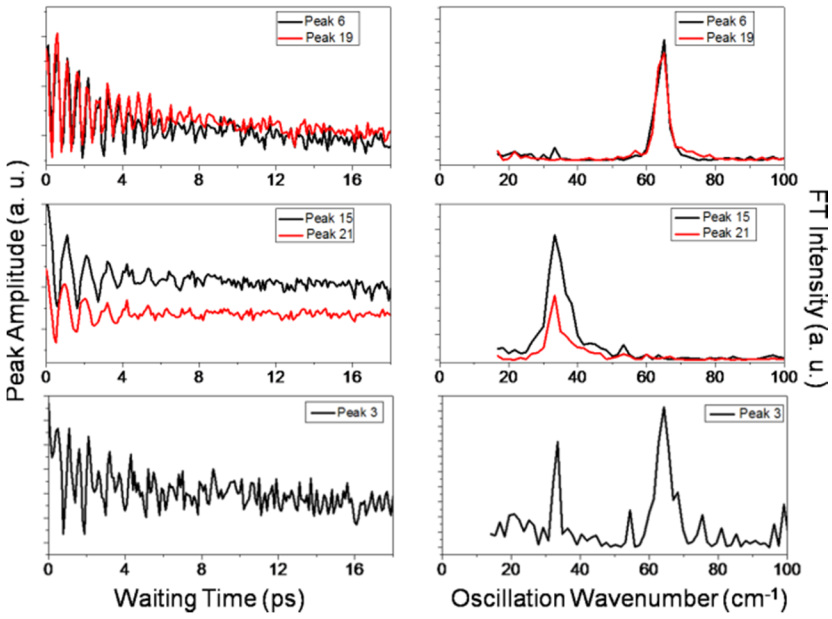

Figure 6.12: Experimental peak amplitude oscillations along the waiting time with their corresponding Fourier-transforms. The labels correspond to the peaks labeled 1-22 in the experimental spectrum shown in -22 in Figure 6.8. The bottom panel (Peak 3) shows the dual-frequency oscillations observed due to of coherence-transfer. Adapted with permission from Nee, M., Baiz, C., Anna, J., McCanne, R., and Kubarych, K., *J Chem Phys 129*, 084503.(2008). Copyright 2008 American Institute of Physics.

c. Dual-frequency oscillations as a signature of coherence transfer: A comparison with experiment

To the best of our knowledge, the observation of dual-frequency oscillations of certain cross peaks in the rephasing spectra of $Mn_2(CO)_{10}$ represented the first direct experimental evidence for vibrational coherence transfer.[26] The theory and simulations presented herein are meant to shed light on the mechanism for coherence transfer in terms of the underlying molecular structure and dynamics. The present simulations are indeed found to be in semi-quantitative agreement with experiment, i.e. intra-band coherence transfer is seen to give rise to dual-frequency oscillations similar to those observed in the experiment. For comparison, the experimental 2DIR spectrum and corresponding peak oscillations for selected peaks are shown in Figure 6.8 and Figure 6.12 respectively. As shown in Figure 6.10 and described in the previous section, in the absence of coherence transfer the cross peaks oscillate at the difference frequency of the corresponding diagonal peaks: 30 (32) cm^{-1} for coherences between the center peak (2013 cm^{-1}) the high- (low-)

frequency peak, and 62 cm^{-1} for coherences involving the high- and low-frequency peaks. Due to the intrinsic dephasing of the oscillations, the 30 cm^{-1} and 32 cm^{-1} coherences are indistinguishable in the frequency-domain plots. Most interestingly, in the presence of coherence transfer, the peaks that normally oscillate at 62 cm^{-1} exhibit dual-frequency oscillations, but the peaks that oscillate 32 cm^{-1} do not. These observations can be straightforwardly explained as follows. Since the 2013 cm^{-1} mode is degenerate, there are eight possible coherences that oscillate at 30 (or 32) cm^{-1} but only two possible coherences at 62 cm^{-1}. Thus, once a 62 cm^{-1} intra-band coherence is created, it is likely that it will be transferred to a 30 (or 32) cm^{-1} intra-band coherence, while the reverse coherence-transfer process is much less probable. In the frequency-domain plots, the largest amplitude component appears near 30 cm^{-1} for all peaks, including the peaks that normally oscillate at 62 cm^{-1}. It can be observed, that even in the absence of coherence transfer all oscillations show a small amplitude component at either low or high frequency. These components arise from the fact that, for absolute-value rephasing spectra, the oscillations are not simply described by a purely sinusoidal function due to the contributions from ground-state pathways (full discussion given in Reference 79). Instead these t_2 oscillations can be described by an equation of the type

$$A(t_2) \propto \left| 1 + e^{-i(\omega_{ab} + i\Gamma_{ab})t_2} \right| \tag{15}$$

Where ω_{ab} represents the difference in frequency between levels a and b, and Γ_{ab} is the dephasing rate constant. These observations are also consistent with the experimental results.

In addition, experimental measurements of the dephasing rates for the intra-band coherences provided a direct observation of the frequency-frequency cross correlation functions for states within the same manifold. Consider the limit where the two frequencies are fully correlated. In this case, the frequency difference is constant and there should be no dephasing of the intra-band coherence. In the other limit, where the frequency fluctuations remain uncorrelated, the intra-band dephasing rate should be similar to the dephasing rate of the ground-to-first-manifold coherences, and thus the Fourier-transform peak widths of the oscillations should exhibit a similar width to that of the parent peaks. Indeed, the

experimental data suggests that the frequency fluctuations are uncorrelated. The results are consistent with the MD simulations which showed that the force fluctuations along different modes remain uncorrelated.

d. Diagonal peak oscillations are induced by coherence-coherence coupling

Liouiville pathways that involve intra-band coherences along t_2 only contribute to off-diagonal peaks in the rephasing signal. In the absence of coherence transfer or coherence-population coupling, the dynamics of the diagonal peaks as a function of the waiting time are solely dictated by the populations and therefore no oscillations should be observed. Monitoring the amplitudes of the diagonal peaks in the rephasing spectrum provides an additional test for coherence transfer and coherence-population coupling.

Figure 6.11 shows the amplitudes corresponding to the three diagonal peaks (D1-D3) simulated using the different relaxation models as indicated in each plot. The upper left plot is calculated using only intra-band and inter-band dephasing. In this case there should be no oscillations observed, however there are very small dual-frequency oscillations present. The oscillations are due to a small overlap between the Lorentzian tails of the oscillating off-diagonal peaks and the diagonal peaks. In the absence of coherence transfer the diagonal peaks oscillate in phase with respect to the off-diagonal peaks, but the phase changes in the presence of coherence transfer, indicating that there are additional effects leading to the oscillations of the diagonal peaks. The lower left panel shows the dynamics in the presence of nonsecular coherence-population coupling terms. In this case the peaks decay exponentially but the oscillations remain small. We can therefore conclude that, within the present model, coherence-population couplings do not induce oscillations of the diagonal peaks but only an additional decay. Experimentally isolating the extra decay due to coherence-population coupling may be difficult as the signal contains relaxation factors from intramolecular vibrational redistribution, orientational relaxation, and vibrational energy relaxation. It is worth noting that similar to coherence transfer, some coherences are strongly coupled to populations, as shown in Figure 6.9. This accounts for the different decay rates observed for the three diagonal peaks.

Unlike coherence-population coupling, coherence transfer does undoubtedly induce extra oscillations of the diagonal peaks, as shown in the upper right panel of Figure 6.13. Naturally, coherence transfer enables new Liouiville pathways that lead to coherences during the waiting time, yet contribute to diagonal peaks. Analogous to the off-diagonal peaks, the oscillation frequency remains at 30 cm^{-1}, as there is a larger number of coherences near this frequency (see discussion in the previous section). Unfortunately, since the oscillation amplitudes are small, roughly 10% of the total peak amplitude in our model, they have not been observed in the experiment. Further theoretical modeling may reveal additional information regarding the coherence-coherence or coherence-population coupling contained in the phase difference between the diagonal and off-diagonal peak oscillations. In our case the phase difference between the diagonal peaks D1 and D3 and the off-diagonal peaks connecting D1 and D3 to the center diagonal peak (D2) is 109±4 degrees. It remains unclear, however, how this phase difference can be interpreted in terms of an interference between different Liouiville paths.

Finally, including coherence transfer and coherence-population coupling terms (Figure 6.13, lower right plot) shows oscillations and an overall decay of the peaks, but no additional features. Thus we conclude that the two effects of coherence-coherence and coherence-population coupling are additive and may be treated separately. From a Liouiville-pathway point of view it is not clear why oscillations are induced by coherence-coherence but not population-coherence coupling as both terms enable new pathways that ought to contribute to oscillations. However, since in our systems there are N[N-1] coherences and N populations, from a probabilistic perspective it is more likely that a coherence will transfer to another coherence instead of to a population. It would be informative to perform similar simulations on smaller systems such as RDC, where there are only two intra-band coherences and two populations. Similar to $Mn_2(CO)_{10}$ no diagonal oscillations of the rephasing spectra have been experimentally observed in RDC.

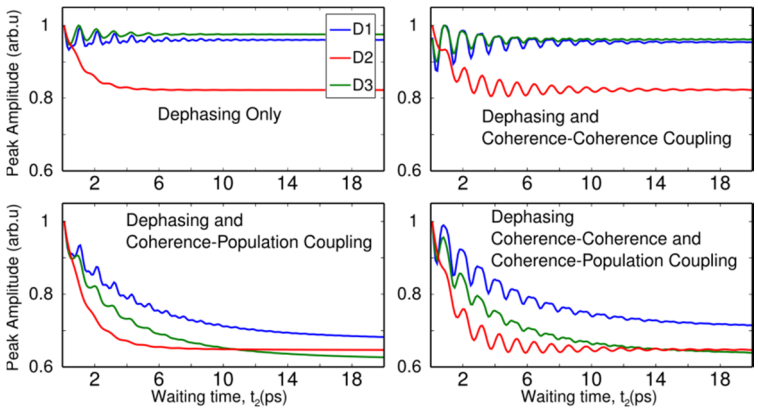

Figure 6.13: Amplitude oscillations of the three diagonal peaks labeled D1-D3 in Figure 6.4. The spectra were obtained using the same model described in Figure 6.10 and Figure 6.11. The relaxation coefficients included in each simulation are indicated within each plot.

We would like to comment on the relationship between our findings and the recent experimental studies[80, 81] which argued that population-coherence coupling, so called quantum entanglement,[82] may contribute to efficient energy transport in photosynthetic complexes. Despite the rapid dephasing that characterizes electronic states, long-lived coherences were observed in these systems even at ambient temperature.[83] In the light of these experiments, Mukamel and coworkers investigated the effect of coherence transfer and coherence-population coupling in excitonic complexes that mimic photosynthetic reaction centers.[84] Their model is different from ours in several respects, including the assumption of bilinear system-bath coupling to a harmonic bath and the fact that the system's dynamics are modeled in terms of a QME of the Linblad type. In contrast to our simulations, the authors observe direct oscillations of the populations, to which they attribute the experimentally observed long-lived oscillatory behavior of the diagonal peaks as a function of the waiting time. The authors concluded that coupling between the populations and the coherences leads to longer-lived coherences, as the populations 'feed' the electronic coherences. In our case coherence-coherence coupling does not lead to oscillations of the populations as these elements remain decoupled from the coherences. Including coherence-population coupling terms leads to multi-exponential evolution of the population with an additional growth and decay for some elements, but not to oscillatory behavior. Furthermore, the transfer rates of coherences to populations are faster than the transfer rates from populations to coherences (Figure 6.9). As a result, coherences can get 'trapped' into populations but not the reverse. The origin for the difference appear to lie in the different

nature of the system (vibrational vs. electronic), the bath (nonpolar liquid vs. protein in aqueous solution) and the coupling between them. In our cases, the relative simplicity of the system allows us to trace back each and every observation to the underlying molecular dynamics and electronic structure, while the same is still not possible in the case of photosynthetic complexes in light of their complexity and the fact that modeling the dynamics of excited electronic states remains extremely challenging for modern electronic structure methods even for systems of modest size. The question of whether the oscillations of populations is an important phenomenon in vibrational systems remains open, but it is clear that coherence transfer can lead to oscillations of the diagonal peaks in the rephasing spectrum. We believe that future ultrafast measurements will further elucidate the complex issue of nonsecular effects, particularly in vibrational systems such as $Mn_2(CO)_{10}$ where peaks remain narrow and coherences long-lived.

6.5 Conclusion and Outlook

We presented a general and comprehensive theoretical and computational framework for modeling ultrafast multidimensional infrared spectra of a vibrational excitonic system in liquid solution. Using this approach we were able to provide new molecular insight into the vibrational dynamics of metal carbonyls. By disentangling the different contributions to the relaxation matrix one can understand the individual signatures of coherence transfer and coherence-population coupling on the spectra. Three different models which included, four, five, and six normal modes were explored in an effort to understand the role of dark modes on the dephasing and coherence transfer rates of our $Mn_2(CO)_{10}$ model system.

The simulation results are consistent with the experimental data and the previous interpretation of the experiment. Coherence transfer leads to dual-frequency oscillations of the cross peaks in the rephasing signal and, in a four level system with a degenerate state like the one presented here, the number of coherences at a given frequency dictates the dominant oscillation frequency for the cross peaks. The uncorrelated fluctuations of the energy levels yield similar inter- and intra-band dephasing rates; thus the width of the low-frequency peaks along ω_2 are similar to the widths of the parent peaks along ω_1 and ω_3. Coherence-population coupling was observed to not have a significant effect on the peak

dynamics, but coherence transfer was observed to lead to dual-frequency oscillations of the cross peaks as well as oscillations of the diagonal peaks. Though the amplitudes seem to remain small, given a suitable signal-to-noise ratio, these effects may be observed in future experiments.

Our approach can provide a rather rigorous theoretical framework for analyzing the vibrational dynamics of a variety of systems, and understanding the system-bath interactions in different combinations of molecules and solvents. The nice agreement of the results with experiment is encouraging. The fact that the simulations predict fine effects such as oscillations of the diagonal peaks in the rephasing spectra, provide motivation for improving the accuracy of the spectra in order to test these predictions experimentally. Importantly, since the model inputs are derived from electronic structure and molecular dynamics simulations, at least in principle, there is no need for employing phenomenological fitting parameters. Once a chemical structure and a solvent are selected, the only 'free' choices are the level of electronic-structure theory and particular choice of molecular dynamics force field. Finally, the model can be readily applied to a wide range of systems and extended to support other nonlinear spectroscopic techniques, as long as the system-solvent interactions remain weak.

It should be noted that the approach presented here relies heavily on the excitonic band structure that makes it possible to distinguish between low frequency intraband and high frequency interband transitions. These distinctions will no longer be valid in a scenario where molecules are strongly coupled to the solvent, for example, in liquid water, so major modifications will have to be made to treat such systems; in addition, it is not yet clear whether it may be possible use a Markovian QME approach in a strongly-coupled system where the bath fluctuations are on the same timescale as the system dynamics and Markovity may not be justified. It should also be noted that that although the linear system-bath coupling mechanism presented here has produced quite satisfactory results, it is not unique. In particular, it would be interesting to test the case of quadratic coupling. Indeed a simulation with quadratic coupling is currently underway and the results will be presented in a future publication. Unlike the linear coupling method, the quadratic coupling equations are greatly simplified by treating the system harmonically.

References

1. M. Cho, "Coherent Two-Dimensional Optical Spectroscopy," Chemical Reviews **108**, 1331-1418 (2008).

2. D. M. Jonas, "Two-dimensional femtosecond spectroscopy," Annual Review of Physical Chemistry **54**, 425-463 (2003).

3. S. Mukamel, "Multidimensional femtosecond correlation spectroscopies of electronic and vibrational excitations," Annual Review of Physical Chemistry **51**, 691-729 (2000).

4. M. D. Fayer, "Dynamics of Liquids, Molecules, and Proteins Measured with Ultrafast 2D IR Vibrational Echo Chemical Exchange Spectroscopy," Annual Review of Physical Chemistry **60**(1), 21 (2009).

5. C. J. Fecko, J. J. Loparo, S. T. Roberts, and A. Tokmakoff, "Local hydrogen bonding dynamics and collective reorganization in water: Ultrafast infrared spectroscopy of HOD/D2O," Journal of Chemical Physics **122**(5), 18 (2005).

6. A. A. Bakulin, C. Liang, T. L. Jansen, D. A. Wiersma, H. J. Bakker, and M. S. Pshenichnikov, "Hydrophobic Solvation: A 2D IR Spectroscopic Inquest," Accounts of Chemical Research **42**(9), 1229-1238 (2009).

7. S. T. Roberts, K. Ramasesha, and A. Tokmakoff, "Structural Rearrangements in Water Viewed Through Two-Dimensional Infrared Spectroscopy," Accounts of Chemical Research **42**(9), 1239-1249 (2009).

8. R. A. Nicodemus, K. Ramasesha, S. T. Roberts, and A. Tokmakoff, "Hydrogen Bond Rearrangements in Water Probed with Temperature-Dependent 2D IR," Journal of Physical Chemistry Letters **1**(7), 1068-1072 (2010).

9. S. Garrett-Roe and P. Hamm, "What Can We Learn from Three-Dimensional Infrared Spectroscopy?," Accounts of Chemical Research **42**(9), 1412-1422 (2009).

10. S. Garrett-Roe and P. Hamm, "Three-point frequency fluctuation correlation functions of the OH stretch in liquid water," Journal of Chemical Physics **128**(10), 104507 (2008).

11. P. T. Callaghan, *Principles of nuclear magnetic resonance microscopy* (Oxford University Press, 1991), pp. xvii, 492 p.

12. J. R. Schmidt, S. T. Roberts, J. J. Loparo, A. Tokmakoff, M. D. Fayer, and J. L. Skinner, "Are water simulation models consistent with steady-state and ultrafast vibrational spectroscopy experiments?," Chemical Physics **341**(1-3), 143-157 (2007).

13. S. A. Corcelli, C. P. Lawrence, and J. L. Skinner, "Combined electronic structure/molecular dynamics approach for ultrafast infrared spectroscopy of dilute HOD in liquid H2O and D2O," Journal of Chemical Physics **120**(17), 8107-8117 (2004).

14. J. Asbury, T. Steinel, C. Stromberg, S. Corcelli, C. Lawrence, J. Skinner, and M. Fayer, "Water dynamics: Vibrational echo correlation spectroscopy and comparison to molecular dynamics simulations," Journal of Physical Chemistry A **108**(7), 1107-1119 (2004).

15. K.-I. Oh, J.-H. Choi, J.-H. Lee, J.-B. Han, H. Lee, and M. Cho, "Nitrile and thiocyanate IR probes: Molecular dynamics simulation studies," The Journal of Chemical Physics **128**(15), 154504-154510 (2008).

16. J. H. Choi, K. I. Oh, and M. H. Cho, "Azido-derivatized compounds as IR probes of local electrostatic environment: Theoretical studies," Journal of Chemical Physics **129**(17), 11 (2008).

17. D. Massiot, F. Fayon, M. Capron, I. King, S. Le Calve, B. Alonso, J. O. Durand, B. Bujoli, Z. H. Gan, and G. Hoatson, "Modelling one- and two-dimensional solid-state NMR spectra," Magnetic Resonance in Chemistry **40**(1), 70-76 (2002).

18. Z. Ganim, K. C. Jones, and A. Tokmakoff, "Insulin dimer dissociation and unfolding revealed by amide I two-dimensional infrared spectroscopy," Physical Chemistry Chemical Physics **12**(14), 3579-3588 (2010).

19. Z. Ganim and A. Tokmakoff, "Spectral signatures of heterogeneous protein ensembles revealed by MD Simulations of 2DIR spectra," Biophysical Journal **91**(7), 2636-2646 (2006).

20. Z. Ganim, H. Chung, A. Smith, L. Deflores, K. Jones, and A. Tokmakoff, "Amide I two-dimensional infrared Spectroscopy of proteins," Accounts of Chemical Research **41**(3), 432-441 (2008).

21. A. W. Smith, J. Lessing, Z. Ganim, C. S. Peng, A. Tokmakoff, S. Roy, T. L. C. Jansen, and J. Knoester, "Melting of a beta-Hairpin Peptide Using Isotope-Edited 2D IR Spectroscopy and Simulations," Journal of Physical Chemistry B **114**(34), 10913-10924 (2010).

22. S. Roy, T. L. C. Jansen, and J. Knoester, "Structural classification of the amide I sites of a beta-hairpin with isotope label 2DIR spectroscopy," Physical Chemistry Chemical Physics **12**(32), 9347-9357 (2010).

23. T. L. Jansen and J. Knoester, "A transferable electrostatic map for solvation effects on amide I vibrations and its application to linear and two-dimensional spectroscopy," Journal of Chemical Physics **124**(4), 11 (2006).

24. T. L. Jansen, A. G. Dijkstra, T. M. Watson, J. D. Hirst, and J. Knoester, "Modeling the amide I bands of small peptides," Journal of Chemical Physics **125**(4), 9 (2006).

25. M. Khalil, N. Demirdoven, and A. Tokmakoff, "Vibrational coherence transfer characterized with Fourier-transform 2D IR spectroscopy," Journal of Chemical Physics **121**(1), 362-373 (2004).

26. M. Nee, C. Baiz, J. Anna, R. McCanne, and K. Kubarych, "Multilevel vibrational coherence transfer and wavepacket dynamics probed with multidimensional IR spectroscopy," Journal of Chemical Physics **129**(8), 084503 (2008).

27. N. Demirdoven, M. Khalil, O. Golonzka, and A. Tokmakoff, "Correlation effects in the two-dimensional vibrational spectroscopy of coupled vibrations," Journal of Physical Chemistry A **105**(34), 8025-8030 (2001).

28. O. Golonzka, M. Khalil, N. Demirdoven, and A. Tokmakoff, "Coupling and orientation between anharmonic vibrations characterized with two-dimensional infrared vibrational echo spectroscopy," The Journal of Chemical Physics **115**(23), 10814-10828 (2001).

29. O. Golonzka, M. Khalil, N. Demirdoven, and A. Tokmakoff, "Vibrational anharmonicities revealed by coherent two- dimensional infrared spectroscopy," Physical Review Letters **86**(10), 2154-2157 (2001).

30. N. Demirdoven, M. Khalil, and A. Tokmakoff, "Correlated vibrational dynamics revealed by two-dimensional infrared spectroscopy," Phys. Rev. Lett. **89**(23), 237401 (2002).

31. M. Khalil, N. Demirdoven, and A. Tokmakoff, "Coherent 2D IR spectroscopy: Molecular structure and dynamics in solution," Journal of Physical Chemistry A **107**(27), 5258-5279 (2003).

32. V. Cervetto, J. Helbing, J. Bredenbeck, and P. Hamm, "Double-resonance versus pulsed Fourier transform two-dimensional infrared spectroscopy: An experimental and theoretical comparison," Journal of Chemical Physics **121**(12), 5935-5942 (2004).

33. C. Baiz, M. Nee, R. McCanne, and K. Kubarych, "Ultrafast nonequilibrium Fourier-transform two-dimensional infrared spectroscopy," Optics Letters **33**(21), 2533-2535 (2008).

34. J. M. Anna, M. J. Nee, C. R. Baiz, R. McCanne, and K. J. Kubarych, "Measuring absorptive two-dimensional infrared spectra using chirped-pulse upconversion detection," Journal of the Optical Society of America B **27**(3), 382-393 (2010).

35. C. R. Baiz, P. L. McRobbie, N. K. Preketes, K. J. Kubarych, and E. Geva, "Two-Dimensional Infrared Spectroscopy of Dimanganese Decacarbonyl and Its Photoproducts: An Ab Initio Study," The Journal of Physical Chemistry A **113**(35), 9617-9623 (2009).

36. C. R. Baiz, P. L. McRobbie, J. M. Anna, E. Geva, and K. J. Kubarych, "Two-Dimensional Infrared Spectroscopy of Metal Carbonyls," Accounts of Chemical Research **42**(9), 1395-1404 (2009).

37. C. R. Baiz, R. McCanne, and K. J. Kubarych, "Transient Vibrational Echo versus Transient Absorption Spectroscopy: A Direct Experimental and Theoretical Comparison," Applied Spectroscopy **64**(9), 1037-1044 (2010).

38. M. J. Nee, R. McCanne, K. J. Kubarych, and M. Joffre, "Two-dimensional infrared spectroscopy detected by chirped pulse upconversion," Optics Letters **32**(6), 713-715 (2007).

39. N. A. Mathew, L. A. Yurs, S. B. Block, A. V. Pakoulev, K. M. Kornau, E. L. Sibert, and J. C. Wright, "Fully and Partially Coherent Pathways in Multiply Enhanced Odd-Order Wave-Mixing Spectroscopy," Journal of Physical Chemistry A **114**(2), 817-832 (2010).

40. A. V. Pakoulev, M. A. Rickard, K. M. Kornau, N. A. Mathew, L. A. Yurs, S. B. Block, and J. C. Wright, "Mixed Frequency-/Time-Domain Coherent Multidimensional Spectroscopy: Research Tool or Potential Analytical Method?," Accounts of Chemical Research **42**(9), 1310-1321 (2009).

41. A. V. Pakoulev, M. A. Rickard, N. A. Mathew, K. M. Kornau, and J. C. Wright, "Frequency-domain time-resolved four wave mixing spectroscopy of vibrational coherence transfer with single-color excitation," Journal of Physical Chemistry A **112**(28), 6320-6329 (2008).

42. A. M. Moran, J. Dreyer, and S. Mukamel, "Ab initio simulation of the two-dimensional vibrational spectrum of dicarbonylacetylacetonato rhodium(I)," The Journal of Chemical Physics **118**(3), 1347-1355 (2003).

43. F. Haake, "Statistical treatment of open systems by generalized master equations," Springer Tracts Mod. Phys. **66**, 98 (1973).

44. R. Alicki and K. Lendi, *Quantum Dynamical Semigroups and Applications* (Springer-Verlag, Berlin, 1987).

45. B. Yoon, J. M. Deutch, and J. H. Freed, "A comparison of generalized cumulant and projection operator methods in spin-relaxation theory," Journal of Chemical Physics **62**, 4687 (1975).

46. I. Oppenheim, K. E. Shuler, and G. H. Weiss, *Stochastic Processes in Chemical Physics: The Master Equation* (MIT Press, Cambridge MA, 1977).

47. S. Mukamel, I. Oppenheim, and J. Ross, "Statistical reduction for strongly driven simple quantum systems," Physical Review A **17**, 1988 (1978).

48. V. Romero-Rochin, A. Orsky, and I. Oppenheim, "Theory of spin relaxation processes," Physica A **156**, 244 (1989).

49. K. Blum, *Density matrix theory and applications* (Plenum, New York, 1996).

50. R. K. Wangsness and F. Bloch, "The dynamical theory of nuclear induction," Physical Review **89**, 728 (1953).

51. A. G. Redfield, "On the theory of relaxation processes," IBM Journal **1**, 19 (1957).

52. N. G. van Kampen, *Stochastic Processes in Physics and Chemistry* (North-Holland, Amsterdam, 1981).

53. R. Kubo, M. Toda, and N. Hashitsume, *Statistical Physics II: Nonequilibrium Statistical Mechanics* (Springer-Verlag, New York, 1985).

54. B. B. Laird, J. Budimir, and J. L. Skinner, "Quantum-mechanical derivation of the Bloch equations: Beyond the weak coupling limit," Journal of Chemical Physics **94**, 4391 (1991).

55. W. T. Pollard, A. K. Felts, and R. A. Friesner, "The Redfield equation in condensed-phase quantum dynamics," Advances in Chemical Physics **XCIII**, 77 (1996).

56. W. T. Pollard and R. A. Friesner, "Solution of the Redfield equation for the dissipative quantum dynamics of multilevel systems," Journal of Chemical Physics **100**, 5054 (1994).

57. E. Geva, R. Kosloff, and J. L. Skinner, "On the relaxation of a two-level system driven by a strong electro-magnetic field," Journal of Chemical Physics **102**, 8541 (1995).

58. E. Geva and R. Kosloff, "The quantum heat engine and heat pump: An irreversible thermodynamic analysis of the three-level amplifier," Journal of Chemical Physics **104**, 7681 (1996).

59. D. Kohen, C. C. Marston, and D. J.Tannor, "Phase space approach to theories of quantum dissipation," Journal of Chemical Physics **107**, 5236 (1997).

60. J. Cao, "Phase space study of Bloch-Redfield theory," Journal of Chemical Physics **107**, 3204 (1997).

61. Y. J. Yan, "Quantum Fokker-Planck theory in a non-Gaussian-Markovian medium," Physical Review A **58**, 2721 (1998).

62. M. Berman, R. Kosloff, and H. Tal-Ezer, "Solution of the time-dependent Liouville-von Neumann equation: Dissipative evolution," Journal Phys. A **25**, 1283 (1992).

63. G. Ashkenazi, U. Banin, A. Bartana, R. Kosloff, and S. Ruhman, "Quantum description of the impulsive photodissociation dynamics of I3- in solution," Advances in Chemical Physics **100**, 229 (1997).

64. G. Ashkenazi, R. Kosloff, and M. A. Ratner, "Photoexcited electron transfer: Short time dynamics and turnover control by dephasing relaxation and control," Journal of the American Chemical Society **121**, 3386 (1999).

65. R. Kosloff, M. A. Ratner, and W. B. Davis, "Dynamics and relaxation in interacting systems: Semigroup approach," Journal of Chemical Physics **106**, 7036 (1997).

66. A. Suarez and R. Silbey, "Hydrogen tunneling in condensed media," Journal of Chemical Physics **94**, 4809 (1991).

67. D. Li and G. A. Voth, "Feynman path integral approach for studying intramolecular effects in proton-transfer reactions," Journal of Physical Chemistry **95**, 10425 (1991).

68. K. F. Everitt, E. Geva, and J. L. Skinner, "Determining the solvation correlation function from three-pulse photon echoes in liquids," Journal of Chemical Physics **114**, 1326 (2001).

69. B. J. Ka and E. Geva, "A nonperturbative calculation of nonlinear spectroscopic signals in liquid solution," Journal of Chemical Physics **125**, 214501 (2006).

70. S. Mukamel, *Principles of nonlinear optical spectroscopy*, Oxford series in optical and imaging sciences 6 (Oxford University Press, New York, 1995),

71. A. D. Becke, "Density-functional exchange-energy approximation with correct asymptotic behavior," Physical Review A **38**(6), 3098 (1988).

72. J. P. Perdew, "Density-functional approximation for the correlation energy of the inhomogeneous electron gas," Physical Review B **33**(12), 8822 (1986).

73. P. J. Hay and W. R. Wadt, "Ab initio effective core potentials for molecular calculations. Potentials for the transition metal atoms Sc to Hg," Journal of Chemical Physics **82**(1), 270-283 (1985).

74. D. M. Adams, M. A. Hooper, and A. Squire, "A Raman spectroscopic study of dimanganese and dirhenium decacarbonyls," Journal of the Chemical Society A, 71-77 (1971).

75. J. Wang, W. Wang, P. A. Kollman, and D. A. Case, "Automatic atom type and bond type perception in molecular mechanical calculations," Journal of Molecular Graphics and Modeling **25**(2), 247-260 (2006).

76. C. R. Baiz, R. McCanne, M. J. Nee, and K. J. Kubarych, "Orientational Dynamics of Transient Molecules Measured by Nonequilibrium Two-Dimensional Infrared Spectroscopy," The Journal of Physical Chemistry A **113**(31), 8907-8916 (2009).

77. Ryckaert, J.-P., Ciccotti, G., and Berendsen, H. J. C. Numerical integration of the cartesian equations of motion of a system with constraints: molecular dynamics of n-alkanes, Journal of Computational Physics *23*, 327-341(1977).

78. D. Van Der Spoel, E. Lindahl, B. Hess, G. Groenhof, A. E. Mark, and H. J. C. Berendsen, "GROMACS: Fast, flexible, and free," Journal of Computational Chemistry **26**(16), 1701-1718 (2005).

79. J. P. Oglivie and K. J. Kubarych, "Chapter 5 Multidimensional Electronic and Vibrational Spectroscopy: An Ultrafast Probe of Molecular Relaxation and Reaction Dynamics," Advances In Atomic, Molecular, and Optical Physics **57**, 249-321 (2009).

80. G. S. Engel, T. R. Calhoun, E. L. Read, T. K. Ahn, T. Mancal, Y. C. Cheng, R. E. Blankenship, and G. R. Fleming, "Evidence for wavelike energy transfer through quantum coherence in photosynthetic systems," Nature **446**(7137), 782-786 (2007).

81. H. Lee, Y. C. Cheng, and G. R. Fleming, "Coherence dynamics in photosynthesis: Protein protection of excitonic coherence," Science **316**(5830), 1462-1465 (2007).

82. S. Mukamel, "Communications: Signatures of quasiparticle entanglement in multidimensional nonlinear optical spectroscopy of aggregates," Journal of Chemical Physics **132**(24), 241105 (2010).

83. E. Collini, C. Y. Wong, K. E. Wilk, P. M. G. Curmi, P. Brumer, and G. D. Scholes, "Coherently wired light-harvesting in photosynthetic marine algae at ambient temperature," Nature **463**(7281), 644-U669 (2010).

84. D. Abramavicius and S. Mukamel, "Quantum oscillatory exciton migration in photosynthetic reaction centers," Journal of Chemical Physics **133**(6), 9 (2010).

Chapter 7

Theoretical Studies of hydrogen-atom transfer reactions

The work presented in this chapter has been published in the following two papers:

1. C.R. Baiz, and B.D. Dunietz, "*Theoretical Studies of Conjugation Effects on Excited State Intramolecular Hydrogen-atom Transfer Reactions in Model Systems*", The Journal of Physical Chemistry A, **111** (40), 10139-10143, 2007.
2. C.R. Baiz, S.J. Ledford, K.J. Kubarych, and Barry. D. Dunietz, "*Beyond 7-Azaindole: Conjugation Effects on Intermolecular Double Hydrogen-Atom Transfer Reactions"* , The Journal of Physical Chemistry A, **113** (17), 4862-4867, 2009

7.1 Introduction

In this chapter we explore molecular conjugation effects and charge delocalization on the thermodynamics of hydrogen-atom transfer; reactions that are central in a variety of chemical and biological processes. The chapter describes two different theoretical studies performed using the same electronic structure methods. In the first part we explore *intramolecular* hydrogen-atom transfer—or tautomerization reactions—in a variety of conjugated with varying degrees of conjugation. In the second study we extend the simulations to *intermolecular* double-hydrogen atom transfer reactions in the ground and excited states.

Intramolecular hydrogen-transfer (IHT) processes have been thoroughly studied experimentally in the ground and excited states[1-10] and theoretically using electronic structure methods.[11-19] Some of these theoretical studies have been revealing unexpected behaviors

related to electronic structure changes induced upon excitation.[13, 20] With the recent development of new ultrafast spectroscopic methods such as infrared echo peak shifts and two-dimensional infrared spectroscopy,[21-23] it has become possible to directly observe reaction dynamics, including hydrogen bonding,[24-26] in real-time with femtosecond time resolution. In addition, non-equilibrium multidimensional spectroscopy can follow dynamics induced by photoexcitation[27, 28] and thus offer insight into the mechanisms of hydrogen-atom transfer. We believe that the studies presented here will aid in the development of future experiments and the interpretation of the results.

Because many theoretical studies use smaller model systems to mimic IHT reactions in larger, more conjugated, systems, it is important to investigate the effect of the backbone conjugation on the potential energy surface of the ground and excited state IHT reactions. In this report we use a set of model molecules to obtain a physical insight into the nature of the IHT reaction and the correlation between backbone conjugation and excited state reaction energy barriers. We extend our set of model systems to include Curcumin (Model **IV** in Figure 7.1, which is a natural compound derived from *curcuma longa* known for its antioxidant and anti-inflammatory properties.[29-31] Curcumin and several of its analogs[32] have also shown tumor inhibiting properties and potential as a cure for Alzheimer's Disease.[33]

Intermolecular double hydrogen-atom transfer reactions have been the subject of a large experimental and theoretical effort.[13, 34-39] Beginning with the experimental work of Taylor *et al*, [40]many studies have used simplified model systems such as 7-azaindole dimers to investigate excited-state tautomerization reactions[41-48] where ultraviolet photoexcitation favors hydrogen-atom transfer. Several results have been interpreted in the context of biologically relevant systems such as DNA base-pairs. Therefore, in order to properly interpret and extend previous results, it is important to understand the role of the extended molecule, namely the coupled conjugation, on the thermodynamics of these reactions. Intense debate over the mechanism of these reactions has motivated various theoretical studies as well as multiple experiments; some evidence has been found to support a step-wise[48-51] mechanism while other evidence indicates that the mechanism is concerted[42, 52-55]. The interpretation of these mechanistic studies are further complicated since quantum effects, particularly tunneling, should not be neglected.[44, 56, 57] Most of the debate is focused on the excited state potential energy surface. The heart of this debate stems from the

complexity of the proton-transfer reaction coordinate. The reaction coordinate involves low frequency vibrations that are added to the proton motion between the two nitrogen sites. The time scale of the excited state hydrogen transfer is set not only by the N-H stretching motions but also by other low-frequency modes. In this report, however, we focus mainly on utilizing model systems to obtain insight into the effects of extended conjugation on the *thermodynamics* of these reactions in the ground and lowest-excited electronic states without special regard to the mechanism.

7.2 Intramolecular H-atom Transfer: Computational Methods and Models

To study the effects of conjugation on excited state IHT reaction barriers we constructed a set of model molecules where the backbone conjugation is varied as shown in Figure 7.1. We did not include the smallest related system, malonaldehyde, because excited state studies of this system have been previously reported in the literature [14, 58-61] and we have found that the IHT barrier of this small system differs by approximately 10 kJ mol^{-1} in the ground state from our next larger system (Model **I**) whereas the difference in IHT barrier among our models **I-IV** is in the order of 2 kJ mol^{-1}. Thus malonaldehyde is inherently a different system and not an accurate model for the bigger molecules involving backbone conjugation.

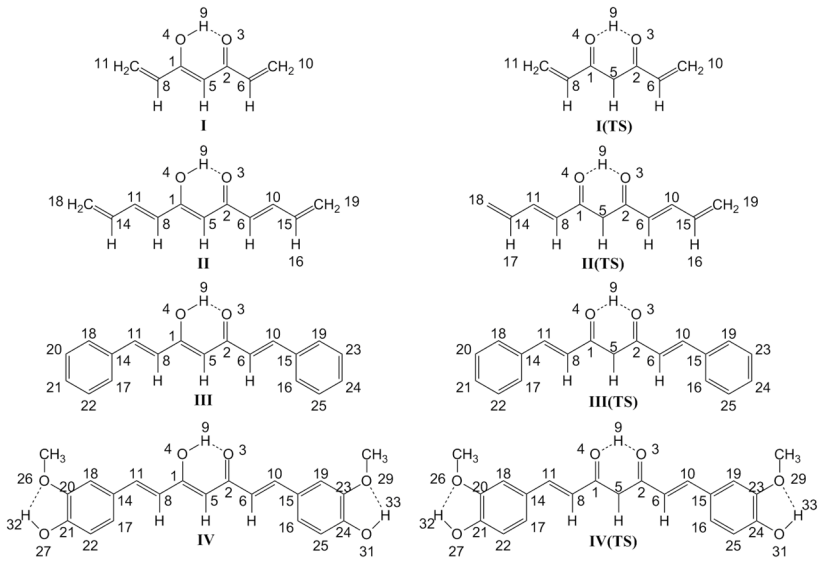

Figure 7.1: Molecular structures of the four model systems in their enol and transition state (TS) configurations.

Initial structures for all models were obtained with the Density Functional Theory (DFT) method using Becke's three parameter B3 nonlocal exchange[62] and Lee-Yang-Parr's correlation functional (LYP)[63] with the 6-31G basis set. These ground state geometries were then further optimized with the spin-restricted Hartree-Fock and B3-LYP methods using two different basis sets 6-31G(d) and 6-31++G(d,p), to obtain the final ground state geometries. As previously reported, the planar enol geometry is lower in energy than the non-planar diketo conformation.[64] Excited state geometries were obtained by optimizing the corresponding ground state geometries employing the configuration interaction single-excitations (CIS) method[65] with the spin-restricted Hartree-Fock reference ground state. The same basis sets employed in the ground state computations were used with the CIS method. Excited-state geometries were optimized in the lowest singlet excited state corresponding to the $^1\pi\pi^*$ transition. This particular excited state was chosen because it is the only one of the lower energy states that exhibits a large transition dipole moment.

Due to molecular symmetry, the transition dipole moments corresponding to the two lower energy $^3\pi\pi^*$ and $^3\pi\pi^*$ electronic transitions are exactly zero, whereas the transition dipole moment for the $^1\pi\pi^*$ transition in our Model **IV** system is approximately 4.90 atomic units in the plane of the molecule. Therefore, this state is likely the only (low) excited state experimentally accessible.

Transition state (TS) geometries were obtained by minimizing along all coordinates except for the coordinate corresponding to the IHT reaction. The ground and excited state TS geometries exhibited one imaginary frequency corresponding to the motion of the hydrogen-atom along the IHT reaction coordinate. All calculations were performed employing the pre-release version of QChem 3.1 package of programs.[66] Density of states plots were obtained using our own code implementing a Green's function based description.[67]

The degree of conjugation was measured by defining a generalized non-conjugation index ξ as the difference in length between the longest and shortest carbon-carbon bonds. We focus the analysis of the degree of conjugation on the core of the system involving atoms C_1, C_2, C_5, C_6 and C_8 as shown in Figure 7.1 Therefore, electronic conjugation at this region is referred to as the core-conjugation. The rest of the molecule, which is coupled to

the core, is referred to as the backbone. The core-conjugation is shown below to depend on the extent of the coupled conjugated backbone and to affect the energy barrier for the proton transfer reaction.7.3 Intramolecular Hydrogen-atom Transfer: Results and Discussio

Table 7.1: Ground and excited state total electronic energies (TE) in atomic units, zero point vibrational energies (ZPVE) in atomic units, and corresponding IHT barriers (ΔE) in kJ mol^{-1} calculated at the HF/6-31++G(d,p), HF/6-31G(d) and CIS/6-31++G(d,p), CIS/6-31G(d) respective levels of theory.

	Ground			Excited		
	6-31++G(d,p) Basis					
	TE	**ZPVE**	**ΔE**	**TE**	**ZPVE**	**ΔE**
I	-419.4465919	0.1446018		-419.2619062	0.1409508	
I(TS)	-419.4337271	0.1394943	20.37	-419.2546496	0.1371852	9.16
II	-573.2378096	0.2161481		-573.0721402	0.2151393	
II(TS)	-573.2254591	0.2111569	19.32	-573.0634643	0.210298	10.07
III	-878.5836092	0.3182868		-878.4289042	0.3200015	
III(TS)	-878.5715504	0.3133785	18.77	-878.4190864	0.314784	12.08
IV	-1256.082236	0.3981039		-1255.932156	0.3998218	
IV(TS)	-1256.070387	0.393194	18.22	-1255.922274	0.3945215	12.03
	6-31++G(d,p) Basis					
	TE	**ZPVE**	**ΔE**	**TE**	**ZPVE**	**ΔE**
I	-419.41353	0.1452233		-419.2219327	0.140664	
I(TS)	-419.3985949	0.1401684	25.94	-419.2147256	0.1364043	7.74
II	-573.1928294	0.2172652		-573.0212668	0.2137163	
II(TS)	-573.1784496	0.2121896	24.43	-573.011619	0.208843	12.54
III	-878.5248829	0.3197608		-878.3649958	0.316639	
III(TS)	-878.5107351	0.314682	23.81	-878.3538263	0.3116335	16.18
IV	-1255.998182	0.4002234		-1255.843358	0.397433	
IV(TS)	-1255.984312	0.3951509	23.1	-1255.832051	0.3922107	15.97

The B3-LYP/6-31++G(d,p) method, when applied to model systems (**I-IV**), failed to predict an energy barrier. The obtained barriers, after adding the respective zero point vibrational energy (ZPVE) corrections, were in the order of -3 $kJmol^{-1}$. The DFT method grossly underestimates hydrogen transfer barriers in the ground state. This may be attributed to an overestimation of electron correlation energy. Previous studies have shown that the computed IHT barrier is lowered when electron correlation is added perturbatively to ground state Hartree-Fock calculations,[13] and that the DFT computational method underestimates the ground state proton transfer barrier in $(FHF)^-$.[68]

A recent molecular dynamics study suggests that this barrier completely vanishes in the $^1\pi\pi^*$ state.[20] However, it is important to point out that the overall decrease in ground state hydrogen-atom transfer barrier with increasing backbone conjugation, as discussed below, was correctly predicted by the B3-LYP method.

Table 7.2: Generalized non-conjugation coefficient ξ (in Å) for each of the models in Figure 7.1. The different basis sets show nearly identical results. A smaller value of ξ represents a more conjugated system as the variance in the C-C bond lengths is smaller. The results show that the degree of conjugation increases in the excited state. Also it is observed that the conjugation dependence on the molecule size is different for the electronic state and for the transition state.

	Ground		**Excited**	
Model	**enol**	**TS**	**enol**	**TS**
	6-31++G(d,p) Basis			
I	0.135	0.075	0.046	0.001
II	0.126	0.068	0.052	0.003
III	0.125	0.068	0.057	0.008
IV	0.123	0.066	0.061	0.011
	6-31G(d) Basis			
I	0.137	0.076	0.043	0.001
II	0.129	0.069	0.051	0.004
III	0.128	0.069	0.056	0.007
IV	0.126	0.067	0.061	0.011

As previously reported,[69] the computed ground state IHT barriers are not strongly dependent on the choice of basis set. We have observed that the ground state IHT barriers predicted by the 6-31G(d) basis set are on average 5 kJ mol^{-1} higher than those predicted by the larger 6-31++G(d,p) basis set. As shown in Table 7.1, ground state IHT barriers are in the order of 18-20 kJ mol^{-1} and 23-26 kJ mol^{-1} as calculated with the 6-31++G(d,p), and 6-31G(d) basis sets respectively. The excited state barriers are more dependent on the choice of basis set; we observe that with the smaller basis set the barrier at the excited electronic state for the small model (**I**) is lowered from 9.16 kJ mol^{-1} to 7.74 kJ mol^{-1} , but in the larger systems this is reversed and the energy barrier with the smaller 6-31G(d) basis set is increased from 12.03 kJ mol^{-1} to 15.97 kJ mol^{-1} in the case of curcumin (Model **IV**).

One important observation is that at the ground electronic state the energy barrier is slightly lowered for the larger systems. The barrier decreases from 20.37 kJ mol^{-1} in Model **I** to 18.22 kJ mol^{-1} in Model **IV** as computed with the larger 6-31++G(d,p) basis set. This

reaction, as revealed by Mulliken charge analysis and comparison of the projected density of states plot of the enol to the identified TS, involves a charge transfer towards the system core. The core atoms are denoted in Figure 7.1 as C_1, C_2, O_3,O_4, C_5 and H_9, whereas the rest are considered the backbone. We find, for example, that for Model **I** the sum of the Mulliken charges on the core atoms changes from -0.286 to -0.319 in the enol to the TS respectively. In addition, the Mulliken analysis reveals that the hydrogen-atom, H_9, becomes more positive in the transition state.

The hydrogen-atom transfer reaction coordinate, therefore, involves the charge transfer from the hydrogen-atom and the backbone of the molecule to the atoms that compose the core, mainly 0_3 and 0_4. In addition we also observe some geometrical relaxation of the core structure along the reaction coordinate as shown in Table 7.3. The data shows that a decrease in the distance between the two oxygen atoms of 0.3 Å occurs as the system moves along the reaction coordinate from the equilibrium to the transition states.

We now compare the different models in the ground state. A Mulliken charge population analysis reveals that the charge on the two oxygen atoms (O_3, O_4) decreases slightly from -0.706 in Model **I(TS)** to -0.703 in model **IV(TS)** in the ground state and that the charge separation between the two oxygens in the enol form decreases from 0.025 in Model **I** to 0.005 in Model **IV**. The charge on the hydrogen-atom (H_9) also decreases from 0.490 in Model **I(TS)** to 0.488 in Model **IV(TS)**. Considering, as shown in Table 7.3, the corresponding O_3-O_4 distances, the values show that the oxygen interatomic distance is smaller (2.606 Å) in Model **IV** than for the less conjugated Model **I** (2.621Å). The decrease in the distance facilitates the hydrogen transfer reaction in the larger systems. These observations suggest that the backbone conjugation helps stabilize the system during the hydrogen-atom transfer process by reducing the charge buildup on the hydrogen atom and the two oxygen atoms involved in the IHT process. Previous studies have shown that the IHT barrier in the ground and excited states decreases linearly with respect to the oxygen-oxygen distance[13], and that more conjugated systems exhibit a lower reaction barrier.[70]

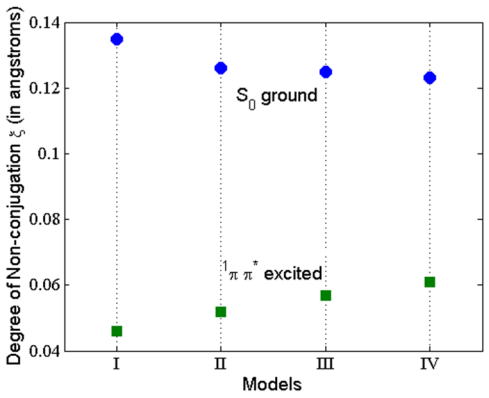

Figure 7.2: Non-conjugation coefficients computed at the HF/6-31++G(d,p) and CIS/6-31++G(d,p) levels of theory for models **I - IV** in the ground state (circles) and $^1\pi\pi^*$ excited state (squares). The plot shows that the systems become more core-conjugated in the excited state with respect to the ground state. Increase in core-conjugation causes a lowering in the IHT barrier.

In the $^1\pi\pi^*$ excited state, the IHT barrier becomes lower compared to the ground state. This decrease in IHT barrier, along with a strengthening of the hydrogen-bond (the $O_3 - H_9$ distance decreases, namely, the longer O-H distance becomes shorter), has been observed previously in other model systems including malonaldehyde.[59, 71] The attachment/detachment electronic densities[72] corresponding to the $1\pi\pi^*$ excitation in Model **I** are provided in Figure 7.3, where the π bonding to anti-bonding transition is very clear. Projected density of states plots confirm that indeed the $^1\pi\pi^*$ excitation does not involve charge redistribution between the core atoms and the rest of the molecule. Therefore the transition state at the electronic excited state is not stabilized by a transfer of charge.

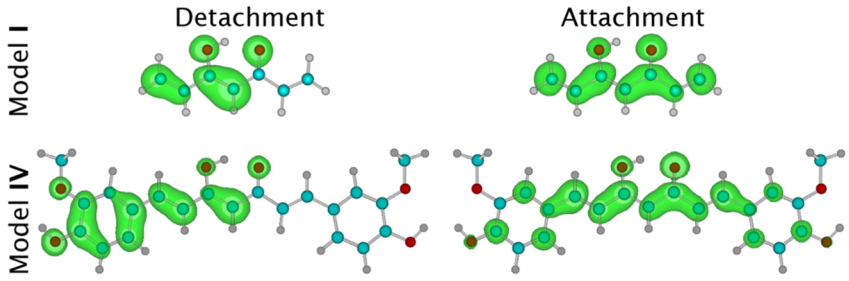

Figure 7.3: Electron attachment (top) and detachment (bottom) density plots involved in the $^1\pi\pi^*$transition in Model **I**. This electronic transition corresponds predominantly to a HOMO-LUMO excitation. As expected, the electronic excitation energy is lower in the larger systems. This excitation energy decreases from 4.70 eV in Model **I** to 3.76 eV in Model **IV** as calculated at the CIS/6-31++G(d,p) level of theory.

In order to obtain further physical insight into the nature of the IHT process and its dependence on conjugation, we consider, now, the generalized non-conjugation ξ coefficient as described in the previous section. A smaller value of ξ represents a more conjugated core system. As expected, we observe that the conjugation of the system increases in the ground state with an increase in the size of the backbone. This is shown in Table 7.2 and Figure 7.2 where ξ =0.135Å and 0.123 Å for models **I** and **IV** respectively. Moreover, when the difference between the two oxygen-carbon bond lengths (C_1-O_4 and C_2-O_3) is considered, a decrease from 0.0836 Å in Model **I** to 0.0808 Å in Model **IV** is observed. This change therefore emphasizes the connection between higher core conjugation and lower ground state IHT barrier. Assuming that conjugation indeed stabilizes the transition state, the decrease in the ground state IHT barrier in larger systems is explained by the decrease in the non-conjugation coefficient along with the equalization of the carbon-oxygen bond lengths. We now turn to analyze the non-conjugation parameter at the electronic excited state.

An important observation is that the overall conjugation of the system is larger in the $^1\pi\pi^*$ excited state compared to the ground state. For example, in Model **I** the non-conjugation coefficient in the ground state (ξ) equals 0.135 Å, and in the excited state ξ =0.046 Å, indicating the increase in the core-conjugation in the excited state. This is related to the decrease in reaction energy barrier upon excitation.

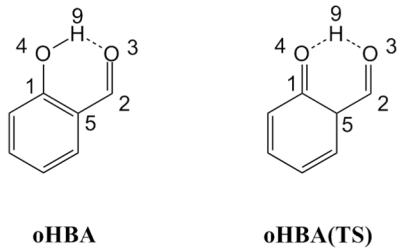

Figure 7.4: Molecular structure of o-hydroxybenzaldehyde (oHBA) in its enol and transition state (TS) configurations.

A related geometrical feature is revealed when the C_1-O_4 and C_2-O_3 distances are considered. The difference between these two distances decreases from 0.097 Å in the ground state to 0.057 Å in the excited state. Most importantly, the non core-conjugation coefficients become larger for the larger systems in the excited state. This suggests that the larger systems, which are more conjugated in the ground state, become less core-conjugated

than the smaller systems upon $^1\pi\pi^*$ excitation. Thus the reaction barrier for smaller systems is lower compared to larger systems in the excited state.

Table 7.3: Distances (R, in Å) and angles (A, in degrees) for Models **I** and **IV** calculated with the HF/6-31++G(d,p) method in the ground state, S^0, and CIS/6-31++G(d,p) method in the excited $^1\pi\pi^*$ state.

	S0 **I**(enol, TS)	ππ* **I**(enol, TS)	S0 **IV**(enol, TS)	ππ* **IV**(enol, TS)
R(O_4-H_9)	0.959, 1.185	0.976, 1.195	0.961, 1.184	0.966, 1.187
R(O_3-H_9)	1.795, 1.185	1.683, 1.195	1.769, 1.184	1.727, 1.187
R(O_3-O_4)	2.621, 2.320	2.559, 2.342	2.606, 2.321	2.587, 2.333
R(C_1-C_5)	1.355, 1.401	1.447, 1.440	1.358, 1.401	1.402, 1.417
R(C_5-C_2)	1.454, 1.401	1.434, 1.440	1.452, 1.401	1.433, 1.417
R(C_1-O_4)	1.316, 1.265	1.305, 1.227	1.318, 1.270	1.325, 1.285
R(C_2-O_3)	1.219, 1.265	1.248, 1.227	1.224, 1.270	1.242, 1.285
A($C_1O_4H_9$)	109.3, 103.2	108.7, 103.8	108.8, 103.1	108.3, 103.2
A($C_1C_5C_2$)	121.8, 116.8	122.3, 118.5	121.9, 117.2	122.2, 118.4

We now focus on the relation of backbone-conjugation to the proton-transfer process, especially at the excited state level. In a previous study, in a model where an aromatic ring is directly part of the IHT core (Figure 7.4) a decrease in IHT barrier upon excitation is associated with a *decrease* in the aromaticity of the considered molecule.[13] We note that this is consistent with our observations above where an *increase* in the conjugated backbone leads to an *increase* of the reaction barrier at the excited state, while we find that the backbone-conjugation in our models is changing only slightly. In this regard, we have first examined the aromaticity in oHBA molecule using the same computational tools as described above and have confirmed the decrease in the aromaticity of the benzene ring in the transition state oHBA(TS) compared to the enol form. We found that the non-aromaticity parameter corresponding to the coupled benzene ring bonds increases from $\xi_{benzene}$=0.029 Å in the enol form to 0.075 Å in the transition state confirming the decrease in aromaticity at the excited state. We comment that these are bigger changes than observed on the backbone-conjugation of the model systems considered in our study above. However, more importantly, *we find that also for this system as in the above considered models systems the core-conjugation actually increases in the transition state with respect to the enol form* (ξ =0.063 Å in enol reduces to 0.034 Å in the TS). We have also analyzed the oHBA geometries reported in

the study by Aquino *et al.* [14] where the time-dependent DFT method was employed, and observe that in the $^1\pi\pi^*$ state, the core conjugation increases with respect to the ground state. Previous spectroscopic studies suggest that indeed an increase in conjugation leads to a lower IHT barrier in oHBA.[73]

7.3 Intermolecular Double H-atom Transfer: Computational Methods and Models

In order to investigate the effects of extended conjugation on hydrogen-atom transfer reactions we constructed a set of model systems starting with 7-azaindole dimer and then varying the conjugation by adding aromatic rings in two different positions as shown in Figure 7.5. The models were chosen to test the energetics of hydrogen-transfer with regard to the size of the coupled aromatic system as well as the position of the added rings.

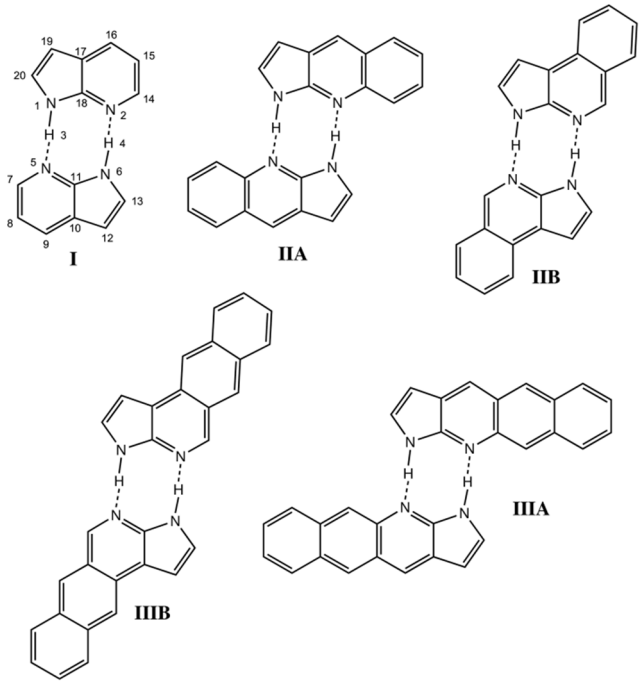

Figure 7.5: Molecular structures of the five model systems in their normal base pair (BP) configurations. The atom numbering indicated in Model **I** (7-azaindole C_{2h} dimer) is the used for all models.

In all the systems detailed below the two sites are only coupled by hydrogen bonding interactions. The change in proton-transfer energy due to the varied conjugation is discussed in detail below. Structure optimizations and harmonic frequency analyzes in the

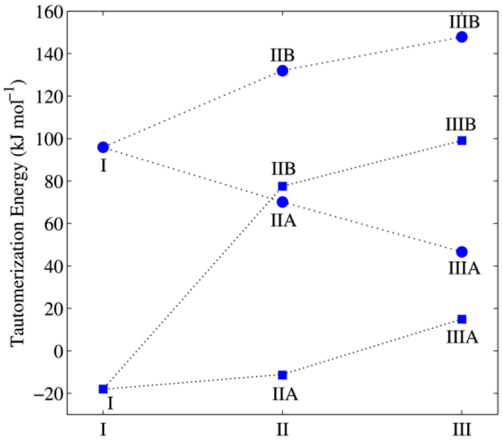

Figure 7.6: Tautomerization energies for our model systems in the ground (circles) and excited (squares) electronic states. The plot shows a similar trend in the ground and excited states (i.e. addition of a ring in the **B** position raises the energy required for tautomerization. Dashed lines serve only to guide the eye and do not indicate continuity.

ground state were performed using spin-restricted Hartree-Fock theory with the 6-31G(d) Pople basis set. Excited-state geometries were optimized starting from the corresponding ground-state geometries using the configuration interaction single-excitations (CIS) method[65] with the corresponding Hartree-Fock reference ground state. We note that the use of optimized structures at the DFT level and the extension of the basis set to use polarizing basis function (6-31++G(d,p)) have not changed significantly the energetic differences as reported below. For example, upon using the larger basis-set the ground state tautomerization energies only decreased by 3-6 kJ/mol, which is much smaller than the observed energy differences between the different models. Therefore, our analysis of the energetic trends due to the extended conjugation remains unaffected by the addition of polarization functions. Additionally, density functional theory [B3LYP/6-31++G(d,p)] yields similar ground-state results. Although the DFT energy differences are about 60% smaller than Hartree-Fock, the observed trends remain unchanged. The trends in excited-state energies are also reproduced by computing the vertical excitations via time-dependent DFT with the corresponding ground-state geometries. All geometries were optimized in the lowest singlet excited state corresponding to a $^1\pi\pi^*$ excitation. This particular state was chosen as it is the lowest state that leads to tautomerization in 7-azaindole. This excitation predominantly involves the highest occupied and lowest unoccupied molecular orbitals in all

the considered model systems. Equilibrium structures exhibit no imaginary frequencies, indicating true minima in the potential energy surface. All computations were performed using the Q-Chem 3.1 package of programs.[66]

Table 7.4: Ground and excited state total electronic energies (TE) in atomic units, zero point vibrational energies (ZPVE) in atomic units, and corresponding energy differences (ΔE) between base-pair (BP) and tautomer (TAU) in kJ mol^{-1} calculated at the HF/6-31G(d) and CIS/6-31G(d) levels of theory. These data are shown graphically in Figure 7.6

	Ground			**Excited**		
Model	TE	ZPVE	ΔE	TE	ZPVE	ΔE
I [BP]	-754.956 251 5	0.256 631 93		-754.756 422 5	0.251 926 02	
I [TAU]	-754.920 328 7	0.257 223 15	95.9	-754.763 107 5	0.251 750 73	-18.0
IIA [BP]	-1 060.262 20	0.356 311 68		-1 060.088 501	0.352 471 1	
IIA [TAU]	-1 060.236 1 0	0.356 998 52	70.1	-1 060.094 403	0.354 007 33	-11.5
IIIA [BP]	-1 365.545 833	0.456 102 98		-1 365.401 814	0.452 263 99	
IIIA [TAU]	-1 365.528 804	0.456 816 91	45.6	-1 365.397 992	0.454 110 98	14.9
IIB [BP]	-1 060.262 165	0.357 271 02		-1 060.088 479	0.352 649 58	
IIB [TAU]	-1 060.211 962	0.357 325 21	131.9	-1 060.059 358	0.353 063 92	77.5
IIIB [BP]	-1 365.551 406	0.457 277 46		-1 365.404 84 0	0.453 282 3	
IIIB [TAU]	-1 365.494 837	0.457 022 48	147.8	-1 365.367 135	0.453 298 24	99.0

The degree of conjugation was measured by computing a generalized non-conjugation index ξ which is defined as the difference in length between longest and shortest pyridinic C-N bonds. A small value of ξ corresponds to a conjugated system whereas a large value represents a system with alternating single and double bonds corresponding to a specific resonance structure. We note that we analyze the dimer interactions at the different structural minima of the different models by following the N-H bond lengths and by population analysis of the different models. As discussed above, however, the reaction mechanism is complex and may involve additional structural features beyond the evolving distances of the transferred proton between the two nitrogen sites. To ensure that the observed changes in tautomerization energy are due to orbital delocalization and not simple constraints in the carbon-carbon bond lengths imposed by the added rings, we artificially constrained the bonds C_8-C_9,C_{15}-C_{16} and C_7-C_8,C_{14}-C_{15} in Model **I** to the equilibrium ground- and excited-state carbon-carbon bond lengths in the benzene molecule.

No appreciable changes in tautomerization energies were observed, confirming that the differences in energy observed in our models are a consequence of the changes in electronic structure imposed by the extended conjugation of the system.

7.4 Intermolecular Double H-atom Transfer: Results and Discussion

As shown in Table 7.4, ground state tautomerization is highly endothermic in all models, ranging from 45.6 kJ mol^{-1} in Model **IIIA** to 147.9 6 kJ mol^{-1} in Model **IIIB**, while excited state energies range from -18.0 6 kJ mol^{-1} in Model **I** to 99.0 kJ mol^{-1} in Model **IIIB**. These results show that the thermodynamics of tautomerization are highly sensitive to the extended conjugation of the system and that model molecules may not accurately capture the reaction energetics observed in larger systems. The results also indicate that the position of the added rings has a significant effect on the relative tautomerization energies in the ground and excited states. Naturally, a decrease in the energy required for tautomerization can be accomplished by either destabilization of the base pair or stabilization of the tautomer. Bond length and Mulliken charge analyzes, as detailed below, indicate that the energy differences are mainly due to changes in the electronic structure of the tautomers. We will now discuss these effects in detail pertaining to both the ground and excited electronic states.

Ground State

The calculated tautomerization energies of the different models at the ground and excited states are provided in Table 7.4 and Figure 7.6. It is shown that the addition of a ring in position **A** lowers the energy required for tautomerization by 26 kJ mol^{-1} while a ring addition in position **B** increases this energy by 360 kJ mol^{-1} relative to 7-azaindole. Adding a second ring in either position **A** further follows the corresponding trend of the tautomerization.

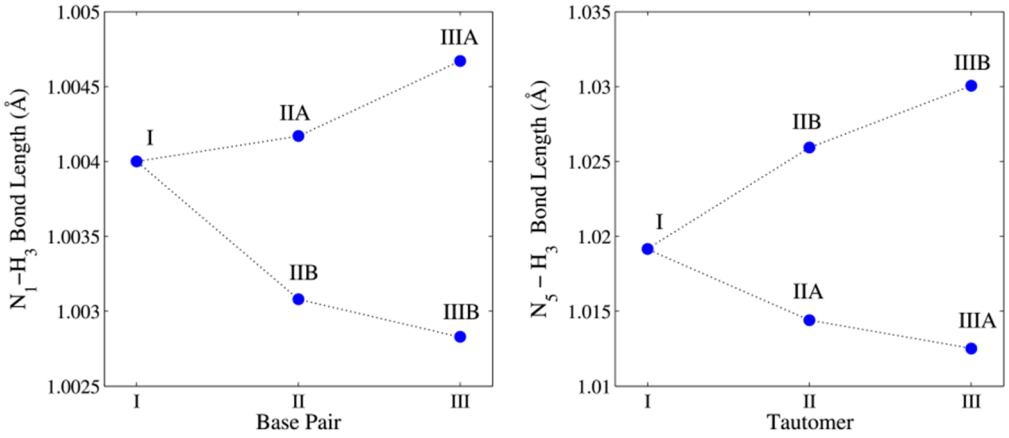

Figure 7.7: N-H Bond lengths for our model systems in the ground state. Lengths corresponding to the base pair are shown on the left plot and the tautomer lengths are shown on the right. Small changes in N-H bond length are observed in the base-pairs, these changes become larger in the tautomer conformations. Note the difference in the ordinate scales.

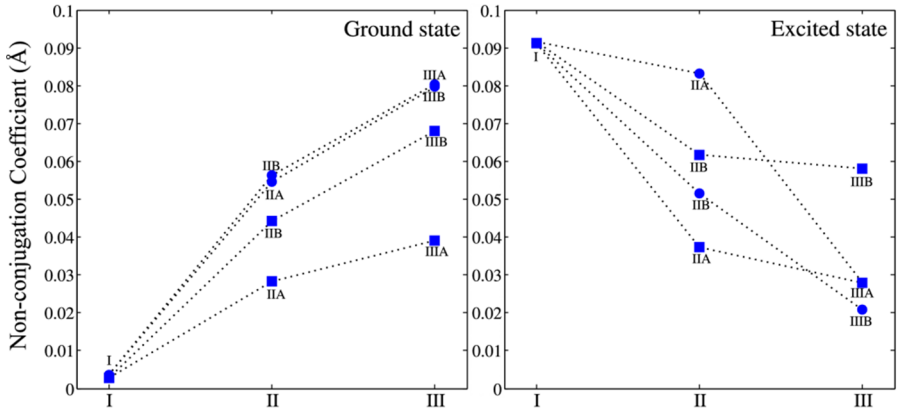

Figure 7.8: Ground and excited-state non-conjugation coefficients (ξ) corresponding to the four models in the base pair (circles) and tautomer (squares) conformations. In the ground state, the coefficient in the base-pairs is similar regardless of the position of the added rings while larger deviations are observed in the tautomers. Electronic excitation decreases the conjugation of 7-azaindole; an increase in conjugation for the excited-state is seen in the larger models.

An N-H bond analysis (Figure 7.7) indicates that a ring added in position **A** tends to stabilize the tautomer but does not have a large effect on the stability of the base pair. The N-H bond lengths remain relatively constant in the base-pair, indicated by a standard deviation of 7.7×10^{-4} Å (Models **I-III**), the same analysis in the tautomeric conformations shows a standard deviation of 1.5×10^{-2} Å indicating a larger change in N-H bond strength. The same analysis for bond lengths (N_2-H_4, N_5-H_3) shows that these bonds are little affected by conjugation in the base pair but exhibit larger variations in the tautomer forms.

Therefore, energy differences are mainly due to stabilization of the tautomer relative to the base pair. Furthermore, Figure 7.7 shows that attaching a ring in position **A** lengthens the N-H bonds in the base pair and shortens them in the tautomer. The addition of a ring in this position slightly destabilizes the base pair while stabilizing the tautomer. These observations are also evident in the ground state energy trends (Figure 7.6). Although the tautomerization energy changes are about equal in magnitude for Models **IIA-IIIA** and **IIB-IIIB** relative to 7-azaindole, the change in bond length is more pronounced in the case of models of the **B** type. It is important to note that the observed changes in bond lengths in systems with different attached conjugation are relatively small overall, but the effect on the energetics of tautomerization is large. This indicates that the position of the added conjugation has large effects on the overall electronic structure of the system whereas the N-H bond lengths are relatively insensitive.

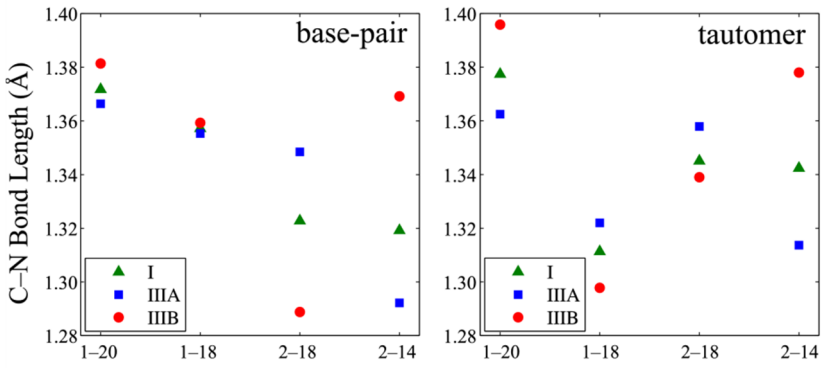

Figure 7.9: Bond lengths corresponding to the four C-N bonds, N_1-C_{20}, N_1-C_{18}, N2-C_{18}, N_2-C_{14}, for the model systems in the ground state. Large deviations are observed in the base-pair and tautomer conformation. The bond-length structure in Model **I** is more closely matched by Model **IIA**.

Further insight into the tautomerization process can be obtained by separating the reaction into dimerization (i.e. hydrogen-bonding) and hydrogen transfer steps. These separate energies are obtained from computing the total energy of each monomer in the normal "base-pair" and "tautomer" conformations and comparing the energies of the monomers to those of the dimers. The results reveal that dimerization energy plays an important role in determining the thermodynamics of the reaction. As expected, dimer formation is more favored in the tautomeric conformation than in the base-pair, thus subtracting from the overall endothermicity of the reaction in the ground state. These results

are in agreement with the previous observations: lower tautomerization energy, achieved mainly by stabilizing the product, shows stronger N-H bonds in the tautomer conformation, which also correlates to lower dimerization energy and weaker intermolecular hydrogen bonds.

We now analyze the conjugation at the core of the hydrogen transfer reaction as measured by the non-conjugation coefficient. The corresponding coefficients are provided in Figure 7.8 for both the base-pair and tautomer forms in the **A** and **B** models. The addition of extra rings decreases the conjugation in the ground state with the base-pairs showing a similar coefficient, regardless of the added ring position, and the tautomers showing a more pronounced difference. It is observed that the **A** models exhibit a larger degree of conjugation than the **B** models in their respective tautomer configurations. It may be argued that the increased conjugation lowers the tautomerization energy by stabilizing the tautomers due to delocalization effects. However, since all larger models exhibit higher conjugation with respect to model **I**, the addition of extra rings enhances a specific resonance structure resulting in more complex effects that compete with the localization that dominates the smaller system.

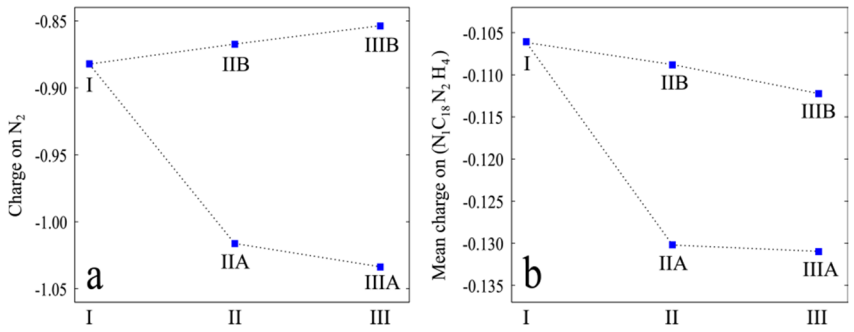

Figure 7.10: Mean Mulliken charge population on (a) N_2 and N_5, and (b) the main reaction center, (N_1,C_{18},N_2,H_4) for the tautomeric configurations. Similar trends are observed in the base-pair conformations (not shown).

The localization effect, due to the addition of extra rings, can be concisely described by considering a detailed bond length analysis provided in Figure 7.9. Two different resonance structures are selected by the addition of a ring in the **A** or **B** position. The position of the added ring enhances the structure corresponding to having a double bond where the ring is attached. Because the most stable resonance structure of models **IIA** and

IIIA more closely matches that of 7-azaindole, tautomerization energy is lower for these two models. In contrast, models **IIB** and **IIIB** enhance the "wrong" resonance structure, and thus tautomerization energy becomes higher for these molecules.

Mulliken charge population analyzes (Figure 7.10) reveal that, in the tautomer conformation, models **IIA**, **IIIA** lead to a larger negative charge on the reaction center. A ring attached to the **A** position increases the ability for charge delocalization, which reduces the buildup of charge on N_2 and N_5, thus stabilizing the tautomer conformation partially by strengthening the N_2-H_4 and N_5-H_1 bonds.

To further highlight the difference in the schemes for adding a ring on delocalization of charge, we consider several simplified model molecules. These simplified systems, illustrated in Figure 7.11, represent monomers **I**, **IIA**, and **IIB** in the tautomeric configuration with the five-membered pyrrole ring removed. The reduced models exhibit the same behavior as the larger systems. Namely, the rings added in scheme **A** couple more efficiently to the central N atom, delocalizing the positive charge on the nitrogen atom more effectively and thus strengthening the N-H bond. Rings added through scheme **B** are however, less effective in their coupling to the core and a dominating resonance structure with the similar charge as the basic model **i** is maintained.

Excited State

The nature of the lowest singlet excitation in 7-azaindole, $^1\pi\pi^*$, has been previously analyzed in detail.[44, 46] Briefly, the excitation is localized in one of the moieties and involves breaking of the C_{2h} symmetry of the dimer, lowering it to a corresponding C_s point group. Bond lengths remain near their ground state values in the unit that does not participate in the excitation, but vary greatly in the unit where the HOMO and LUMO orbitals are localized. Our results indicate that the addition of extra rings does not change the fundamental nature of this excitation. Figure 7.12 shows the frontier orbitals in models **I**, **II** in their respective base-pair conformations computed at the excited state geometries. Vertical excitation energies decrease from 5.0 eV in model **I**, to 3.6 eV in models **IIIA** and **IIIB** in the base-pair configuration. Interestingly, there are no appreciable changes in excitation energy with respect to the position of the added rings. Tautomerization also

lowers the excitation energy, decreasing from 5.0 eV to 3.7 eV in model **I**, and from 3.6 eV to 3.0 eV in model **IIIA**.

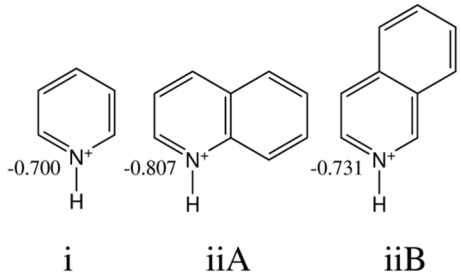

Figure 7.11: Models **i**, **iiA**, **iiB**, representing the addition of rings in positions **A** and **B** in the tautomeric conformations. The figure includes Mulliken charges on the nitrogen atoms. These models were studied in the ground state (singlet, positive charge), at the level of theory described in the methods section. In this configuration a formal positive charge can be assigned to the nitrogen atom.

Excited-state hydrogen-atom transfer is exothermic only in models **I** and **IIA**, and highly endothermic for models **IIB** and **IIIB** (Table 7.4). Unlike the ground state, the effect of the added ring on the excited energy levels in to increase the endothermic nature of the reaction. However, the overall energy trend observed in the ground state, namely, that models **IIA** and **IIIA** exhibit lower tautomerization energy than models **IIB** and **IIIB**, is preserved in the excited state as well. This indicates that the effect of coupled conjugation is similar in both ground and excited states. N-H bond length analyzes (not shown) also confirm the observed trends in the excited state. Additionally, the Mulliken charge trends observed in the ground state (Figure 7.10) are preserved in the excited state.

The differences in tautomerization energies can be understood in terms of the conjugation effects induced by the extra rings. Figure 7.8 shows that the trends in conjugation are *reversed* in the excited state. Larger systems exhibit lower non-conjugation. Previous studies[74] have shown that in the ground-state higher conjugation decreases the barrier for hydrogen transfer whereas the opposite trend is observed in the excited state, lower conjugation shows a smaller barrier. The same behavior is observed for the reaction described here. At the excited state, model **I**, which is the least conjugated exhibits the lowest tautomerization energy. The assumption that excited-state hydrogen-transfer reactions are indeed stabilized by lower conjugation correctly predicts that the least conjugated system, (Model **I**) should exhibit the lowest tautomerization energy in the excited

state (Table 7.4). In addition, it is observed that the tautomerization energies in models **A** are overall lower than models **B** which is evidence that, analogous to the ground state, a lower energy resonance structure is enhanced by the addition of rings in the **A** position.

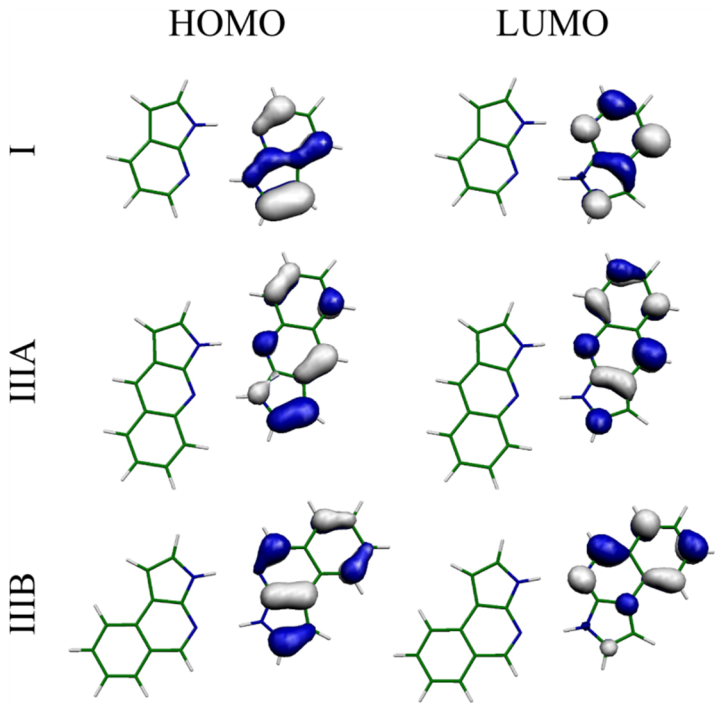

Figure 7.12: HOMO and LUMO orbitals involved in the $^1\pi\pi^*$transitions in models **I**, **IIIA**, and **IIIB** in the base-pair conformation showing a large increase in electron density on N_2 and N_5 upon excitation. The corresponding orbitals in the tautomeric configuration (not shown) exhibit no qualitative difference.

7.5 Conclusion and Summary

The intramolecular hydrogen transfer barriers for various model molecules have been determined using Hartree-Fock and CIS methods. The results show that in the ground state the hydrogen transfer barrier is lower for larger systems. At the ground state, the backbone conjugation helps lower the IHT barrier by stabilizing the transition state. However, this trend is reversed in the $^1\pi\pi^*$ excited state where the barrier increases with the increase of the conjugated backbone. The $^1\pi\pi^*$ excitation clearly is not associated with a redistribution of charge in the molecule. We observe, rather, that upon excitation the core-conjugation increases and therefore the transition state is further stabilized leading to a lowered overall reaction barrier. We find, however, that the increase of the core-conjugation at the excited state is reduced with a larger coupled backbone. This results with an increase

of the reaction barrier with the larger backbone at the excited state level. We finally note that although the extent of the conjugation and reaction barrier trends across the different considered models are relatively small, they offer a great deal of physical insight into the nature of the hydrogen-atom transfer process.

The second study on intermolecular double-hydrogen atoms transfer demonstrates that by modifying the resonance structure of 7-azaindole a large effect on the energy required for tautomerization is observed in the ground and $^1\pi\pi^*$ excited electronic states. Furthermore, the conjugation effect is highly dependent on the structural aspects of coupling the extended conjugated system to the core region. We show that the additional rings in positions **A** or **B** lead to qualitatively different tautomerization energies. This different effect on the conjugation of the system can be understood as reflecting stabilizing of different resonance structures. These effects are noted in N-H bond lengths, dimerization energies, C-N bond analysis, and Mulliken charges near the reaction center.

We find that electronic excitation causes an increase in acidity at the pyrrolic site and corresponding increase in basicity at the pyridinic site, clearly explaining the observed decrease in tautomerization energy relative to the ground state in all our model systems. This is in agreement to previous studies by Catalan.[75] At the ground state, the trends of the tautomerization energies are opposite with respect to adding the conjugation in the two positions. The reaction becomes less endothemic with the increase the coupled conjugation along position **A** and more endothermic for site **B**. At the excited state, this dependence is still overall noted, however, with additional aspects due to nature of the excited state. It is show that for both series (**A** and **B**) the reaction becomes more endothermic at the excited state level upon extending the conjugation.

Most importantly, our calculations demonstrate that the effect of conjugation can inhibit the hydrogen transfer reaction both at the ground and excited states. In all the considered models the geometrical features of the reaction core remain very similar indicating that the energetic effects are purely due to electronic conjugation effects. This effect can be exploited by experimentalists aiming to decouple excitations from hydrogen-atom transfer processes in DNA analogs and yields new insight into the mechanism of these reactions. Additionally, it may be possible to control the tautomerization energy and the

respective reaction barriers by constructing systems with specific resonance structures and by employing mixed base-pairs where the conjugation of each base is different.

References

1. P. F. Barbara, P. K. Walsh, and L. E. Brus, "Picosecond kinetic and vibrationally resolved spectroscopic studies of intramolecular excited-state hydrogen atom transfer," Journal of Physical Chemistry **93**(1), 29-34 (1989).

2. R. Rossetti, R. Rayford, R. C. Haddon, and L. E. Brus, "Proton localization in an asymmetric double-minimum potential: 2-methyl-9-hydroxyphenalenone," Journal of the American Chemical Society **103**(15), 4303-4307 (1981).

3. B. J. Schwartz, L. A. Peteanu, and C. B. Harris, "Direct observation of fast proton transfer: femtosecond photophysics of 3-hydroxyflavone," Journal of Physical Chemistry **96**(9), 3591-3598 (1992).

4. T. Sekikawa, T. Kobayashi, and T. Inabe, "Femtosecond Fluorescence Study of Proton-Transfer Process in Thermochromic Crystalline Salicylideneanilines," Journal of Physical Chemistry B **101**(50), 10645-10652 (1997).

5. A. Grabowska, A. Mordzinski, N. Tamai, and K. Yoshihara, "Picosecond kinetics of the excited-state intramolecular proton transfer reaction: Confirmation of the intrinsic potential barrier in 2,5-bis-(benzoxazolyl)-hydroquinone," Chemical Physics Letters **153**(5), 389-392 (1988).

6. A. Douhal, F. Lahmani, A. Zehnacker-Rentien, and F. Amat-Guerri, "Excited-State Proton (or Hydrogen Atom) Transfer in Jet-Cooled 2-(2'-Hydroxyphenyl-5-phenyloxazole," Journal of Physical Chemistry **98**(47), 12198-12205 (1994).

7. P. M. Felker, W. R. Lambert, and A. H. Zewail, "Picosecond excitation of jet-cooled hydrogen-bonded systems: Dispersed fluorescence and time-resolved studies of methyl salicylate," Journal of Chemical Physics **77**(3), 1603-1605 (1982).

8. S. Lochbrunner, A. J. Wurzer, and E. Riedle, "Microscopic Mechanism of Ultrafast Excited-State Intramolecular Proton Transfer: A 30-fs Study of 2-(2'-Hydroxyphenyl)benzothiazole," Journal of Physical Chemistry A **107**(49), 10580-10590 (2003).

9. K. Stock, T. Bizjak, and S. Lochbrunner, "Proton transfer and internal conversion of o-hydroxybenzaldehyde: coherent versus statistical excited-state dynamics," Chemical Physics Letters **354**(5-6), 409-416 (2002).

10. M. Lukeman and P. Wan, "A New Type of Excited-State Intramolecular Proton Transfer: Proton Transfer from Phenol OH to a Carbon Atom of an Aromatic Ring Observed for 2-Phenylphenol," Journal of the American Chemical Society **124**(32), 9458-9464 (2002).

11. M. A. Rios and M. C. Rios, "Ab Initio Study of the Hydrogen Bond and Proton Transfer in 2-(2'-Hydroxyphenyl)benzothiazole and 2-(2'-Hydroxyphenyl) bezimidazole," Journal of Physical Chemistry A **102**(9), 1560-1567 (1998).

12. S. Scheiner, T. Kar, and M. Cuma, "Excited State Intramolecular Proton Transfer in Anionic Analogues of Malonaldehyde," Journal of Physical Chemistry A **101**(33), 5901-5909 (1997).

13. S. Scheiner, "Theoretical Studies of Excited State Proton Transfer in Small Model Systems," Journal of Physical Chemistry A **104**(25), 5898-5909 (2000).

14. A. J. A. Aquino, H. Lischka, and C. Hattig, "Excited-State Intramolecular Proton Transfer: A Survey of TDDFT and RI-CC2 Excited-State Potential Energy Surfaces," Journal of Physical Chemistry A **109**(14), 3201-3208 (2005).

15. A. L. Sobolewski and W. Domcke, "Theoretical investigation of potential energy surfaces relevant for excited-state hydrogen transfer in o-hydroxybenzaldehyde," Chemical Physics **184**(1-3), 115-124 (1994).

16. M. V. Vener and S. Scheiner, "Hydrogen Bonding and Proton Transfer in the Ground and Lowest Excited Singlet States of o-Hydroxyacetophenone," Journal of Physical Chemistry **99**(2), 642-649 (1995).

17. M. Z. Zgierski, A. Fernandez-Ramos, and A. Grabowska, "Theoretical study of excited state proton transfer in 3,6-bis(benzoxazolyl)pyrocatechol (BBPC)," The Journal of Chemical Physics **116**(17), 7486-7494 (2002).

18. J. Palomar, J. L. G. De Paz, and J. Catalan, "Theoretical Analysis of Molecular Structure, Hydrogen Bond Strength, and Proton Transfer Energy in Aromatic Compounds," Journal of Physical Chemistry A **104**(27), 6453-6463 (2000).

19. J. Catalan, J. Palomar, and J. L. G. de Paz, "Intramolecular Proton or Hydrogen-Atom Transfer in the Ground and Excited States of 2-Hydroxybenzoyl Compounds," Journal of Physical Chemistry A **101**(42), 7914-7921 (1997).

20. N. Doltsinis, "Excited state proton transfer and internal conversion in o-hydroxybenzaldehyde: new insights from non-adiabatic ab initio molecular dynamics," Molecular Physics **102**(5), 499-506 (2004).

21. M. Cho, "Coherent Two-Dimensional Optical Spectroscopy," Chemical Reviews **108**(4), 1331-1418 (2008).

22. D. M. Jonas, "Two-dimensional femtosecond spectroscopy," Annual Review of Physical Chemistry **54**, 425-463 (2003).

23. M. Khalil, N. Demirdoven, and A. Tokmakoff, "Coherent 2D IR spectroscopy: Molecular structure and dynamics in solution," Journal of Physical Chemistry A **107**(27), 5258-5279 (2003).

24. C. Kolano, J. Helbing, M. Kozinski, W. Sander, and P. Hamm, "Watching hydrogen-bond dynamics in a [bgr]-turn by transient two-dimensional infrared spectroscopy," Nature **444**, 469-472 (2006).

25. J. R. Zheng, K. Kwak, J. Asbury, X. Chen, I. R. Piletic, and M. D. Fayer, "Ultrafast dynamics of solute-solvent complexation observed at thermal equilibrium in real time," Science **309**(5739), 1338--1343 (2005).

26. P. B. Petersen, S. T. Roberts, K. Ramasesha, D. G. Nocera, and A. Tokmakoff, "Ultrafast N-H Vibrational Dynamics of Cyclic Doubly Hydrogen-Bonded Homo- and Heterodimers," Journal of Physical Chemistry B **112**(42), 13167-13171 (2008).

27. P. Hamm, J. Helbing, and J. Bredenbeck, "Two-dimensional infrared spectroscopy of photoswitchable peptides," Annual Review of Physical Chemistry **59**, 291-317 (2008).

28. C. R. Baiz, M. J. Nee, R. McCanne, and K. J. Kubarych, "Ultrafast nonequilibrium Fourier-transform two-dimensional infrared spectroscopy," Optics Letters **33**(21), 2533--2535 (2008).

29. O. P. Sharma, "Antioxidant activity of curcumin and related compounds," Biochemical Pharmacology **25**, 1811-1812 (1976).

30. B. A. Srivastava KC, Verma SK., "Curcumin, a major component of food spice turmeric (Curcuma longa) inhibits aggregation and alters eicosanoid metabolism in human blood platelets," Leukot Essent Fatty Acids **52**, 223-227 (1995).

31. Y. M. Sun, H. Y. Zhang, D. Z. Chen, and C. B. Liu, "Theoretical Elucidation on the Antioxidant Mechanism of Curcumin: A DFT Study," Organic Letters **4**(17), 2909-2911 (2002).

32. H. Ohori, H. Yamakoshi, M. Tomizawa, M. Shibuya, Y. Kakudo, A. Takahashi, S. Takahashi, S. Kato, T. Suzuki, C. Ishioka, Y. Iwabuchi, and H. Shibata, "Synthesis and biological analysis of new curcumin analogues bearing an enhanced potential for the medicinal treatment of cancer," Molecular Cancer Therapeutics **5**(10), 2563-2571 (2006).

33. K. Balasubramanian, "Molecular orbital basis for yellow curry spice curcumin's prevention of Alzheimer's disease," Journal of Agricultural and Food Chemistry **54**, 3512-3520 (2006).

34. A. Douhal, F. o. Lahmani, and A. H. Zewail, "Proton-transfer reaction dynamics," Chemical Physics **207**(2-3), 477--498 (1996).

35. L. Gorb, Y. Podolyan, P. Dziekonski, W. A. Sokalski, and J. Leszczynski, "Double-Proton Transfer in Adenine-Thymine and Guanine-Cytosine Base Pairs. A Post-Hartree-Fock ab Initio Study," Journal of the American Chemical Society **126**(32), 10119-10129 (2004).

36. J. D. Zhang, Z. Chen, and H. H. F. Schaefer, "Electron Attachment to the Hydrogenated WatsonCrick Guanine Cytosine Base Pair (GC+H): Conventional and Proton-Transferred Structures," Journal of Physical Chemistry A **112**(27), 6217-6226 (2008).

37. J. Gu, Y. Xie, and H. H. F. Schaefer, "Electron attachment induced proton transfer in a DNA nucleoside pair: 2 [sup [prime]]-deoxyguanosine-2[sup [prime]]-deoxycytidine," Journal of Chemical Physics **127**(15), 155107 (2007).

38. S. Kim, T. Meehan, and H. F. Schaefer, "Hydrogen-Atom Abstraction from the Adenine-Uracil Base Pair," Journal of Physical Chemistry A **111**(29), 6806-6812 (2007).

39. M. C. Lind, N. A. Richardson, S. E. Wheeler, and H. F. Schaefer, "Hydrogen-Abstracted Adenine-Thymine Radicals with Interesting Transferable Properties," Journal of Physical Chemistry B **111**(19), 5525-5530 (2007).

40. C. A. Taylor, M. A. El-Bayoumi, and M. Kasha, "Excited-State Two-Proton Tautomerism in Hydrogen-Bonded N-Heterocyclic Base Pairs," Proceedings of the National Academy of Sciences of the United States of America **63**, 253-260 (1969).

41. M. Chachisvilis, T. Fiebig, A. Douhal, and A. H. Zewail, "Femtosecond Dynamics of a Hydrogen-Bonded Model Base Pair in the Condensed Phase: Double Proton Transfer in 7-Azaindole," Journal of Physical Chemistry A **102**(4), 669-673 (1998).

42. J. Catalan, P. Perez, J. C. Del Valle, J. L. G. De Paz, and M. Kasha, "H-bonded N-heterocyclic base-pair dhototautomerizational notential barrier and mechanism: The 7-azaindole dimer," Proceedings of the National Academy of Sciences of the United States of America **101**(2), 419--422 (2004).

43. J. Catalan, and de Paz J. L. G., "Study of 7-azaindole in its first four singlet states," Journal of Chemical Physics **122**(24), 244320 (2005).

44. K. Sakota, C. Okabe, N. Nishi, and H. Sekiya, "Excited-State Double-Proton Transfer in the 7-Azaindole Dimer in the Gas Phase. 3. Reaction Mechanism Studied by Picosecond Time-Resolved REMPI Spectroscopy," Journal of Physical Chemistry A **109**(24), 5245-5247 (2005).

45. R. Gelabert, M. Moreno, and J. M. Lluch, "Charge-Transfer Excited State in the 7-Azaindole Dimer. A Hybrid Configuration Interactions Singles/Time-Dependent Density Functional Theory Description," Journal of Physical Chemistry A **110**(3), 1145-1151 (2006).

46. L. Serrano-Andres and M. Merchan, "Theoretical CASPT2 study of the excited state double proton transfer reaction in the 7-azaindole dimer," Chemical Physics Letters **418**(4-6), 569--575 (2006).

47. J. R. Dwyer, J. Dreyer, E. T. J. Nibbering, and T. Elsaesser, "Ultrafast dynamics of vibrational N-H stretching excitations in the 7-azaindole dimer," Chemical Physics Letters **432**(1-3), 146--151 (2006).

48. M. Moreno, A. Douhal, J. M. Lluch, O. Castano, and L. M. Frutos, "Ab Initio Based Exploration of the Potential Energy Surface for the Double Proton Transfer in the First Excited Singlet Electronic State of the 7-Azaindole Dimer," Journal of Physical Chemistry A **105**(15), 3887-3893 (2001).

49. A. Douhal, S. K. Kim, and A. H. Zewail, "Femtosecond Molecular-Dynamics Of Tautomerization In Model Base-Pairs," Nature **378**(6554), 260--263 (1995).

50. O.-H. Kwon and A. H. Zewail, "Double proton transfer dynamics of model DNA base pairs in the condensed phase," Proceedings of the National Academy of Sciences **104**(21), 8703-8708 (2007).

51. W.-T. Hsieh, C.-C. Hsieh, C.-H. Lai, Y.-M. Cheng, M.-L. Ho, K. K. Wang, G.-H. Lee, and P.-T. Chou, "Excited-State Double Proton Transfer in Model Base Pairs: The Stepwise Reaction on the Heterodimer of 7-Azaindole Analogues," Chemical Physics Physical Chemistry **9**(2), 293--299 (2008).

52. J. Catalan, J. C. d. Valle, and M. Kasha, "Resolution of Concerted versus Sequential Mechanisms in Photo-Induced Double-Proton Transfer Reaction in 7-Azaindole H-Bonded Dimer," Proceedings of the National Academy of Sciences of the United States of America **96**(15), 8338--8343 (1999).

53. S. Takeuchi and T. Tahara, "Observation of dimer excited-state dynamics in the double proton transfer reaction of 7-azaindole by femtosecond fluorescence up-conversion," Chemical Physics Letters **277**(4), 340--346 (1997).

54. S. Takeuchi and T. Tahara, "Excitation-wavelength dependence of the femtosecond fluorescence dynamics of 7-azaindole dimer: further evidence for the concerted double proton transfer in solution," Chemical Physics Letters **347**(1-3), 108--114 (2001).

55. S. Takeuchi and T. Tahara, "The answer to concerted versus step-wise controversy for the double proton transfer mechanism of 7-azaindole dimer in solution," Proceedings of the National Academy of Sciences **104**, 5285-5290 (2007).

56. H. Sekiya and K. Sakota, "Excited-State Double-Proton Transfer in the 7-Azaindole Dimer in the Gas Phase. Resolution of the Stepwise versus Concerted Mechanism Controversy and a New Paradigm," Bulletin of the Chemical Society of Japan **79**(3), 373-385 (2006).

57. J. Catalan and M. Kasha, "Photophysics of 7-Azaindole, Its Doubly-H-Bonded Base-Pair, and Corresponding Proton-Transfer-Tautomer Dimeric Species, via Defining Experimental and Theoretical Results," Journal of Physical Chemistry A **104**(46), 10812-10820 (2000).

58. Z. Latajka and S. Scheiner, "Proton transfer in the ground and first excited triplet states of malonaldehyde," Journal of Physical Chemistry **96**(24), 9764-9767 (1992).

59. K. Luth and S. Scheiner, "Excited-State Energetics and Proton-Transfer Barriers in Malonaldehyde," Journal of Physical Chemistry **98**(14), 3582-3587 (1994).

60. A. A. Arias, T. A. W. Wasserman, and P. H. Vaccaro, "Proton transfer dynamics in the first excited singlet state of malonaldehyde," Journal of Chemical Physics **107**(14), 5617-5620 (1997).

61. V. Barone and C. Adamo, "Proton transfer in the ground and lowest excited states of malonaldehyde: A comparative density functional and post-Hartree--Fock study," The Journal of Chemical Physics **105**(24), 11007-11019 (1996).

62. A. D. Becke, "Density-functional thermochemistry. III. The role of exact exchange," The Journal of Chemical Physics **98**(7), 5648-5652 (1993).

63. C. Lee, W. Yang, and R. G. Parr, "Development of the Colle-Salvetti correlation-energy formula into a functional of the electron density," Physical Review B **37**(2), 785--789 (1988).

64. T. M. Kolev, E. A. Velcheva, B. A. Stamboliyska, and M. Spiteller, "DFT and experimental studies of the structure and vibrational spectra of curcumin," International Journal of Quantum Chemistry **102**(6), 1069-1079 (2005).

65. J. B. Foresman, M. Head-Gordon, J. A. Pople, and M. J. Frisch, "Toward a systematic molecular orbital theory for excited states," Journal of Physical Chemistry **96**(1), 135-149 (1992).

66. Y. Shao, L. Molnar, Y. Jung, J. Kussmann, C. Ochsenfeld, S. Brown, A. Gilbert, L. V. Slipchenko, S. V. Levchenko, D. P. O'Neill, R. A. DiStasio, R. C. Lochan, T. Wang, G. J. O. Beran, N. A. Besley, J. M. Herbert, C. Y. Lin, T. Van Voorhis, S. H. Chien, A. Sodt, R. P. Steele, V. A. Rassolov, P. E. Maslen, P. P. Korambath, R. D. Adamson, B. Austin, J. Baker, E. F. C. Byrd, H. Dachsel, R. J. Doerksen, A. Dreuw, B. D. Dunietz, A. D. Dutoi, T. R. Furlani, S. R. Gwaltney, A. Heyden, S. Hirata, C. P. Hsu, G. Kedziora, R. Z. Khalliulin, P. Klunzinger, A. M. Lee, M. S. Lee, W. Liang, I. Lotan, N. Nair, B. Peters, E. I. Proynov, P. A. Pieniazek, Y. M. Rhee, J. Ritchie, E. Rosta, C. D. Sherrill, A. C. Simmonett, J. E. Subotnik, H. L. Woodcock, W. Zhang, A. T. Bell, A. K. Chakraborty, D. M. Chipman, F. J. Keil, A. Warshel, W. J. Hehre, H. F. Schaefer, J. Kong, A. I. Krylov, P. M. W. Gill, and M. Head-Gordon, "Advances in methods and algorithms in a modern quantum chemistry program package," Physical Chemistry Chemical Physics **8**(27), 3172-3191 (2006).

67. M. P. Lopez Sancho, J. M. Lopez Sancho, and J. Rubio, "Highly convergent schemes for the calculation of bulk and surface Green functions," Journal of Physics F: Metal Physics **15**(4), 851-858 (1985).

68. Z. Latajka, Y. Bouteiller, and S. Scheiner, "Critical assessment of density functional methods for study of proton transfer processes. (FHF)," Chemical Physics Letters **234**(1-3), 159-164 (1995).

69. L. Kong, K. I. Priyadarsini, and H. Y. Zhang, "A theoretical investigation on intramolecular hydrogen-atom transfer in curcumin," Journal of Molecular Structure-Theochem **684**(1-3), 111-116 (2004).

70. D.-P. Wang, S.-G. Chen, and D.-Z. Chen, "Theoretical studies of conjugate and substituent effects on the intramolecular proton transfer: an HF/CIS study," Journal of Photochemistry and Photobiology A: Chemistry **162**(2-3), 407-414 (2004).

71. D.-Z. Chen, D.-P. Wang, H.-Y. Zhang, and B. Tang, "Theoretical study on the ground and excited state intramolecular proton transfer in perylenequinone," Chemical Physics Letters **353**(1-2), 119-126 (2002).

72. M. Head-Gordon, A. M. Grana, D. Maurice, and C. A. White, "Analysis of Electronic Transitions as the Difference of Electron Attachment and Detachment Densities," Journal of Physical Chemistry **99**(39), 14261-14270 (1995).

73. M. A. Morgan, E. Orton, and G. C. Pimentel, "Characterization of ground and electronically excited states of o-hydroxybenzaldehyde and its non-hydrogen-bonded photorotamer in 12 K rare gas matrixes," Journal of Physical Chemistry **94**(20), 7927-7935 (1990).

74. C. R. Baiz and B. D. Dunietz, "Theoretical studies of conjugation effects on excited state intramolecular hydrogen-atom transfer reactions in model systems," Journal of Physical Chemistry A **111**(40), 10139 - 10143-10139 - 10143 (2007).

75. J. Catalan, "Spectrothermodynamic relationship of cationic vs anionic species derived from protonation vs deprotonation of pyrrolo-aza-aromatic bases in homologous series," Journal of the American Chemical Society **123**(48), 11940-11944 (2001).

Chapter 8

Conclusions

8.1 Key Results

The experiments presented in the previous chapters have followed along two central themes: *1.* Exploring the solute-solvent relationship from a solute-centric standpoint with particular attention to the role of the solvent in determining dynamics of the solute (Chapters 2, 3, 7). *2.* Understanding chemical dynamics from the solvent's perspective by measuring the response of the nearby solvent to an electronic redistribution within the solute (Chapter 4). Experimentally, it is very challenging to address the solvent molecules that influence a chemical reaction, and often solvation dynamics are inferred by their effect on the solute dynamics.[1-3] However, in many cases overlooking the solvent provides an incomplete view of a chemical reaction,[2, 4] particularly in electron-transfer reactions where the solvent reorganization not only determines the reaction rate, but essentially defines the reaction coordinate.[5-7]

The experiments presented in this work emphasize the capability of ultrafast infrared spectroscopy to resolve complex structure-dynamics relationships in the liquid phase, where the solute modes act as reporters of the solvent dynamics and vice versa. In this last chapter we summarize and discuss the main findings and provide further, discussion of a few selected results.

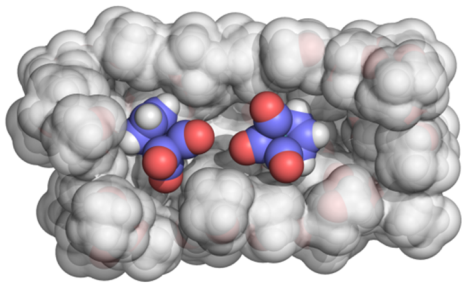

Figure 8.1: Conceptual illustration of molybdenum tricarbonyl radicals reacting inside an ethyl acetate cage.

Polar or ionic species in polar solvents are a typical example of strong system-solvent coupling where, as a result of strong electrostatic forces, solute molecules are to some extent slaved to the solvent motions.[1] However in this work we have shown that for ($CpMo(CO)_3$) radicals in a polar solvent (ethyl acetate) the geminate recombination timescales and reaction channels remain unaffected by the solvent. Similar recombination rates were measured in non-polar solvents (n-hexane, squalane). We believe that this is a special case where the ($CpMo(CO)_3$) radical pairs form a solvent-cage in which the radical-radical interactions dominate over the radical-solvent interactions(see Figure 8.1). Although the recombination rate is unaffected by the solvent, the cage-escape rate is dependent on the viscosity but remains largely insensitive to the solvent polarity. This is consistent with the idea that in order to escape the cage, the solute molecules must physically displace the solvent. Though we've been able to successfully compute the potential energy surface along the reaction path, there is still much to be learned from this particular reaction; mechanistically, it is not clear what type of interactions lead to the cage-escape versus recombination pathways. The role of the solvent polarity, if any, still remains an open question.

In Chapter 4 we presented a novel ultrafast experimental technique—Vibrational-Stark effect (VSE) spectroscopy—which offers a direct view of solvation dynamics by measuring the projection of the solute electric field onto the vibrational modes of the nearby solvent modes (see Figure 8.2). Next we discuss some possible applications for this novel technique.

In principle, if the solvent molecules remain rigid with respect to the solute and their positions are well determined, the solvent frequencies may be used as 'electrostatic sensors'. By measuring the Stark shifts at various points, the charge redistribution at the chromophore

may be reconstructed. Stark shifts, which remain small compared to the inhomogeneous distribution of frequencies, and the large optical density mismatch between the chromophore and bulk solvent make this new technique experimentally demanding. If the exact nature of the charge-transfer reaction is known, it may be possible to directly correlate spectroscopic changes of the chromophore with the motions of the solvent molecules within the first solvation shell. We believe that by directly measuring the solvent nonequilibrium dynamics, VSE spectroscopy in combination with traditional ultrafast methods that measure equilibrium dynamics of the solvent (e.g. 2DIR spectral-diffusion spectroscopy), has the potential to directly test fundamental assumptions in chemical dynamics, such as linear response theory.

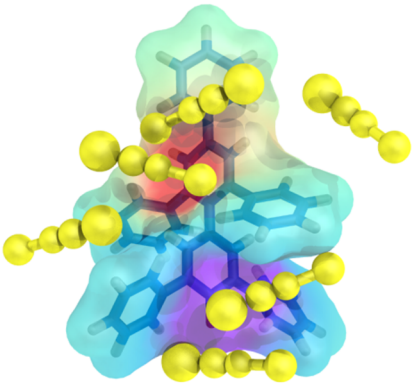

Figure 8.2: Illustration betaine-30 and sodium thiocyanate (yellow). The surface surrounding the molecule represents the solvent-accessible surface of betaine-30, the color map corresponds to the predicted Stark shifts of the CN stretch in sodium thiocyanate at different points near the surface of betaine-30.

Stark tuning rates are easily determined experimentally[8-10] or computed from electronic structure theory.[11] Electronic transition-dipoles and electron density redistributions associated with charge-transfer reactions can be computed to reasonable accuracy with electronic structure methods.[12] Therefore, to model a VSE spectrum, the only remaining unknowns are the positions of the solvent molecules around a chromophore. If the positions can be determined, VSE spectroscopy may be used to calibrate and refine empirical models of intermolecular interactions embedded within molecular dynamics force fields. In addition, since VSE experiments probe inherently nonequilibrium dynamics, MD simulations in these highly nonequilibrium regimes can be tested by comparing experiment

and theory. The experiments should prove useful as most force fields are developed to reproduce equilibrium properties, and there is relatively little experimental data on ultrafast nonequilibrium processes.

Measuring the dynamic Stark spectra of residues near reaction centers in photoactive proteins may provide a view of the structural changes a protein undergoes upon photoexcitation as well as the electrostatic changes near a chromophore. Equilibrium Stark measurements of a nitrile vibrational probe inside a protein have been successful at measuring the strengths of electric fields inside the protein;[8] these electrostatic interactions are considered essential to protein structure and function (e.g. catalysis, ligand recognition, etc.). Since many bioactive compounds contain conjugated moieties, it may be possible to study protein-ligand interactions by exciting electronic transitions within the ligand and monitoring the Stark response of the natural amino-acids, or artificial vibrational probes, within the binding pocket.

Chapter 6 explored the role of the solvent in determining coherence-coherence and coherence-population transfer rates. The model, which is based on a Markovian quantum-master equation, provides an atomistic view of the solvent dynamics through its distinct signatures on multidimensional spectra; for example, coherence-transfer rates between two modes are accelerated when the solvent-induced forces along the same modes are correlated. In a large system with highly-delocalized modes, such as $Mn_2(CO)_{10}$, each mode can serve as a delocalized probe of the low-frequency solvent motions around the molecule. To obtain a more localized model, the normal modes can be decomposed into linear combinations of local modes. In addition to reproducing the experimentally observed dual-frequency oscillations of the cross-peaks, the model predicts that coherence-coherence coupling leads to oscillations of the diagonal peaks in the spectrum. This is significant since oscillations of diagonal peaks in electronic spectra have been attributed to coherence-population coupling (so-called quantum entanglement).[13, 14]

8.2 Vibrational Spectroscopy is Sensitive to Molecular Structure

One issue worth discussing in further detail is the structure-sensitivity of infrared spectroscopy in comparison to electronic spectroscopy. The high sensitivity of electronic energy levels towards the solvent environment is the main origin of the broad spectral lines that characterize UV/Visible absorption spectra.[15] These broad absorptions facilitate the study of solute-solvent interactions (spectral diffusion, etc.) while at the same time obscure structural changes that occur within the chromophore. Electronic absorption only offers indirect information on the nuclear motions of the solute. Recent developments in three-pulse echo peak shift[16] and two-dimensional electronic spectroscopy[17] enable more detailed measurements of electronic spectra, but they too infer the solvent motions indirectly through its effect on the electronic resonances.[18]

In our study of the geminate recombination of $(CpMo(CO)_3)_2$ we have observed a rebinding rate of 31.6 ps whereas transient visible absorption measurements of the same process have reported a recombination rate of 5.6 ps,[19] which we have confirmed through our own transient visible absorption measurements. Though it is clear that further investigation is needed to resolve the observed discrepancies, we believe that the central issue is that, while electronic states are sensitive to molecular changes, electronic transition frequencies in the condensed phase are less well-defined than vibrational ones and structural rearrangements may not always be accurately reflected in the electronic resonances. To illustrate this point consider the following two examples from this work: The first example is the charge-transfer dye betaine-30 (Chapter 4). The absorption maximum is highly dependent on the polarity of the solvent, yet the structure of the molecule remains reasonably rigid in the different solvents.[20] The second example is $(CpMo(CO)_3)_2$, where the *trans* and *gauche* conformations cannot be distinguished in the electronic absorption spectrum even though there are marked structural changes between the two conformations (Chapter 3). These results suggest that one must remain cautious when drawing structural conclusions from electronic absorption spectra.

Broad and featureless lineshapes are also observed in highly disordered vibrational systems such as proteins and peptides.[21] However recent advances in modeling methods are used to extract structural information from these lineshapes.[22] Central to these models is the fact that vibrational energies and couplings are well-defined and can be accurately computed from electronic-structure theory or from simple coupling schemes.[23] Moreover, vibrational

modes can be isolated by isotopic labeling, where as there is no such equivalent in electronic spectroscopy. In contrast to vibrational couplings, electronic-couplings are highly dependent on the overall configuration of the atoms within a molecule. Simplified models such as those based on orbital overlaps are sometimes inadequate. Electronic couplings are mediated by the large-amplitude, low-frequency vibrational modes in the molecule, and change significantly even in slightly different conformations.[24]

8.3 Concluding Remarks

Over the last two decades, ultrafast spectroscopy has been a key technique for investigating the dynamics of numerous systems and molecular processes, which are now beginning to be understood.[25] However the bulk of the experiments have presented a solute-centric view of the dynamics. A prime example of this is dynamic Stokes-shift fluorescence spectroscopy, where the effect of solvation dynamics is inferred by measuring the fluorescence wavelengths following excitation of the chromophore is a series of solvents.[26, 27] New experimental and theoretical techniques are needed to understand the complex relationship between solute and solvent. Investigating the joint dynamics between a chromophore and its solvent remains challenging, nonetheless novel techniques such as vibrational Stark-effect spectroscopy are starting to shed light on this class of problems. We also believe that techniques capable of probing the joint dynamics between a molecule and its first solvation shell such as, two-color 2DIR spectroscopy or ultrabroadband-2DIR spectroscopy will offer a new comprehensive view of chemical dynamics.

Ultrafast multidimensional spectroscopy is far from being a mature field. In fact new techniques and experimental designs are continually being developed. Much progress remains to be made in terms of novel experimental designs and theoretical treatments. Recent structure-frequency maps have greatly empowered 2DIR spectroscopy.[23, 28-32] It is now possible to obtain a molecular-view of protein folding with isotope-edited 2DIR combined with molecular dynamics simulations. These maps, however, have only been applied to isolated modes or weakly-coupled excitonic systems. It would be very useful to develop analogs for highly coupled oscillators (such as the carbonyl stretching modes of $Mn_2(CO)_{10}$) where the frequency-frequency cross-correlations between modes may be used to extract information on the delocalized low-frequency fluctuations of the bath.

Finally, multidimensional spectroscopy can have a broader impact in the field of biophysical chemistry. Much of what is known in this field has come from NMR studies, but NMR spectroscopy cannot reach the subpicosecond timescale of equilibrium fluctuations and cannot probe non-equilibrium light-triggered reactions.[33] Models and interpretations are often based on static views of proteins. Through recent developments in structure-frequency maps for amide-I vibrations,[22, 23] massively-distributed molecular dynamics simulations,[34] and Markov chain models,[35] it is now becoming possible to measure dynamic properties such as protein folding and denaturation with atomistic resolution over several timescales.[36-38] Future applications of multidimensional spectroscopy may include measuring protein secondary and tertiary structure, folding pathways, and timescales, ligand recognition and binding, and the ultrafast interactions between a protein and its hydration shell, including the complex, dynamic role of water in protein folding, structure, and function.

References

1. P. J. Rossky and J. D. Simon, "Dynamics of Chemical Processes in Polar-Solvents," Nature 370(6487), 263-269 (1994).

2. P. F. Barbara, G. C. Walker, and T. P. Smith, "Vibrational-Modes and the Dynamic Solvent Effect in Electron and Proton-Transfer," Science 256(5059), 975-981 (1992).

3. B. Bagchi and B. Jana, "Solvation dynamics in dipolar liquids," Chemical Society Reviews 39(6), 1936-1954 (2010).

4. R. M. Stratt and M. Maroncelli, "Nonreactive dynamics in solution: The emerging molecular view of solvation dynamics and vibrational relaxation," Journal of Physical Chemistry 100(31), 12981-12996 (1996).

5. M. L. Horng, J. A. Gardecki, A. Papazyan, and M. Maroncelli, "Subpicosecond Measurements of Polar Solvation Dynamics - Coumarin-153 Revisited," Journal of Physical Chemistry 99(48), 17311-17337 (1995).

6. A. Nitzan, Chemical dynamics in condensed phases: relaxation, transfer and reactions in condensed molecular systems (Oxford University Press, 2006).

7. P. Barbara, T. Meyer, and M. Ratner, "Contemporary issues in electron transfer research," Journal of Physical Chemistry 100(31), 13148-13168 (1996).

8. I. T. Suydam, C. D. Snow, V. S. Pande, and S. G. Boxer, "Electric Fields at the Active Site of an Enzyme: Direct Comparison of Experiment with Theory," Science 313(5784), 200-204 (2006).

9. S. G. Boxer, "Stark Realities," Journal of Physical Chemistry B 113(10), 2972-2983 (2009).

10. I. T. Suydam and S. G. Boxer, "Vibrational Stark effects calibrate the sensitivity of vibrational probes for electric fields in proteins," Biochemistry 42(41), 12050-12055 (2003).

11. S. H. Brewer and S. Franzen, "A quantitative theory and computational approach for the vibrational Stark effect," Journal of Chemical Physics 119(2), 851-858 (2003).

12. S. R. Mente and M. Maroncelli, "Computer simulations of the solvatochromism of betaine-30," Journal of Physical Chemistry B 103(36), 7704-7719 (1999).

13. D. Abramavicius and S. Mukamel, "Quantum oscillatory exciton migration in photosynthetic reaction centers," Journal of Chemical Physics 133(6), 9 (2010).

14. S. Mukamel, "Communications: Signatures of quasiparticle entanglement in multidimensional nonlinear optical spectroscopy of aggregates," Journal of Chemical Physics 132(24), 241105 (2010).

15. M. Cho, Two-dimensional optical spectroscopy (CRC Press, Boca Raton, 2009)

16. W. P. de Boeij, M. S. Pshenichnikov, and D. A. Wiersma, "Ultrafast solvation dynamics explored by femtosecond photon echo spectroscopies," Annual Review of Physical Chemistry 49, 99-123 (1998).

17. D. M. Jonas, "Two-dimensional femtosecond spectroscopy," Annual Review of Physical Chemistry 54, 425-463 (2003).

18. K. L. M. Lewis, J. A. Myers, F. Fuller, P. F. Tekavec, and J. P. Ogilvie, "Two-dimensional electronic spectroscopy signatures of the glass transition," Spectroscopy-an International Journal 24(3-4), 393-397 (2010).

19. A. B. Oelkers, L. F. Scatena, and D. R. Tyler, "Femtosecond pump-probe transient absorption study of the photolysis of [Cp ' Mo(CO)(3)](2) (Cp ' = eta(5)-C5H4CH3): Role of translational and rotational diffusion in the radical cage effect," Journal of Physical Chemistry A 111(25), 5353-5360 (2007).

20. C. Reichardt, "Solvatochromic Dyes as Solvent Polarity Indicators," Chemical Reviews 94(8), 2319-2358 (1994).

21. L. P. Deflores, Z. Ganim, R. A. Nicodemus, and A. Tokmakoff, "Amide I'-II' 2D IR spectroscopy provides enhanced protein secondary structural sensitivity," Journal of the American Chemical Society 131(9), 3385-3391 (2009).

22. T. L. Jansen, A. G. Dijkstra, T. M. Watson, J. D. Hirst, and J. Knoester, "Modeling the amide I bands of small peptides," Journal of Chemical Physics 125(4), - (2006).

23. T. L. Jansen and J. Knoester, "A transferable electrostatic map for solvation effects on amide I vibrations and its application to linear and two-dimensional spectroscopy," Journal of Chemical Physics 124(4), - (2006).

24. H. Langhals, A. J. Esterbauer, A. Walter, E. Riedle, and I. Pugliesi, "Förster Resonant Energy Transfer in Orthogonally Arranged Chromophores," Journal of the American Chemical Society 132(47), 16777-16782 (2010).

25. M. Cho, "Coherent Two-Dimensional Optical Spectroscopy," Chemical Reviews 108(4), 1331-1418 (2008).

26. M. H. Cho, S. J. Rosenthal, N. F. Scherer, L. D. Ziegler, and G. R. Fleming, "Ultrafast Solvent Dynamics - Connection between Time Resolved Fluorescence and Optical Kerr Measurements," Journal of Chemical Physics 96(7), 5033-5038 (1992).

27. G. Vanderzwan and J. T. Hynes, "Time-Dependent Fluorescence Solvent Shifts, Dielectric Friction, and Nonequilibrium Solvation in Polar-Solvents," Journal of Physical Chemistry 89(20), 4181-4188 (1985).

28. S. A. Corcelli, C. P. Lawrence, J. B. Asbury, T. Steinel, M. D. Fayer, and J. L. Skinner, "Spectral diffusion in a fluctuating charge model of water," Journal of Chemical Physics 121(18), 8897-8900 (2004).

29. S. A. Corcelli, C. P. Lawrence, and J. L. Skinner, "Combined electronic structure/molecular dynamics approach for ultrafast infrared spectroscopy of dilute HOD in liquid H2O and D2O," Journal of Chemical Physics 120(17), 8107-8117 (2004).

30. T. l. C. Jansen and J. Knoester, "Calculation of two-dimensional infrared spectra of ultrafast chemical exchange with numerical Langevin simulations," Journal of Chemical Physics 127(23), 234502-234502 (2007).

31. T. l. C. Jansen and J. Knoester, "Waiting Time Dynamics in Two-Dimensional Infrared Spectroscopy," Accounts of Chemical Research 42(9), 1405-1411 (2009).

32. J. H. Choi, K. I. Oh, H. Lee, C. Lee, and M. Cho, "Nitrile and thiocyanate IR probes: Quantum chemistry calculation studies and multivariate least-square fitting analysis," Journal of Chemical Physics 128(13), - (2008).

33. H. Ishikawa, K. Kwak, J. K. Chung, S. Kim, and M. D. Fayer, "Direct observation of fast protein conformational switching," Proceedings of the National Academy of Sciences of the United States of America 105(25), 8619-8624 (2008).

34. M. Shirts and V. S. Pande, "COMPUTING: Screen Savers of the World Unite!," Science 290(5498), 1903-1904 (2000).

35. V. S. Pande, K. Beauchamp, and G. R. Bowman, "Everything you wanted to know about Markov State Models but were afraid to ask," Methods 52(1), 99-105 (2010).

36. G. R. Bowman, X. Huang, and V. S. Pande, "Network models for molecular kinetics and their initial applications to human health," Cell Research 20(6), 622-630 (2010).

37. G. R. Bowman, K. A. Beauchamp, G. Boxer, and V. S. Pande, "Progress and challenges in the automated construction of Markov state models for full protein systems," Journal of Chemical Physics 131(12), 124101 (2009).

38. G. R. Bowman and V. S. Pande, "Protein folded states are kinetic hubs," Proceedings of the National Academy of Sciences of the United States of America 107(24), 10890-10895 (2010).